Counter-current gas-liquid contacting in a Rotating Spiral Channel: Experimental and Theoretical Study

A Thesis
submitted to the University of Sheffield for the degree of Doctor of Philosophy in the Faculty of Engineering

By

Ahmed A. A. AYASH

Chemical and Biological Engineering Department,

The University of Sheffield,

United Kingdom.

July 2018

Dedication

To my late parents who taught me to love learning, my wonderful wife Milad for her support and my lovely daughters Dema & Dana who wonder what I do all the day.

Ahmed AYASH

Acknowledgments

I would like to express my deepest gratitude to all my family, friends and colleagues who have contributed in finishing this work. I spent almost four years working on this thesis and during this time many people have helped in one way or another to make this work happen.

First of all, I would like to thank my supervisor 'Dr Jordan MacInnes' for his many hours of guidance, patience and material support for this work. Jordan was always available, no matter how busy, to discuss and comment critically on the theoretical and practical aspects of the work. His knowledge, wisdom and enthusiasm in the work are unrivalled, I feel lucky to be supervised by him. I also must thank Professor Willam Zimmerman and Dr Willam Furnass for their help to provide access to Sheffield's high-performance computing system (iceberg). I want to thank also Dr George Dowson for the helpful discussion regarding the safe handling of the chemical materials used in the experiments.

Thanks and appreciation go to all the technicians in our department. Particularly, Mr Mark McIntosh, Mr Mark Jones, Mr James Grinham, Mr Keith Penny and Mr Usman Younis for their appreciable efforts in fixing technical problems experienced during this work. I want to thank also Mr Robert Hanson in the chemistry department/University of Sheffield for helping in the analysis process of the samples.

Special thanks to my wife 'Milad' for her understanding, patience and sacrifice for bearing my period of study. Without her support, this work would not have been finished. I owe her. I would like to thank my sister 'Areej' and my wife's father 'Mr Adel Mahmoud' for their continuous support in Iraq throughout my doctoral journey. I also must thank my friend 'Dr Khalid Murshid' for his support and all the staff of Materials Engineering Department in Al-Mustansriya University. Many thanks to my lovely daughters 'Dema & Dana' who have shown outstanding patience as I have not been able to spend much time with them.

Last, but not least, I thank my country represented by 'the Higher Committee for Education Development in Iraq' for scholarship and every individual in my country as each of them contributes in the fund of this scholarship.

Abstract

Controlled counter-current contacting between a gas and a liquid forms the basis for a wide range of chemical separation operations, including absorption, stripping and distillation. A radical technique based on the rotating of a spiral channel can achieve segregation of any two immiscible phases into two parallel layers, allowing for a detailed control of phase flow rates and phase layer thicknesses. This work experimentally and theoretically studied the mass transfer process of gas-liquid contacting in this novel contactor, aiming for understanding, evaluating and demonstrating its performance.

In order to establish the spiral performance, experiments were conducted over a wide range of contacting conditions. In the experiments, desorption of four different organic solutes from water was studied separately at dilute concentrations, using air as a sweeping gas. The solutes were ethanol, acetonitrile, acetone and 2-butanone (MEK). This collection of solutes at different spiral temperatures (24, 30 and 49°C) gives a range of solute equilibrium distributions (f') from 0.232 to 5.5 (the mole fraction ratio of solute in the two phases). Thus, the performance of the rotating spiral channel was explored using phase and solute systems having different equilibrium characteristics (f') and solute transferring properties. The other contacting conditions were the pressure and the rotation rate, which were fixed to 1.8 bara and 3200 rpm, respectively. For each phase and solute system (f'), the amount of solute desorbed was measured over a range of phase flow rates. Interestingly, the results showed that a fixed channel design can process a variety of systems at any desired conditions, producing solute-free water when operating at the appropriate phase flow rate ratio. Furthermore, the experimental results showed a universal peak in the mass transfer coefficient at a liquid layer thickness between 80-90 μm. The peak occurred independently of the gas phase flow rate and appeared prominently for the systems with large f', where the mass transfer was much affected by the liquid phase. This finding indicates that independent adjustment of the liquid phase flow rate could determine the optimum contacting and this optimum can be tailored to occur at any desired phase flow rates ratio by changing only the gas phase flow rate. Thus, simultaneously, the optimal contactor size and solvent usage could be achieved with rotation spiral contacting.

In addition, the spiral performance, based on the extensive data of the current work, was compared to the performance for the conventional packed column, rotating packed beds and the membrane microchannel using data from the literature for these contactors. The normalised total specific throughput (molar flow rate of the treated stream divided by the contactor volume) was developed here and used as the comparison criterion. The maximum of this measure corresponds to a minimum contactor volume to achieve a given separation task. The comparison showed that the rotating spiral was able to operate in the appropriate range of phase flow rate ratios and gave the highest specific throughput. This suggests that the contactor size for this method can be many times smaller than that of the other methods considered.

A two-dimensional (2-D) computational model was adopted in this work to study the detail of the flow and species fields that determine the mass transfer process. This model is based on a novel combination of the governing equations and an existing interface model to capture accurately the Coriolis acceleration effects and phase interactions. The 2-D model effectively predicted a wide range of experimental conditions, demonstrating that Coriolis secondary motion could double the mass transfer performance. A parametric study was also conducted using the 2-D model, where desorption of acetone was taken as a reference case. The purpose of this study was to examine the role of three key parameters (rotation rate, channel aspect ratio and flow rate of both phases) that were not tested experimentally. The results demonstrated that by adjusting the rotation rate (Ω), the contacting process could be optimised. For a range between 1000 and 20,000 rpm, it was found that Ω =16,000 rpm gave a maximum mass transfer coefficient. Furthermore, the data showed that the spiral performance was enhanced considerably by changing the channel aspect ratio. Reducing the channel width from 4 mm to 1 mm increased the mass transfer coefficient by a factor of two. Finally, at a given rotation rate and channel aspect ratio, an improvement in mass transfer was observed by adjusting the flow rates of the contacting phases. Increasing the flow rate of both phases increased the mass transfer coefficient also by a factor of two.

In general, the experimental and theoretical work in this thesis demonstrate the potential of rotating spiral contacting and establish a useful foundation underpinning its future development.

Main Publications

Ayash, A. A. and MacInnes, J. M., 2017. Mass Transfer Prediction of Gas-Liquid Contacting in a Rotating Spiral Channel. in *the 4th International Conference of Fluid Flow, Heat and Mass Transfer (FFHMT'17)*. Toronto, Canada, pp. 1–8.

MacInnes, J.M. and Ayash, A.A., 2018. Mass transfer characteristics of rotating spiral gas-liquid contacting. *Chemical Engineering Science*, *175*, pp.320–334.

Ayash, A. A. and MacInnes, J. M., 2018. 2-D parametric analysis of Gas-Liquid Contacting in a Rotating Spiral Channel. To be submitted.

Nomenclature

Symbol	Definition
A	Area, m^2
a	Interfacial surface area per passage volume, m^2/m^3
a_{12} and a_{21}	Adjustable parameters of UNIQUAC model
a_L	Purity of the heavy phase (solvent) in absorption process
a_V	Purity of the light phase (target phase) in absorption process
D	Solute diffusion coefficient, m^2/s
d_L	Purity of the heavy phase (target phase) in desorption process
d_V	Purity of the light phase (solvent) in desorption process
E_o	Eötvös number (ratio of the centrifugal force to the interfacial force)
Ek	Ekman number (ratio of viscous force to Coriolis force)
f'	Slope of solute equilibrium relation, $Y_V = f(Y_L)$
Fr	Froude number (ratio of inertial force to centrifugal force)
g	Gravity acceleration, 9.81 m/s^2
h	Channel height, m
h_{Lm}	Minimum liquid layer thickness, mm
h_m	Interface meniscus height, m
j	Solute molar flux across the phase interface, $Kmol/m^2/s$
K	Overall mass transfer coefficient, $Kmol/m^2/s$
k	Individual mass transfer coefficient, $Kmol/m^2/s$
L	Contact length, m
ℓ	Diffusion length, m
ℓ_I	Length of phase interface, m
ℓ_e	Length of one equilibrium stage, m
M	Molar mass, kg/kmol
N	Molar flow rate, Kmol/s
N_e	Number of equilibrium stages
N_E	Number of elements used in the numerical computations

n	Molar density, Kmol/m^3
p	Pressure, Pa
$\hat{p}$	Piezometeric pressure, Pa
$\mathbf{Pe}$	Péclet number (ratio of mass transfer by fluid motion to mass transfer by molecular diffusion)
Q	Volumetric flow rate, m^3/s
Q_{LC}	Liquid phase volumetric flow rate in the meniscus region, m^3/s
q	Phase volumetric flow rates ratio, $q = Q_V / Q_L$
q_n	Phase molar flow rates ratio, $q_n = n_V Q_V / n_L Q_L$
q_{nC}	Critical molar flow rates ratio
R	Spiral radius, m
Re	Reynolds number (ratio of inertial force to viscous force)
Ro	Rossby number (ratio of inertial force to Coriolis force)
r	Interface radius, m
$\mathbf{Sc}$	Schmidt number (ratio of momentum diffusivity to mass diffusivity)
T	Temperature, ^{o}C or K
t	Spacing distance between spiral channels, m
t_m	Residence time, s
t_S	Sampling time, s
u	Velocity component in *x* direction, m/s
$\vec{V}$	Velocity vector, m/s
v	Velocity component in *y* direction, m/s
$\overline{V}$	Root-mean-square velocity, $\overline{V} = \sqrt{\frac{1}{A}\left(\int_A u^2 \, dA + \int_A v^2 \, dA\right)}$
W	Spiral channel width (direction parallel to the phase interface), m
w	Velocity component in z direction, m/s
We	Weber number (ratio of inertial force to interfacial force)
Y	Solute mole fraction
x, y, z	Cartesian Coordinates

Greek Symbols

Symbol	Definition
α	Spiral angle, degrees or radians
Γ	Conservative flux vector in Comsol Multiphysics Software
γ	Liquid phase activity coefficient
γ_r	Ratio of the centrifugal force to the pressure force
δ_C	Capillary height, m
ε	Void fraction
θ	Azimuthal angle of spiral, degrees or radians
λ	Ratio of the centrifugal force to the gravity force
μ	Viscosity, Kg/m/s
ν	Kinematic Viscosity, m^2/s
ξ	Fraction of the passage volume occupied by the heavy phase
ρ	Density, kg/m^3
σ	Surface tension, N/m
τ	Shear stress, Pa
Φ	Specific throughput, s^{-1}
Φ_N	Total Specific throughput, s^{-1}
Ω	Rotation rate, rad/s (1 rad/s equivalent to 9.549 rpm)

Subscripts

Symbol	Definition
B	Bulk (mean value of velocity, concentration or pressure)
C	Critical or corner
e	Equilibrium
I	Interface
L	Heavy phase (liquid)
V	Light phase (gas)
W	Wall or Water

Superscripts

Symbol	Definition
*	Normalised variable
∞	Infinite dilution
Sat	Saturation
.	Rate

Abbreviations

Symbol	Definition
CFD	Computational fluid dynamics
FEM	Finite element method
MEK	Methyl ethyl Ketone or 2-butanone
PDE	Partial differential equation
rms	Root mean square
UNIFAC	UNIQUAC Functional-group Activity Coefficients model
UNIQUAC	Universal QuasiChemical model
WCM	Wide-channel model

Table of Contents

List of Figures

List of Tables

Chapter One

Introduction

Separation of chemical mixtures is indispensable and the backbone of many chemical processing systems. Most of the towers and columns in the typical refineries or chemical plants are there to purify raw materials, intermediate products or even final products before they end up to the consumer. Equally, there are many analytical applications based on separation of chemical components such as gas chromatography, kidney dialysers, blood oxygenators and other laboratory and medical techniques (Still et al., 1978; Cussler, 1997).

Separation operations, whether on a large or small scale, commonly involve gas-liquid contacting. For example, a volatile species can be separated from a liquid stream by adding a second immiscible gas phase. This operation is known as '*liquid desorption*' or '*stripping*'. The typical application of this kind of operation is the removal of volatile organic compounds from waste-water using air stream (Hwang et al., 1992). The opposite operation is also possible, a liquid solvent can be used to purify a stream of gas. This operation is known as '*gas absorption*'. Crude oil, which is a complex chemical mixture, can be separated into a number of useful products by exploiting the difference in boiling points of the individual components. This type of separation is called '*distillation*'. In this case, energy (heat) is used and/or the system pressure is reduced to generate the gas phase (vapour) and so the contacting is between liquids and their vapours.

In all the above examples of gas-liquid contacting, separation is achieved by improving mass transfer of certain species by diffusion relative to its transfer by fluid motion. Enhancing mass transfer by diffusion is achieved by creating an intimate contact between the phases so the diffusion path becomes small and molecules move at high speeds between them, across an interface. The way of achieving this intimate contact has been the subject of numerous studies, involving many approaches based on different contacting principles. Most of these approaches, typically, bring the phases together in such a way that one of the phases is divided into discrete elements (bubbles, droplets or films) within the continuous second phase. Although this way of contacting enhance the

mass transfer of molecules by shortening the diffusion path, they risk the penalties of dispersing one phase into the other. Some of the consequences of this mixing process are: (1) phase ejection (i.e. liquid flooding or gas entraining), (2) difficulties to control phase hydrodynamic characteristics (film thickness, droplet or bubble size and phase velocities), which, in turn, affect adversely the mass transfer between the phases and (3) limitations on the range of phase flow rates ratio that can be handled. This ratio is dictated by solute equilibrium properties. So the approach suitable for one phase and solute system is not necessarily suitable for others. Furthermore, the separation of the phases after the contacting process is necessary and that could pose considerable operational difficulties such as the separation of easily foamed systems (de Santos et al., 1991; Sengupta et al., 1998; Hessel et al., 2005; MacInnes et al, 2012).

The rotating spiral technique is an emerging approach that has the potential to produce a controlled contact between any two immiscible fluid phases (MacInnes et al., 2015). This distinctive feature allows a variety of mass transfer applications to be within the capability of this technique, including gas-liquid contacting. In this technique, the mechanism of contact of fluid phases *avoids* any mixing, providing solutions for most of the difficulties arising as a result of dispersion of one phase into the other. The technique uses a spiral channel spinning around an axis through its origin as shown in Fig. 1.1, producing both centrifugal and Coriolis acceleration. The centrifugal acceleration with adjustment of the pressure gradient along the channel allows the fluid phases to flow either counter-currently or co-currently, side by side as two separate layers. The Coriolis acceleration and spatial variation of streamwise velocity produce secondary flow in each phase (Fig. 1.1) which can enhance mass transfer by convection. In contrast with other dispersed-phase techniques, this organised pattern of contacting can be achieved with a high degree of control. The relative flow rates and the hydrodynamics obtained (i.e. phase layer thicknesses and phase velocities) are decoupled and can be controlled independently with this technique. The former, which is determined mainly by phase equilibrium characteristics, governs the extent of separation. The latter, on the other hand, dictates the separation rate. Therefore, with the ability to control these parameters independently, optimum contacting of systems having different equilibrium and transferring properties can be achieved, in principle, using the rotating spiral technique.

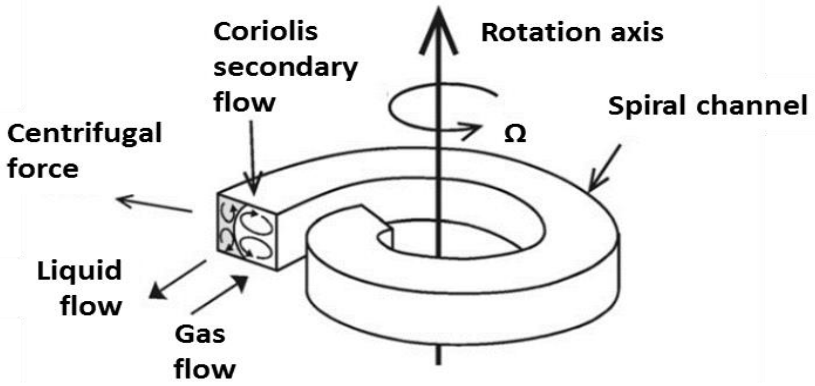

Figure 1.1. Counter-current gas-liquid contacting in a rotating spiral channel (MacInnes et al., 2010).

1.1 Research Motivations and Objectives

Recently, a theoretical study regarding two phase contacting in a rotating spiral channel has been developed in MacInnes et al. (2012). In the study, the authors put forward a model for a case where the channel is very wide and gravity is negligible. As a result, the phase interface is flat and no secondary motion results from Coriolis acceleration. Following up this work, an experimental study has been carried out that focuses only on the hydrodynamic characteristics of gas-liquid contacting (MacInnes and Zambri, 2015). In this study, the first prototype device allowing continuous counter-current contacting was described and a mathematical model '*interface-model*' that can predict the true shape of the interface was developed.

While these recent works significantly make a progress towards understanding fundamental aspects of rotating spiral contacting, this approach is still viewed as a new technology and needs to be investigated thoroughly. Experimental and theoretical study assessing comprehensively the spiral performance for a gas-liquid contacting process have yet to be established. The work reported in MacInnes and Zambri (2015) did not investigate the mass transfer. Therefore, the first motivation for this research is to investigate experimentally the mass transfer performance of rotating spiral approach over a wide range of gas-liquid contacting conditions. In particular, counter-current physical desorption of a range of dilute solutes from water into the air was studied over different phase flow rates. This experimental scheme allows a range of mass transfer data to be

produced. These results are used here to: (1) characterise the mass transfer behaviour of the experimental channel, (2) compare the performance of the spiral channel with other approaches and, most importantly, (3) assess a computational model adopted in this work to simulate the contacting process in spiral channels and that is discussed below.

Understanding the rotating spiral contacting requires modelling work. Although the wide channel model (MacInnes et al., 2012) is helpful in exploring some aspects of the rotating spiral contacting, it does not lead to a full understanding of two-phase contacting in actual channels. The assumption of infinite width (i.e. no end-walls) makes the model unable to capture the effect of the interface shape and Coriolis secondary motion. To understand the mechanism of mass transfer in rotating spiral contacting, it is important to explore the role of these parameters since they affect directly the mass transfer. Based on this fact, a second motivation for this research is to investigate the process of gas-liquid contacting in a rotating spiral channel using a 2-D computational model. The model is based on a 2-D numerical solution of the governing equations, using the actual interface shape determined a priori from the existing interface model. This combination allows, for the first time, investigation of the effect of both the interface profile and Coriolis secondary motion on the rotating spiral contacting. It is believed that such modelling approach will help not only to understand the process of gas-liquid contacting but also to optimise the design of spiral channels and separation processes.

According to the above, the ultimate objectives of this research can be summarised as follows:

I. Investigate experimentally the mass transfer performance of rotating spiral technique over a wide range of gas-liquid contacting conditions (phase flow rates and solute equilibrium distributions).

II. Develop a consistent basis for evaluating contacting performance and compare the performance of rotating spiral with other alternatives approaches that achieve the same separation task.

III. Investigate in detail the mechanism of mass transfer in the experimental spiral channel using a 2-D computational model, established based on the combination of the governing equations and the interface model.

IV. Assess the effectiveness of the 2-D model, determining its limitations.

V. Conduct a computational study to understand quantatively the effect of key parameters on the rotating spiral contacting and to demonstrate the flexibility of this approach.

1.2 Thesis Structure

This thesis consists of nine chapters that describe step by step what has been done to achieve the above objectives and what the main findings are.

Chapter one, as discussed above, gives a general idea about the rotating spiral technique, motivations and main objectives of the current research.

Chapter two is a background about the constraints of two phase contacting and a critical review of common existing gas-liquid contactors. The chapter also provides a detailed review on the rotating spiral, highlighting its features and the current state of the art.

Chapter three presents a general theoretical framework for counter-current physical mass transfer which allows analysis of experimental data for different contacting approaches. In the chapter, a standard relation to calculate the experimental mass transfer coefficients is presented along with a general design equation. The term *'total specific throughput*', which is the throughput of processed phase at a given purification per device volume, is introduced and is argued that should be used to compare different contactors under different conditions.

Chapter four gives a full development of a 2-D computational model of two-phase contacting in a rotating spiral channel. This includes the governing equations, boundary conditions and the interface model. Furthermore, the chapter provides a full description of the numerical solution and a series of computations to demonstrate the general behaviour and the effect of gas and liquid flow rate on the contacting process.

Chapter five describes the experimental procedure used in this work to collect the mass transfer data. This includes an overview about the experimental apparatus, the experimental measurements, the evaluation of water evaporation effect, the method developed to collect valid samples and finally the analysis techniques used to measure liquid phase composition.

Chapter six is a brief chapter describing in detail the method for determining the solute and phase physical properties used throughout this study.

Chapter seven presents the mass transfer results collected using the method described in Chapter 5. The effect of phase flow ratio and solute equilibrium distribution on the degree of the purification and the contacting effectiveness are discussed. Also, the mass transfer coefficients are characterised in terms of the liquid layer thickness. At the end of the chapter, a comparative study between the rotating spiral and the other approaches (packed bed column, rotating packed bed and membrane microchannel) is presented.

Chapter eight presents the computational results. This includes a comparison between the experimental data and the predictions of the 2-D computational model. Further, the chapter includes a parametric study to investigate the role of rotation rate, channel aspect ratio and phase flow rates.

Chapter nine summarises and discusses the main conclusions of the research findings and suggests promising directions for future investigations.

At the end of the thesis, six appendices are compiled (A, B, C, D, E, and F) to provide further information. Appendix A demonstrates the implementation of the governing equations and the boundary conditions in Comsol Multiphysics software (Ver. 5.2). Appendix B describes the method of spiral pressure and temperature determination. Appendix C gives a sensitivity analysis study to evaluate the effect of the measurement uncertainties on the mass transfer coefficient estimated from the experimental data. The materials used in the experiments are presented in Appendix D. The calibration procedure and curves for the instrumental analysis techniques used in this work are presented in Appendix E. Finally, a presentation of the UNIQUAC model and the method to determine the liquid phase activity coefficients as a function of solute mole fraction and temperature are given in Appendix F.

Chapter Two

Background and Literature Review

This chapter presents a general background concerning two phase contacting and reviews the principal topics of this work. The gas-liquid contacting and the challenges to achieving a controlled counter-current contacting are discussed first. This is followed by a brief summary of the constraints associated with phase contacting and brief details of the common existing gas-liquid contactors. Next, a description of the rotating spiral technique is presented, highlighting key features and the role of the centrifugal and Coriolis accelerations. Finally, the previous theoretical and experimental work on this technique are reviewed and the main theme of the current work is described.

2.1 Gas-Liquid Contacting

Gas-liquid contacting is widely practiced in various industrial and analytical applications using different types of contactors. Of these contactors, the type based on counter-current contacting of phases is most commonly used (Yang et al., 2009). Comparing to co-current flow mode, counter-current contacting is an effective way to maintain the necessary concentration difference between the phases (De Santos et al., 1991).

Most existing counter-current contactors employ at least one of the following approaches to achieve a gas-liquid contacting process: (1) breaking up the gas phase into small bubbles in a continuous liquid phase (e.g. plate and bubble columns, Fig. 2.1), (2) dividing the liquid phase into small drops in a continuous gas phase (e.g. spray towers, Fig. 2.1) and (3) spreading the liquid phase over static or rotating solid surfaces to flow as a thin film or flying droplets through a continuous gas phase (e.g. packed bed columns and rotating packed beds, Fig. 2.1) (Treybal, 1981; McCabe et al., 1993; Kohl and Nielsen, 1997; Seader and Henley, 2006).

Although these approaches appear to be radically different in Fig. 2.1, they have much in common due to the fact that they are based on the dispersion of one of the phases into the other. In many practical cases, this way of contacting produces successfully the close association needed to allow solute species transfer to occur. However, this method also brings the complexities of phase-mixing which leads to a number of limitations and

difficulties. The breakup process of one of the phases and forcing it to move through the other phase puts both phases under great drag forces. As a direct consequence, they suffer from severe 'velocity limits' restrictions which make it possible to maintain counter-current contacting only at a quite limited range of relative phase flow rates. Exceeding the limiting flow rate of one of the phases relative to the other phase causes phase ejection (Ramshaw, 1993) which is inherent in all dispersed-phase contactors, in particular non-rotating ones. Therefore, the throughput of the processed phase relative to the contactor size is often limited with these approaches.

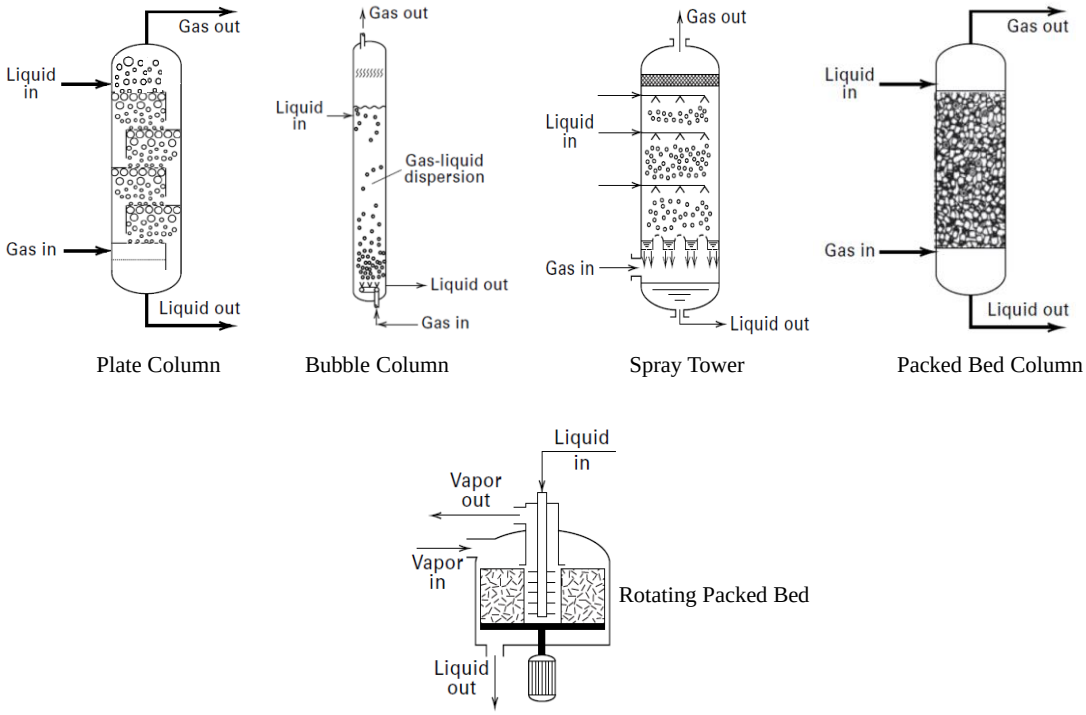

2.1. Some examples of rotating and non-rotating gas-liquid contactors (adapted from Seader and Henley, 2006).

Furthermore, the desired solute species is transferred between the phases at a rate that depends on phase geometries (film, droplet or bubble sizes), the velocity scale of the phases and the solute concentration in each phase. By mixing the phases, the hydrodynamics obtained (i.e. phase geometries and velocities) are determined in a complex way by many parameters. The most crucial parameter, arguably, is the phase flow rates ratio along with other parameters, including the forces that drive the fluids, packing geometry (if any), surface tension and phase physical properties (Hessel et al.,

2005; Lam et al., 2013; MacInnes et al, 2015). Unfortunately, the allowable phase flow rates ratio is limited by the usual constraint of phase equilibrium. Thus, it is likely that there is difficulty in obtaining an optimum mass transfer with the dispersed phase approaches and this difficulty is very fundamental. On the one hand, the phase flow rates ratio must satisfy the equilibrium constraint and, on the other hand, this ratio determines the mass transfer parameters (phase geometries and velocities). So detailed control of the contacting process such that both the flow rate ratio and the mass transfer rate are optimum seems unattainable with these approaches and if achieved may be limited to narrow ranges of phase and solute property values and operating conditions.

Another point to note is that, in general, there is uncertainty regarding maintaining constant phase geometries and hence the amount of interfacial area per unit volume in a dispersed-phase contactor. Bubbles and droplets tend to coalescence, leading to a variable contacting time. Similarly, for rotating systems like a rotating packed bed in Fig. 2.1, it is difficult to maintain conditions that are effective throughout the device. The flow area and the strength of the centrifugal force, which drives the liquid phase, vary with the radial position. This means that the liquid velocity and liquid element size are not constant, but change during the contacting process. Thus, with mixing phases methods (whether relying on rotation or not), it is difficult to establish controlled contacting prevailing everywhere in the contacting volume, typically with the result that the contactor must be large to achieve a specific separation task.

As pointed out in Chapter 1, the technique considered here is a departure from these approaches. It rests on the principle of guiding a gas and a liquid to flow in a continuous path and keeping the phase integrity by avoiding the phase mixing. This simple configuration of contacting under the effect of rotation, uniquely, has features towards controlling the contacting process between any two immiscible fluid phases. The relative flow rates and relative layer thicknesses of the phases can be controlled independently and simultaneously by changing the rotation rate and the pressure drop, each of which is under external control. This enables adjustment to obtain optimum mass transfer and allows handling fluid-phase systems having widely differing viscosities, densities, solute equilibrium characteristics and solute diffusivities.

In order to fully understand the key differences between the rotating spiral and other approaches, the constraints for two-phase contacting and the existing gas-liquid contactors are discussed in the next sections.

2.2 Constraints for Phase Contacting

The molecular diffusion of species within a single phase is enhanced by reducing the characteristic size of the diffusion length; the smaller the diffusion path, the higher the rate of mass transfer. However, when two phases are in contact, which is a typical situation in many separation processes, a diffusion process occurs in each phase simultaneously and both must be considered. Additionally, through the contacting process, equilibrium can be established between the phases due to mass transfer. To transfer a solute out of a target phase and hence achieve the required purity, it is necessary to depart from this equilibrium (de Santos et al., 1991). This means that operating at conditions approaching equilibrium limits must be avoided, otherwise a sharp separation cannot be achieved.

These fundamentals, i.e. considering the contribution of each phase to mass transfer and the phase equilibrium, are common constraints to all two-phase contacting. In many literature sources, the implications of these constraints are discussed but rather limited to a specific case such as desorption of a liquid phase or absorption of a gas phase. For the present purpose, it is helpful to discuss these constraints from a general point of view, clarifying the implications for relative phase flow rates and relative phase element sizes. This discussion is presented in the next subsections.

2.2.1 Thermodynamic Equilibrium and Flow Rate Restrictions

The first constraint for two-phase contacting comes from thermodynamic equilibrium. The equilibrium characteristics place limits on the allowed phase flow rates. In general, there is a critical flow rate ratio of the phases beyond which it becomes impossible to achieve the required purification.

The critical flow rate ratio (q_{nC}) can be found simply by making a solute material balance for two phases contacting counter-currently where the outlet solute concentration in the solvent stream has reached equilibrium with the inlet process stream (e.g. Sherwood et al., 1975; Treybal, 1981; McCabe et al., 1993). To give a general account of q_{nC}, two possible cases are considered here. The case in which solute transfers from the light phase to the heavy phase (absorption) and the case in which the transfer occurs in the opposite direction (desorption). Fig. 2.2 shows a schematic representation of these

possible cases, where Y_V and Y_L are solute mole fraction in the light phase and heavy phase, respectively.

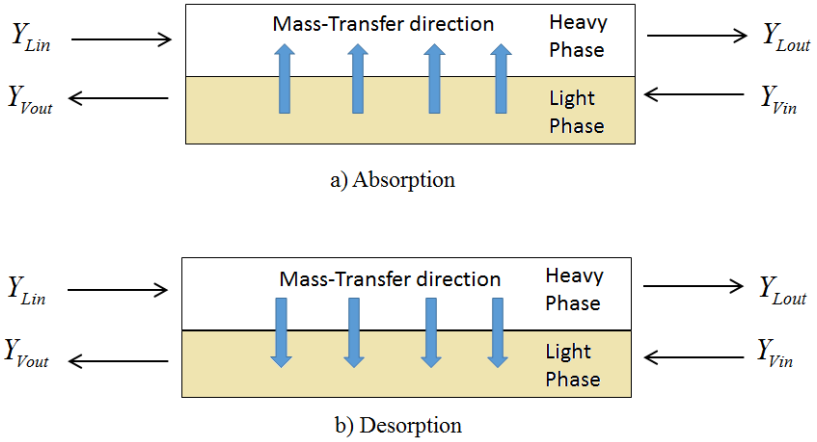

Figure 2.2. Two possible cases of a solute transfer between two phases.

For the two cases shown in Fig. 2.2, q_{nC} can be represented by the ratio of the light phase molar flow rate to that of the heavy phase and has a negative sign for counter-current contacting. Further, it is often a good approximation to take the equilibrium solute mole fraction in one of the phases as proportional to that in the second phase. In this case, the general relation $Y_V = f(Y_L)$ can be written as:

$$Y_V = f' Y_L \tag{2.1}$$

where f' is the solute equilibrium distribution at a given pressure and temperature.

Use of this equilibrium relation and requiring the mole fraction of solute in the outlet solvent phase to be in equilibrium with the inlet process phase, the following relations for the critical flow rate ratio result:

$$\text{For absorption} \qquad -q_{nC} = \frac{1 - f' a_L}{f'(1 - a_V)} \tag{2.2}$$

$$\text{For desorption} \qquad -q_{nC} = \frac{1 - d_L}{f' - d_V} \tag{2.3}$$

a_V and a_L represent the required purity of the outlet stream and the solvent inlet purity, respectively, for absorption process and they are given by:

$$a_V = \frac{Y_{V\,out}}{Y_{V\,in}} \quad , \quad a_L = \frac{Y_{L\,in}}{Y_{V\,in}} \tag{2.4}$$

Similarly, for desorption, the purification parameters d_L and d_V are defined by:

$$d_L = \frac{Y_{L\,out}}{Y_{L\,in}} \quad , \quad d_V = \frac{Y_{V\,in}}{Y_{L\,in}} \tag{2.5}$$

The situation where $a_V = 0$ and $d_L = 0$ corresponds to full purification whereas $a_V = 1$ and $d_L = 1$ means that there is no purification at all. Further, for the case where $a_L = 0$ and $d_V = 0$, the equations describe a separation process using a pure solvent, without any solutes.

It is clear from Eqs. 2.2 and 2.3 that the critical flow rate ratio depends on the value of f', the purity of the inlet solvent stream and the desired purification. To achieve a given purification, it is necessary to operate with an excess flow of the solvent phase. This means that the operating molar flow rate ratio $(-q_n)$ must be less than the critical flow rate ratio for absorption (i.e. $-q_n < -q_{nC}$) and the opposite for desorption ($-q_n > -q_{nC}$) since q_{nC} is defined for both cases as the ratio of the light phase flow rate to that of the heavy phase. Thus, in the case of using pure solvent ($a_L = d_V = 0$), which is typical for separation processes, the allowed phase flow rates ratio can be expressed as:

For absorption $$-f'q_n < \frac{1}{1-a_V} \tag{2.6}$$

For desorption $$-f'q_n > 1-d_L \tag{2.7}$$

where $-f'q_n$ is the purification factor and is referred to as the stripping factor in desorption work and the absorption factor in absorption work (e.g. Edmister, 1957). It is more convenient, perhaps, to express the above equations in terms of the phase volumetric flow rates (Q_V and Q_L) as in Eqs. 2.8 and 2.9:

For absorption $$-f'\frac{Q_V}{Q_L} < \frac{n_L}{n_V}\frac{1}{1-a_V} \tag{2.8}$$

For desorption $$-f'\frac{Q_V}{Q_L} > \frac{n_L}{n_V}(1-d_L) \tag{2.9}$$

where n_L and n_V are the molar density of the light phase and heavy phase, respectively.

Eqs. 2.8 and 2.9 make clear that the relative phase flow rates required to achieve a particular degree of separation are governed by the solute equilibrium distribution (f'). For desorption, for example, very large values of f' require relatively small amounts of solvent (Q_V) since this phase is able to hold more solute than the heavy phase. On the other hand, when f' is very small, a relatively large solvent flow rate is required. Further, at a given f', using too little solvent will lead to a violation of Eq. 2.7 (or Eq. 2.9), making achieving purification (d_L) is not possible. For example, if $-f'q_n = 0.7$, the best purification that can be reached is 0.3 according to Eq. 2.7. Similarly, for absorption, using too little solvent (in this case Q_L in Eq. 2.8) cannot achieve a given target purification. In either case, an excessive use of solvent satisfies the restriction imposed by phase equilibrium but with operating cost.

In general, it can be inferred that for a given phase and solute system (that determines f') operating at the optimum flow rate ratio is possible. Such optimum can be identified once the degree of purification (a_V or d_L) has been decided along with other external factors such as solvent inventory and subsequent solvent recovery process.

2.2.2 Phase-diffusion Lengths

When a separation process involves contacting two phases, mass transfer in each phase must be considered. In principle, the two phases should be arranged to give the best contribution to mass transfer such that it is not limited by one of the phases (MacInnes and Zambri, 2015). To satisfy this condition, an adjustment of the relative size of phase diffusion layers (i.e. the ratio of the lengths in the two phases, ℓ_L/ℓ_V) is required. It must be that there is an optimum ratio of lengths such that the diffusion time required for a solute to penetrate each phase layer equals the residence time of each phase in the same contacting length L_C . Fig. 2.3 shows the intended situation for a case where the characteristic diffusion lengths correspond to the phase element sizes.

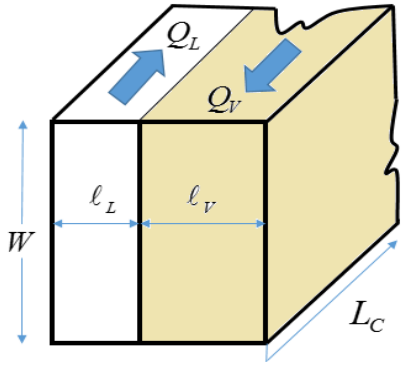

Figure 2.3. A section of contactor with W width showing the scales ℓ_V and ℓ_L and the contacting distance travelled in the flow direction (L_C).

The residence time of each phase depends on the bulk velocity (w_B) and the contacting distance (L_C). The diffusion time scale can be expressed by the characteristic size (ℓ) and the diffusion coefficient (D). Equating the phase residence time and solute diffusion time gives:

$$\text{Light phase} \quad \frac{L_{CV}}{w_{VB}} = \frac{\ell^2{}_V}{D_V} \tag{2.10}$$

$$\text{Heavy phase} \quad \frac{L_{CL}}{w_{LB}} = \frac{\ell^2{}_L}{D_L} \tag{2.11}$$

From Eqs. 2.10 and 2.11, the optimum ℓ_L/ℓ_V can be established by setting $L_C = L_{CV} = L_{CL}$:

$$\frac{\ell^2{}_L}{\ell^2{}_V} = \frac{w_{VB}}{w_{LB}}\frac{D_L}{D_V} \tag{2.12}$$

For the approaches mentioned in the introduction of this chapter, the scales ℓ_V and ℓ_L may represent the diameter of a bubble, droplet or film thickness over a solid surface. With the rotating spiral technique, the phase geometries are clearly defined and the scales ℓ_V and ℓ_L can be taken to represent the largely uniform phase layer thicknesses in the case of simple laminar flow (as depicted in Fig. 2.3). This allows a direct representation of the phase volumetric flow rates in Eq. 2.12 instead of the bulk velocities since the flow area and the element size (ℓ_L) are directly linked (i.e. $Q = w_B A$ where $A = W\ell$). Thus, Eq. 2.12 can be expressed in terms of the volumetric flow rate of the phases as (e.g. MacInnes and Zambri, 2015):

$$\frac{\ell_L}{\ell_V} = \frac{Q_V}{Q_L}\frac{D_L}{D_V} \tag{2.13}$$

This basic equation shows that the optimum phase element sizes depend on phase diffusion coefficients and phase flow rates. For the gas-liquid contacting of interest, for example, it is easy to expect that the liquid phase will need smaller diffusion length than that required for the gas phase. This is because the diffusion coefficient of liquids, in general, is many times smaller than for gases (Cussler, 1997). Further, the phase with higher flow rate (i.e. has low phase residence time) will need relatively smaller diffusion length to decrease the diffusion time. Violating Eq. 2.13 would result in requiring longer contacting distance for one phase relative to the other (i.e. $L_{CV} > L_{CL}$ or $L_{CV} < L_{CL}$) to achieve the same mass transfer effect. In this case, larger contactor for the same throughput will be needed to achieve the required degree of purification.

Furthermore, it is important to remind here that the flow rate ratio appearing in Eq. 2.13 is restricted by the solute equilibrium characteristics (f') at a particular degree of purification, as has been shown by Eqs. 2.8 and 2.9. So the optimum layer thicknesses for a particular phase and solute system will not be the same optimum for other systems with different equilibrium characteristics. To satisfy Eq. 2.13, therefore, it is necessary to adjust *independently* the flow rate ratio of the phases (to adapt to f') and the relative size of the phase elements (to accommodate both Q_V/Q_L and the solute properties).

2.3 Existing Gas-Liquid Contactors

There are many types of gas-liquid contactors in the field of chemical and biochemical engineering and they are classified in the literature in various ways. Here, the most common contactors in use are considered in terms of the constraints on phase contacting outlined in the previous section. To simplify the task, these contactors are categorised according to whether they mix the phases (*dispersed-phase contactors*) or they keep them continuous (*parallel-phase contactors*). Obviously, the rotating spiral contactor is one of the latter types that avoid mixing phases. But because the rotating spiral is the principal focus of the work, it is addressed separately at the end of the chapter (Section 2.4).

2.3.1 Dispersed-phase Contactors

2.3.1.1 Packed Columns

Packed columns are frequently used in chemical processing systems to perform different types of contacting operations such as absorption, stripping and distillation. Usually, it is a cylindrical vessel filled with small pieces of inert packing materials which are stacked in a random or a structured manner (Geankoplis, 2003; Seader and Henley, 2006). In the irregular passages formed by the packing, a gas and a liquid are contacting counter-currently by introducing the gas phase at the bottom, which flows upward as a result of the pressure gradient along the column, while the liquid phase flows downward under the stronger influence of gravity.

De Santos et al. (1991) describe this type of contacting as complicated, chaotic, and even capricious. The liquid film and the surrounding gas regions tend to expand and contract, divide and recombine continuously during the contacting process. This situation encourages the possibility of increasing/decreasing phase velocities, producing variable phase layer thicknesses (i.e. variable ℓ_L/ℓ_V) to satisfy continuity requirements. Thus, the phases are not contacting well everywhere and at all times if one considers the implications of violating Eq. 2.13. Consequently, lower mass transfer efficiency and hence larger equipment size result than might otherwise be achieved. This assumes that the phases are distributed uniformly inside the packed column and complete wetting occurs. In the usual situation, this ideal distribution is hard to achieve. At low liquid flow rate, for example, only a part of the packing surface may be completely wetted, leaving the others dry or covered by a stagnant liquid film at the best (McCabe et al., 1993). This decreases packed columns performance since not all the packing surface is used effectively for mass transfer.

Moreover, there are other issues that limit the performance of this type of contactor. One of the most important issues is flooding by the liquid phase. Flooding is the lifting of liquid by the upward gas flow in the column (de Santos et al., 1991). It occurs when the gas dynamic pressure becomes larger enough compared to the hydrostatic pressure rise in the liquid over a characteristic height. With the gas superficial velocity u_g and the bed void fraction E, the gas dynamic pressure is $\rho_g(u_g/E)^2/2$. The characteristic height can be expressed in terms of packing surface area per void volume,

a/E. Thus, the hydrostatic pressure scale is $(\rho_L - \rho_g)gE/a$. For $\rho_L >> \rho_g$, the parameter determining flooding then should be the ratio of these pressure terms, $u_g^2 a/2gE^3(\rho_g/\rho_L)$. When this ratio exceeds a particular value, liquid will be carried up the column and it will flood. The onset of flooding in packed columns was successfully correlated by Sherwood et al. (1938) using this parameter. Fig. 2.4 shows a plot of the correlation. The second parameter appearing in the ordinate is the liquid viscosity ratio, μ_L/μ_W, where μ_W is a reference viscosity (water, 293 K). The abscissa in the figure can be viewed as the square root of the ratio of liquid and gas dynamic pressures where *L* and *G* are mass flow rates of the liquid and gas phase, respectively.

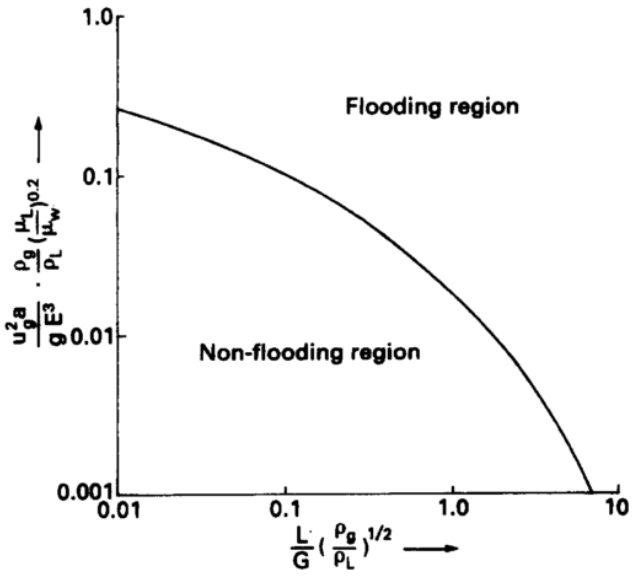

Figure 2.4. General behaviour of flooding for a gas-liquid system in packed columns (adapted by Ramshaw, 1993).

It is clear from Fig. 2.4 that the possible conditions of operation are limited to the region under the curve (the non-flooding area) and there is an increasing limitation on these conditions as L/G increases. This is not surprising since as liquid flow rate increases the amount of the liquid phase holdup in the packing increases and hence a small space will be available for the gas phase. This causes increasing the gas phase velocity, which means greater shear stresses at the gas-liquid interface, and hence increasing the probability of the flooding. Thus, it can be expected that the packed column will be impractical to handle phase and solute systems requiring a low phase flow

rate ratio $(-q_n)$. Since this ratio is inversely related to f', systems having large f' are not expected to be handled successfully using packed columns.

Further, the correlation shows clearly the dependencies on the physical properties of contacting phases. Cases where the gas density is relatively large are seen from Fig. 2.4 to be more restricted than for low density. With an increase in gas density, the allowed gas flow rate decreases both by its effect in the abscissa and in the ordinate of the plotted correlation. Another property that affects flooding is the liquid viscosity. According to the correlation, it is clear that increasing μ reduces the flooding gas flow rate at a given phase flow rates ratio (L/G).

It is important to mention here that there are several other correlations proposed using primarily the same parameters shown in Fig. 2.4 with slight modifications (e.g. Lobo et al., 1945; Leva, 1954 ; Eckert, 1970). While these correlations are based on flooding data for different packings and phase properties, they show the same behaviour of flooding curve illustrated in Fig. 2.4. This suggests that there is an inherent limitation on the allowable phase flow rates ratio in the packed columns.

The packed column evidently has some significant limitations regarding independent control of ℓ_L/ℓ_V and Q_V/Q_L as well as the types of phase and solute systems, that can be handled while avoiding flooding. However, it is considered one of the most important and commonly used methods in many chemical industries.

2.3.1.2 Spray Towers

The use of unpacked spray towers offers advantages over packed columns, particularly for highly soluble solutes (Seader and Henley, 2006). If the solute is very soluble in the liquid phase, f' is small and hence high gas flow rate relative to the liquid flow rate is needed. As discussed in the previous section, the allowable gas phase flow rate is limited in packed columns by the flooding characteristics. For systems having small f', therefore, operating at a high liquid flow rate is also restricted in packed columns for that same reason. At low liquid flow rate, packed columns do not function well due to uneven liquid phase distribution. This maldistribution results in dry regions, which are completely inefficient for mass transfer. In addition, the packed columns suffer

from other operational issues such as degradation of packing materials when operating at high gas phase temperature and blocking of packing voids due to deposition (Javed et al., 2010). Because the spray tower has no-internals, it avoids all these operational issues. Equally, it allows a high treatment capacity of gas phase and a reduction of gas pressure gradient comparing to packed columns (Pinilla et al., 1984).

In the spray tower, the gas is introduced from the bottom as a continuous stream and the liquid enters from the top through a series of spray nozzles to fall as small droplets, typically as that shown in Fig. 2.1. However, producing an efficient mass transfer rate using this approach tends to be difficult. Both the droplet size and inter-drop distance alter rapidly through the tower as a result of droplet coalescence and the droplet impingement on the walls (Javed et al., 2006 ; Coulson et al., 2002). Thus, ℓ_L/ℓ_V does not remain optimum throughout the contacting process since it is as desired in some regions (if it can be controlled in the first place) and is not in others. Additionally, the pattern of flow suffers from the effect of backmixing flow (sometimes referred as axial mixing). Purely counter-current contacting does not occur, and always there is a part of both phases that flows in the opposite direction. This is mainly due to the non-uniform distribution of the droplets (Vinci et al., 1996) which creates regions with different densities. Regions with a large volume of droplets have a greater average density and sink relative to the regions with small volume of droplets, causing undesirable axial mixing (Fig. 2.5). Such mixing has a detrimental effect on the performance of the contacting process since it reduces the concentration difference required for mass transfer.

The spray tower might be expected to be more effective when the liquid phase is broken up into very fine droplets. This enhances the mass transfer rate by decreasing the diffusion scale (high surface area per unit volume). But also the small droplet size makes the interphase drag force to increase in relation to the buoyancy force ($\Delta\rho g$) and often, especially at high gas velocity, becomes sufficient to lift the entire liquid phase causing flooding. Thus, similar to packed columns, the performance of this approach is dictated by the flooding characteristics of the contacting phases.

Studies have been carried out to investigate ways to enhance the mass transfer in this kind of contactor. Javed et al. (2006) investigated the enhancement of mass transfer for gas and liquid contacting in a spray tower using swirling gas flow. In this work, the absorption of NH_3 by water from an air–NH_3 mixture was studied experimentally. The

results were reported in terms of the overall mass transfer coefficient based on the gas phase ($K_V a$). They showed that $K_V a$ is enhanced by 13-20% due to imparting a swirling motion to the axial gas flow through the spray tower. The same authors investigated the chemical absorption of CO_2 from air by NaOH (Javed et al., 2010). They also noticed an enhancement in the overall gas phase mass transfer coefficient due to the effect of swirling motion.

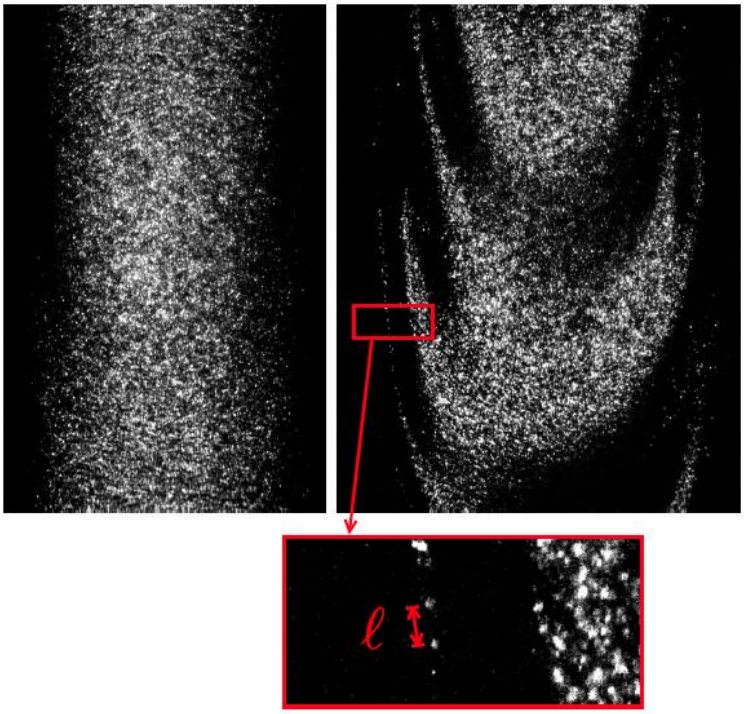

Figure 2.5. Images of spray of water droplets flow taken at the top region of a channel (left) and far from the top region (right) showing a case of unstable flow (de Rivas and Villermaux, 2016).

2.3.1.3 Bubble Columns

The bubble column can be viewed as moving in an appropriate direction from a packed column as the spray tower. In this case, the liquid is the continuous phase while the gas phase is dispersed into it as small bubbles. Such approach allows a small throughput of the gas phase relative to the liquid and may allow successful operation when the solubility of a solute in the liquid phase is relatively low (Seader and Henley, 2006). Similar to the spray tower, this approach suffers from the occurrence of bubble coalescence and back-mixing (Charpentier et al.,1976). These undesirable effects contribute to a variable residence time of the dispersed phase and hence mass transfer is not effective everywhere in the column. A good amount of studies have been performed

trying to quantify the effect of coalescence phenomenon and to enhance the mass transfer rate by minimizing its effect.

Prince and Blanch (1990) proposed a model to predict the rate of bubble coalescence and the rate of bubble breakup. They tested the proposed model with experimental results for distilled water and salt solutions and they found a favourable agreement.

Bredwell and Worden (1998) presented an approach to enhance the mass transfer rate in bubble columns using microbubbles and adding surfactants to reduce the bubble coalescence. They demonstrated the effect of this approach in the fermentation process of synthesis gas where a spinning disc apparatus was used to produce the microbubbles. It was found that the overall liquid volumetric mass transfer coefficient was enhanced by approximately six-fold. Further, the authors noticed that an increase in surfactant concentration caused a reduction in the value of liquid mass transfer coefficient.

Zimmerman et al. (2009) described a novel approach of generating microbubbles using fluidic oscillation. They reported that this approach is able to produce a cloud of microbubbles with a high degree of control (approximately monodisperse with uniform space). In this study, information about the benefits of microbubbles and advantages of using fluidic oscillation in airlift reactor are given. In addition, many potential applications for this approach have been listed in Zimmerman et al. (2011) such as biofuels production, water treatment, chemicals production, etc. Following the work of Zimmerman et al. (2011), two recent experimental studies carried out independently by Al-yaqoobi et al. (2016) and Abdulrazzaq et al. (2016) demonstrate successfully distillation of ethanol-water using microbubbles. The former work studied mixtures with different compositions whereas the latter focused on azeotropic mixtures. Both studies are based on the injection of a hot air through a thin stagnant layer of liquid mixture to achieve separation. Unlike conventional distillation, the process is semi-continuous with a throughput limited by the thickness of the liquid layer. Although the process is not continuous, it seems more energy-efficient and is capable of handling heat-sensitive mixtures.

Despite this valuable advance in the methods of bubbles generation, the counter-current contacting of dispersed gas and continuous liquid is still limited to the case where the solute has low solubility in the liquid phase. In this case, f' is generally large and a small gas phase flow rate to the liquid phase is needed.

2.3.1.4 Plate Columns

Another contactor encountered widely in gas-liquid separation processes is the plate column (or tray tower). Unlike the approaches discussed above, contacting occurs in a stage-wise manner. A series of stages or plates allows the gas and liquid to be contacted as shown in Fig. 2.6. The liquid phase is fed from the top and flows across the plate down to the next plate. The gas phase flows upward from openings distributed over the plate to bubble through the liquid layer and then disengages to pass up to the next plate. In this way, the overall effect is counter-current contacting, although a cross flow of the two phases occurs over each plate.

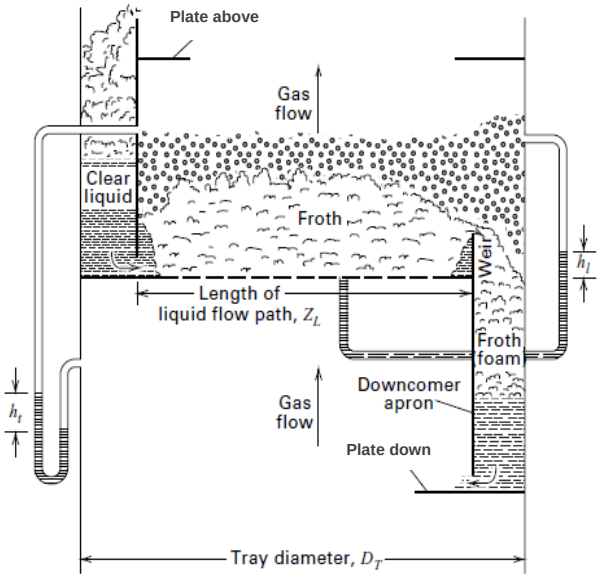

Figure 2.6. Details of gas-liquid plate contacting in a plate column (Smith, 1963).

Clearly, mass transfer between the phases and hence the plate efficiency is determined mainly by the phase flow rates ratio. By increasing the ratio of the gas phase flow rate to that of the liquid phase, the cross-flow pattern can change from bubble or emulsion to froth or spray (Lockett, 1986). This non-uniformity of two phase flow, in turn, changes ℓ_L/ℓ_V and hence the interphase diffusion. Thus, in terms of the optimum contacting, either the phase flow rates ratio or ℓ_L/ℓ_V may be suitable but not both at the same time.

Further, maintaining effective cross-flow contacting requires both the gas phase velocity and the liquid head over the plate to be relatively high. This condition ensures that the gas phase is dispersed thoroughly through the liquid phase and an adequate contact time is achieved for the two phases (Treybal, 1981). However, high gas phase

velocity causes excessive entrainments. In this case, some of the liquid phase is carried by the gas phase to the plate above. This worsens the mass transfer and hence plate efficiency by reducing the solute composition difference required for mass transfer. Also, a large head of liquid and high gas phase velocity lead to a large pressure drop per plate. The effect of high pressure drop is not limited to increasing pumping cost but also may cause, particularly in distillation, unnecessarily higher boiling temperature. This, in turn, leads to heating difficulties and damage to thermally sensitive mixtures (Treybal, 1981).

Further, several undesirable conditions can occur at various phase flow rates. Using too small liquid phase flow rate leads to too low liquid head over the plate. Consequently, *coning* phenomenon may occur, i.e. the gas phase forming a direct cone channel from the plate holes through the liquid layer without effective contacting. The other extreme of too high liquid flow rate is also undesirable as it causes downcomer flooding, leading to liquid accumulation over the plate.

There are also limitations on the gas phase flow rates. If the gas rate is small, the liquid phase weeps from the plate openings and thus failing to maintain complete cross-flow over the plate. Extremely small gas flow rate sometimes leads to a case where all the liquid phase flows through the plate openings and none through the downcomer (dump point). All these limits, shown schematically in Fig. 2.7, lead to a limited operating regime for flow rate of the phases, and hence a limited range of phase and solute system can be handled. This is usually with the result that the column must be large due to the difficulties to control ℓ_L/ℓ_V and the necessity to leave a distance between the plates for gas phase disengagement.

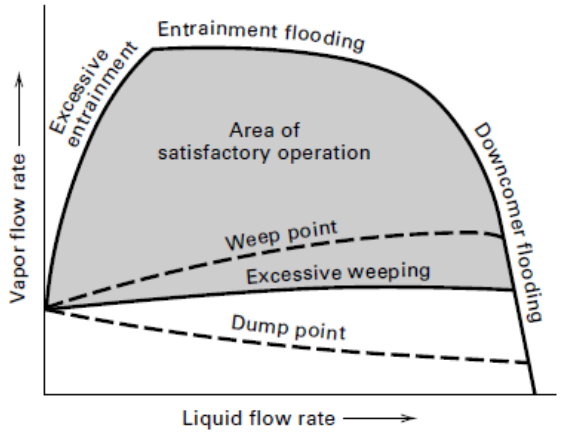

Figure 2.7. Regime of stable operations of a plate column (Kister, 1992).

Over many decades, research has been devoted to studying the hydrodynamics of flow on the plate and improving column efficiency using different plate designs. A recent study by Zarei et al. (2013) investigated experimentally the hydrodynamic characteristics of a new type of plates termed the conical cap plate. The performance of the plates was compared to conventional bubble cap and valve tray plates and the results showed some enhancements in terms of the weeping rate and pressure drop. Other recent study performed by the same main author (Zarei et al., 2017) focused on understanding the hydrodynamics of valve plates. The study involved experiments (using air-water contacting in a large scale plate column) supported by CFD computational work. A wide range of parameters was investigated (weeping rate, pressure drop, entrainment, froth height and average liquid hold up) and a comparison with the CFD results was made. The results showed an acceptable agreement between the computations and experiments.

In general, the plate column does not differ radically from the other dispersed-phase contactors presented in the previous sections. It, perhaps, suffers from even more limitations as shown in Fig. 2.7. However, similar to the packed bed, it is one of the most mature contactors and it is used heavily in many vital chemical processing plants.

2.3.1.5 Rotating Beds

Because centrifugal acceleration can be orders of magnitude greater than gravity, techniques based on rotation could produce a higher rate of mass transfer comparing to conventional techniques (Bašić and Duduković, 1995). The enhanced body force obtained by rotation produces smaller droplets size or thinner liquid layer thickness, improving mass transfer. This results in smaller equipment size and hence expensive solvent having higher solubility becomes feasible economically. Also, more expensive corrosion-resistant materials and coatings can be used, improving safety and increasing the operational lifetime of equipment. Additionally, using small-sized equipment reduces the quantity of waste produced and as a result lowers the environmental impact. Another advantage of using enhanced body force is the improvement of the flooding characteristics. It may be noticed in Fig. 2.4 that flooding is dependent on gravitational acceleration. Thus, using an enhanced acceleration of $R\Omega^2$ instead of g enables both the gas throughput and the interfacial area per unit volume (a) to increase before the onset of flooding is reached. This allows for operation at conditions that are conventionally

inaccessible, such as high Q_V/Q_L ratio, as well as handling of systems with different properties, such as ones involving viscous liquids (Ramshow, 1993; Trent, 2003; Van Der Schaaf and Schouten, 2011; MacInnes and Zambri, 2015).

Perhaps the most common rotating contactor encountered in chemical processing is that based on rotating beds filled with packings, baffles or perforated plates. Using rotating beds to perform gas-liquid contacting operations is not a recent development. Podbielniak (1942), in a patent filed in 1937, used perforated spiral passages as a rotating bed for a gas-liquid contacting. In another patent, Placek (1942) described gas-liquid centrifugal contactors based on perforated cylindrical shells with different designs. Pilo and Dahlbeck (1960) proposed an apparatus using various types of beds comprising plates and fillers for counter-current contacting of gas-liquid systems. They claimed that it could also be used for liquid-liquid systems. However, all the experiments were limited to gas-liquid systems (scrubbing of benzene from town gas and removal of hydrogen sulphide using liquid ammonia from coke oven gas).

Vivian et al. (1965) studied desorption of carbon dioxide from water into air in a conventional packed bed subjected to a centrifugal field. In the work, a small column was fixed on the horizontal arm of a large centrifuge and the centrifugal acceleration was varied from *g* to 6.4*g*, which. Although, this acceleration is relatively mild for rotating devices, the authors found that the liquid mass-transfer coefficient was directly proportional to the value of centrifugal force.

Ramshaw and Mallinson (1981) described using rotating beds filled with random packing materials such as filament metal gauze and glass beads (so-called 'Higee Technology'). In the work, the authors demonstrated experimentally distillation and absorption processes. They observed that the rate of mass transfer was enhanced by up to orders of magnitude compared to results of conventional packed beds. Following this patent, the rotating packed bed has attracted growing interest and a large number of academic works have been published. Some of these works focused on studying the hydrodynamic and mass transfer characteristics of gas-liquid contacting and developing correlations (Munjal et al., 1989; Kumar and Rao, 1990; Liu et al., 1996; Chen and Liu, 2002). Other studies examined various types of packing materials and bed designs (Lin et al., 2004; Chen et al., 2005; Lin and Chien, 2008; Chiang et al., 2009; Hsu and Lin, 2012; Li et al., 2017). Investigating different applications of rotating packed bed has

also been of interest such as nanoparticles preparation, polymerization (Zhao et al., 2010), removal of gases pollutant emissions (Pan et al., 2017) and the development of a stripper/regenerator for solvent-based carbon capture (Joel et al., 2017).

While all these versions of rotating packed beds have differences in packing type, device configuration and mechanical design, they use the same principle of contacting, which is illustrated in Fig. 2.8. The liquid phase is fed radially into the packing and flows outward through the packing under the effect of centrifugal acceleration. At the same time, the gas phase is introduced from the outside periphery and is forced by pressure gradient to flow through the packing counter to the liquid phase. Unlike gravitational columns, the film thickness or droplet size is determined by the level of centrifugal force in addition to the packing geometry and the phase physical properties. Unfortunately, the effect of centrifugal force is not maintained constant during the contacting process since it increases with radial position. Thus, the liquid layer thickness and droplet sizes vary and hence optimum contacting can only occur at a single radial position, leaving the remaining volume of contacting at a lower mass transfer rate.

Further, Burns and Ramshaw (1996) explored the pattern of flow in the rotating packed bed. The authors observed that the liquid phase flows in a series of rivulets and droplets rather than as a continuous, uniform film flow. This type of flow causes incomplete wetting of the packing (i.e. some areas are dry or partly wetted). Thus, not all of contacting volume is exploited for mass transfer operations.

While many chemical processes could take advantage of rotating beds, they still mix phases together and as a result share the same drawbacks accompanied with conventional techniques.

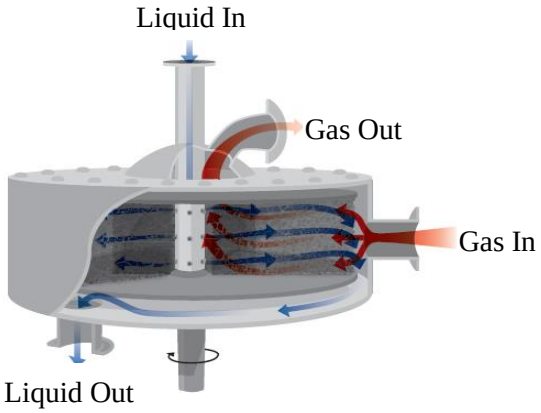

Figure 2.8. An illustrative diagram showing gas-liquid contacting in a rotating packed bed (Górak and Stankiewicz, 2011).

2.3.1.6 Spinning Cone Columns

The spinning cone column is another approach that uses centrifugal acceleration to perform gas-liquid contacting. This approach had its start in 1937 with an application to separate the oxygen isotopes in water (Huffman and Urey, 1937). More recently, the spinning cone column has been developed for use in the food and beverage industry to remove volatile materials such as flavours and sulphur compounds (Wright and Pyle, 1996 ; Saffarionpour and Ottens, 2018).

The column comprises of two sets of conical plates. A set of stationary cones is fixed to the wall of the column and another set fixed to a central shaft rotate in between these (Fig. 2.9). The two sets are arranged in a successive manner along the column allowing transferring the fluids between them. Under the influence of gravity, the liquid phase flows as a thin film down over a stationary cone and falls onto the surface of the rotating cone. The liquid phase is then driven by the centrifugal force to flow upward and outward over the surface of the rotating cone, falling again onto the next stationary cone. This pattern of the liquid flow is repeated down the length of the column. The gas phase enters from the bottom of the column and flows up counter-currently to the liquid phase.

A series of computational investigations of the gas-liquid contacting flows in a spinning cone column have been reported in Makarytchev et al. (2002), Langrish et al. (2003), Makarytchev et al. (2004) and Makarytchev et al. (2005). It was found that the mass transfer occurs between the two phases in two distinct regions, where the gas flows adjacent to the rotating cones and where the gas passes across the spray droplets formed at the lip of the rotating cones. Significantly, the authors conclude that the spray-based mechanism of mass transfer dominates in small scale devices, whereas the film-based mechanism is dominant in medium and large scales.

Under the circumstances of contacting discussed above, it tends to be difficult to secure an efficient contacting. In terms of the spray-based mechanism, the formation of droplets depends primarily on the phase flow rates and phase physical properties and any attempt to produce smaller droplets increases the tendency of phase ejection. On the other hand, in the film-based mechanism, the liquid film experiences a variable centrifugal force proportional to the radial distance from the axis of rotation at a fixed angular velocity. This prevents formation a uniform liquid layer (thick in the vicinity of the shaft and thin on the top surface of rotating cone). Thus, controlling the relative phase element

sizes (ℓ_L/ℓ_V) tends to be difficult and as a result low specific throughput (i.e. increasing the volume of the device or decreasing the throughput to achieve a particular degree of separation). Nevertheless, the spinning cone column is used widely in the food sector due to its ability to handle highly viscous fluids and lumpy suspension that preclude the use of other conventional techniques (Saffarionpour and Ottens, 2018).

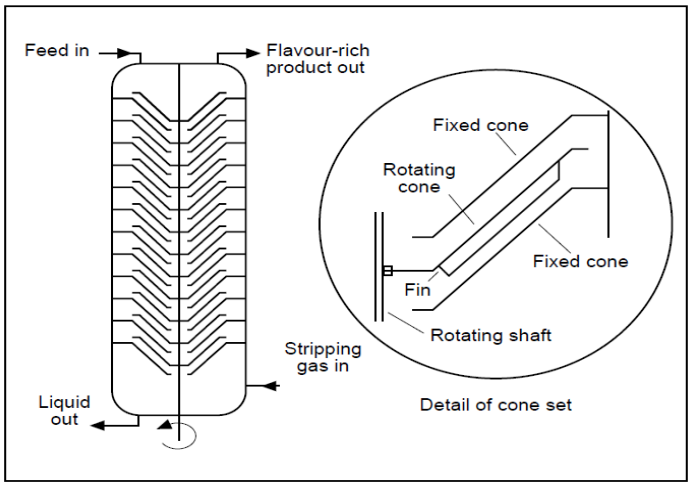

Figure 2.9. Spinning cone column and the detail of contacting element (Pyle, 1994).

2.3.2 Parallel-phase Contactors

These types of contactors can provide solutions for some of the limitations and difficulties associated with the dispersed-phase contactors. In this case, a gas phase and a liquid phase flow separately without dispersing one phase into the other. Thus, flooding, entrainment, difficulties of disengaging the phases after contacting and phase backmixing can be avoided (Zanfir et al., 2008; Sun et al., 2011; MacInnes et al., 2012).

One of the well-known continuous gas-liquid contactors is the wetted–wall column (or falling-film column). This contactor has been employed in many mass transfer studies as a basis to investigate the transfer coefficients because of its simplicity and because the interfacial area between the phases can be precisely known (Thomas and Portalski, 1958 ; Nielsen et al., 1998; Haidl et al., 2016; Rejl et al., 2016). Also, it has seen some industrial applications such as purifying flue gasses (Nielsen et al., 1998). In this contactor, a thin film of the liquid phase flows on the inside wall of a vertical pipe with the gas phase flowing counter-currently. So, as with rotating spiral contacting, the two phases flow in parallel layers side by side during the contacting process, although the

liquid layer thickness cannot be decoupled from the liquid phase flow rate in this case since gravity cannot be changed. Thus, increasing or decreasing the liquid phase flow rate will lead, necessarily, to increasing or decreasing the liquid layer thickness. Further, the stability of the phase interface is crucial for this type of contacting. Effective parallel-phase contacting relies on maintaining the phases separated with phase interface remaining stable (Hessel et al., 2005; Lam et al., 2013; MacInnes et al, 2012). Disrupting this organised flow potentially results in changing phase layer thicknesses (ℓ_L/ℓ_V) or even breaking up the interface into droplets or bubbles and hence uncontrolled contacting. In the wetted-wall column, obtaining unstable flow is highly possible. Operating at large velocity of one of the phases produces a wavy flow, making the contacting more complex and uncontrolled (Boomkamp and Miesen, 1996 ; Nielsen et al., 1998).

The falling film microcontactor is a novel approach developed last decade as an alternative to improve gas-liquid contacting in the wetted-wall column and other conventional approaches (Monnier et al., 2010). This contactor typically consists of a number of straight microchannels extended vertically on a plate (Fig. 2.10). The laminar nature of fluid flow in these channels and their small size result in a flow dominated by surface forces. This helps to stabilise the liquid layer during the contacting process (Lam et al., 2013). Also, using microchannels provides a high surface area per unit volume and hence better contacting can be achieved in relation to the conventional wetted-wall column (Hessel et al., 2005). However, controlling the liquid layer thickness is still not within the capability of this approach since the liquid phase flows under the effect of gravity. Also, gravity is weak to counter the large surface forces which result sometimes in segmented flow rather than continuous flow (Aota et al., 2009), eliminating the benefit of counter-current contacting. Thus, it should be expected that the use of gravity to drive the liquid phase in such small channels can limit the allowable phase flow rates. Additionally, liquids with a large contact angle may not wet the channel completely, causing liquid maldistribution (Al-Rawashdeh et al., 2008). This adversely affects the mass transfer by decreasing the amount of the interfacial area.

A number of studies in the literature investigated the process of gas-liquid contacting in falling film microcontactors. Most of the attention in these studies is on co-current and counter-current chemical absorption, in particular the absorption of CO_2 using NaOH solution (Zanfir et al., 2005; Al-Rawashdeh et al., 2008; Ziegenbalg et al., 2010 ; Al-

Rawashdeh et al., 2012, reviewed by Lam et al., 2013). Relatively few studies focus on physical mass transfer. Monnier et al. (2010) demonstrate counter-current absorption of tetrachloroethylene from air into diethylhexyladipate using a falling film microcontactor. The authors compare the separation efficiency (measured based on the degree of purification) with results of a conventional packed bed for the same phase and solute system. The results were comparable, although an excessive amount of the solvent was used for the packed bed, i.e. $-f'q_n << 1/(1-a_V)$, in relation to the fall film microcontactor to achieve the same degree of separation. Furthermore, a theoretical study has been carried out by Mhiri et al. (2011). The authors analysed the gas-liquid contacting process in the same apparatus of Monnier et al. (2010) using the same phase and solute system. They looked at the effect of the gas layer thickness and they found that a good improvement in mass transfer can be achieved by decreasing the gas layer thickness. This improvement was attributed to the role of f'. The system studied by Monnier et al. (2010) and Mhiri et al. (2011) has a small f', which means that the solute is very soluble in the liquid phase. Hence, decreasing the gas layer thickness resulted in an improvement in mass transfer since most of the mass resistance lies in the gas-side.

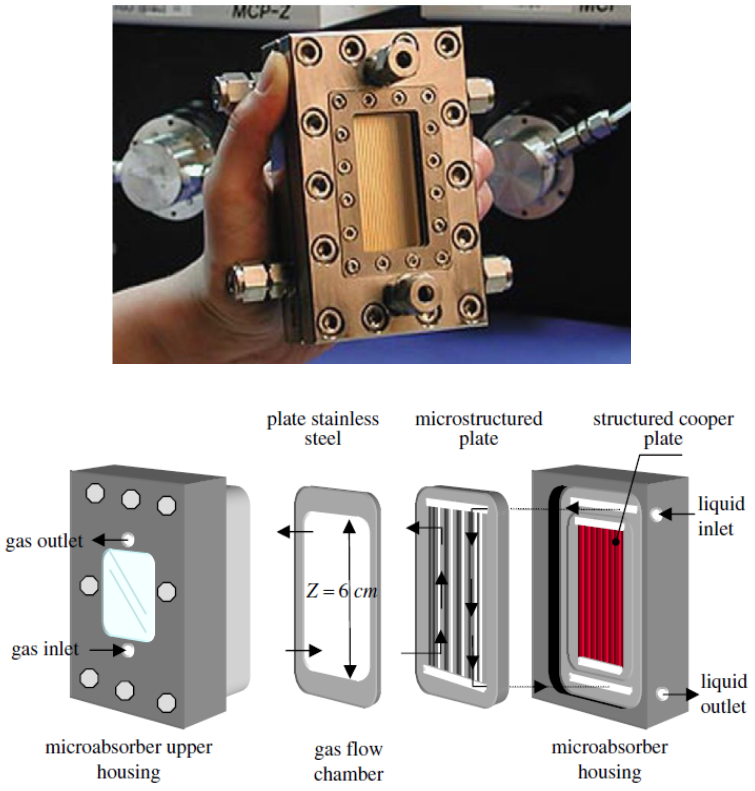

Figure 2.10. A falling film microcontactor developed by Institut für Mikrotechnik Mainz and its expanded view (adapted from Monnier et al., 2010).

A further, rather different, method of continuous gas-liquid contacting employs a membrane barrier. The membrane, essentially, acts as a means of allowing a gas and a liquid phase to contact in small pores distributed inside it (Mahmud et al., 1998; Simons, et al., 2009). Unlike the wetted-wall column, this method of contacting enables the phase element sizes (ℓ_L/ℓ_V) to be independent of the phase flow rates, providing a constant and high specific interfacial area (Zanfir et al., 2008). But equally, these elements are fixed and cannot be adjusted since they are determined by the contactor internal design (the size of the fluid passages and the membrane configuration). So a design suitable for one phase and solute system may not be suitable for others. Further, a solute species needs to diffuse through the membrane to transfer between the phases. This means that there is an additional mass transfer resistance created by the membrane which will reduce the mass transfer effectiveness. Another important point is that handling completely wetting liquids can be problematic. Such liquids pass easily through the membrane pores into the gas side, reducing in this way the contacting efficiency. There are also other operational issues inherent in membrane contactors such as fouling, which strongly affects mass transfer performance, and a limited membrane lifespan (Gabelman and Hwang, 1999; Zanfir et al., 2008; Sun et al., 2011).

Recently, a mesh microcontactor has been developed to minimise membrane limitations (Wenn et al., 2003; Zanfir et al., 2008). This contactor is based on using a mesh with straight micropores distributed in a regular and organised manner (Fig. 2.10). This micromesh provides less resistance, higher porosity and more organised pore structure comparing to membrane (Zanfir et al., 2008; Sun et al., 2011). On the downside, however, using a thin mesh with large pore size increases the possibility of breakthrough of one phase into the other (Lam et al., 2013). Thus, precise control of the operating conditions, especially the difference of pressure between phases, is required to avoid such phase intermixing (Zanfir et al., 2008 ; Sun et al., 2011).

A number of studies have been conducted using the mesh microcontactor in various separation applications. Some of these studies focused on co-current physical desorption (Zanfir et al., 2008; Sun et al., 2011; Constantinou et al., 2014). Counter-current desorption is reported in Cypes and Engstrom (2004) and Chasanis et al. (2011). Both groups investigated stripping of toluene from water into a nitrogen stream. It was shown in both studies that the overall coefficient obtained is higher by up to two orders of

magnitude than that of a conventional packed column treating the same phase and solute. Different than these studies, Adiche (2018) recently reported desorption of acetone-water-N_2 system using a hydrophobic/oleophobic membrane microcontactor based on two meandering channels. The author investigated the effect of the liquid channel depth and hence the liquid layer thickness on the stripping efficiency over a range of phase flow rate ratios. The results showed that the smaller the channel depth, the higher is the mass transfer over the tested range of phase flow. Finally, as the falling film microcontactor, there are some studies that focus on the co-current chemical absorption of CO_2 using NaOH solution (Constantinou and Gavriilidis, 2010; Constantinou et al., 2012).

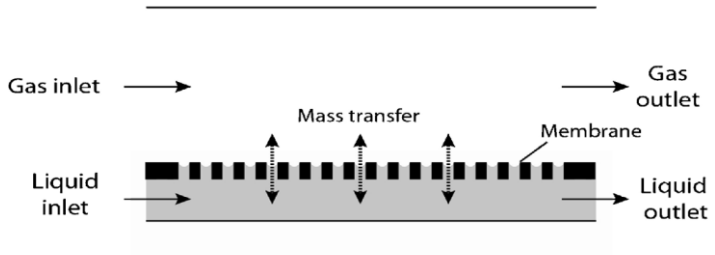

Figure 2.11. Schematic diagram showing the principle of contacting in a mesh microcontactor (Lam et al., 2013).

2.4 Rotating Spiral Technique

2.4.1 An Overview of Attempts to Use Rotating Spiral

A considerable number of patents have been granted concerning the exploitation of centrifugal acceleration in separation processes. However, a survey of these reveals that the concept of rotating spiral contacting only appears in the earliest patents of Podbielniak in the 1930s (Podbielniak 1935, 1936, 1937, 1938). In these patents, the rotating spiral technique was presented as a promising approach capable of handling gas-liquid and liquid-liquid counter-current separations. Podbielniak and his co-workers were the first to develop commercially a rotating device for separation (extraction) in 1947 (Trent, 2003; Coulson et al., 2002). Different forms of rotating contacting element have been proposed by this group; the original design of a spiral element was apparently soon replaced by a perforated spiral and then, for reasons related to design flexibility and ease of manufacturing, with perforated concentric shells (Todd and Podbielniak, 1965).

Of these proposed contacting elements, only the final version of modifications found its way to commercial use in penicillin extraction (Podbielniak et al., 1970), while the original spiral design (non-perforated spiral) was never exploited. MacInnes and Zambri (2015) attributed the dropping of the rotating spiral design to two main reasons, which probably led to an unsuccessful operation. Firstly, all the proposed designs were restricted to a horizontal axis orientation as shown in Fig. 2.12. This unfortunate choice of operation allows the phase layer thicknesses to be crucially affected by gravity. The centrifugal component along the spiral channel, the driving force of the heavy phase, is strengthened by gravity at some positions and weakened by it at others, producing variable layer thicknesses (ℓ_L/ℓ_V). Secondly, using a large channel size indicates that the operation was performed at large values of Reynolds numbers, which were probably high enough to create interfacial instability and loss of control (MacInnes et al., 2012).

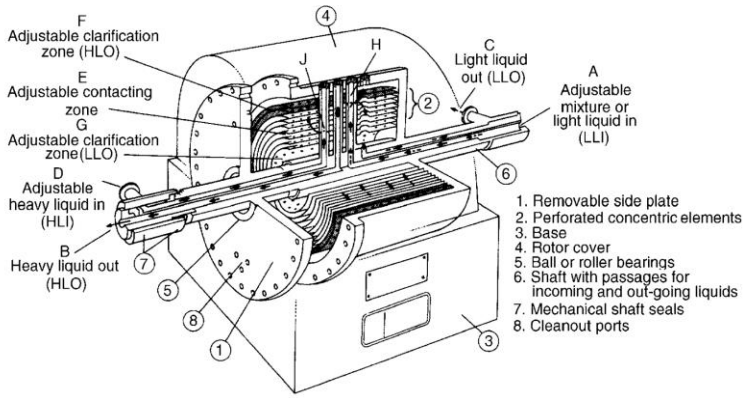

Figure 2.12. Podbielniak Contactor (Coulson et al., 2002).

Unrelated to the Podbielniak et al.'s work, the next investigation of rotating spiral technique appears to be a theoretical study of Mochalova et al. (1973). The authors looked at the hydrodynamic characteristics and the mass transfer performance in a rotating spiral channel, considering a stable laminar flow. This modelling work was extended by Zhavoronkov et al. (1977) to include the behaviour of flow and the mass transfer rate at the entrance region of the spiral. In either case, the solution of the governing equations of motion was approximated for the case of external flow over a rotating spiral surface to find the liquid layer thickness and mass transfer coefficient in the liquid side. Unfortunately, there is no indication in the literature that these theoretical works were ever utilized or even compared with experimental work. Thus, the accuracy of these models was not proved. However, approximating the solution to the case of

external flow means the effect of end-walls, surface tension, and interfacial shear stresses were not considered. All these factors affect directly the shape and size of phase layers (MacInnes et al., 2012; MacInnes et al., 2015). Thus, a reliable prediction of the liquid layer thickness and mass transfer coefficient using these models is not expected in general.

The first comprehensive consideration and analysis of the rotating spiral technique were described in MacInnes et al. (2012). In that paper, there is an account of the issues discussed above. The axis of rotation is vertical, eliminating the contribution of gravity along the channel direction and thus a uniform film contacting can be established along the entire contacting length. Further, using small channel size offers a high mass transfer area per fluid volume and hence, significantly, high throughput per volume of the device can be produced. Experimental work focusing on the hydrodynamics of gas-liquid contacting has followed this paper and serves as a stepping-stone to the research presented in this thesis. In the work to date, many features and benefits of using the rotating spiral contacting have been clearly established. Before presenting the recent studies, however, consideration of the role of the centrifugal acceleration and related phenomena is necessary in order to understand the main features of rotating spiral channel.

2.4.2 The Role of the Centrifugal Acceleration

Using a spiral channel rotating around its axis produces an enhanced body force through centrifugal acceleration. This acceleration has two components whose relative magnitudes depend on the spiral angle (signified by α in Fig. 2.13). The first component is transverse to the channel (*y* direction in Fig. 2.13) and can be expressed as $\rho R \cos\alpha\, \Omega^2$, where ρ is the fluid density, $R(\theta)$ is the radius of the spiral at azimuthal angle θ, and Ω is the rotation rate. Relying on a difference in phase densities, this component keeps the phases segregated so that they can flow side by side as two parallel streams that do not mix. This pattern of the flow generally lessens the possibility of developing large drag forces between the phases, only shear forces at the gas-liquid interface are present with no form drag whatsoever. Thus, crucial issues discussed in connection with the dispersed-phase approaches, for example phase ejection, do not arise. Also, unlike parallel-flow microcontactors, using enhanced centrifugal force overcomes the large surface forces in microchannels, allowing organised counter-current flow over a wide range of phase flow rates and at small layer thickness (MacInnes et al, 2005).

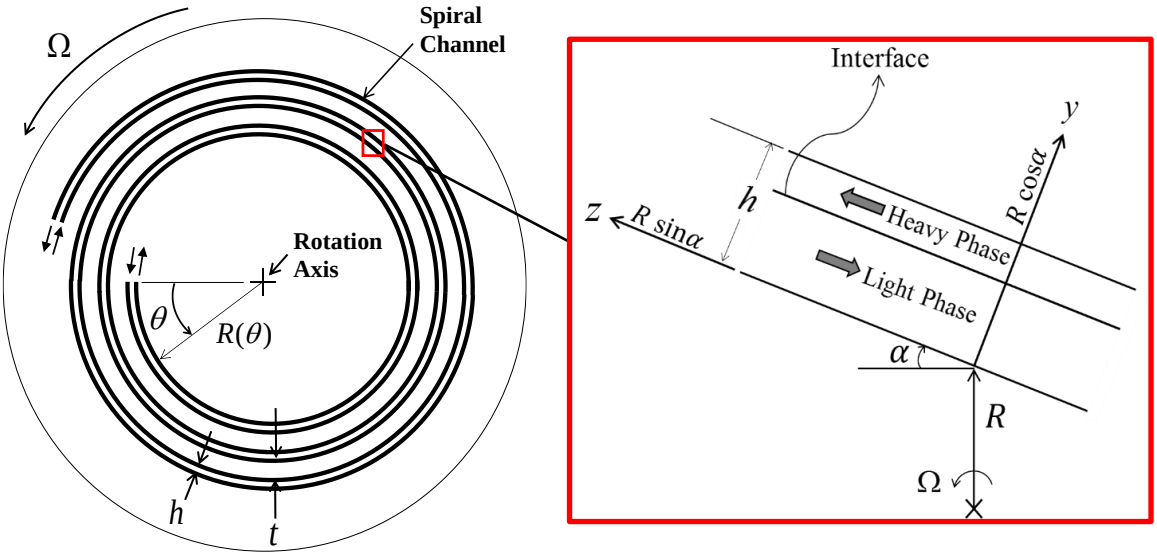

Figure 2.13. Rotating spiral contactor: geometric parameters and principle of operation.

The second component of centrifugal force acts along the channel (z direction in Fig. 2.13) and is $\rho R \sin\alpha\, \Omega^2$. This component acts on both the liquid and the gas phase, affecting flows along the channel. Since the density of the liquid phase, in general, is significantly larger than that for the gas phase, this component mainly affects the liquid phase. It is employed to drive the liquid forward along the spiral while the gas phase can travel counter-currently under the influence of pressure gradient. Thus, for a given phase and solute system, the phase layer thickness ratio (ℓ_L/ℓ_V) depends on the spiral geometry (through $R\sin\alpha$), the rotation rate and the pressure gradient. The geometric parameters of the Archimedean spiral, which is considered here, can be related by the following polar equation (MacInnes et al., 2005; MacInnes et al., 2010):

$$R(\theta) = R(0) + \frac{(h+t)}{2\pi}\theta \tag{2.15}$$

where h and t (identified in Fig. 2.13) are the channel height and the distance between adjacent revolutions, respectively.

For practical spirals, α is small (MacInnes et al., 2012) and thus, the change in spiral radius with θ can be expressed by:

$$\frac{1}{R}\frac{dR}{d\theta} = \sin\alpha \approx \alpha \tag{2.16}$$

Noting that $dR/d\theta = (h+t)/2\pi$ from Eq. 2.15, so $R\sin\alpha$ and hence the centrifugal

force along the channel remains constant provided $\boldsymbol{h}$ and t are constant. This corresponds to an Archimedean channel of fixed shape and size (Fig. 2.13). Thus, the centrifugal body force remains constant along the channel and a large component is applied in the transverse direction ($R\cos\alpha >> R\sin\alpha$). This means that suitable adjustment of the rotation rate and pressure gradient change ℓ_L/ℓ_V and this ratio remains uniform along the full length of spiral. Hence, in contrast to most available methods, ℓ_L/ℓ_V and Q_V/Q_L may be adjusted to the values that achieve optimum contacting and this optimum prevails throughout the contacting process.

Further, this flexibility of controlling the phase flow rate and element sizes enables a wide range of phase and solute systems to be within the capability of this technique. An unpublished study carried out by MacInnes (2013) shows that a single channel design with moderate adjustment of the pressure gradient and the rotation rate can operate at flow rate ratios from 10^{-4} to 10^{4} and handle liquid viscosities from 0.2 to 800 cP and density ratios from 0.1 up to 0.99. As one may note, this easily encompasses the widest conceivable range of possible practical phase and solute systems and required operating conditions.

2.4.3 Coriolis Acceleration and Secondary Motion

The motion of fluids in a rotating channel is subject to Coriolis acceleration that produces distinctive features in rotating flows (Barua, 1954; Benton, 1956). Coriolis acceleration has the effect of a force which is perpendicular to both the direction of the flow and the rotation vector (Tritton, 1988). For two phases flowing in a rotating channel (Fig. 2.14) then, this force per unit volume can be expressed in each phase as $-2\rho\vec{\Omega}\times\vec{V}$ where ρ is the phase density, $\vec{\Omega}$ the rotation vector and $\vec{V}$ the velocity vector in the rotating reference frame (e.g. Speziale, 1982). It is clear from this basic definition and the case depicted in Fig. 2.14 that there is no Coriolis effect in the direction parallel to Ω, whereas $2\rho\Omega w$ and $-2\rho\Omega v$ (Fig. 2.14 a) are the remaining Coriolis terms in y and z directions, respectively, in each phase. The direction of these forces is determined merely by the direction of both the velocity and the rotation vector. For counter-current contacting, positive rotation rate and negative v component, therefore, one would expect that the direction of Coriolis terms is exactly as that shown in Fig. 2.14 a.

It should be noted in Fig. 2.14 a that the force involving the main streamwise velocity ($2\rho\Omega w$) is the principal term that gives rise to the Coriolis secondary motion in each phase. Because of the presence of end-walls, the streamwise velocity (w) has a non-uniform distribution, i.e. fast in the centre and slow near the walls. This means that Coriolis force is larger at the centre of the fluid stream and smaller near the end-walls where the fluid velocity is very small. In contrast, the radial pressure gradient is developed uniformly in the flow section. Consequently, the large Coriolis force throws the fast-moving core of each fluid toward the wall as shown in Fig. 2.14 b. Near the end-walls, where the fluid velocity is very small, the Coriolis force is no longer able to balance the pressure gradient. This pressure force drives each phase to return along the channel walls and phase interface, satisfying the continuity requirement. Due to this mechanism, i.e. the motion of the fluids as a result of the imbalance of Coriolis and pressure forces, secondary motions will arise in each contacting phase as those depicted in Fig. 2.14 c.

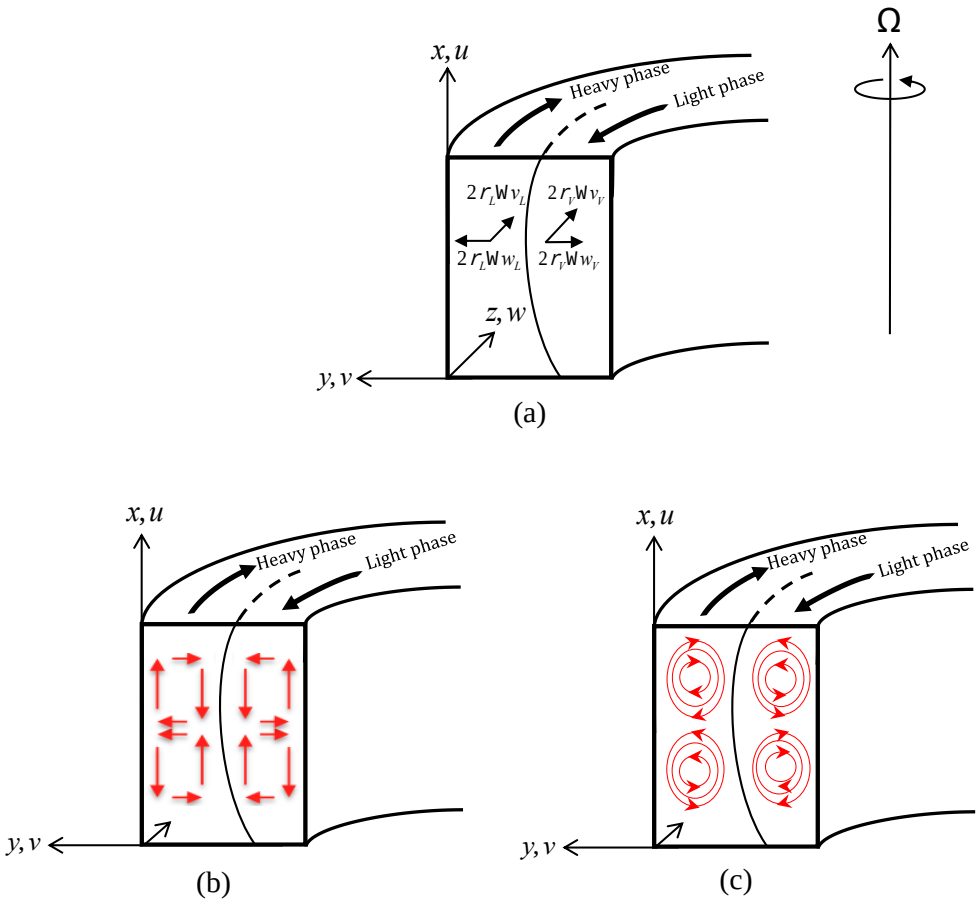

Figure 2.14. Mechanism of secondary motion formation in a two-phase contacting counter-currently in a rotating spiral channel. u, v and w are the velocity components in x, y and z directions, respectively. (a) Coriolis forces (b) onset of secondary motion and (c) illustrative structure of secondary motion.

There is a large volume of published work describing the nature and effects of these secondary motions in various rotating applications and curved channels (e.g. the flow of coolant in channels within turbine blades and the flow in heat exchangers). Hart (1971) studied experimentally the secondary flow in a rectangular channel under rotation. All the observations were carried out using wires acting as electrodes placed horizontally and vertically in a channel filled with an aqueous solution of thyme blue indicator. The channel aspect ratio used in the test is 7:1 and the rotation rate ranges from 0 to 6 rad/s. When a D.C voltage is applied, a small cylinder of coloured fluid forms around the wire placed in the location of the observation due to changing the pH of the working fluid. The coloured fluid formed then moves away with the moving fluid, forming a marker layer which allows visualization of the velocity profile. Over the narrow range of rotation rates tested, this experimental work demonstrated the existence of three distinct regions for the flow of fluid in a rotating channel (shown in Fig. 2.15) by observing the velocity profile of a vertical wire (parallel to *x*-direction in Fig. 2.14). At weak rotation rate, two double roll-cells were observed with a negligible effect on the streamwise velocity (Fig. 2.15 b). As the rotation rate increased, a number of roll-cells appeared, distorting the streamwise velocity profile (2.15 c and d). At more rapid rotation rate, the flow re-stabilised with a streamwise velocity profile as that shown in Fig. 2.15 e.

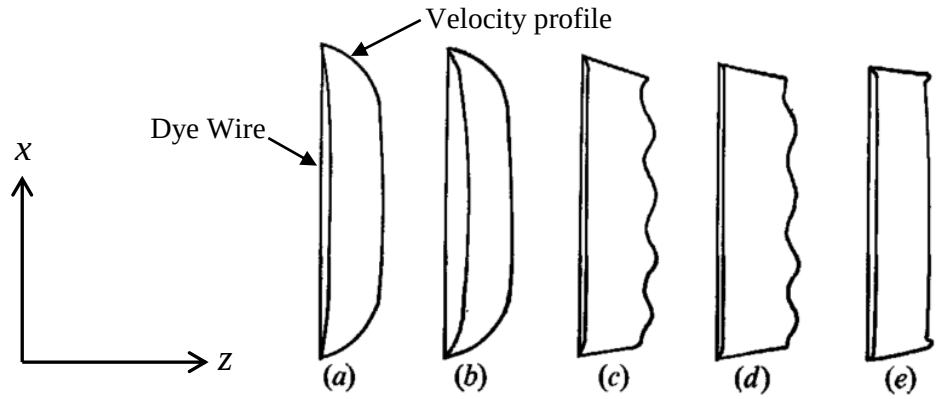

Figure 2.15. Streamwise velocity profiles observed experimentally by Hart (1971) along a centerline in the vertical direction (corresponds to *x*-direction in Fig. 2.14) of a rotating channel. (a) static channel, (b) at a weak rotating rate, (c) and (d) at moderate rotation rate and (e) at the highest rotation rate tested (6 rad/s).

Speziale and Thangam (1983) computed the laminar flow of an incompressible fluid (single-phase) in a large aspect-ratio rectangular channel (8:1). The results were in good agreement with the experiments of Hart (1971). Both studies found that the critical point at which the instability mode (Fig. 2.15 c and d) occurred is at a Reynolds number of about 100 and Rossby number (Ro) of around 1. Ro is the ratio of the inertial force to the Coriolis force and is expressed as $w_B/D\Omega$ where w_B is the bulk streamwise velocity and D is the channel width. Also, the computations of Speziale and Thangam (1983) showed clearly that there is an appreciable distortion in the streamwise velocity profiles along the transverse direction of the channel (corresponds to *y*-direction in Fig. 2.14) in relation to the pure pressure driven flow in a static channel (Poiseuille flow). Such distortion was confirmed by other computational studies made by Kheshgi and Scriven (1985) and Selmi et al. (1994). The former studied the behaviour of laminar flow of a single phase in a straight rotating channel, while the latter focused on the laminar flow in a curved channel under rotation. Fig. 2.16 shows the pattern of the secondary motion and the corresponding streamwise velocity profile computed by Selmi et al. (1994) at different Ro. The figure shows clearly the change in the distortion pattern of the streamwise velocity (Figs. 2.16 b, d, f and h) as the secondary flow changes (Figs. 2.16 a, c, e and g) with Ro.

Numerical studies have also been carried out to investigate the flow analogy in stationary curved ducts and rotating ducts (Lee and Baek 2001, 2002, 2006). For both laminar and turbulent flow, the authors found that the secondary motion increases the mean friction factor and they pointed out to that these secondary motions induce the heat transfer rate. In terms of the mass transfer, Ikehata et al. (2004) studied the effect of Coriolis force on the counter-current chromatographic separation by changing the direction of column rotation (i.e. anticlockwise or clockwise). For all solvent systems used, they found that there is a pronounced effect of Coriolis force on the performance of separation. The results also show that the clockwise rotation considerably enhances the separation performance with a lower retention time, irrespective of what the type of mobile phase is.

Similarly, in the rotating spiral contacting, Coriolis secondary motion is present and affects consequently the flow characteristics and mass transfer. As far as the author knows, the role of this motion, its structure and how it affects the mass transfer process in the spiral channel have not yet been explored. In this work, the effect of this secondary

motion will be investigated thoroughly over different contacting conditions. As will be seen, it will emerge as a significant factor in determining the mass transfer mechanism for counter-current gas-liquid contacting in a rotating spiral channel.

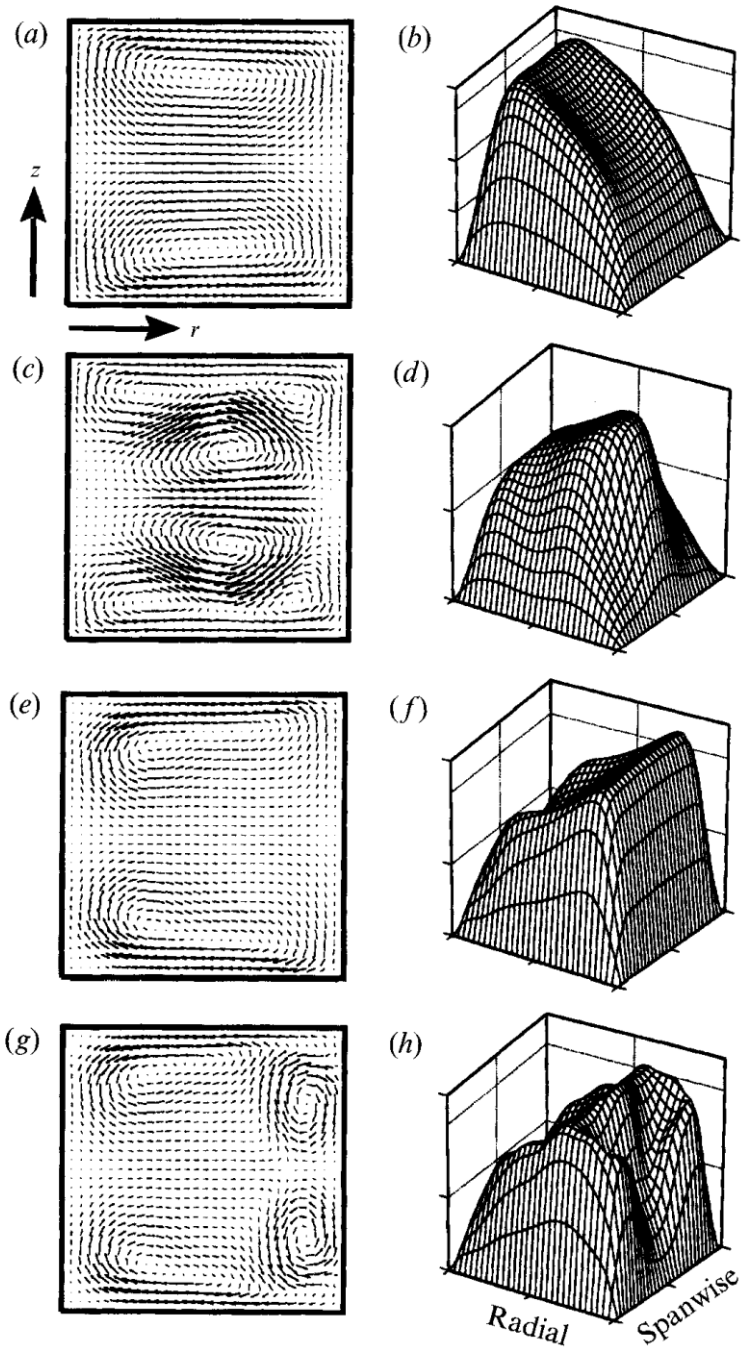

Figure 2.16. Vector plots of secondary flow and the corrsponding plots of streamwise velocity for flow through a curved channel of square cross section where plots (a and b) at Ro = 5, (c and d) at Ro = 10, (e and f) and (g and h) at Ro = 40 (Selmi et al., 1994).

2.4.4 Recent Studies of the Rotating Spiral

A theoretical study of rotating spiral contacting was performed by MacInnes et al. (2005). In the study, a hydrodynamic analysis was carried out for a vapour-liquid system flowing counter-currently to explore the feasibility of this technique. It was found that with minor changes to geometric parameters such as the channel angle, the pressure gradient and the centrifugal force could be controlled to produce a suitable counter-current flow.

Ortiz-Osorio et al. (2009) performed a numerical computation for a specific experimental condition of a rotating spiral distillation reported later by MacInnes et al. (2010). In the computation, the interface is assumed to be a perfect circle (Fig. 2.17). Such assumption is likely acceptable since the channel has micro-dimensions, causing the variation in the pressure across the interface to be negligible in relation to the surface tension. The bulk concentration in the liquid and vapour phase was computed and the results showed a good agreement with those measured experimentally.

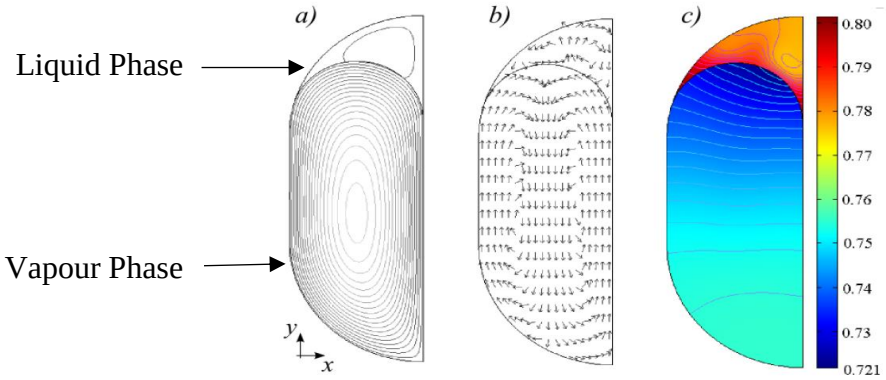

Figure 2.17. The results of computation for two phases with a circular interface, (a) the main velocity distribution, (b) the direction of the secondary motion (no magnitudes) and (c) the solute concentration distribution (Ortiz-Osorio et al., 2009).

An experimental exploration of rotating spiral contacting has been performed by MacInnes et al. (2010). In the study, a rotating apparatus was developed using a spiral microchannel (Fig. 2.18) to conduct a stripping distillation. A binary mixture of hydrocarbons (50:50 of 2,2-dimethylbutane and 2-methyl-2-butene) was used as a feedstock. The idea of bringing two immiscible phases (vapour-liquid) to flow side by

side counter-currently at micro-level was achieved successfully via this technology, resulting in an efficient multiple stages distillation.

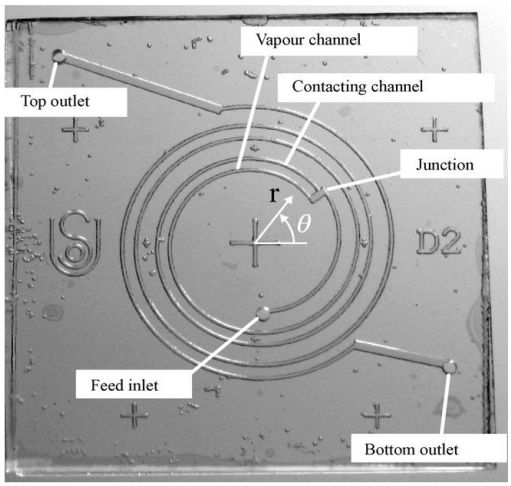

Figure 2.18. Spiral microchannel (255 × 95) μm^2 formed into a glass chip.

Fig. 2.19 shows the components of the apparatus used. As can be seen, it is equipped with a relatively large rotating unit. This unit holds all the main parts: the feed reservoir (only its atmospheric vent shown in Fig. 2.19 a), the distillate and the bottom collecting reservoirs (vials shown in Fig. 2.19 a), the spiral channel chip (not shown) and the heating and cooling elements (Fig. 2.19 b). The work gives a detail description of the temperature distribution and the flow network of the phases. These are crucial factors to control the evaporation process to generate the second phase (vapour). As the feed travels along the spiral channel, the temperature increases in a consistent manner such that evaporation occurs beyond the junction region (Fig. 2.18). This evaporation creates a pressure difference along the spiral which is enough to push the vapour phase backward to oppose the liquid that is primarily driven by the centrifugal force.

The above work demonstrated experimentally the feasibility of this technique by producing a distillation-like process. It was shown that a stable counter-current film contacting could be achieved practically by adjusting both the rotation rate and pressure drop along the channel.

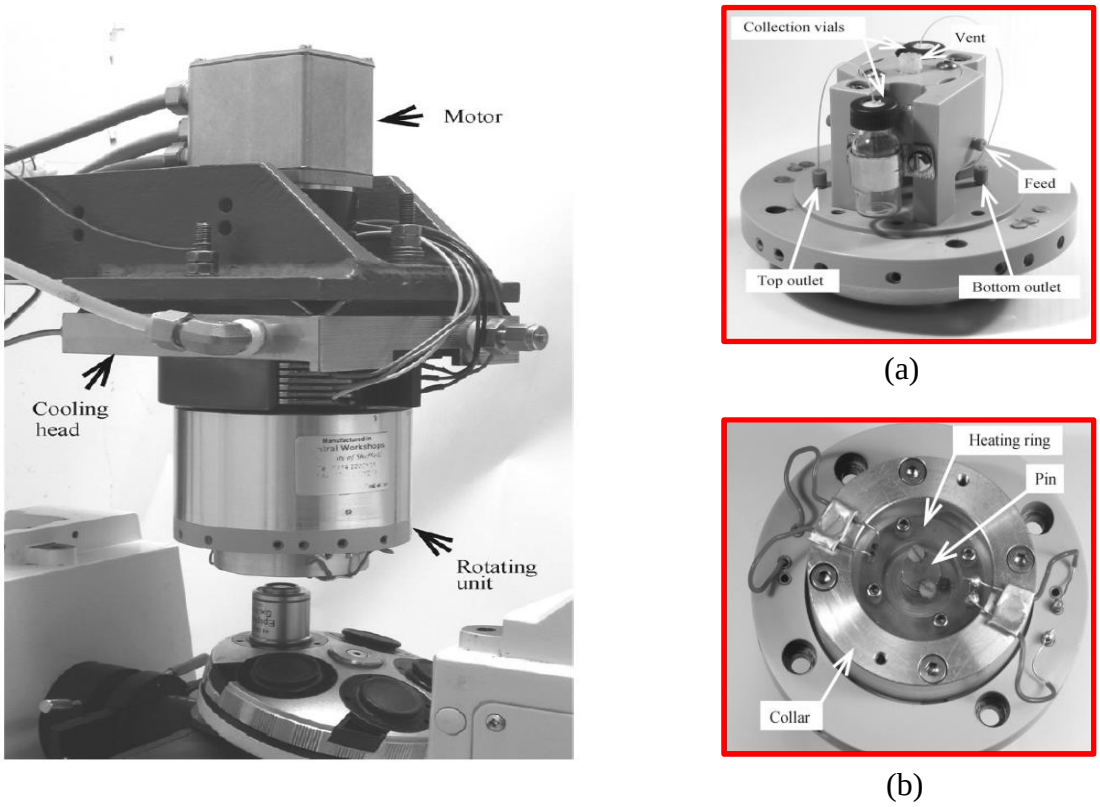

Figure 2.19. The main parts of the apparatus: (a) top view of the rotating unit and (b) the bottom view of the rotating unit.

Subsequently, a theoretical study has been reported in MacInnes et al. (2012). The study included analysis and modelling of two-phase contacting in a rotating spiral with infinite-width. As a result, an analytical model '*wide-channel model*' was developed. The solution of the model defines explicitly the relations between the hydrodynamics parameters, transfer coefficients, spiral geometry and operating conditions (pressure drop and rotation rate) in closed-formed expressions. In the work, MacInnes et al. (2012) also proposed dimensionless parameters as a preliminary guide to obtain a stable flow. Using the same notation identified in Figs. 2.13 and 2.14, the minimum radial position of the spiral channel ($R_{\min}$) and the heavy phase volume fraction (ξ), these parameters can be expressed as:

$$\mathrm{Re}_V = \frac{\rho_V w_{VB} h(1-\xi)}{\mu_V} \qquad \mathrm{Re}_L = \frac{\rho_L w_{LB} h \xi}{\mu_L}$$

$$\mathrm{Fr} = \frac{w_{LB}}{\sqrt{R_{\min}\Omega^2 \xi h}} \qquad \mathrm{We} = \frac{\rho_V \left(w_{LB} - w_{VB}\right)^2 \xi h}{\sigma}$$

$$\mathrm{E_O} = \frac{\left(\rho_L - \rho_V\right) R_{\min}\Omega^2 h^2}{\sigma} \qquad \frac{R_{\min}\Omega^2}{g} >> 1 \qquad (2.17)$$

The first two (Re_V and Re_L) are Reynolds numbers in the two phases and must remain less than some critical values to maintain steady and laminar flow. The third and fourth parameters are Froude number (Fr) and Weber number (We), respectively. The former can indicate where centrifugal body force waves at the phase interface may present. The latter represents the tendency to form interfacial surface tension waves or to disintegrate the interface into drops under high gas phase force. Each number must be less than some critical value. The final two are Eötvös number ($\mathrm{E_O}$), here based on the centrifugal rather than the gravitational acceleration, and the ratio of centrifugal and gravitational acceleration ($R_{\min}\Omega^2/g$). These two constraints affect the interface shape. $\mathrm{E_O}$ must be large enough to overcome the surface forces which tend to confine the gas phase into pockets surrounded by slugs of liquid phase, preventing ideal counter-current contacting. $R_{\min}\Omega^2$, on the other hand, must be larger than g to ensure obtaining an interface parallel to the channel walls and consequently phase layers of uniform thickness. These non-dimensional numbers, along with the wide channel model, help to determine the appropriate spiral dimensions and operating conditions under which stable interfacial contacting can be achieved.

MacInnes and Zambi (2015) studied the hydrodynamics of gas-liquid contacting using a newly developed apparatus. In contrast to the apparatus used in MacInnes et al. (2010), this allows continuous, counter-current contacting of fluid phase over a wide range of operating conditions. In the work, the variation of the liquid layer thickness (measured at the minimum distance between the interface shape and the channel wall) was examined as a function of phase flow rates, rotation rate and liquid viscosity. The minimum liquid layer thickness and hence the interface position was traced by taking digital images and analysing them using a model for the interface shape. The model was verified in that same work by comparing to experimental results over a wide range of conditions. Fig. 2.20 shows images taken to the phase layers at different conditions. In each image, there are three distinct regions: air on the left side, water on the right side and in between (grey region) the light reflected from the interface. Any changes in the position or shape of the interface with the conditions appear in Fig. 2.20 as changes in the grey region (interface region).

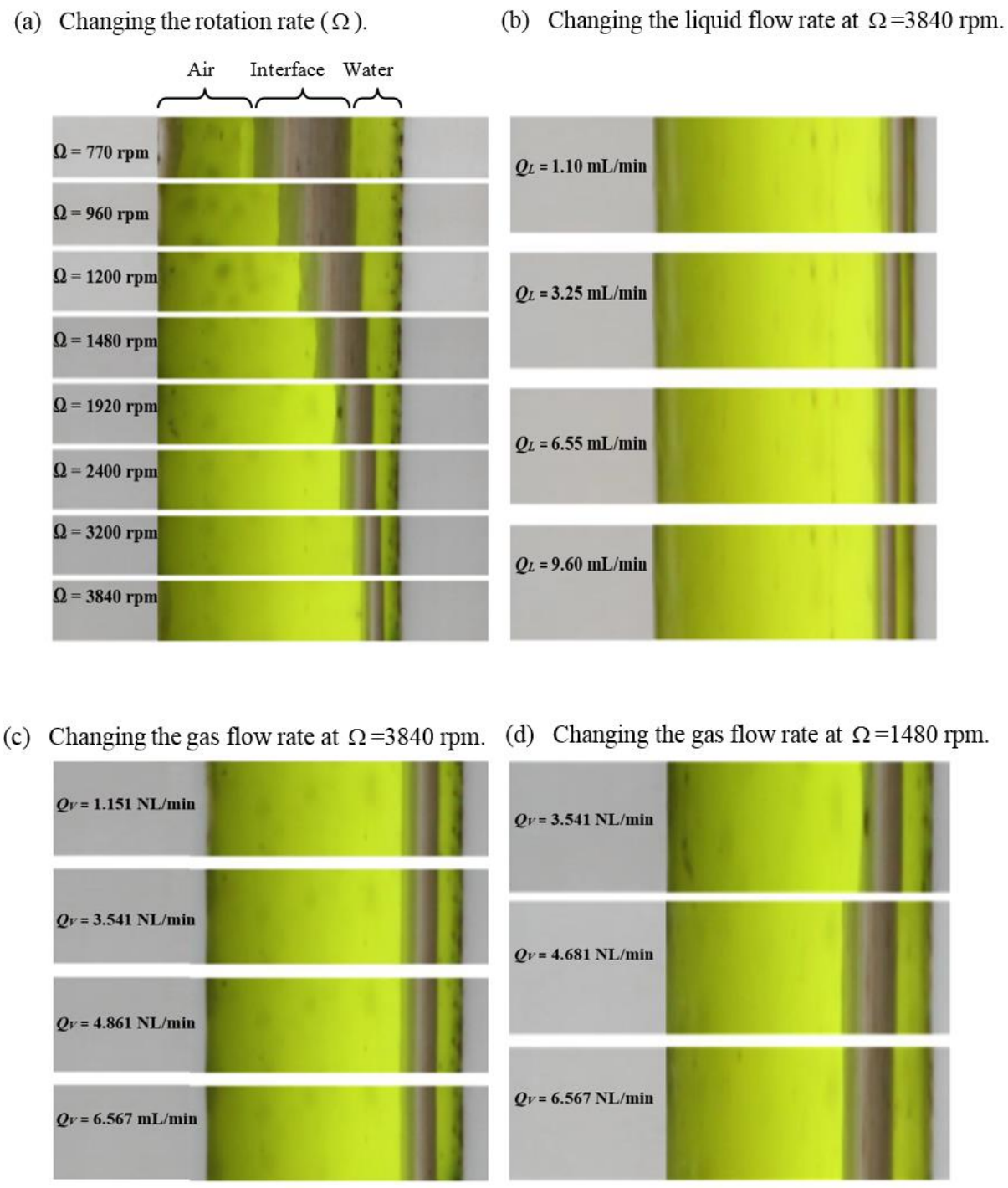

Figure 2.20. Images showing the phase layer thicknesses and meniscus size at different operating conditions (Zambri, 2014). The images are taken from the bottom of the channel which corresponds to the plane *y*-z in Fig. 2.14.

As expected, the authors found that by changing the rotation rate or the phase flow rates, the position of the interface could be adjusted as required. For the changes of the rotation rate (Fig. 2.20 a), they noticed that increasing the rotation rate at constant phase flow rates decreases the liquid layer thickness and also decreases both the interface tilt

and the meniscus height at the end-walls. Also, they found that increasing the flow rate of the liquid phase increases the liquid layer thickness as shown in Fig. 2.20 b. On the other hand, the results showed that the effect of the gas phase flow rate is minor at high rotation rate (Figs. 2.20 c) but becomes more pronounced at low rotation rate (2.20 d). Additionally, liquids with a considerable range of viscosities (from about 0.6 to 60 cP) were tested in that same work. The results showed that at constant rotation rate (3200 rpm), gas pressure (2.1 bar) and gas phase flow rate (1.15 NL/min), the liquid layer thickness increases with increasing the liquid viscosity.

Recently, chemical counter-current absorption of carbon dioxide from nitrogen using aqueous mixtures of diethanolamine (DEA) was investigated by MacInnes et al. (2017). The work demonstrated the use of the rotating spiral as a rapid and accurate tool to determine the optimum amine-water composition. This was made by comparing the amount of the gas phase treated by different DEA compositions under conditions where the liquid layer thickness is fixed (86 μm) and 90% removal of CO_2 is required. The study found that a DEA mass fraction of about 31% gave a maximum gas phase throughput at the required degree of purification.

2.5 This Research

The current work is linked strongly to the previously described works on the rotating spiral and is designed to build on systematically. The most crucial outcome emerging from the studies presented is that a full theoretical treatment of rotating spiral contacting is possible. This conclusion opens up the way to establish a general modelling approach to two phase contacting in a rotating spiral channel. The approach is based on a combination of the interface shape model (MacInnes and Zambri, 2015) and the 2-D governing equations. This helps to simulate the process of contacting, using the actual shape of the interface and including the Coriolis acceleration. In this way, the details of the flow and species fields can be calculated under different contacting conditions, opening up the possibility of deeply understanding the mass transfer process in rotating spiral channel which is one of the main aims here.

The work also includes an extensive experimental investigation of physical mass transfer (desorption) in a rotating spiral channel. These experiments aimed to study and understand the characteristics of the physical mass transfer in this novel contactor over

different phase flow rates. It has been argued in this chapter that the rotating spiral, uniquely, possesses the characteristics of producing improved contacting: independent control of the phase element length scales and phase flow rates. Quantifying this improvement is a significant step. Therefore, another direction here is to use the experimental results obtained to quantify the performance of the spiral in relation to alternative contacting approaches. For this purpose, a theoretical framework that allows a comparison between different approaches is developed and given in Chapter 3. The mass transfer results are also used to test critically the 2-D numerical model adopted in this work, determining its limitations. The theory behind the model is given in Chapter 4 while the comparison with the experimental data is discussed in Chapter 8, after presenting the experimental work (Chapter 5), determining the required physical properties (Chapter 6) and characterising the mass transfer behaviour using the experimental results (Chapter 7).

Chapter Three

Bulk Mass Transfer Analysis and Basic Relations

The previous chapter discusses gas-liquid contacting including the most common types of contactors and highlights features of rotating spiral channel. For most of these contactors a simple mass transfer analysis for a solute being transfer between the two immiscible phases is possible. Such analysis can be applied for both co-current and counter-current contacting, whether the process is absorption or desorption and whether the flow is linear or radial such as for rotating packed bed. In either case, ordinary differential equations based on the bulk quantities of the phases and transfer coefficients govern the mass transfer. Useful relations can be derived from the solution of these equations, linking the measurable inlet and outlet solute concentrations (bulk) to mass transfer coefficients. Therefore, it is possible to gain insight into the mass transfer performance at any contacting condition of interest. Also, the derived relations can be used to analyse results for any contacting method. So they can be employed as a basis for comparing different contacting devices. This can be done regardless of solute properties and operating conditions, allowing direct comparison between the rotating spiral and other contactors performing similar separation task.

This chapter gives a full presentation of the bulk mass transfer analysis and the resulting relations. As in the experiments in this work, attention is focused on counter-current contacting and the case of dilute solute. Counter-current flow enables an unlimited number of equilibrium stages to be reached and hence a high degree of purification. The case of a dilute solute ensures constant physical properties in each phase and linear representation of the solute equilibrium curve. Further, a broad range of applications involve the purification of dilute solute, such as removal of organic compounds or other trace toxics from waste water (Hartwick and Howat, 1995; Sherman et al., 1996).

Relations for determining the mass transfer coefficients are developed first. These relations lead to a useful design equation which links purification with the phase flow rates ratio, the residence time of the processed phase and the contacting effectiveness. The contacting effectiveness is represented here by the specific throughput which is the volumetric flow rate of the processed phase per volume of one equilibrium stage

(MacInnes et al, 2012). Another important parameter introduced is the total specific throughput, which is the specific throughput divided by the number of stages required to achieve a given purification. This parameter is used in this work to compare the rotating spiral channel with other alternative approaches over a range of solute properties and contacting conditions as discussed in Chapter 7.

3.1 Counter-current Contacting Analysis

A general state of counter-current fluid-phase contacting in a contactor with length L is depicted in Fig. 3.1 where the notation a and ξ are the interfacial area per unit volume of the passage and the volume fraction occupied by the heavy phase, respectively. To give a general context and simplify the discussion, the gas phase is referred to as the 'light' phase with subscript 'V ' and the term 'heavy' phase with subscript 'L ' is used to designate the liquid phase.

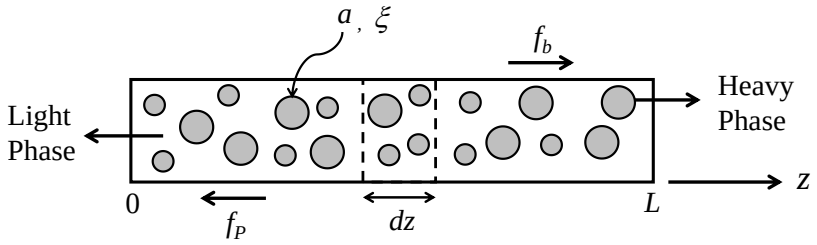

Figure 3.1. Counter-current contacting of two phases over length L produced by a suitable magnitude of body force (f_b) and pressure force (f_p).

The flow of the phases in Fig. 3.1 is in the direction of the *z*-coordinate. When a body force per unit volume (f_b) acts in the positive *z*-direction and a pressure force (f_p) acts in the negative *z*-direction, a counter-current mode of flow is possible. In this case, the heavy phase, represented by dispersed droplets, travels in the direction of the body force since it has a larger density while the light continuous phase flows in the opposite direction. Similarly, co-current flow may occur in either direction along z. Both phases can flow in the positive direction when the body force is dominant or in the negative direction when the pressure force is sufficiently large. It is also possible for the heavy phase to be the continuous phase, e.g. in bubble columns, or both phases could be continuous as the case for rotating spiral and falling film contactors. All these possible cases are described in Chapter 2 and they do not change the analysis in this chapter.

The mass transfer experiments performed in this work consider desorption in which the solute transfers from the liquid to the gas phase. Accordingly, a differential mole balance for a solute being desorbed from the heavy phase into the light phase over a region of dz length (Fig. 3.1) can be expressed as:

Heavy phase: $$\frac{d(-n_L w_{LB} \xi Y_{LB})}{dz} = j_L a \tag{3.1}$$

Light phase: $$\frac{d(n_V w_{VB} (1-\xi) Y_{VB})}{dz} = j_V a \tag{3.2}$$

where n_V and n_L are the phase molar densities , w_{VB} and w_{LB} are the bulk velocities with w_{VB} negative according to the coordinates used in Fig. 3.1, Y_{VB} and Y_{LB} are the bulk solute mole fractions and j_V and j_L are the solute molar flux transferred across the phase interface based on the two phases.

The flux in Eqs. 3.1 and 3.2 may be expressed in terms of two individual mass transfer coefficients (k_V and k_L) and the difference between the bulk solute mole fractions and those at the interface (Y_{VI} and Y_{LI}):

Heavy phase: $$j_L = k_L (Y_{LB} - Y_{LI}) \tag{3.3}$$

Light phase: $$j_V = k_V (Y_{VI} - Y_{VB}) \tag{3.4}$$

Substituting Eqs. 3.3 and 3.4 in Eqs. 3.1 and 3.2, respectively, gives:

Heavy phase: $$\frac{d(-n_L w_{LB} \xi Y_{LB})}{dz} = k_L a (Y_{LB} - Y_{LI}) \tag{3.5}$$

Light phase: $$\frac{d(n_V w_{VB} (1-\xi) Y_{VB})}{dz} = k_V a (Y_{VI} - Y_{VB}) \tag{3.6}$$

The derivatives on the left hand sides of the above equations can be expanded as:

$$\frac{d(-n_L w_{LB} \xi Y_{LB})}{dz} = -n_L w_{LB} \xi \frac{dY_{LB}}{dz} + Y_{LB} \frac{d(-n_L w_{LB} \xi)}{dz} \tag{3.7}$$

$$\frac{d(n_V w_{VB} (1-\xi) Y_{VB})}{dz} = n_V w_{VB} (1-\xi) \frac{dY_{VB}}{dz} + Y_{VB} \frac{d(n_V w_{VB} (1-\xi))}{dz} \tag{3.8}$$

The change in phase molar flow rates appeared in Eqs. 3.7 and 3.8 equals the amount of solute being transferred, i.e.:

In Eq. 3.7: $$\frac{d(-n_L w_{LB}\xi)}{dz} = k_L a\,(Y_{LB} - Y_{LI}) \tag{3.9}$$

In Eq. 3.8: $$\frac{d(n_V w_{VB}(1-\xi))}{dz} = k_V a\,(Y_{VI} - Y_{VB}) \tag{3.10}$$

Combining Eqs. 3.7, 3.8, 3.9 and 3.10 and substituting for the derivatives in Eqs. 3.5 and 3.6, give:

Heavy phase: $$\frac{-n_L w_{LB}\xi}{(1-Y_{LB})}\frac{dY_{LB}}{dz} = k_L a\,(Y_{LB} - Y_{LI}) \tag{3.11}$$

Light phase: $$\frac{n_V w_{VB}(1-\xi)}{(1-Y_{VB})}\frac{dY_{VB}}{dz} = k_V a\,(Y_{VI} - Y_{VB}) \tag{3.12}$$

Eqs. 3.11 and 3.12 give the variation of the bulk mole fraction in each phase in terms of the individual mass transfer coefficients, specific interfacial area, bulk and interfacial mole fractions and phase molar flow rates per unit area. The factors $(1-Y_{LB})$ and $(1-Y_{VB})$ in these equations account for the change in molar flow rates due to changing bulk mole fractions along the contacting length as a result of solute transport.

3.2 Overall Coefficients

The difficulty in using Eqs. 3.11 and 3.12 to analyse experiments directly centres around the problem of knowing solute mole fractions at the interface (Y_{LI} and Y_{VI}). This makes an analysis based on the individual coefficients impractical. By using 'overall' mass transfer coefficients, the flux (the right-hand terms in Eqs. 3.11 and 3.12) can be expressed equivalently in terms of the bulk mole fractions in the two phases, eliminating the need to determine Y_{LI} and Y_{VI}:

Heavy phase: $$k_L\,(Y_{LB} - Y_{LI}) = K_L(Y_{LB} - Y^*_{LB}) \tag{3.13}$$

Light phase: $$k_V\,(Y_{VI} - Y_{VB}) = K_V\,(Y^*_{VB} - Y_{VB}) \tag{3.14}$$

where K_L and K_V are the overall mass transfer coefficients, Y^*_{LB} is a hypothetical solute mole fraction that would be in equilibrium with that in the gas phase and Y^*_{VB} is similar to Y^*_{LB} but in equilibrium with the liquid phase composition. The concept of these hypothetical mole fractions (Y^*_{LB} and Y^*_{VB}) stems from the fact that mass transfer occurs

due to a departure from the equilibrium (i.e. $Y_{LB} - Y_{LB}^{*}$). Thus, one might expect that if the light phase becomes fully saturated with solute, Y_{LB} will be exactly Y_{LB}^{*} and hence the net solute flux is zero. In practice, approaching such equilibrium case should be avoided by choosing appropriate phase flow rates ratio, as discussed in Chapter 2, if a convenient degree of purification is required.

Locally, the overall mass transfer coefficients can be expressed purely in terms of the individual coefficients and the slopes of the equilibrium curve. In almost all situations, this can be done under three conditions. First of all, the interface must be an extremely thin layer without any contaminants or extra layers which might add resistance. In this case, the interface does not store mass and equilibrium exists between Y_{LI} and Y_{VI}. Second, there are no interfacial ripples or turbulence which can affect the individual mass transfer coefficients. Third, the transfer of the solute across the interface is not associated with chemical reaction (Sherwood et al., 1975). Under these conditions, the interfacial mole fractions (Y_{LI} and Y_{VI}) lie on the solute equilibrium curve, $Y_{VB} = f(Y_{LB})$, as shown in Fig. 3.2.

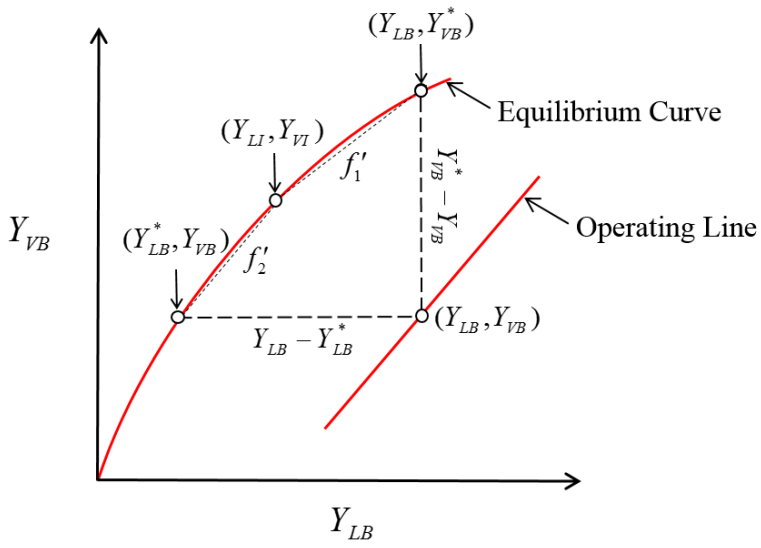

Figure 3.2. Graphical representation showing the relation between the local slopes of the equilibrium curve and the bulk solute mole fractions in the light and heavy phase.

In the figure, (Y_{LB} , Y_{VB}) is any local position along the contacting length and f_1' and f_2' are the local slopes of the equilibrium curve. These slopes can be determined graphically using the values of the solute mole fractions (Y_{LB}, Y_{VB}, Y_{LI} and Y_{VI}):

$$f_1' = \frac{Y_{VB}^* - Y_{VI}}{Y_{LB} - Y_{LI}} \tag{3.15}$$

$$f_2' = \frac{Y_{VI} - Y_{VB}}{Y_{LI} - Y_{LB}^*} \tag{3.16}$$

Using Eqs. 3.13 and 3.14, the solute mole fractions in Eqs. 3.15 and 3.16 can be replaced by the transfer coefficients,

$$\frac{k_L}{K_V} = \frac{k_L}{k_V} + f_1' \tag{3.17}$$

$$\frac{k_V}{K_L} = \frac{1}{f_2'} + \frac{k_V}{k_L} \tag{3.18}$$

From Eqs. 3.17 and 3.18, it is clear that the local mass transfer coefficients can be expressed in terms of the individual mass transfer coefficients and the slopes of the equilibrium curve. However, these relations can only be used when a linear representation of equilibrium curve is feasible.

To this point, the governing equations (Eqs. 3.11 and 3.12) can be expressed in terms of the overall mass transfer coefficients using Eqs. 3.13 and 3.14:

Heavy phase: $$-n_L w_{LB} \xi \frac{dY_{LB}}{dz} = K_L a\,(Y_{LB} - Y_{LB}^*)(1 - Y_{LB}) \tag{3.19}$$

Light phase: $$n_V w_{VB} (1-\xi) \frac{dY_{VB}}{dz} = K_V a\,(Y_{VB}^* - Y_{VB})(1 - Y_{VB}) \tag{3.20}$$

These differential equations are non-linear and must be solved by integrating along the contacting length from the inlet to the outlet:

Heavy phase: $$\int_0^L dz = \int_{Y_{LB}(0)}^{Y_{LB}(L)} \left(\frac{-n_L w_{LB} \xi}{K_L a} \right) \left(\frac{dY_{LB}}{(1 - Y_{LB})(Y_{LB} - Y_{LB}^*)} \right) \tag{3.21}$$

Light phase: $$\int_0^L dz = \int_{Y_{VB}(0)}^{Y_{VB}(L)} \left(\frac{n_V w_{VB} (1-\xi)}{K_V a} \right) \left(\frac{dY_{VB}}{(1 - Y_{VB})(Y_{VB}^* - Y_{VB})} \right) \tag{3.22}$$

In general, the integration requires numerical or graphical evaluation, i.e. evaluation of the integrands over the relevant range of mole fractions. However, a full analytical solution is possible with further approximation and that will be discussed in the next section.

3.3 Dilute Solute Approximation

When the solute exists at infinitely dilute level in both phases, the change in phase molar flow rates is small, the phase properties do not significantly alter along the contacting length, the equilibrium relationship is linear and analytical solution is possible. Accordingly, n_L, n_V, w_{LB}, w_{VB}, ξ and a are independent of Y_{LB} and Y_{VB}. K_L and K_V are constant along the contacting length. Further, the factors $1-Y_{LB}$ and $1-Y_{VB}$ are approximately one and the equilibrium relation can be expressed as:

$$Y_{VB} = f' Y_{LB} \tag{3.23}$$

where f' is a constant, representing the solute equilibrium distribution over the contacting length. These approximations reduce Eqs. 3.21 and 3.22 to,

Heavy phase: $$\frac{-K_L a\, L}{n_L w_{LB} \xi} = \int_{Y_{LB}(0)}^{Y_{LB}(L)} \frac{dY_{LB}}{(Y_{LB} - Y_{LB}^*)} \tag{3.24}$$

Light phase: $$\frac{K_V a\, L}{n_V w_{VB} (1-\xi)} = \int_{Y_{VB}(0)}^{Y_{VB}(L)} \frac{dY_{VB}}{(Y_{VB}^* - Y_{VB})} \tag{3.25}$$

and simplify Eqs. 3.17 and 3.18 so that the overall coefficients can be expressed in terms of k_L and k_V along the contacting length since $f_1' = f_2' = f'$:

$$K_L = \left(\frac{1}{k_V f'} + \frac{1}{k_L} \right)^{-1} \quad \text{and} \quad K_V = \left(\frac{1}{k_V} + \frac{f'}{k_L} \right)^{-1} \tag{3.26}$$

Now, making overall balance over a section of the contacting length (Fig. 3.3) gives a relation (operating line) that links the heavy and light phase bulk solute mole fractions over any section in the contacting length:

$$Y_{VB}(z) = Y_{VB}(L) - \frac{Y_{LB}(z) - Y_{LB}(L)}{q_n} \tag{3.27}$$

where q_n is the constant ratio of the phase molar flow rates and has a negative sign for counter-current flow since $w_{VB} < 0$ in this case:

$$q_n = \frac{n_V w_{VB} (1-\xi)}{n_L w_{LB} \xi} \tag{3.28}$$

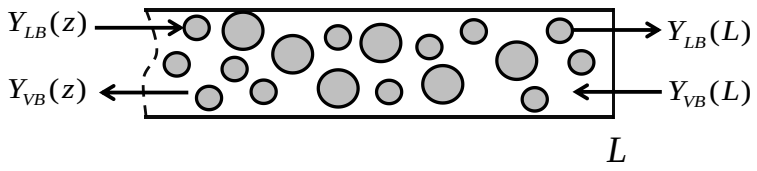

Figure 3.3. A section of contacting length.

Since both Eqs. 3.23 and 3.27 are linear relations between Y_{LB} and Y_{VB}, the difference in concentration (i.e. $Y_{LB} - Y_{LB}^*$ and $Y_{VB}^* - Y_{VB}$ in Fig. 3.2) must also be linear with Y_{LB} and Y_{VB}, thus:

$$dY_{LB} \propto d(Y_{LB} - Y_{LB}^*) \quad \text{and} \quad dY_{VB} \propto d(Y_{VB}^* - Y_{VB}) \tag{3.29}$$

Using the abbreviations $\Delta Y_{LB} = Y_{LB} - Y_{LB}^*$ and $\Delta Y_{VB} = Y_{VB}^* - Y_{VB}$, Eq. 3.29 gives:

$$\frac{d\Delta Y_{LB}}{dY_{LB}} = \frac{\Delta Y_{LB}(L) - \Delta Y_{LB}(0)}{Y_{LB}(L) - Y_{LB}(0)} \tag{3.30}$$

$$\frac{d\Delta Y_{VB}}{dY_{VB}} = \frac{\Delta Y_{VB}(L) - \Delta Y_{VB}(0)}{Y_{VB}(L) - Y_{VB}(0)} \tag{3.31}$$

So, the integrals in Eqs. 3.24 and 3.25 may be expressed in terms of the variables ΔY_{LB} and ΔY_{VB} and integrated to give two relations in terms $K_L a$ and $K_V a$ (e.g. Sherwood et al., 1975):

$$\frac{-K_L a\, L}{n_L w_{LB} \xi} = \frac{Y_{LB}(L) - Y_{LB}(0)}{\overline{\Delta Y_{LB}}} \tag{3.32}$$

$$\frac{K_V a\, L}{n_V w_{VB}(1-\xi)} = \frac{Y_{VB}(L) - Y_{VB}(0)}{\overline{\Delta Y_{VB}}} \tag{3.33}$$

$$\text{where} \quad \overline{\Delta Y_{LB}} = \frac{\Delta Y_{LB}(L) - \Delta Y_{LB}(0)}{\ln[\Delta Y_{LB}(L)/\Delta Y_{LB}(0)]} \tag{3.34}$$

$$\text{and} \quad \overline{\Delta Y_{VB}} = \frac{\Delta Y_{VB}(L) - \Delta Y_{VB}(0)}{\ln[\Delta Y_{VB}(L)/\Delta Y_{VB}(0)]} \tag{3.35}$$

It is helpful to note here that Y_{LB}^* and Y_{VB}^* in the expressions for ΔY_{LB} and ΔY_{VB} are linked to the solute mole fraction in each phase through the equilibrium relation (Eq. 3.23) and can be expressed as $Y_{LB}^* = Y_{VB}/f'$ and $Y_{VB}^* = f' Y_{LB}$.

Now, Eqs. 3.32 to 3.35 can be used directly to determine $K_L a$ and $K_V a$ from the inlet and outlet solute mole fractions for each phase, phase flow rates and equilibrium constant. In practice, these parameters either can be measured directly such as the solute mole fractions and the phase flow rates or estimated from the contacting conditions such as f', allowing a determination of the experimental $K_L a$ and $K_V a$ values.

3.4 Mass Transfer Performance

For fluid-fluid contacting, the mass transfer relies on two essential factors: the phase *flow rate ratio*, which is represented by the purification factor ($-f'q_n$), and the phase *contacting effectiveness*. The first is important to make ensure that a sufficient amount of solvent is used to achieve the required degree of purification. The constraint on this factor has been discussed in Chapter 2 (Section 2.2.1). For desorption, for example, $-f'q_n$ must satisfy the limit $-f'q_n > 1 - d_L$ (Eq. 2.7) where $d_L = Y_{LB}(L)/Y_{LB}(0)$ according to the notations in Fig. 3.1. The contacting effectiveness, on the other hand, depends on the way that the two phases are brought together in each particular contactor. In literature, there are different measures that quantify this factor. The overall mass transfer coefficient is the usual measure. Another measure is the length of a "transfer unit" based on one of the phases (Anvaripour et al., 1995). It has a unit of length and represents the inverse of the terms multiplying L on the right-hand side of Eqs. 3.33 and 3.34 (i.e. $n_L w_{LB} \xi / K_L a$ or $n_V w_{VB}(1-\xi)/K_V a$). Equivalently, the specific throughput (Φ) measures the contacting effectiveness and will be used here. This term represents the volumetric flow rate of fluid to be processed per passage volume corresponding to one equilibrium stage (MacInnes, et al., 2012), i.e.:

$$Specific\ throughput = \frac{Volumetric\ \ flow\ \ rate\ \ of\ \ the\ \ process\ \ stream}{Passage\ \ volume\ \ used\ \ based\ \ on\ \ one\ \ equilibrium\ \ stage} \quad (3.36)$$

The equilibrium stage is taken to have a contacting length of ℓ_e which is required for the exiting phases to have a solute composition corresponding to equilibrium. Using the equilibrium stage concept, the length of a contactor then can be expressed as:

$$L = \ell_e N_e \quad (3.37)$$

where N_e is the number of equilibrium stages.

For any contacting task, when a suitable phase flow rates ratio is selected ($-f'q_n > 1 - d_L$), the required degree of separation (d_L) determines N_e and hence the total passage length from Eq. 3.37 once ℓ_e has been determined. The number of equilibrium stages in Eq. 3.37, therefore, is simply a multiplicative factor, independent of the contacting effectiveness. Hence, in a qualitative sense, a larger specific throughput at a given value of $-f'q_n$ indicates that larger volumetric flow rate of the process stream can be treated in a given size of contactor (L) and degree of separation (d_L). Specific throughput also can be defined as the inverse of the processing time needed to accomplish one equilibrium stage. Its reciprocal measures the passage volume required for each equilibrium stage per unit volumetric flow rate of the process phase. Thus, the larger the specific throughput at a given value of $-f'q_n$ and d_L (which fix N_e) the smaller ℓ_e and hence contactor size needed (Eq. 3.37) to purify a given throughput of the processed phase.

3.4.1 Specific Throughput

The basic definition of the specific throughput given in Eq. 3.36 may be expressed in terms of the heavy phase flow rate (process stream in desorption) which is $w_{LB}\,\xi\,A$ and the passage volume based on one equilibrium stage ($\ell_e A$) as:

$$\Phi_L = \frac{w_{LB}\xi A}{\ell_e A} = \frac{w_{LB}\xi}{\ell_e} \tag{3.38}$$

where A is the passage cross sectional area of a contactor.

For continuous, differential-contacting where there are no physically distinguishable stages, ℓ_e is an arbitrary length for which the contacting phases are at equilibrium. Eq. 3.24 can be used directly to determine this arbitrary length by taking its position to be $z = 0$ along the contacting and replacing L by ℓ_e as:

$$\ell_e = \frac{-n_L w_{LB}\xi}{K_L a} \int_{Y_{LB}(0)}^{Y_{LB}(\ell_e)} \frac{dY_{LB}}{(Y_{LB} - Y_{LB}^*)} \tag{3.39}$$

The integral term in Eq. 3.39 can be handled in the same manner used for Eq. 3.24 and this gives:

$$\ell_e = \frac{n_L w_{LB} \xi}{K_L a} \frac{Y_{LB}(0) - Y_{LB}(\ell_e)}{\Delta Y_{LB}(\ell_e) - \Delta Y_{LB}(0)} \ln\left[\Delta Y_{LB}(\ell_e)/\Delta Y_{LB}(0)\right] \tag{3.40}$$

Using the general mole balance relation (Eq. 3.27) and setting $z = 0$ and $L = \ell_e$, the relation between the heavy and light phase bulk solute mole fractions over the equilibrium length may be given as:

$$Y_{VB}(0) = Y_{VB}(\ell_e) - \frac{Y_{LB}(0) - Y_{LB}(\ell_e)}{q_n} \tag{3.41}$$

Using the above equation and the fact that $Y_{VB}(0) = f' Y_{LB}(\ell_e)$, Eq. 3.40 may be simplified to:

$$\ell_e = \frac{n_L w_{LB} \xi}{K_L a} \frac{f' q_n \ln(-f' q_n)}{(1 + f' q_n)} \tag{3.42}$$

Substituting Eq. 3.42 in 3.38, the corresponding relation for the specific throughput is:

$$\Phi_L = \frac{K_L a}{n_L} \frac{(1 + f' q_n)}{f' q_n \ln(-f' q_n)} \tag{3.43}$$

This relation allows the calculation of the specific throughput from the overall mass transfer coefficient, the molar density of the heavy phase and the purification factor $(-f' q_n)$.

3.4.2 Total Specific Throughput

While the specific throughput is useful to judge the contacting effectiveness at a particular $-f' q_n$, it becomes imprecise when different contacting conditions from different equipment are involved. In this case, the purification factor $(-f' q_n)$, the degree of purification (d_L), the throughput achieved and the size of the contactor used to achieve the throughput must be considered. Comparison considering these factors needs to look at the throughput per volume of the total passage required to achieve a specific purity. This 'total' specific throughput, Φ_{LN}, differs from Φ_L precisely by the number of the equilibrium stages required, i.e.:

$$\Phi_{LN} = \frac{w_{LB} \xi}{L} = \frac{w_{LB} \xi}{\ell_e N_e} = \frac{\Phi_L}{N_e} \tag{3.44}$$

Since N_e in Eq. 3.44 implies the effect of $-f'q_n$ and d_L, the total specific throughput is more comprehensive than Φ_L, allowing different phase flow rate ratios ($-f'q_n$) at any given purification (d_L) to be compared.

The number of stages is given by $N_e = L/\ell_e$ from Eq. 3.37. The contacting length (L) appeared explicitly in Eq. 3.32. Thus, using this equation, L can be expressed in terms of the mass transfer coefficient and purity parameters d_L and d_V as:

$$\frac{-K_L a\, L(1+f'q_n)}{n_L w_{LB} \xi\, f'q_n} = \ln\left\{\frac{-q_n d_V + f'q_n d_L}{1-d_L-q_n d_V + f'q_n}\right\} \tag{3.45}$$

Hence, from Eq. 3.42 and Eq. 3.45, the relation for N_e can be given by:

$$N_e = -\frac{1}{\ln(-f'q_n)} \ln\left\{\frac{-q_n d_V + f'q_n d_L}{1-d_L-q_n d_V + f'q_n}\right\} \tag{3.46}$$

Using the specific throughput relation (Eq. 3.43) and the above equation, the total specific throughput can be expressed as:

$$\Phi_{LN} = \frac{\Phi_L}{N_e} = \frac{-K_L a(1+f'q_n)}{n_L\, f'q_n}\left[\ln\left\{\frac{-q_n d_V + f'q_n d_L}{1-d_L-q_n d_V + f'q_n}\right\}\right]^{-1} \tag{3.47}$$

In general, two fundamental points can be inferred from Eq. 3.47. First, the mass transfer coefficient appearing in the equation can be calculated from an experiment using Eq. 3.32. This implies that Eq. 3.47 uses experimental results from different contacting conditions and translates them into throughput per volume of the device used to achieve a specific degree of purification (d_L). In this way, a comparison based on a common basis between different approaches or different conditions is possible. Second, there is a clear dependency of the total specific throughput on the purification factor $-f'q_n$, which determines the usage of the solvent. Such dependency is shown clearly in Fig. 3.4 for three different purities d_L = 0.1, 0.01 and 0.001 and constant $K_L a/n_L$. The value of Φ_{LN} is normalised by the limiting value $\Phi_{LN\infty}$, the limit as $-f'q_n \to \infty$, so a value of $K_L a/n_L$ does not need to be specified. It is clear in Fig. 3.4 that as the purification factor ($-f'q_n$) is decreased towards unity, total specific throughput decreases and at an

increasing rate. On the other hand, high $-f'q_n$ means excessive solvent flow rate. In general, the precise optimum for $-f'q_n$, for a particular phase and solvent system, will depend on d_L and d_V, on how $K_L a/n_L$ changes with $-f'q_n$ along with other external factors related to process inventory and must be determined for each situation individually. However, a value lying in the range $-f'q_n$ = 2 to 4 appears to be a reasonable compromise between specific throughput (equipment size) and flow rate ratio (solvent cost).

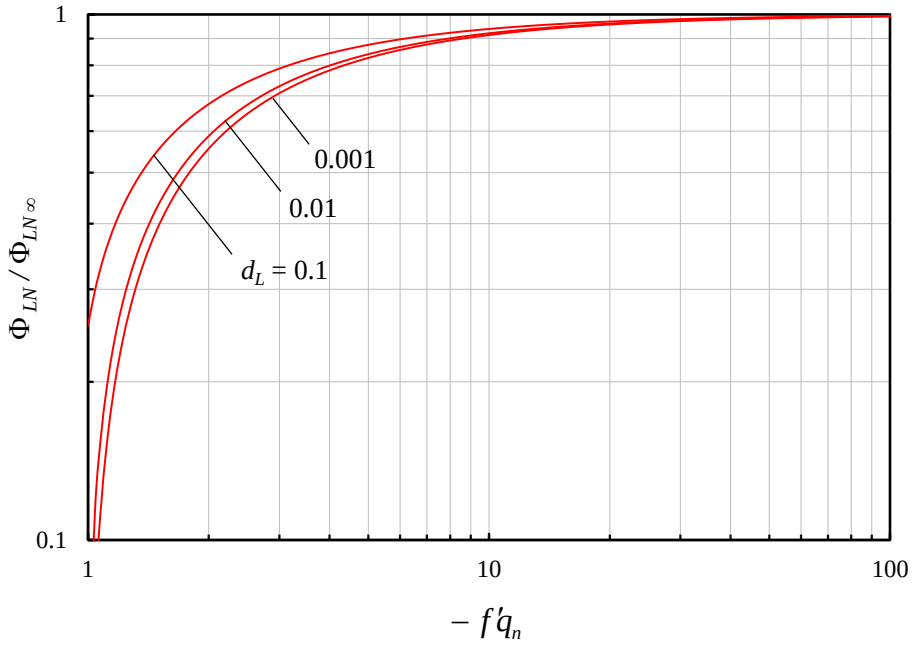

Figure 3.4. Dependence of the total specific throughput on $-f'q_n$ at three different purifications.

3.5 Purification Relation

Based on the liquid phase, Eq. 3.45 explicitly links the most important parameters for any contacting task: the size of contactor represented by L, the mass transfer rate represented by $K_L a$ which can be linked with the specific throughput, actual throughput per unit area ($n_L w_{LB}$) and finally the purity parameters (d_L and d_V) and the purification factor ($-f'q_n$). This equation may be combined with the specific throughput (Eq. 3.43) to determine a general relation relating all the major contacting parameters. Thus, re-arranging the specific throughput relation (Eq. 3.43) gives:

$$K_L a(1+f'q_n) = \Phi_L n_L f'q_n \ln(-f'q_n) \qquad (3.48)$$

Combining with Eq. 3.45 yields:

$$\frac{L}{w_{LB}\xi}\Phi_L \ln\left(-f'q_n\right) = \ln\left\{\frac{-q_n d_V + f'q_n d_L}{1 - d_L - q_n d_V + f'q_n}\right\} \tag{3.49}$$

The group $L/w_{LB}\xi$ appearing on the left hand side is the reciprocal of the total specific throughput and represents the mean residence time of the liquid phase (t_{mL}), i.e.:

$$t_{mL} = \frac{L}{w_{LB}\xi} \tag{3.50}$$

To give the final relation, substitute Eq. 3.50 in Eq. 3.49 and solve for the purification:

$$d_L = \frac{q_n d_V + \left(1 - q_n d_V + f'q_n\right)\left(-f'q_n\right)^{-\Phi_L t_{mL}}}{f'q_n + \left(-f'q_n\right)^{-\Phi_L t_{mL}}} \tag{3.51}$$

This general relationship allows the explicit connection between the specific throughput, purification factor ($-f'q_n$), flow rate ratio ($-q_n$), solvent purity (d_V) and the residence time. To give insight into the nature of this relationship, plotting Eq. 3.51 would be useful. This is done for the case of pure solvent at inlet (d_V = 0) for a number of $\Phi_L t_{mL}$ values and the results are shown in Fig. 3.5. The influence of the inlet solvent purity is also considered for the case where $\Phi_L t_{mL}$ = 2.7 and f' = 1. These results are shown in Fig. 3.6. As one may note, three expected trends can be drawn from the results of Figs. 3.5 and 3.6. First, it is clear from Fig. 3.5 that d_L decreases with the value of $\Phi_L t_{mL}$ term. This term is a product of the liquid phase residence time (t_{mL}) and the specific throughput (Φ_L). So, in practice, it is possible to decrease d_L either by lengthening the contacting distance which increases t_{mL} (Eq. 3.50) or increasing the contacting effectiveness (Φ_L). This means that achieving higher purification ($d_L \approx 0$) does not mean necessarily that the contacting is effective. Second, insufficient solvent flow rate ($-f'q_n$ <1) prevents full purification (i.e. d_L = 0), even when the contacting occurs at maximum $\Phi_L t_{mL}$ which is represented by the red dashed line in Fig. 3.5. Third, entering solvent containing solutes (d_V > 0 in Fig. 3.6) reduces purification. At $-f'q_n$ = 1, for example, using a solvent containing 30% solute increases the d_L value by more than 60% comparing to using a pure solvent (d_V = 0).

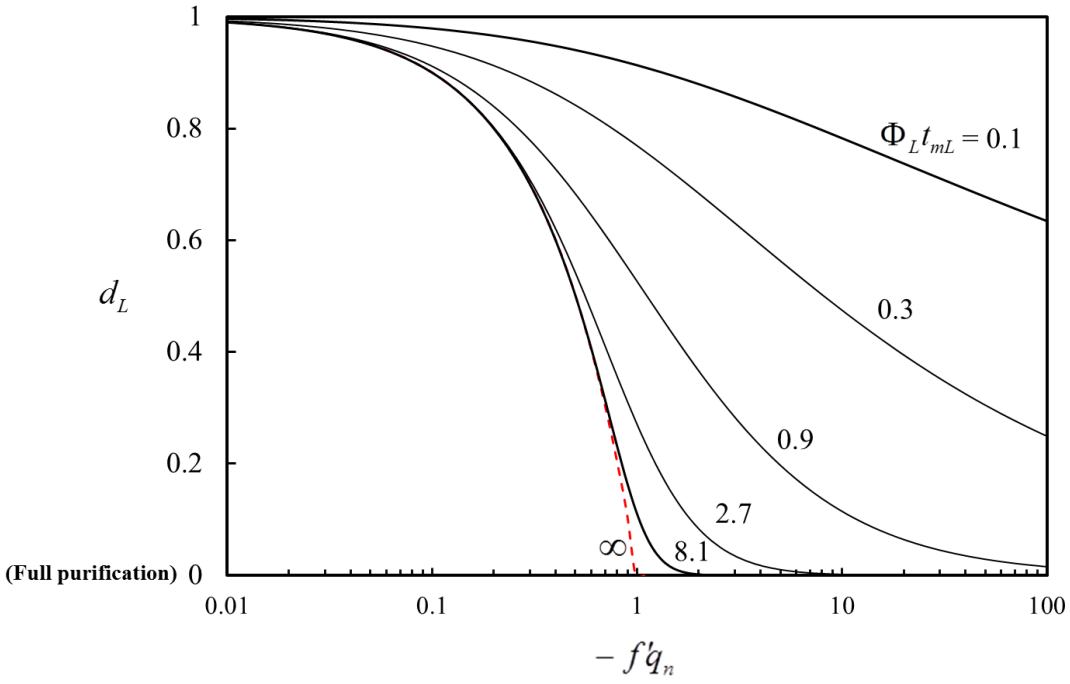

Figure 3.5. The purification function at several values of $\Phi_L t_{mL}$. The red dashed curve is the maximum effectiveness that can be achieved where $\Phi_L t_{mL} = \infty$.

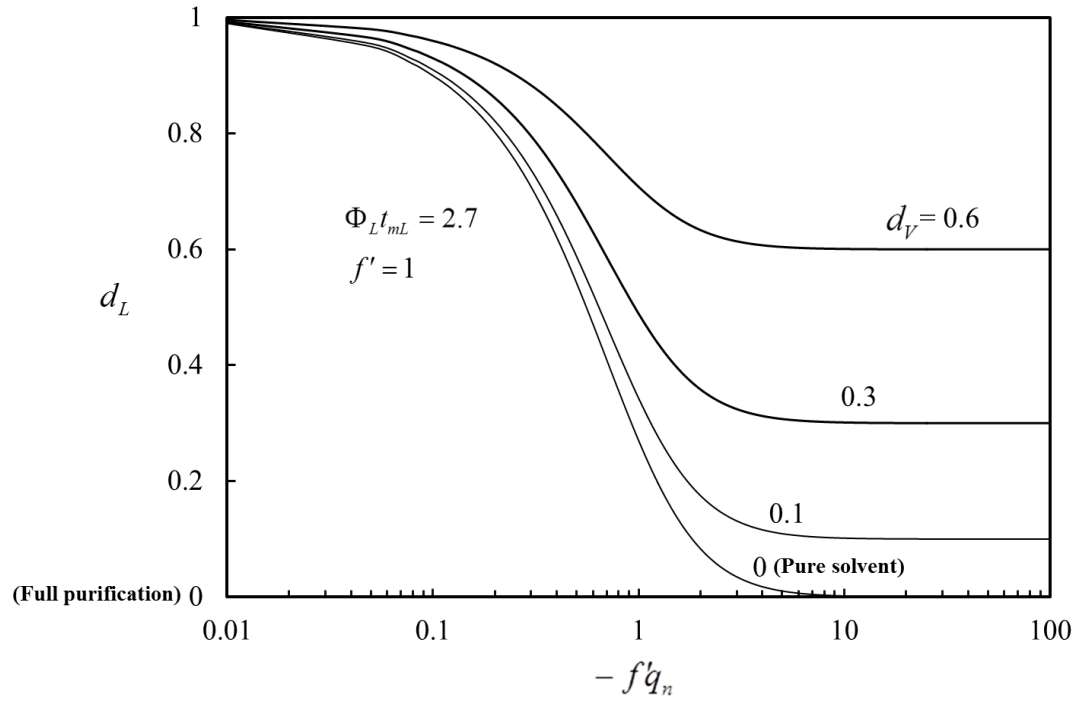

Figure 3.6. The purification function at $\Phi_L t_{mL} = 2.7$ and $f' = 1$ for different degrees of purity of inlet solvent.

3.6 Modification for Rotating Packed Beds

The relations developed so far can be applied to any counter-current contacting device for which the body force is constant and hence the flow conditions remain uniform along the contacting length. This situation holds to a good approximation for packed columns, falling film columns and rotating spirals. However, relations for rotating packed beds differ since the geometry is cylindrical with flow in the radial direction as shown in Fig. 3.7. This means that the velocity and the section area vary radially along the bed. So it should be expected that the volumetric mass transfer coefficient also varies with the radial position and some adjustments are needed to the relations given in the preceding sections.

Making a material balance on a solute being desorbed in a differential element has a volume $2\pi rHdr$ (Fig. 3.7), the relations corresponding to Eqs. 3.24 and 25 are:

$$\int_{Y_L(r_I)}^{Y_L(r_O)} \frac{dY_{LB}}{(Y_{LB}-Y_{LB}^*)} = -\int_{r_I}^{r_O} \frac{2\pi H\varepsilon}{N_L} K_L a\, r dr \tag{3.52}$$

$$\int_{Y_V(r_I)}^{Y_V(r_O)} \frac{dY_{VB}}{(Y_{VB}^*-Y_{VB})} = \int_{r_I}^{r_O} \frac{2\pi H\varepsilon}{N_V} K_V a\, r dr \tag{3.53}$$

where ε is the bed void fraction and N_L and N_V are the phase molar flow rates which can be expressed in terms of the area available for the flow (A_f) and velocity as $N_L = n_L w_{LB} \xi A_f$ and $N_V = n_V w_{VB}(1-\xi)A_f$.

Integration of the left hand side is exactly as before, but the right hand side varies in the integration because the mass transfer coefficients and the interface area per unit volume are functions of r. The usual treatment for rotating packed bed is to use average products of the mass transfer coefficients and specific interface area (e.g. Chiang et al., 2009). Accordingly, the mass transfer coefficient relations corresponding to Eqs. 3.32 and 3.33 are:

$$-\frac{\overline{K_L a}\,\pi H\varepsilon\left(r_O^2 - r_I^2\right)}{N_L} = \frac{Y_{LB}(r_O) - Y_{LB}(r_I)}{\overline{\Delta Y_{LB}}} \tag{3.54}$$

$$\frac{\overline{K_V a}\,\pi H\varepsilon\left(r_O^2 - r_I^2\right)}{N_V} = \frac{Y_{VB}(r_O) - Y_{VB}(r_I)}{\overline{\Delta Y_{VB}}} \tag{3.55}$$

The relation for a specific throughput is unchanged, although it is now in terms of the average mass transfer coefficients. Thus, the equivalent of Eq. 3.43 becomes,

$$\Phi_L = \frac{\overline{K_L a}}{n_L} \frac{(1+f'q_n)}{f'q_n \ln(-f'q_n)} \tag{3.56}$$

Similar to Eq. 3.45, Eq. 3.54 can be expressed in terms of the inlet and outlet mole fraction ratios:

$$\frac{\overline{K_L a}\,\pi H\varepsilon(r_O^2 - r_I^2)(1+f'q_n)}{N_L f'q_n} = \ln\left\{\frac{-q_n d_V + f'q_n d_L}{1-d_L - q_n d_V + f'q_n}\right\} \tag{3.57}$$

The relation for the number of stages (Eq. 3.46) and hence for the total specific throughput (3.47) is unchanged. Further, from Eqs. 3.56 and 3.57, the same relation for purification as before holds (Eqs. 3.51) with the mean residence time given by passage volume per volumetric flow rate in this case.

$$t_{mL} = \frac{\pi H\varepsilon(r_O^2 - r_I^2)}{Q_L} \tag{3.58}$$

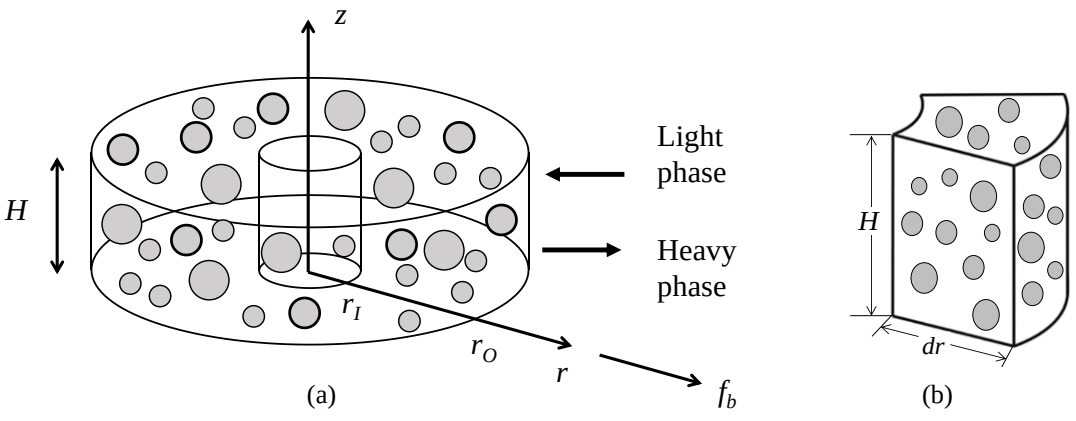

Figure 3.7. Rotating packed bed: (a) bed geometry where H is the axial height, r_I bed inner radius and r_O outer radius and (b) an element taken at radial position r.

3.7 Summary

Bulk mass transfer analysis for counter-current contacting was carried out in this chapter. As a result, useful relations were derived and will be used along this study. The first relations developed here were those for the overall mass transfer coefficients (Eqs. 3.32, 3.33, 3.54 and 3.55). These relations are used to estimate the overall transfer coefficients from the experimental measurements (inlet and outlet bulk solute compositions and the phase flow rates). Relations for the specific throughput (Eqs. 3.43) and the total specific throughput (Eq. 3.47) were also developed here. These terms are used to assess the spiral contacting effectiveness and to compare the spiral with other alternative approaches. Finally, a novel design equation (Eq. 3.51) that links the mass transfer parameters was presented in this chapter. This relation is used to help interpretations, to check the consistency of the experimental data and to calculate d_L values from the computational results.

So far relations based on bulk quantities to analyse experiments under different conditions have been presented. These relations can be applied to desorption process in any fluid-fluid phase contactors. For absorption process, the relations are not quite different and they are presented at the end of Chapter 7 to compare absorption and desorption results. However, understanding the mass transfer process in a rotating spiral channel needs a precise model that allows prediction and detailed analysis. Such model is considered in this work and is presented in the next chapter.

Chapter Four

Modelling of Two-phase Contacting in a Rotating Spiral Channel

A computational model is presented in this chapter. The model is employed in this work to investigate the process of gas-liquid contacting in a rotating spiral channel. The concept of this model is based on a 2-D numerical solution of the flow and species equations using an interface shape computed independently using the interface model of MacInnes and Zambri (2015). This allows prediction of the true character of the main flow and Coriolis secondary motion. These parameters are of primary importance since they determine the mass transfer mechanism in the channel and hence gain insight into the details of rotating spiral contacting. Further, knowing the flow and species fields allows the individual mass transfer coefficients to be quantified. These coefficients are the most important parameters of interest since they determine the specific throughput and hence the effectiveness of contacting.

The chapter is organised as follows: the governing equations and the appropriate approximations for the spiral flow are given first. This is followed by a presentation of the interface model and the required boundary conditions. After that, the numerical solution is discussed and a series of computations is conducted. The purpose of these computations is to understand the general behaviour of gas-liquid contacting and to investigate the main effects of the gas and liquid phase flow rate that are tested experimentally. The chapter closes with the analytical solution for an infinite-width channel (MacInnes et al., 2012), which is used here to assess the 2-D numerical solution.

4.1 Model Description

The physical situation of two immiscible phases contacting in a rotation spiral channel is depicted in Fig. 4.1 where a heavy and a light phase flow counter-currently with a dilute solute transferring between them. The figure shows the coordinate system, the channel geometry and a 2-D section through the channel along with the nomenclature used.

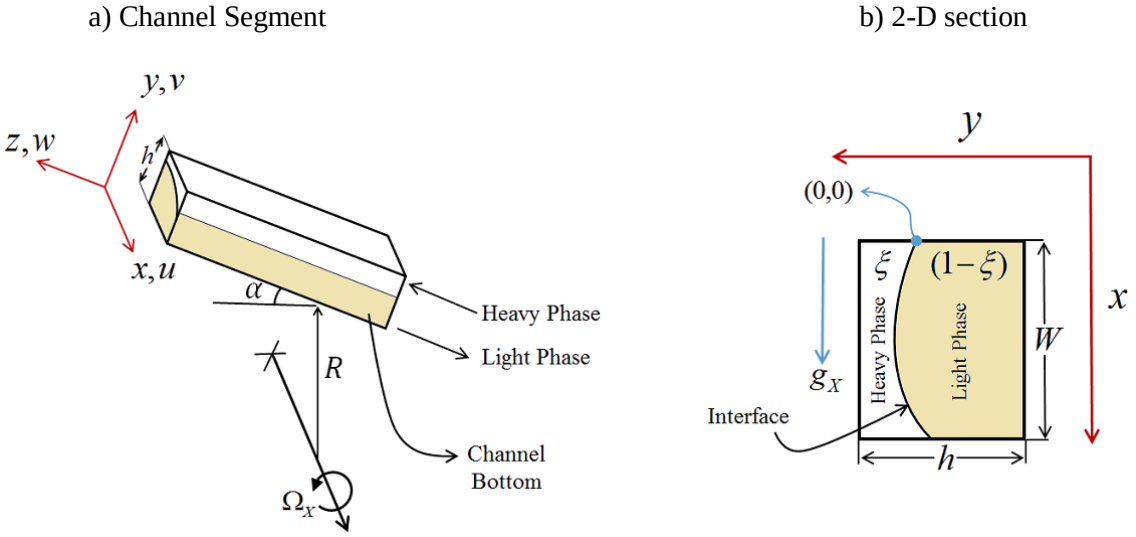

Figure 4.1. Coordinate system and channel geometry: (a) segment of a spiral channel and (b) the 2-D section.

Since practical spiral channels have relatively a large radius of curvature in relation to the channel height ($R >> h$), the channel is treated as straight at any location and is inclined at angle α relative to the tangential direction (Fig. 4.1 a). The validity of this approximation has been verified by performing computations using local cylindrical coordinates fit to a section of the spiral channel. In Fig. 4.1, *x* and *y* are coordinates of the flow section and *z* is the direction along the channel. u , v and w represent the velocity components in the *x*, *y* and *z* direction, respectively. The axis of rotation is parallel to the *x* direction and the channel is located at a distance R from the channel wall to this axis. The channel section (Fig. 4.1 b) has height h and width W . In the section, the heavy phase occupies ξ fraction of the flow area (hW) which is determined by the position and shape of the phase interface. For the counter-current contacting of interest, the heavy phase is driven primarily by the centrifugal effect and flows as a layer over the outer wall in the positive *z* direction. For the light phase, which has much lower density, the flow is driven mainly in the opposite direction by the pressure gradient.

As discussed in Chapter 2 (Section 2.4.4), MacInnes et al. (2012) argue that a stable layer flow must be obtained when flow conditions are laminar and below critical values of the Froude and Weber numbers (Eq. 2.17). Hence, flow in the spiral channel below these critical conditions and for dilute solute concentration is considered laminar, isothermal and steady in each phase.

4.2 Governing Equations

In the spiral, the motion and the mass transfer of solute in each phase are governed by exactly the same equations but with the physical property values those for the particular phase. These equations will be expressed using the coordinate system and geometric parameters defined in Fig. 4.1.

4.2.1 Conservation of mass (continuity)

The general form of continuity equation for steady-state flow considered here is:

$$\nabla \cdot \left(\rho \vec{V}\right) = 0 \tag{4.1}$$

where ρ is the fluid density and $\vec{V}$ is the velocity vector. This vector may be defined in terms of the velocity components (u, v and w) shown in Fig. 4.1 as:

$$\vec{V} = u(x,y,z)\mathbf{i} + v(x,y,z)\mathbf{j} + w(x,y,z)\mathbf{k} \tag{4.2}$$

For typical conditions, pressure variation along the channel results in a minor change in gas density so the approximation of incompressible flow for both gas and liquid phases is appropriate here. Furthermore, for dilute solute, the fluid properties are unaffected by the varying solute composition. Thus, to a good approximation, the density of each phase is uniform and Eq. 4.1 reduces to:

$$\frac{\partial u}{\partial x} + \frac{\partial v}{\partial y} + \frac{\partial w}{\partial z} = 0 \tag{4.3}$$

4.2.2 Momentum Equation

Before presenting the momentum equation, it is necessary to recognise that the coordinate system used in Fig. 4.1 is in rotational motion. So the fluids are subject to centrifugal and Coriolis accelerations, not present in the standard form of the momentum equations. In this case, the actual acceleration ($\vec{a}$) that a moving fluid experiences in the rotating channel can be written as (Tritton, 1988; White, 2008):

$$\vec{a} = \vec{a}_{\text{ref.}} + \underbrace{\vec{\Omega} \times (\vec{\Omega} \times \vec{R})}_{\substack{\text{Centrifugal} \\ \text{acceleration}}} + \underbrace{2\vec{\Omega} \times \vec{V}}_{\substack{\text{Coriolis} \\ \text{acceleration}}} \tag{4.4}$$

where $\vec{\Omega}$ and $\vec{R}$ are the rotation and position vectors, respectively. The term $\vec{a}_{\text{ref.}}$ represents the convective acceleration associated with changing a fluid velocity spatially. Using the notation given in Fig. 4.1, the vectors appearing in Eq. 4.4 may be expressed as:

$$\vec{\Omega} = \Omega\,\mathbf{i} \tag{4.5}$$

$$\vec{R} = x\mathbf{i} + (R\cos\alpha + y)\mathbf{j} + R\sin\alpha\,\mathbf{k} \tag{4.6}$$

Including the additional acceleration terms in the usual momentum equations and using the above expressions for the rotation rate and radial position, the three component equations for momentum are:

$$\rho u\frac{\partial u}{\partial x} + \rho v\frac{\partial u}{\partial y} + \rho w\frac{\partial u}{\partial z} = -\frac{\partial p}{\partial x} + \mu\left(\frac{\partial^2 u}{\partial x^2} + \frac{\partial^2 u}{\partial y^2} + \frac{\partial^2 u}{\partial z^2}\right) + \rho g \tag{4.7}$$

$$\rho u\frac{\partial v}{\partial x} + \rho v\frac{\partial v}{\partial y} + \rho w\frac{\partial v}{\partial z} = -\frac{\partial p}{\partial y} + \mu\left(\frac{\partial^2 v}{\partial x^2} + \frac{\partial^2 v}{\partial y^2} + \frac{\partial^2 v}{\partial z^2}\right) + \underbrace{\rho\Omega^2(R\cos\alpha + y)}_{\substack{\text{Centrifugal}\\ \text{term}}} + \underbrace{2\rho\Omega w}_{\substack{\text{Coriolis}\\ \text{term}}} \tag{4.8}$$

$$\rho u\frac{\partial w}{\partial x} + \rho v\frac{\partial w}{\partial y} + \rho w\frac{\partial w}{\partial z} = -\frac{\partial p}{\partial z} + \mu\left(\frac{\partial^2 w}{\partial x^2} + \frac{\partial^2 w}{\partial y^2} + \frac{\partial^2 w}{\partial z^2}\right) + \underbrace{\rho R\Omega^2\sin\alpha}_{\substack{\text{Centrifugal}\\ \text{term}}} - \underbrace{2\rho\Omega v}_{\substack{\text{Coriolis}\\ \text{term}}} \tag{4.9}$$

The above set of partial differential equations governs fluid flow in a rotating spiral channel. As can be seen, the equations are modified for the rotating reference frame by the appearance of centrifugal and Coriolis terms. These terms appear in both the transverse and streamwise momentum equations (Eqs. 4.8 and 4.9). The Coriolis term in the transverse equation is represented by the streamwise velocity (w). This term is directly responsible for producing secondary motion in each phase. The centrifugal term in the same equation determines along with the gravity body force in Eq. 4.7 the level of the hydrostatic pressure in each phase and that affects directly the interface shape. The other centrifugal term appeared in the streamwise momentum equation drives the flow along the channel. The flow is also driven by the pressure gradient ($\partial p/\partial z$) and is modified by the other Coriolis term ($2\rho\Omega v$ in Eq. 4.9). This term depends on the local velocity in the *y* direction (v). So one can expect that the main flow (w) is to be affected, depending on the direction and magnitude of v component velocity at a given Ω.

4.2.3 Species Conservation Equation

The transport of a solute in a rotating spiral channel could occur in *x*, *y*, and *z* directions by two mechanisms: molecular diffusion and convection by fluid motion. The general form of the solute conservation equation including these two terms in the absence of chemical reaction is given as (Bird et al., 1997):

$$\underbrace{n\left(\vec{V}\cdot\nabla Y\right)}_{\text{Convection term}}=\underbrace{nD\left(\nabla^2 Y\right)}_{\text{Diffusion term}} \tag{4.10}$$

where n is the molar density, D the solute mass diffusivity and Y the solute mole fraction. In terms of Cartesian coordinates, Eq. 4.10 can be expressed:

$$u\frac{\partial Y}{\partial x}+v\frac{\partial Y}{\partial y}+w\frac{\partial Y}{\partial z}=D\left(\frac{\partial^2 Y}{\partial x^2}+\frac{\partial^2 Y}{\partial y^2}+\frac{\partial^2 Y}{\partial z^2}\right) \tag{4.11}$$

As can be seen, the three velocity components appear explicitly in Eq. 4.11, showing a clear dependency of solute transport on Coriolis secondary motion and the streamwise velocity.

Up to this point, the governing equations have been presented for laminar, incompressible flow but are otherwise general. More approximations, however, are appropriate in the case of the contacting flow in rotating spiral channels. These are examined next.

4.2.4 Two-dimensional Approximations

The driving force remains constant along the channel, provided the component $R\sin\alpha$ remains constant and the density and viscosity are uniform in each phase. The former is ensured by the correct design of the spiral and corresponds to a spiral that maintains a fixed spacing between revolutions (Chapter 2, Section 2.4.2). The latter follows from the approximately constant composition in each phase. Hence, beyond an entry length at either end of a spiral channel, the flow will be independent of the *z* direction for uniform phase properties and no mass exchange between the phases, except a transfer of a dilute solute. This developed flow state is two-dimensional with velocity components dependent only on *x* and *y* direction and also the pressure gradient is constant along the channel and independent of *x* and *y*. This is an excellent approximation in a channel of uniform

section. So it is also necessary for the individual phase sections to be uniform and this depends on the constancy of the interface shape. Here, there is also approximation as that shape changes somewhat depending on radial position. Since radial position changes with distance along the spiral channel, the interface will also (as will be seen in Section 4.3). For flow, therefore, the main behaviour can be usefully represented as 2-D developed flow in the usual manner.

One would like also to approximate solute transfer for two dimensional problem, but here further approximation is required in the two phases. Unlike the velocity approximations, spatial derivatives of the solute mole fraction in the *z* direction are not zero and the presence of these requires a full three-dimension solution of the species equation. These spatial derivatives arise in two distinct terms in Eq. 4.11: change in solute mole fraction due to solute diffusion and that due to solute convection. The streamwise convection of solute is neither negligible, constant along the channel nor uniform with *x* and *y* in each phase region. However, since solute concentration varies gradually with *z*, the streamwise bulk solute gradient may be taken as locally constant, with different values applying at different portions along the channel. This allows the solute concentration change at any location in the section to be approximated by the local bulk gradient, i.e.,

$$\frac{\partial Y(x,y,z)}{\partial z} = \frac{dY_B}{dz} \quad \text{where } Y_B \text{ is the solute bulk mole fraction} \tag{4.12}$$

This essentially assumes that changes in the lateral mole fraction differences are small, which may be justified by the fact that the concentration difference between the phases does not differ greatly over the contacting length.

Further, another approximation could be made that the streamwise diffusion is small in relation to the axial convection and is neglected. This can be justified in terms of the Peclet number (Pe). For mass transfer, Pe is the ratio of the characteristic convective transport to diffusive transport and can be expressed in terms of Reynolds (Re) and Schmidt (Sc) numbers (Seader and Henley, 2006):

$$\mathrm{Pe} = \mathrm{ReSc} \quad \text{where} \quad \mathrm{Re} = \frac{wh}{\mu/\rho} \quad \text{and} \quad \mathrm{Sc} = \frac{\mu/\rho}{D} \tag{4.13}$$

As mentioned previously, air-water system is used here as a representative system for gas-liquid contacting. The mass diffusivity (D) of the common solutes in air and in water are typically about 10^{-5} m^2/s and 10^{-9} m^2/s, respectively (Cussler, 1997). Also, it is

known that the momentum diffusivity (μ/ρ) for air and water are approximately within 10^{-5} m^2/s and 10^{-6} m^2/s, respectively (White, 2008). This suggests that water has a large Sc in general. Such Sc results in a large Pe even at small values of Re (e.g. Re = 1) according to Eq. 4.13. For the gas phase, however, Sc is approximately one and Pe is mainly determined by the value of Re. In this work, the lowest gas phase Reynolds number tested is about 400. So, Pe is also a large value in the gas phase. From this simple analysis, therefore, one must expect that in both phases the convective transport in *z* direction (mainstream) is orders of magnitude greater than the solute molecular diffusion in the same direction. Thus, dropping the axial molecular diffusion from Eq. 4.11 would be a reasonable approximation.

According to the approximations discussed above, the system governing equations (continuity, momentum and species) reduce to describe a mass transfer process in a section of the spiral channel. As mentioned, the equations can be applied equally in each phase simply by using the particular values for density, viscosity and diffusion coefficient. So, again, using 'L' to designate the heavy phase region and 'V' the light phase region, the equations that apply in each phase can be expressed as follows.

Light-phase region

$$\frac{\partial u_V}{\partial x}+\frac{\partial v_V}{\partial y}=0 \tag{4.14}$$

$$\rho_V u_V \frac{\partial u_V}{\partial x}+\rho_V v_V \frac{\partial u_V}{\partial y}=-\frac{\partial \hat{p}_V}{\partial x}+\mu_V\left(\frac{\partial^2 u_V}{\partial x^2}+\frac{\partial^2 u_V}{\partial y^2}\right) \tag{4.15}$$

$$\rho_V u_V \frac{\partial v_V}{\partial x}+\rho_V v_V \frac{\partial v_V}{\partial y}=-\frac{\partial \hat{p}_V}{\partial y}+\mu_V\left(\frac{\partial^2 v_V}{\partial x^2}+\frac{\partial^2 v_V}{\partial y^2}\right)+2\rho_V \Omega w_V \tag{4.16}$$

$$\rho_V u_V \frac{\partial w_V}{\partial x}+\rho_V v_V \frac{\partial w_V}{\partial y}=-\frac{dp_0}{dz}+\mu_V\left(\frac{\partial^2 w_V}{\partial x^2}+\frac{\partial^2 w_V}{\partial y^2}\right)+\rho_V R\Omega^2 \sin\alpha-2\rho_V \Omega v_V \tag{4.17}$$

$$u_V \frac{\partial Y_V}{\partial x}+v_V \frac{\partial Y_V}{\partial y}=-w_V \frac{dY_{VB}}{dz}+D_V\left(\frac{\partial^2 Y_V}{\partial x^2}+\frac{\partial^2 Y_V}{\partial y^2}\right) \tag{4.18}$$

Heavy-phase region

$$\frac{\partial u_L}{\partial x}+\frac{\partial v_L}{\partial y}=0 \tag{4.19}$$

$$\rho_L u_L\frac{\partial u_L}{\partial x}+\rho_L v_L\frac{\partial u_L}{\partial y}=-\frac{\partial \hat{p}_L}{\partial x}+\mu_L\left(\frac{\partial^2 u_L}{\partial x^2}+\frac{\partial^2 u_L}{\partial y^2}\right) \tag{4.20}$$

$$\rho_L u_L\frac{\partial v_L}{\partial x}+\rho_L v_L\frac{\partial v_L}{\partial y}=-\frac{\partial \hat{p}_L}{\partial y}+\mu_L\left(\frac{\partial^2 v_L}{\partial x^2}+\frac{\partial^2 v_L}{\partial y^2}\right)+2\rho_L\Omega w_L \tag{4.21}$$

$$\rho_L u_L\frac{\partial w_L}{\partial x}+\rho_L v_L\frac{\partial w_L}{\partial y}=-\frac{dp_0}{dz}+\mu_L\left(\frac{\partial^2 w_L}{\partial x^2}+\frac{\partial^2 w_L}{\partial y^2}\right)+\rho_L R\Omega^2\sin\alpha-2\rho_L\Omega v_L \tag{4.22}$$

$$u_L\frac{\partial Y_L}{\partial x}+v_L\frac{\partial Y_L}{\partial y}=-w_L\frac{dY_{LB}}{dz}+D_L\left(\frac{\partial^2 Y_L}{\partial x^2}+\frac{\partial^2 Y_L}{\partial y^2}\right) \tag{4.23}$$

It is important to note that the pressure appearing in the above equations ($\hat{p}_V$, $\hat{p}_L$) is a piezometeric pressure in the flow section. In most cases of flow in rotating or curved channels, the true pressure can be expressed in a reduced form (piezometeric) in *x*-*y* section. Usually, this is made by combining the gravity force in Eq. 4.7 and the transverse centrifugal force in Eq. 4.8 with $\partial p/\partial x$ and $\partial p/\partial y$, respectively (e.g. Speziale and Thangam, 1983; Beak and Ko, 2000; Lee and Beak, 2002). In general, such treatment is acceptable since the effect of gravity and transverse centrifugal force are present whether there is flow or not and balance the pressure gradient in *x* and *y* directions in both cases. So these forces do not have any influence on the main flow and can be combined with the pressure force terms. Accordingly, the actual pressure derivatives in the transverse directions (Eqs. 4.7 and 4.8) and the centrifugal and gravity terms in the same equations may reduce to:

In Eq. 4.7: $$\frac{\partial \hat{p}}{\partial x}=\frac{\partial p}{\partial x}-\rho g \tag{4.24}$$

In Eq. 4.8: $$\frac{\partial \hat{p}}{\partial y}=\frac{\partial p}{\partial y}-\rho(R\cos\alpha+y)\Omega^2 \tag{4.25}$$

where $\hat{p}$ is the piezometeric pressure and can be found at any point in *x*-*y* section by integrating Eqs. 4.24 and 4.25, thus for the light phase and heavy phase:

$$\hat{p}_V(x,y) = p_V(x,y) - \rho_V\left((Ry\cos\alpha + \frac{y^2}{2})\Omega^2 + gx\right) - p_{V0}(x,y) \tag{4.26}$$

$$\hat{p}_L(x,y) = p_L(x,y) - \rho_L\left((Ry\cos\alpha + \frac{y^2}{2})\Omega^2 + gx\right) - p_{L0}(x,y) \tag{4.27}$$

In the above equations, p_{V0} and p_{L0} are reference pressures taken at the position $x = 0$ and $y = 0$ on the phase interface (Fig. 4.1).

Finally, the bulk mole fraction gradients in the light and heavy phase (dY_{LB}/dz and dY_{VB}/dz) appearing in Eqs. 4.18 and 4.23 are related through solute conservation and thus are not independent. Equating mass transfer rates in the two phases at the interface and using Eqs. 3.1 and 3.2 (given in Chapter 3) requires that:

$$-n_L w_{LB}\xi\frac{dY_{LB}}{dz} = n_V w_{VB}(1-\xi)\frac{dY_{VB}}{dz} \tag{4.28}$$

Hence, setting the bulk gradient in one phase determines that in the other.

4.3 Interface Shape

The part of the channel section occupied by each phase must be established to solve the governing equations. Two parameters determine these sections: the interface shape and its location inside the channel. These two parameters depend on fluid flow and can be obtained simultaneously as part of the solution of the flow equations (Wörner, 2012). MacInnes and Zambri (2015), however, point out that for practical conditions in the spiral the component of centrifugal acceleration driving the flows is far smaller than the transverse component that determines interface shape, i.e. $R\Omega^2\cos\alpha >> R\Omega^2\sin\alpha$, since α is small. This means that the interface shape is insignificantly affected by flow stresses and can be calculated independently of the flow solution, considering only the effect of stresses at static conditions and surface tension. The pressure difference across the interface (stresses), the interfacial surface tension, σ, and the interface shape are linked by Young-Laplace law as:

$$p_V - p_L = \sigma\left(\frac{1}{r_1} + \frac{1}{r_2}\right) \tag{4.29}$$

where r_1 and r_2 are respectively the curvature radii of the interface in the *x*-*y* section and along the channel. For rotating spiral contacting, the difference in pressure across the interface $(p_V - p_L)$ can be determined directly from Eqs. 4.26 and 4.27 by setting $\hat{p}_V = \hat{p}_L$. Therefore, according to the coordinates given in Fig. 4.2, $p_V - p_L$ can be written as:

$$p_V - p_L = \Delta p_0 + (\rho_L - \rho_V)\left((R\cos\alpha + \frac{y}{2})\Omega^2 y - gx\right) \tag{4.30}$$

where $\Delta p_0 = p_{V0} - p_{L0}$ at $x = 0$ and $y = 0$ (Fig. 4.1 or Fig. 4.2 below).

Eq. 4.29 can be simplified by dropping $1/r_2$ since the curvature of the interface along the channel is smaller than that in the transverse direction, $1/r_1$. Further, since $R >> h$ and $\cos\alpha \approx 1$ for small α, the term $R\cos\alpha + y/2$ in Eq. 4.30 can be approximately replaced by the outer wall radial position (R_0 in Fig. 4.2). Using these simplifications and taking $r_1 = r$, substitution of Eq. 4.30 into Eq. 4.29 results in:

$$\Delta p_0 + (\rho_L - \rho_V)(R_0\Omega^2 y - gx) = \sigma\left(\frac{1}{r}\right) \tag{4.31}$$

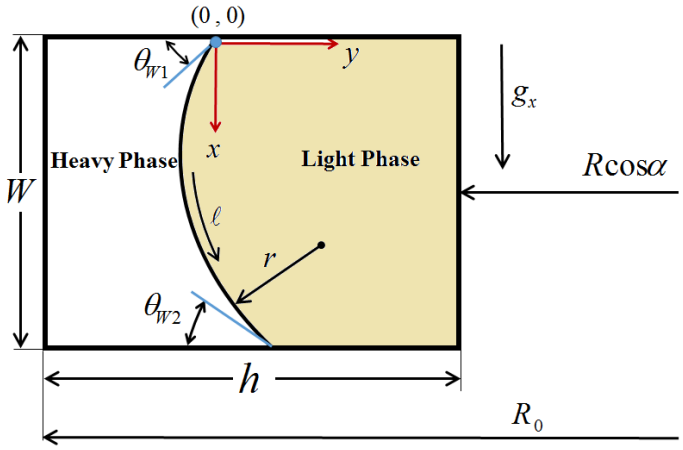

Figure 4.2. An illustrative diagram showing the geometry of the interface in a section of spiral channel. θ_{W1} and θ_{W2} are the contact angles at both ends.

The radius (r) in Eq. 4.31 can be expressed in terms of the arc length (ℓ) to obtain parametric equations for the interface coordinates. Normalising by the channel width, the resulting equations can be written as (MacInnes and Zambri, 2015):

$$\frac{d^2 y^*}{d\ell^{*2}} = \left\{ \Delta p_0^* + \left(\frac{W}{\delta_C} \right)^2 \left[y^* - \lambda x^* \right] \right\} \frac{dx^*}{d\ell^*} \tag{4.32}$$

$$\frac{dx^*}{d\ell^*} = \left\{ 1 - \left(\frac{dy^*}{d\ell^*} \right)^2 \right\}^{1/2} \tag{4.33}$$

The asterisked indicates normalised variables: $y^* = y/W$, $x^* = x/W$, $\ell^* = \ell/W$ and $\Delta p^* = W\Delta p_0^*/\sigma$. In addition, two new parameters emerge from this non-dimensional representation: the characteristic capillary height (δ_C/W) and the gravity parameter (λ):

$$\frac{\delta_C}{W} = \sqrt{\frac{\sigma}{(\rho_L - \rho_V) R_0 \Omega^2 W^2}} \quad \text{and} \quad \lambda = \frac{g}{R_0 \Omega^2} \tag{4.34}$$

δ_C/W is the root of the ratio of the interfacial surface force to the centrifugal force. This parameter reflects the relative characteristics meniscus height for the interface. Thus, the smaller the value of δ_C/W the more effective the centrifugal force is to overcome the interface curvature and hence results in a flatter interface between the two phases. On the other hand, λ indicates to what degree the interface is tilted due to the effect of gravity (Eq. 4.34). In general, as the rotation rate increases, the effect of gravity becomes minor and approximately less tilted interface can be obtained at a given radial position.

From Eqs. 4.32, 4.33 and 4.34, it is clear that the shape of the interface depends only on the phase density difference ($\rho_L - \rho_V$), surface tension (σ), the radial position of the interface along the spiral (R_0), the channel width (W) and the rotation rate (Ω). Also, the shape depends on the contact angles (θ_{W1} and θ_{W2} in Fig. 4.2) which determine the slope at the end-walls:

$$\tan\theta_{W1} = \frac{\sin\theta_{W1}}{\cos\theta_{W1}} = \frac{dx^*/d\ell^*}{-dy^*/d\ell^*} \quad , \quad \tan\theta_{W2} = \frac{\sin\theta_{W2}}{\cos\theta_{W2}} = \frac{dx^*/d\ell^*}{dy^*/d\ell^*} \tag{4.35}$$

Specifying these parameters, the profile of the interface can be determined by numerical integration of Eqs. 4.32 and 4.33 over a given channel width. The solution starts from both ends where the slopes are defined by the contact angles (Eq. 4.35). The solution also requires adjustment of Δp_0^* in Eq. 4.32 at either side such that the arc length extends from each end to match (having the same slope) at a central point (MacInnes and Zambri, 2015).

Fig. 4.3 gives an example of a channel section with an interface calculated for 3200 rpm (red curve). R_0 is 25 mm and the phase physical properties are those of air and water at 49 °C and 1.8 bara. The dimensions shown correspond to those of the spiral channel used in the experiments here. The liquid layer thickness, h_{Lm}, is 120 µm and is measured from the minimum point of the profile to the channel wall. Furthermore, Fig. 4.3 shows clearly that there is a difference between the ends of the computed profile. This asymmetry is mainly due to both the effect of gravity (λ in Eq. 4.34) and different end wall materials used in the experiments (plastic at the top wall and glass at the bottom wall). The former causes slight tilting as discussed above while the latter gives different contact angles (i.e. θ_{W1} and θ_{W2} in Fig. 4.2) and hence different meniscus heights.

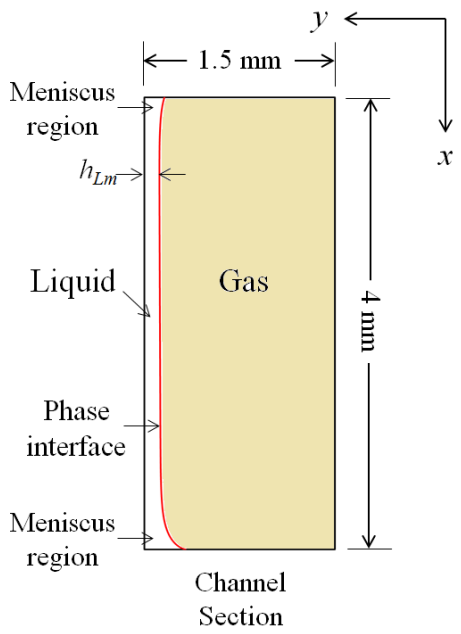

Figure 4.3. Channel section divided by an interface computed at Ω = 3200 rpm and a radial position (R_0) of 25 mm for conditions typical of the experiments conducted in this work.

4.4 Boundary Condition

The system governing equations and the interface shape that divides the solution domain are now specified. The governing equations are satisfied at every point in each phase, including the boundaries that determine the domain of each separate phase. The conditions at these boundaries are known and can be employed to solve these equations. Two types of boundaries are relevant here: solid walls and the gas-liquid interface and the conditions at these boundaries are described in detail below.

4.4.1 Walls

For fixed and non-absorbing walls, the conditions are no-slip velocity and zero normal mass flux of solute. The mass flux can be expressed using the species flux vector and the unit vector normal to the wall (i.e. $\vec{n} = n_x \mathbf{i} + n_y \mathbf{j}$). Using these expressions, the boundary conditions at the wall surfaces in the light phase are:

$$u_V = 0\ ,\ v_V = 0\ ,\ w_V = 0 \ \text{ and } \ \frac{\partial Y_V}{\partial x} n_X + \frac{\partial Y_V}{\partial y} n_y = 0 \tag{4.36}$$

Similarly, where the heavy phase is in contact with the wall,

$$u_L = 0\ ,\ v_L = 0\ ,\ w_L = 0 \ \text{ and } \ \frac{\partial Y_L}{\partial x} n_X + \frac{\partial Y_L}{\partial y} n_y = 0 \tag{4.37}$$

4.4.2 Interface

The conditions at the interface can be obtained from the fact that the interface has a negligible mass and therefore can store no momentum or mass. This constrains the velocities to be continuous and the stress and mass flux to balance across the interface. Further, since the macroscopic length scales are larger than the molecular spacing in both the gas and the liquid, it is a good approximation that a local equilibrium prevails at the interface. Additionally, the interface is fixed in the geometry section. This means that the interface is not in motion in *x-y* plane and the normal velocity of the phases on the interface is zero.

Now, in terms of the unit normal vector ($\vec{n}$) to the interface, the conditions of the velocity components at the interface are:

$$u_V n_x + v_V n_y = 0 \text{ (normal velocity)},\ u_L n_x + v_L n_y = 0\ ,\ v_V = v_L\ ,\ \ w_L = w_V \tag{4.38}$$

The stress at the interface has normal and tangential components. All components must be balanced at each location on the interface. In the normal direction (Batchelor, 2000),

$$-\hat{p}_L + (\tau_{xx})_L n_x^2 + (\tau_{yy})_L n_y^2 + 2(\tau_{xy})_L n_x n_y = -\hat{p}_V + (\tau_{xx})_V n_x^2 + (\tau_{yy})_V n_y^2 + 2(\tau_{xy})_V n_x n_y$$

which, on substitution the Newtonian stress law gives:

$$-\hat{p}_L + 2\mu_L\left(\frac{\partial u_L}{\partial x}n_x^2 + \frac{\partial v_L}{\partial y}n_y^2\right) + 2\mu_L\left(\frac{\partial u_L}{\partial y} + \frac{\partial v_L}{\partial x}\right)n_x n_y = \tag{4.39}$$
$$-\hat{p}_V + 2\mu_V\left(\frac{\partial u_V}{\partial x}n_x^2 + \frac{\partial v_V}{\partial y}n_y^2\right) + 2\mu_V\left(\frac{\partial u_V}{\partial y} + \frac{\partial v_V}{\partial x}\right)n_x n_y$$

It is important to note that the above equation is written in terms of the piezometeric pressure ($\hat{p}_V$ and $\hat{p}_L$), the same variable appearing in the flow equations. Expressing Eq. 4.39 in this way means that the surface tension effect is implicitly taken into account. This is clear from the expression of the piezometeric pressure (Eqs. 4.26 and 4.27) which includes the effect of hydrostatic pressure that balances σ/r (Eq. 4.31). Thus, it must be expected that at static conditions, Eq. 4.39 can reduce to the scalar Young-Lapace equation given in Eq. 4.29, as expected.

It is also important to emphasise here that the normal stress will not be balanced precisely since the interface shape is calculated for conditions where the flow stresses make no contribution to the pressure change across the interface. Excluding the flow stresses from Eq. 4.39 means that at all positions on the interface, the piezometeric pressure should remain the same on either side, as assumed in the interface model. This constraint is imposed on the interface at the wall contact line which corresponds to the point (0,0) in Fig. 4.1. In this case, differences in piezometeric pressure across the interface in the 2-D computation reflect the extent to which flow stresses affect interface shape and hence the error in interface shape determination. A typical pressure deviation at 3200 rpm, for example, is about 20 Pa. This corresponds to less than 1% of the centrifugal pressure difference taken into account in the interface shape.

The balance of the tangential stress components in the *x*-*y* plane results in (Batchelor, 2000),

$$\left(\tau_{xx} - \tau_{yy}\right)_L n_x n_y + \left(\tau_{xy}\right)_L \left(n_x^2 - n_y^2\right) = \left(\tau_{xx} - \tau_{yy}\right)_V n_x n_y + \left(\tau_{xy}\right)_V \left(n_x^2 - n_y^2\right)$$

or

$$2\mu_L\left(\frac{\partial v_L}{\partial y} - \frac{\partial u_L}{\partial x}\right)n_x n_y + \mu_L\left(\frac{\partial u_L}{\partial y} + \frac{\partial v_L}{\partial x}\right)\left(n_x^2 - n_y^2\right) =$$
$$2\mu_V\left(\frac{\partial v_V}{\partial y} - \frac{\partial u_V}{\partial x}\right)n_x n_y + \mu_V\left(\frac{\partial u_V}{\partial y} + \frac{\partial v_V}{\partial x}\right)\left(n_x^2 - n_y^2\right) \tag{4.40}$$

There is other tangential stress component in the *z* direction. This is expressed

$$(\tau_{xz})_L n_x + (\tau_{yz})_L n_y = (\tau_{xz})_V n_x + (\tau_{yz})_V n_y$$

so,

$$\mu_L\left(\frac{\partial w_L}{\partial x}\right)n_x + \mu_L\left(\frac{\partial w_L}{\partial y}\right)n_y = \mu_V\left(\frac{\partial w_V}{\partial x}\right)n_x + \mu_V\left(\frac{\partial w_V}{\partial y}\right)n_y \tag{4.41}$$

The solute flux must also be balanced at the interface. This requires:

$$n_L D_L \frac{\partial Y_L}{\partial x} n_x + n_L D_L \frac{\partial Y_L}{\partial y} n_y = n_V D_V \frac{\partial Y_V}{\partial x} n_x + n_V D_V \frac{\partial Y_V}{\partial y} n_y \tag{4.42}$$

Finally, the solute mole fraction jump across the interface is expressed:

$$Y_{VI} = f(Y_{LI}) \tag{4.43}$$

where Y_{VI} and Y_{LI} are the values of solute mole fraction along the interface in the light and heavy phase, respectively.

4.5 Numerical Solution

A direct solution for the 2-D governing equations given in Section 4.2.4 is not possible even with the simplification made. The equations are nonlinear and coupled through the conditions at the interface and hence a numerical solution is required. Comsol Multiphysics Software (general PDE mode) can be used to achieve the numerical solution. The applicability and accuracy of this software to handle different partial differential equations (PDEs) have been demonstrated in many entries to the literature (e.g. Zimmerman, 2004; Li et al., 2009). In Comsol, the numerical solution is based on the finite element method (FEM) in which the computational domain is discretised into small subdomains, forming a mesh of cells (Fig. 4.4). The generated mesh determines locations (nodes) over the solution domain. At these nodes, the variables are calculated by approximating the PDEs to a set of algebraic equations and solving them. Typically, a large number of nodes is used to obtain a reliable solution. In turn, this leads to a large number of algebraic equations which are solved often by iteration to reach a converged solution.

Before describing the computational method used to solve the governing equations, there are three essential parameters should be selected to achieve an accurate numerical

solution. These parameters are the shape, type and size of the elements. In this work, the basic and the most commonly used parameters are selected and this will be discussed first.

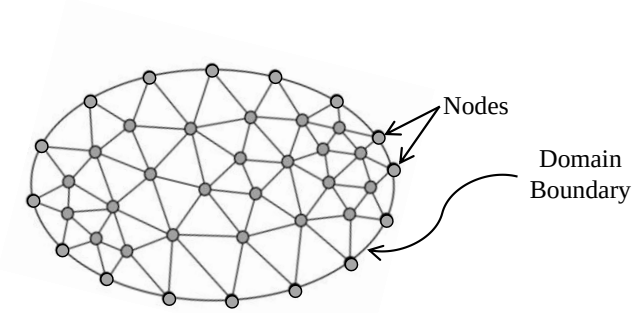

Figure 4.4. An arbitrary domain discretised using triangular elements.

4.5.1 Shape of Element

Triangular elements are often preferred in representing irregular domain shape since they involve less error compared to other 2-D element shapes (Reddy, 1984; Ho-Le, 1988; Pepper and Heinrich, 2006). The irregularity, in this case, arises from the curving shape of the interface as shown in Fig. 4.3. So triangular elements are used throughout this work to generate the mesh in each separate domain.

4.5.2 Type of Element

As a default choice, Comsol Multiphysics uses Lagrange polynomials as the interpolation function to describe the variation of variables within the elements. Elements are classified according to the order of the interpolation polynomial (linear, quadratic, cubic, etc.). The difference between these types is just the number of nodes used for the Lagrange function to represent a variable over an element (the higher polynomial order the more nodes are needed and hence higher order element). Fig. 4.5 shows the number of nodes in triangular elements up to third order.

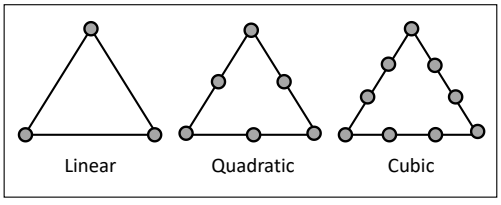

Figure 4.5. Types of triangular elements up to cubic order.

The common approach to obtaining a stable numerical solution for the incompressible Navier-Stokes equation is to use mixed element types where the pressure should be less than the velocity by one order. Typically, quadratic Lagrange element for the velocity components and linear Lagrange element for the pressure are employed (Reddy, 1984; Zimmerman, 2004; Olesen et al., 2006; Gregersen et al., 2009; Sheng and Zhu, 2014). Such treatment is because that the order of velocity in the momentum equations is higher than that for pressure. Hence, for consistency, the order of the Lagrange function used for the pressure should be less than that used for the velocities (Reddy, 1984). Here, first-order and second-order Lagrange elements are used for the pressure and the velocity component, respectively. For the solute mole fraction, second-order elements are also used since they give accurate results with a reasonable computation time when a suitable element size is selected.

4.5.3 Element Size Distribution

The size of elements determines the accuracy of the solution. The smaller the element size, the better the approximation and hence the more accurate solution can be achieved. But this accuracy is at the expense of increased computational time and memory. To reduce that, elements with different sizes in a non-uniform mesh are used and distributed so that size suits accuracy requirement in each location.

At the molar flow rate ratio of interest, the contacting occurs in the spiral between a thin liquid layer (small ξ) and a gas phase occupied most the channel (typically as that shown in Fig. 4.3). This is mainly due to the inherent difference between the molar densities of the contacting phases which results in a smaller liquid volumetric flow rate relative to that for the gas phase. Thus, one should expect a small mesh size is needed in the liquid side to compute accurately the velocity and concentration fields in such small spatial scale. Further, the liquid phase in general, as argued previously, has a larger Schmidt number comparing to the gas phase which is typically around one. So one should expect also a much steeper concentration gradient in the liquid side since larger Sc results in larger Peclet number even at small values of Reynolds number (i.e. $\mathrm{Re_L} \geq 1$), according to Eq. 4.13. This also suggests that a small element size is needed in the liquid side. Another location required to be treated carefully is the region around the interface. This region is strongly curved at the end-walls. Furthermore, since the mass flux and the stresses must match at the interface, an abrupt change in the velocity and concentration

field occurs there due to the difference in the properties of the contacting phases. Consequently, a small size of elements needs to be placed near the interface compared to the element size in the far field.

Considering the regions where small element size is expected to be needed, a finer grid size by a factor of 8 to10 times is used in the liquid domain as compared to that in the gas. Further, the maximum element growth rate, which determines the maximum allowable size ratio of two adjacent elements, is constrained in both regions to be 1.1. This ensures a large number of small elements to be packed in the region around the phase interface. So the curved boundary between the two phases and the large change in the solution gradients there can be captured reliably. The other element size parameters which can be adjusted are the curvature factor (which is the ratio of element size to the curved boundary radius) and the minimum allowable element size. These are left as specified in Comsol to be 0.2 and 8×10^{-5} mm, respectively, since they are sufficiently small to obtain a mesh independent solution as will be described subsequently.

As an illustrative example, Fig. 4.6 below shows the elements distribution using the size parameters discussed above. The maximum element size in the gas and liquid side used are 0.3 mm and 0.03 mm, respectively, giving a total number of elements, N_E, of 5259.

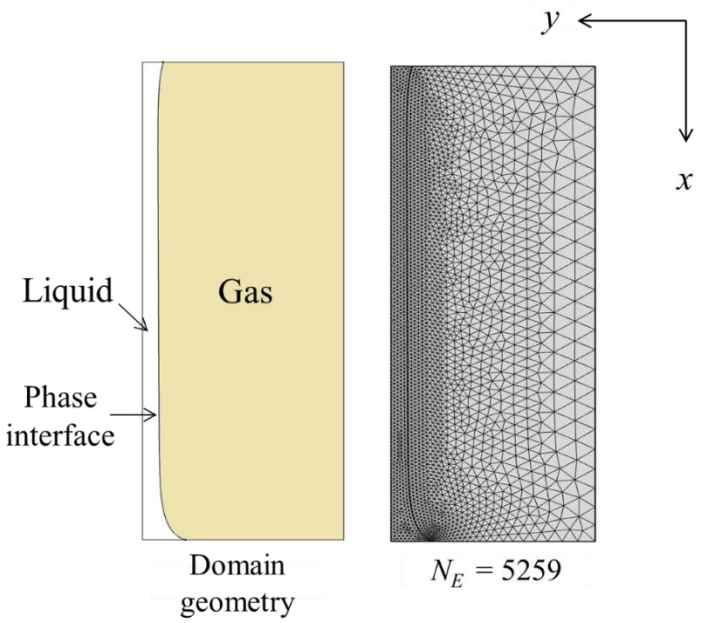

Figure 4.6. Non-unifrom mesh using maximum element size of 0.3 mm and 0.03 mm in the gas and liquid side, respectively.

4.5.4 Quantities Derived from the Numerical Solution

The solution of the governing equations gives the velocity, pressure and concentration values at any *x* and *y* coordinates in the spiral section. As a result, the bulk flow rate and concentration, and the mass transfer coefficient in each phase can be determined. These bulk quantities are of interest since they can be measured experimentally and hence a numerical analysis and comparison with the experiments are possible.

Since both phases have a uniform density along the channel, the bulk flow rates can be determined directly by integrating the streamwise velocity (w_V and w_L):

$$Q_V = w_{VB} A_V = \int_{A_V} w_V \, dA_V \quad \text{and} \quad Q_L = w_{LB} A_L = \int_{A_L} w_L \, dA_L \tag{4.44}$$

where w_{VB} and w_{LB} are the bulk velocities and A_V and A_L are the section areas occupied by the light and heavy phase, respectively.

Similarly, the bulk mole fraction in each phase (Y_{VB} and Y_{LB}) can be found by dividing the integration of the product of velocity and mole fraction by the volumetric flow rate:

$$Y_{VB} = \frac{1}{w_{VB} A_V} \int_{A_V} w_V Y_V dA_V \quad \text{and} \quad Y_{LB} = \frac{1}{w_{LB} A_L} \int_{A_L} w_L Y_L dA_L \tag{4.45}$$

In terms of the individual mass transfer coefficients (k_V and k_L), they can be calculated locally from the fact that the mass transfer rate in each phase must equal the total amount of solute transferred across the interface. Taking the interface length as ℓ_I in the channel section, this balance may be expressed in an appropriate form as:

Light phase: $$k_V \ell_I (Y_{VI} - Y_{VB}) = n_V D_V \int_{\ell_I} \vec{n} \cdot \nabla Y_V d\ell_I = n_V w_{VB} A_V \frac{dY_{VB}}{dz} \tag{4.46}$$

Heavy phase: $$k_L \ell_I (Y_{LB} - Y_{LI}) = n_L D_L \int_{\ell_I} \vec{n} \cdot \nabla Y_L d\ell_I = -n_L w_{LB} A_L \frac{dY_{LB}}{dz} \tag{4.47}$$

where the bulk solute mole fraction (Y_B) are calculated from Eqs. 4.45 and Y_{VI} and Y_{LI} can be found by integrating Y_V and Y_L along the interface length (ℓ_I):

$$Y_{VI} = \frac{1}{\ell_I}\int_{\ell_I} Y_V d\ell \quad \text{and} \quad Y_{LI} = \frac{1}{\ell_I}\int_{\ell_I} Y_L d\ell \tag{4.48}$$

It is helpful to indicate here that for rotating spiral contacting, the interfacial area per unit volume of the passage (a) can be calculated easily since the geometry of the space occupied by each phase is known:

$$a = \frac{\ell_I}{A} \tag{4.49}$$

where A is the cross-section area of the channel (hW).

Thus, when values of volumetric mass transfer coefficients are required, it is just a matter of multiplying the values of k_V and k_L calculated from Eqs. 4.46 and 4.47, respectively, by the value of a from Eq. 4.49.

It should be clear now that having obtained a full solution, the bulk flow rate (Q_V and Q_L) and bulk mole fraction in each phase (Y_{VB} and Y_{LB}) can be calculated from Eq. 4.44 and 4.45, respectively. Y_{VI} and Y_{LI} can be calculated from Eq. 4.48. These results then allow determination of the individual mass transfer coefficients (k_V and k_L) using Eqs. 4.46 and 4.47. From these coefficients, the overall mass transfer coefficient based on one of the phases can be found using the relations given in Chapter 3 (Eq. 3.26). The degree of purification (d_L) can also be determined using the purification formula (Eq. 3.51).

4.5.5 Solution Approach

A number of input parameters are required to solve the governing equations (Eqs. 4.14 to 4.23) using the boundary conditions given in Section 4.4. These parameters are the pressure gradient (dp_0/dz), the bulk solute mole fraction gradient (dY_B/dz) in each phase, the rotation rate (Ω), the liquid layer thickness along with the physical properties of each phase and the geometric parameters ($R\sin\alpha$). The properties of the phases (ρ, μ and D) and the solute equilibrium distribution (f') can easily be determined at a given spiral temperature and pressure. This is discussed in details in Chapter 6. The geometric parameters of the spiral are fixed and the rotation rate can be decided. Using this information, the shape of the interface can be computed at any radial position along

the channel by solving the equations of the interface model (as described in Section 4.3). Once the interface shape has been determined, the interface position can be decided, determining the liquid layer thickness (h_{Lm}) and hence the flow domain for each phase as shown in Fig. 4.3. In the numerical solution, the liquid phase flow rate is sensitive to the liquid layer thickness while the gas phase flow rate is determined mainly by the level of dp_0/dz set. In terms of species equation, dY_{LB}/dz and dY_{VB}/dz are linked by the solute conservation constraint (Eq. 4.28), so value of just a single bulk mole fraction gradient is required. Furthermore, since only gradients of pressure and mole fraction appear in the equations, it is necessary to specify the level of each at some position in the section to close the solution.

To predict what happens in the experiments, it is necessary to compute the volumetric flow rates at which the contacting occurs. Numerically, obtaining a solution (i.e. velocity and mole fraction distribution) directly for a given gas and liquid flow rate is not possible. This requires adjusting, by trial and error, both the value of the pressure gradient and the liquid layer thickness to compute particular phase flow rates. In this work, however, it will be often of interest to solve for a given gas phase flow rate and compute a number of different liquid phase flow rates. Thus, for a given liquid layer thickness, it is only necessary to adjust the pressure gradient along the channel to match the gas phase flow rate with the liquid flow rate determined from the solution. For the solute, as pointed out, setting one of the bulk mole fraction gradient (dY_{LB}/dz or dY_{VB}/dz) and a reference solute mole fraction determines (together with the flow solution) the mole fraction field in both phases (Y_V and Y_L). The bulk mole fraction gradient is selected such that avoids the value of mole fraction distribution falling outside the physically-possible range which is between zero to unity at all positions in the section.

As mentioned previously, the general PDE mode in Comsol Multiphysics (Ver.5.2) is employed to achieve the numerical solution. In this mode, the governing equations for both phases and the relevant boundary conditions are implemented using a general PDE equation. Details concerning the implementation of the governing equations and the boundary conditions in Comsol are described in Appendix A. The equations are solved using an iterative solver with a relative convergence tolerance of 10^{-6} which means that the solution is converged only when the estimated error in the iterative calculation is less

than 10^{-6}. The numerical solution has been carried out using a computer supplied with Intel Core i7 processor (2.5 GHz) and 16 GB of installed memory. This is the case for all computations made except when a very fine mesh size was required to check the grid dependency of the obtained solution. In this case, the University of Sheffield's high performance computing cluster (Iceberg) was employed to run the computation.

4.5.6 Grid Dependence

While the accuracy of the quantities derived from the numerical solution increases as decreasing the element size, there should be a certain size beyond which this dependency becomes negligible. This has been tested directly by reducing the elements size using the distribution and parameters selected in Section 4.5.3. The computational work is intended here to simulate different experimental conditions. So judging the dependency of solution accuracy based on a single computation for a particular condition does not seem a reliable approach. For example, the liquid layer thickness shown in Fig. 4.6 is about 120 μm (measured at minimum). This corresponds to a liquid flow rate of approximately 13 mL/min at 3200 rpm, which is at the upper end of the range used in the experiments. Reducing the liquid flow rate simply shifts the interface closer to the outer wall. At the lowest liquid flow rate used in this work which is about 0.2 mL/min, the minimum liquid layer thickness is below 20 μm. In this case, the liquid layer is right next to the wall and elements with very small size are needed there to approach an accurate solution. So taking 20 μm as a reference case to determine the element size for cases with larger layer thickness will certainly define unnecessary number of elements. On the other hands, considering 120 μm case (which needs larger element size) will lead to a significant numerical error particularly at the lower flow rate where the liquid layer thickness is too small. Accordingly, for each single computation made, the grid dependency has been tested separately to ensure obtaining a solution with a minimal numerical error.

In the computations, two sets of parameters were monitored to judge the dependency of the solution on the grid size: the average phase flow rates (Q_V and Q_L) and the individual mass transfer coefficients (k_V and k_L). As an example, Fig. 4.7 shows the mesh refinement process for a case where Q_V = 1.3 NL/min[†] and Q_L = 3.7 mL/min, starting

[†] The letter N in the unit of the gas phase volume flow rate refers to a flow under normal conditions (1 atm and 20 °C).

from an initial grid of 8451 elements (N_E). The specifications of each grid are summarized in Table 4.1. The values of flow rates and mass transfer coefficients against the number of elements are plotted in Figs. 4.8 and 4.9, respectively. It is clear from Fig. 4.8 that the effect of the mesh elements size on the phase flow rates is negligible beyond $N_E > 8451$ elements, leaving only slight differences which may be due to round-off errors. The same behaviour can be seen for k_V in Fig. 4.9 but with an obvious change in k_L values between $8451 < N_E < 39{,}212$. Thus, in this case, using $N_E \geq 39{,}212$ will ensure that the sensitivity of Q_V, Q_L, k_V and k_L to the element size is negligible, giving a maximum error less than 0.7% in k_L value when it is compared to that determined using $N_E = 168{,}408$.

It should be expected that using the same element size parameters listed in Table 4.1 for a lower liquid flow rate results in a larger error. Indeed, at $Q_L = 0.5$ mL/min for the same gas phase flow rate using the same parameters at $N_E = 39{,}212$ (Table 4.1) leads to an error about of 8% in k_L value in relation to that computed using the parameters at $N_E = 168{,}408$. So a finer mesh is needed particularly in the liquid side to reduce the error associated with decreasing the liquid flow rate and vice versa.

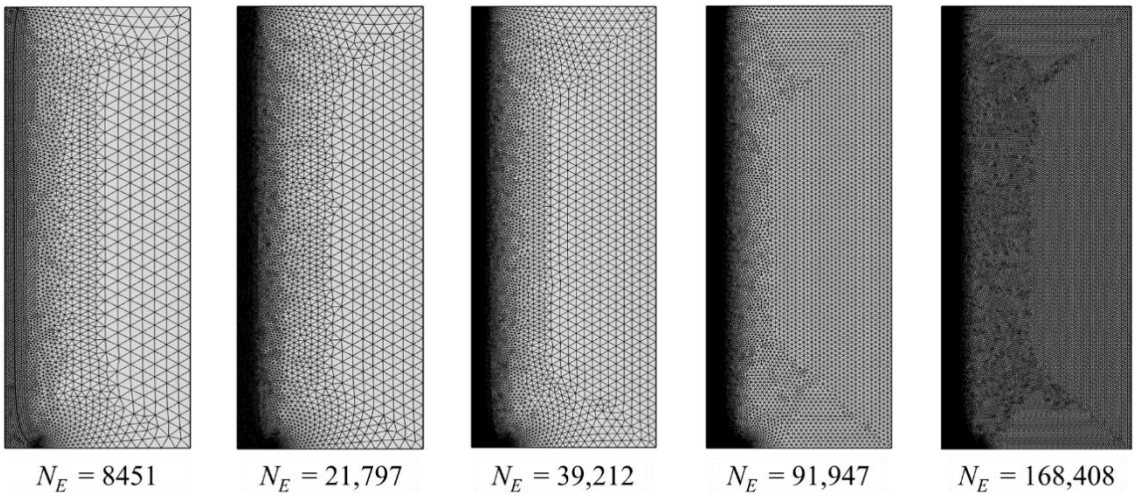

Figure 4.7. Different grids produced by Comsol using the element size parameters listed in Table 4.1.

Table 4.1. Maximum element size and the number of elements in the gas and liquid region. The other element size parameters are fixed in both regions to be 8×10^{-5} mm, 1.1 and 0.2 for the minimum element size, maximum element growth rate and curvature factor, respectively.

	Gas Phase		**Liquid Phase**	
N_E	Max. Element Size (mm)	No.of Elements	Max. Element Size (mm)	No.of Elements
8451	0.12	6207	0.02	2244
21,797	0.1	13325	0.01	8472
39,212	0.08	17278	0.008	21934
91,947	0.04	40184	0.004	51763
168,408	0.02	76317	0.0025	92091

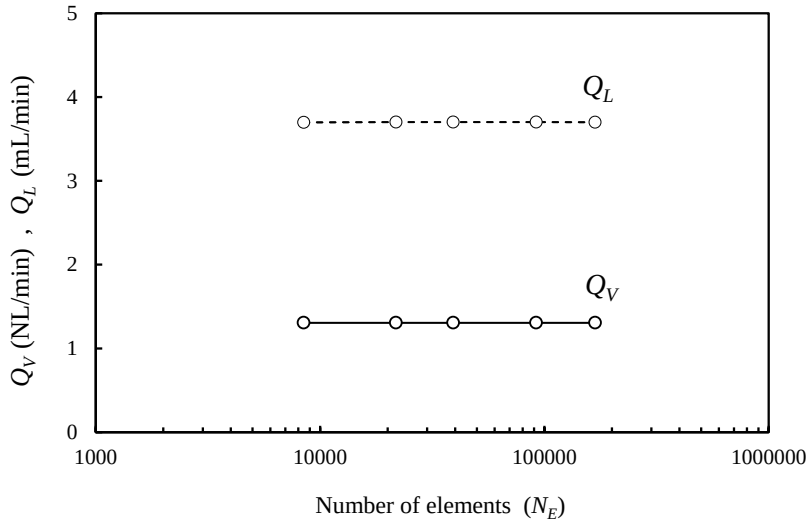

Figure 4.8. Values of the gas and the liquid phase flow rates versus the number of mesh elements.

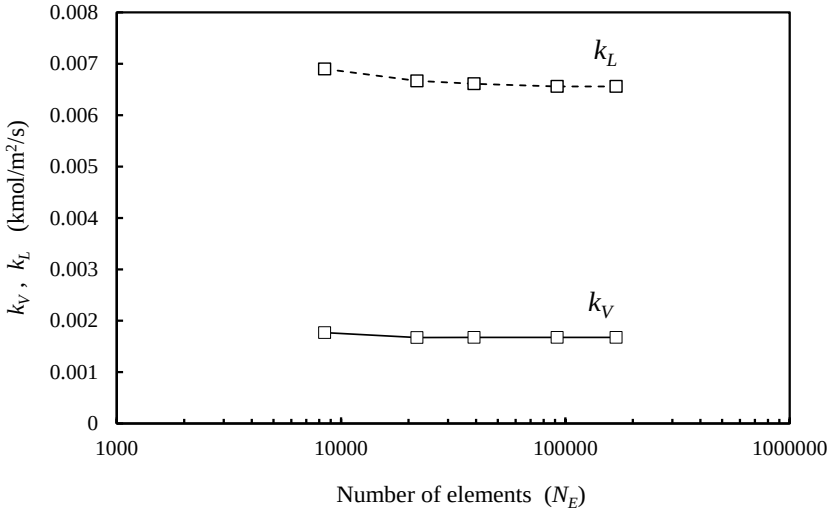

Figure 4.9. Values of the gas and the liquid phase mass transfer coefficients versus the number of mesh elements.

4.6 Illustrative Computations

In this section, computations are carried out following the numerical solution developed in the previous section. The objective of these computations is to investigate the essential characteristics of rotating spiral contacting and the main effects of the gas and liquid flow rate. The computations are made at Ω=3200 rpm, which is used experimentally, for a hypothetical solute desorbing from water into air at atmospheric pressure and 20 °C. The phase properties at these conditions are listed in Table 4.2. The values listed for the end-wall contact angles (θ_{W1} and θ_{W2}) are those established for the experimental channel used here (MacInnes and Zambri, 2015) for the same phase system. The geometry used in the computations also is for the experimental channel (h and W as those shown in Fig. 4.3 and $R\sin\alpha = 5.57\times10^{-4}$ m).

Table 4.2. Properties of air-water system at 20 °C and 1 atm.

	Phase	
Properties	Air	Water
ρ (kg/m^3)	1.2	1000
μ (Pa s)	1.8×10^{-5}	10^{-3}
	Solute	
D (m^2/s)	2×10^{-5}	10^{-9}
f'	1	
	Interfacial properties	
σ (N/m)	0.07	
θ_{W1} (glass)	15°	
θ_{W2} (plastic)	75°	

4.6.1 General Behaviour

For rotation rate 3200 rpm, liquid layer thickness (h_{Lm}) 50 μm and pressure gradient (dp_0/dz) 2250 Pa/m, the computation produces counter-current flow with rates 3.5 NL/min and 2.5 mL/min for the gas phase and liquid phase, respectively. This corresponds to $-f'q_n \approx 1$ and so represents an appropriate condition of operation for the particular solute f' value. Fig. 4.10 shows vector and contour plots of the computed streamwise velocity, secondary motion and solute mole fraction fields.

In each phase, the colours are shaded from blue through green to red corresponding to the range of values from minimum to maximum. In the liquid phase, the minimum w velocity is at the channel walls and reaches a maximum near the interface. For the counter-flowing gas flow, the velocity is generally negative and the minimum (dark blue) occurs in the core of the flow away from the channel walls and interface where the magnitude is greatest but velocity is negative. The velocity of the gas phase is thus highest (red) at the walls and interface, where the liquid actually drags the gas in the positive z direction. As pointed out previously, the interface shape is asymmetric both since the end-wall contact angles differ (Table 4.2) and because gravity tilts the interface slightly. The effect of the interface asymmetry on the streamwise liquid flow is quite strong with considerably higher velocity in the lower thicker end of the layer (i.e. the dark red core near the bottom end wall).

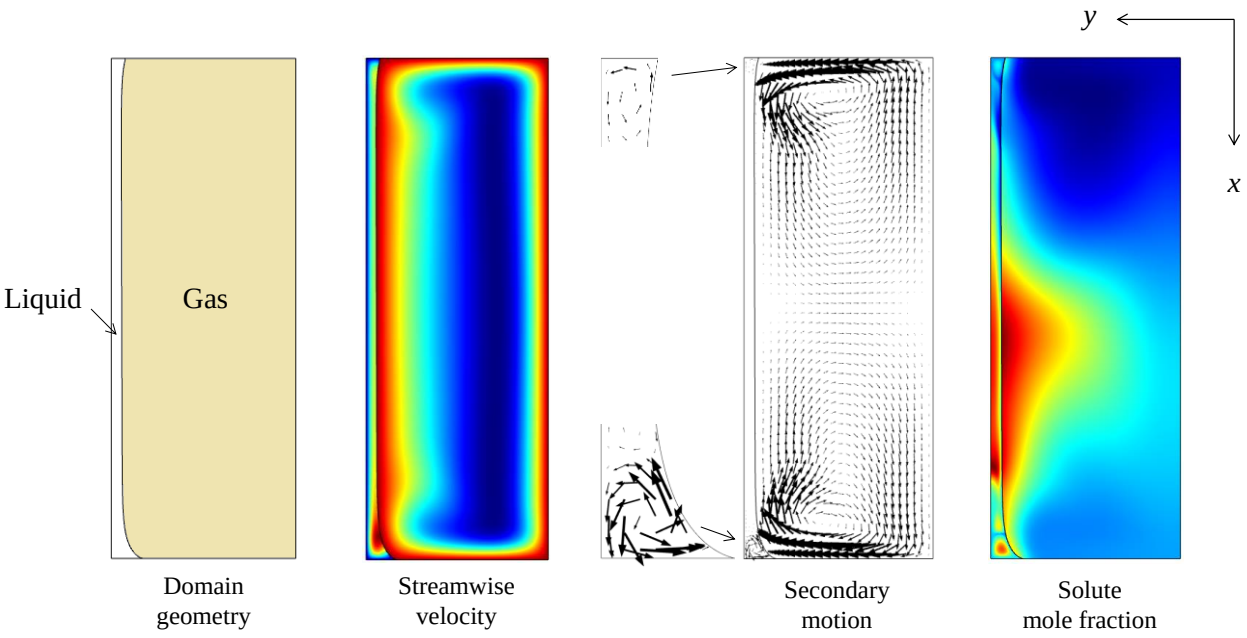

Figure 4.10. Numerical results for Q_V = 3.5 NL/min and Q_L = 2.5 mL/min at 3200 rpm: streamwise velocity contours, vector plot revealing the secondary motion (arrow length proportional to magnitude for each phase) and solute mole fraction contours.

The vector plot of the secondary motion reveals the primary effect of the Coriolis acceleration. Without the term $2\rho\Omega w$ in the y-component momentum equation (Eqs. 4.16 and 4.21) there would be no motion in either x or y. As discussed in Chapter 2 (Section 2.4.3), the secondary motion is produced by the non-uniformity of w velocity in x and y directions. Fluid near the end walls has lower w velocity magnitude than that further

away so the pressure gradient that developed in the channel section overbalanced the slow fluid near the walls but underbalanced that in the core region. The consequence is the secondary motion near the end walls, which is magnified in the liquid phase, rotating in the opposite direction in the two phases since they have opposite streamwise motion. It can be noted that while the secondary motion affects the entire width of the flow in the gas phase, it only penetrates into the liquid from the end walls at a distance approximately similar to the liquid layer thickness.

Further, in Fig. 4.10, the effect of this secondary motion on the streamwise velocities is clear in the distortion of gas streamwise velocity. Fig. 4.11 shows w velocity profile along the y direction at mid-channel both with and without the Coriolis acceleration term $2\rho\Omega w$ that causes the secondary motion. To show clearly the velocity profile, w velocity in each phase is normalised by its absolute maximum value, ranging the values of the velocities from -1 to 1. So the difference (jump) between the velocities in Fig. 4.11 is simply due to using different normalisation for the gas and liquid. As can be seen in Fig. 4.11, a strong asymmetric in the velocity profile (red line) is evident, confirming the distortional effect of the Coriolis term in the streamwise momentum equation particularly in the gas phase ($-2\rho\Omega v$). Since Ω is positive in this computation, this term serves to drive the gas flow when v_V is positive and retard the gas flow when negative. Without the term $2\rho\Omega w$, the numerical solution would, in turn, result in standard developed flow profile for w (dashed line in Fig. 4.11), even including the Coriolis term $-2\rho\Omega v$ in the z-component momentum equation. The streamwise velocity profile at the vertical centreline of the gas layer is also plotted and shown in Fig. 4.12. While the profile is nearly symmetric, it is also distorted by the strong Coriolis secondary motions at the top and the bottom of the channel. This velocity profile shown in Fig. 4.12 is consistent with the experimental observations of Hart (1971) for a single phase flowing in a channel at the highest rotation rate tested (shown in Chapter 2, Fig. 2.15 e). Also, the distorted gas phase velocity profile observed in Fig. 4.11 is qualitatively similar to the computed profiles reported by Speziale (1982), Kheshgi and Scriven, (1985) and Beak and Ko (2000) which are also for a single phase in a rectangular channel under rotation. This is, perhaps, not surprising since the gas phase in the spiral occupied most the channel with a small fraction of the liquid phase. So the flow in the spiral is approximately corresponding to a single phase flow and hence a good agreement with the single phase literature results.

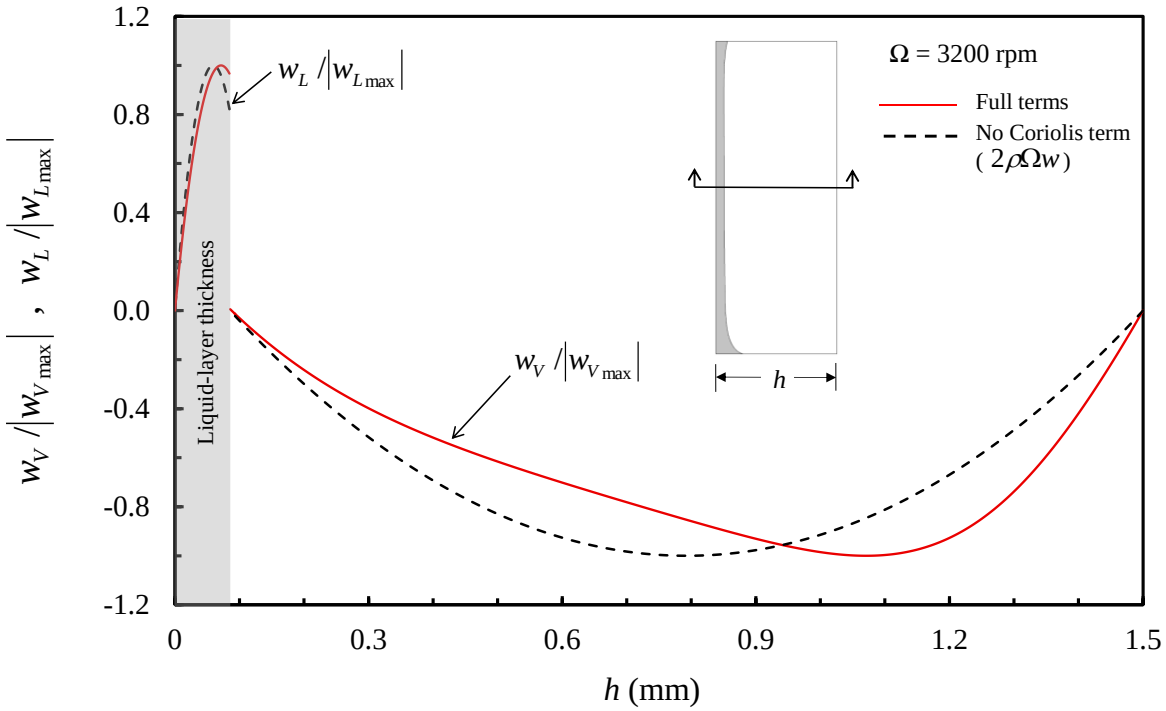

Figure 4.11. Normalised profile of the phase streamwise velocity at the centreline along the *y*-axis in the absence and presence of Coriolis terms in the flow equations.

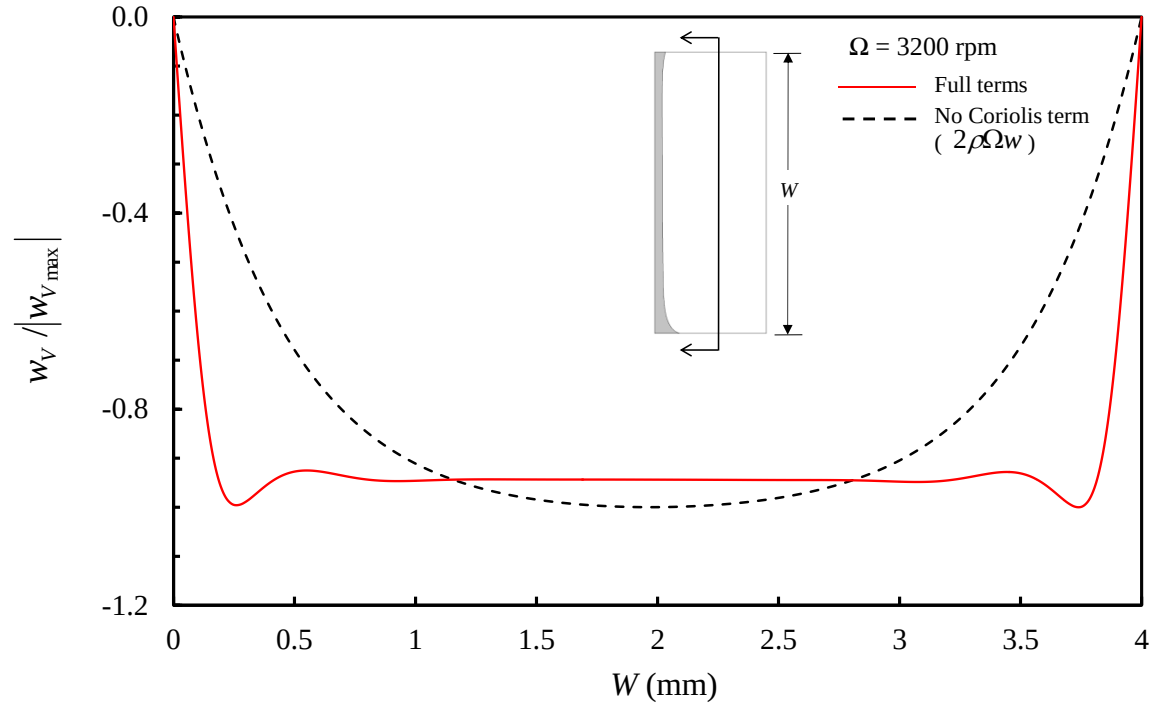

Figure 4.12. Normalised profile of the gas phase streamwise velocity at the vertical centreline in the absence and presence of Coriolis terms in the flow equations.

The final contour plot of species distribution in the two phases reveals considerable complexity. First of all, one notes extreme values appear in the core region of the gas flow (solute minima). These are simply the results of strong convection of solute from upstream in this high-speed core region, bringing gas of low solute concentration. The top and bottom difference in streamwise velocity in the liquid associated with liquid layer thickness variation appears to have a strong influence on solute distribution. Where liquid velocity is low (top), gas and liquid may come to equilibrium and mass transfer is not strong. Below, where streamwise liquid velocities are higher, variations in solute mole fraction are more pronounced in the liquid and this has an evident effect on the gas distribution.

4.6.2 Rotation Direction

The rotation direction may be positive or negative. The centrifugal terms are insensitive to the rotation direction since they depend on the square of rotation value. The Coriolis components, on the other hand, change sign and hence the direction of action. This is examined here by repeating the computation in the previous computation but for $\Omega = -3200$ and compare the results. The same interface shape shown in Fig. 4.10 has been used since the rotation direction does not change the level of the centrifugal force. Also, the same phase flow rates in the previous computation have been re-produced here by adjusting both the liquid layer thickness and the pressure gradient. Fig. 4.13 shows the results at $\Omega = -3200$ rpm which are the same set of plots shown in Fig. 4.10.

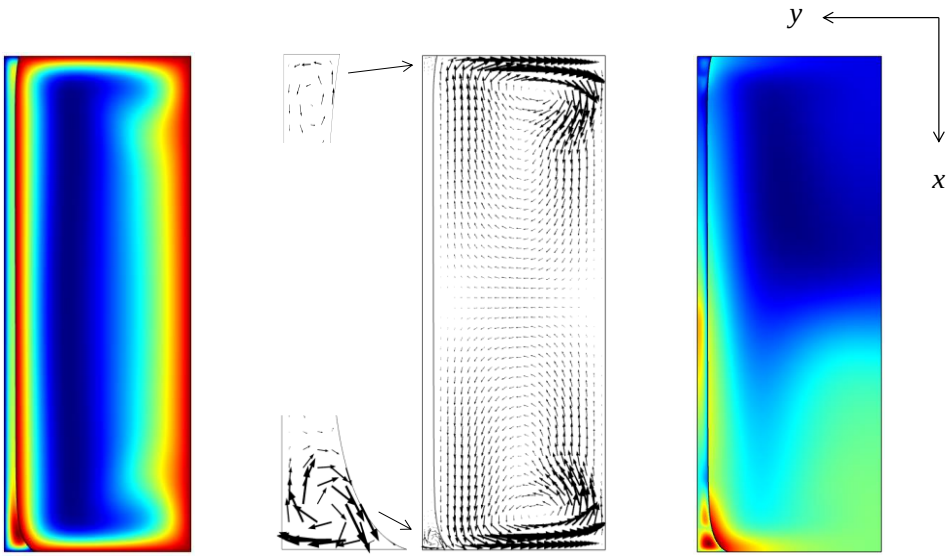

Figure 4.13. Same set of plots shown in Fig. 4.10 but at $\Omega = -3200$ rpm.

As in the previous computation, the gas phase streamwise velocity profile is distorted but with high speed core region (blue) shifted towards the interface. This is consistent with the expected flow reversal occurred in the secondary motion which is captured correctly by the 2-D numerical solution. These changes in the flow pattern yield a different mole fraction distribution in Fig. 4.13 than that shown in Fig. 4.10, particularly in the gas side. In this case, lower solute mole fraction prevails in the most region of the gas layer near the interface. As discussed previously, this is a result of the larger streamwise velocity there, producing stronger convection of solute from upstream and hence gas of lower solute mole fraction. In the liquid side, the streamwise velocity and hence solute mole fraction distribution is not much sensitive to rotation direction. Thus, similar to what has been observed in Fig. 4.10, the streamwise liquid velocity is high near the bottom end wall (red core in the meniscus region) and it is low at the top, causing variations in solute mole fraction along the layer. However, this variation is less pronounced than that observed in Fig. 4.10.

Quantitatively, reversing the rotation rate leads to 10% increase in the liquid layer thickness and approximately the same pressure gradient to re-produce the same phase flow rates in the previous computation (values given in Table 4.3). In both computations, the component $-dp_0/dz + \rho_L R\Omega^2 \sin\alpha$ in the w equation is approximately the same. So the increase in the liquid layer thickness is simply because the longitudinal Coriolis term ($-2\rho_L\Omega v_L$) is larger here than for positive Ω case. Thus, one must expect that this term lessens the component that drives the liquid phase when Ω is negative, leading clearly to such difference in the liquid layer thickness for the same liquid phase flow rate. For the gas phase, on the other hand, $-2\rho_V\Omega v_V$ has a negligible effect in w_V equation since the gas density is small. So changing the rotation direction does not affect the pressure gradient and hence same value approximately has been obtained (Table 4.3). In terms of the mass transfer coefficient, there is a slight reduction in $K_L a$ value comparing with the previous computation and that is consistent with the increase in the liquid layer thickness.

Table 4.3. Values of the liquid layer thickness, pressure gradient and overall volumetric mass transfer coefficient for Ω = 3200 and $-$ 3200 rpm.

Quantities	$+\Omega$	$-\Omega$
Liquid layer thickness (μm)	50	55
dp_0/dz (Pa/m)	2250	2270
$K_L a$ (kmol/m^3/s)	1.07	0.98

4.6.3 Different Liquid Flow Rates

In this section, the variation of the liquid phase flow rate is examined. Fig. 4.14 shows the results of two different liquid flow rates where the rotation rate and the gas phase are fixed as those used in the first computation (Ω = 3200 rpm and Q_V = 3.5 NL/min). First of all, it is clear from the figure that the liquid layer thickness increases with the liquid phase flow rate. The interface shape, as argued, is independent of the phase flow rates. So the change in the interface position in Fig. 4.14 is only due to the effect of the liquid flow rate. As mentioned in the previous section, the flow of the liquid phase is mainly driven by the component $\rho_L R \sin\alpha\, \Omega^2$ (Eq. 4.22) along the channel against the wall and gas phase shear stresses and the pressure force. This body force is constant in both cases shown in Fig. 4.14 since the rotation rate is constant. So increasing the liquid flow rate must produce a thicker layer to maintain balancing forces and hence accommodate the increase in flow rate. Comparing with the images shown in Fig. 2.20 b (MacInnes and Zambri, 2015), the same behaviour has been observed. That is, the liquid layer thickness increases with the liquid phase flow rate at constant rotation rate.

It is also quite clear in Fig. 4.14 that the interface shape has a less effect on the streamwise liquid flow as the liquid layer thickness increases. The liquid flow rate is distributed approximately evenly with a higher velocity shifted towards the centre of the layer (dark red core). Another point to note in Fig. 4.14 is that the secondary motion in the liquid side evolves as the liquid flow rate increases. This is mainly due to increasing the effect of the transverse Coriolis term ($2\rho_L w_L \Omega$) in the v_L equation. As can be seen in the vector plot, the configuration of this motion in the liquid phase starts with two vortices, occupying the menisci regions at small Q_L. As increasing Q_L then, the structure of the secondary motion develops by producing small streamwise vortices (roll cells), stretching gradually towards the middle of the liquid layer. The effect of these roll cells is quite evident in the solute mole fraction contour plot.

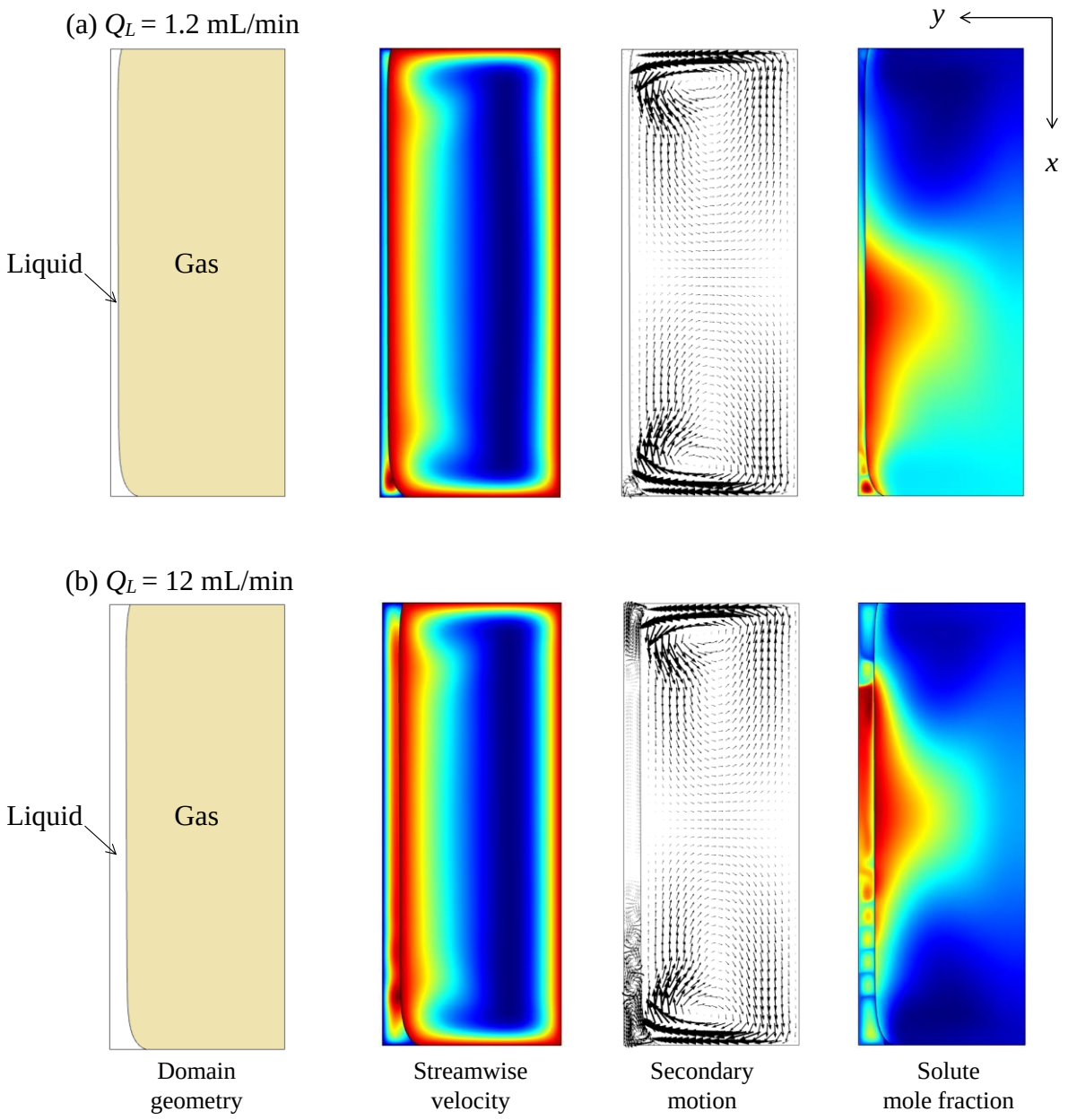

Figure 4.14. Numerical results at Q_L = 1.2 mL/min and Q_L = 12 mL/min. The rotation rate is 3200 rpm and Q_V = 3.5 NL/min.

In terms of the mass transfer quantities, Fig. 4.15 shows the values of the mass transfer coefficients. As can be seen, a noticeable increase in the individual liquid phase transfer coefficient (grey bar) as the liquid phase flow rate increases. This could be attributed to the developed secondary flow in the liquid side which can boost the mass transfer rate, resulting in a larger mass transfer coefficient. Fig. 4.16 provides information about the solute molar flux along the interface for the two different Q_L cases. As can be seen, the mass transfer rate is improved as the liquid flow rate increases, as expected. The peaks in the plot (black curve) correspond to locations where the streamwise vortices are active, indicating clearly the role of secondary motion in enhancing the mass transfer.

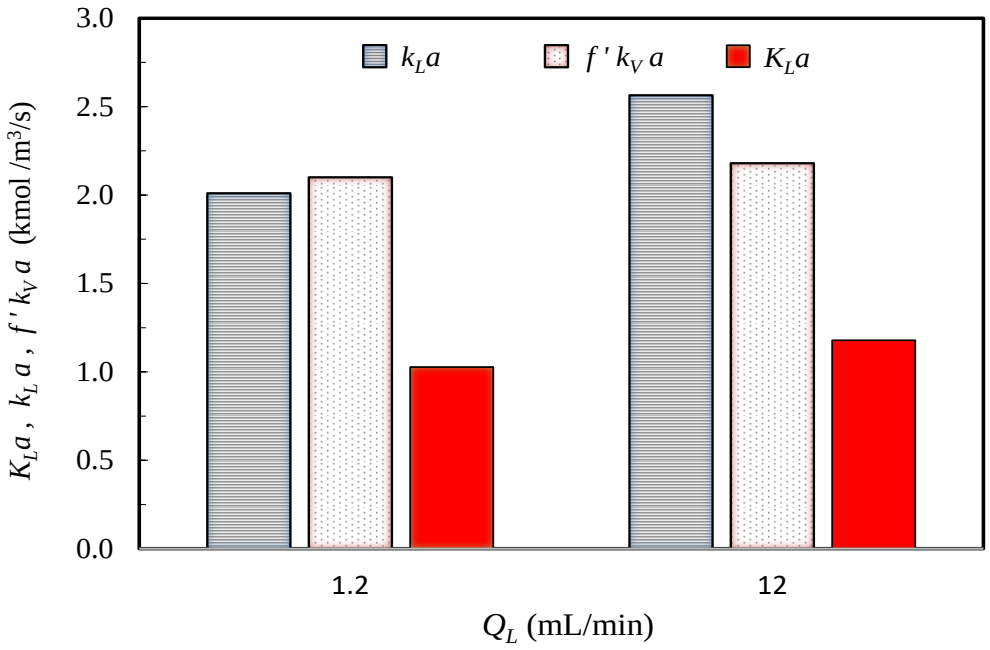

Figure 4.15. The volumetric mass transfer coefficients at Q_L = 1.2 mL/min and 12 mL/min. The other operating conditions as in Fig. 4.14.

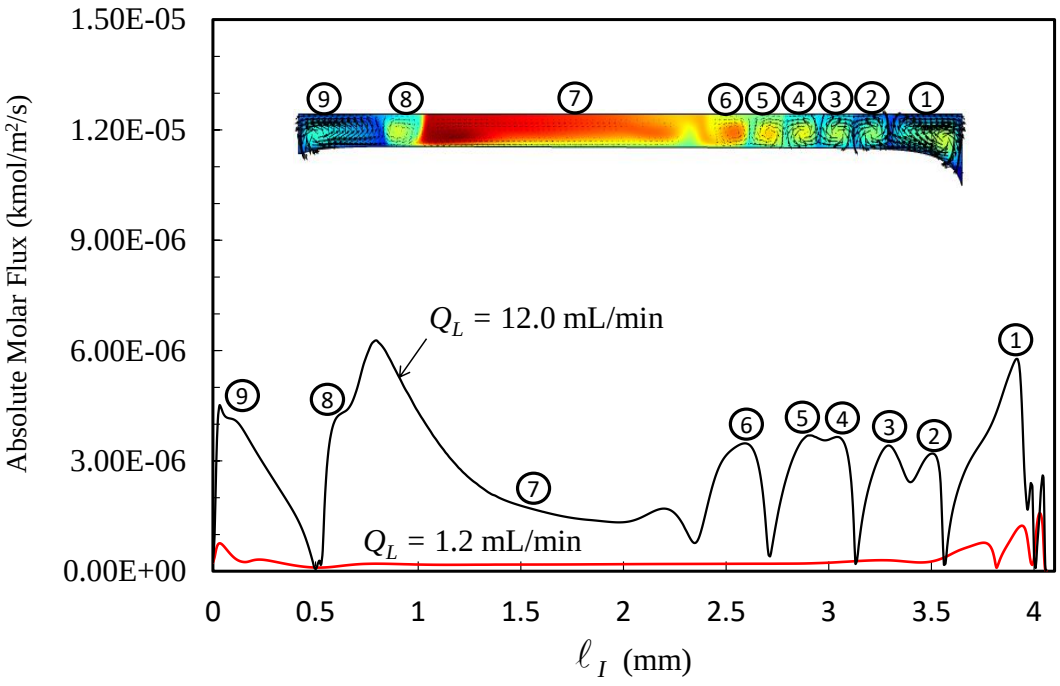

Figure 4.16. Solute molar flux across the interface for Q_L = 1.2 mL/min (red curve) and 12 mL/min (black curve). The other operating conditions as in Fig. 4.14.

4.6.4 Different Gas Flow Rates

The variation of the gas phase flow rate is now examined by computing for a range from 1 to 6 NL/min with the liquid phase flow rate held constant at Q_L = 2.5 mL/min. This range of gas phase flow rate gives a range of Reynolds numbers approximately between 300 and 1800. So it falls within the laminar flow regime where the 2-D model equations can be applied. The computed streamwise velocity, secondary flow and solute mole fraction distribution for the highest and lowest gas phase flow rate are shown in Fig. 4.17 and will be discussed first.

As can be seen in the figure, the general features observed in the previous computations do not change as the gas phase flow rate changes however there are some interesting points that can be made. First, comparing to the effect of liquid phase flow rate, it is quite clear that the gas phase has a minor effect on the liquid layer thickness. The computations show that increasing the gas phase flow rate by a factor of 6 requires adjusting the liquid layer thickness (h_{Lm}) by about 20% (from 45 to 55 μm) to maintain the same liquid phase flow rate. This behaviour is linked directly to the layer thickness which is quite thin at 3200 rpm. At such thin layer, the order of magnitude of shear stress exerted by the gas on the liquid phase interface is small in relation to the wall shear stress (MacInnes and Zambri, 2015). Hence, the liquid layer thickness is slightly sensitive to the variation of gas phase flow rate at this particular rotation rate, which is considered relatively high. However, as the rotation rate decreases, h_{Lm} increases and the effect of gas phase flow rate may become more pronounced. This is simply because the thicker layer provides a smaller flow passage available for the gas phase. This leads, in turn, to increasing the gas shear stress on the liquid side due to both increasing the gas velocity and decreasing the characteristic spatial length. This is tested here by re-producing the conditions of Fig. 4.17 but for Ω = 1480 rpm. At this rotation rate, h_{Lm} = 110 μm and dp_0/dz = 600 Pa/m produce counter-current flow with Q_V = 1 NL/min and Q_L = 2.5 mL/min. Increasing h_{Lm} and dp_0/dz to be 356 μm and 6000 Pa/m, respectively, counter-current flow with Q_V = 6 NL/min and Q_L = 2.5 mL/min can be produced. So, clearly, the results show that under the same variation of gas phase flow rate (from 1 to 6 NL/min), the liquid layer thickness increases by approximately 3 times (from 110 to 356 μm) at the low rotation rate. These computational results are consistent with the experimental

observations of MacInnes and Zambri (2015) shown in Chapter 2. The images at Ω = 1480 rpm (Fig. 2.20 d) show the strong sensitivity of the liquid layer thickness to the gas phase flow rate while this sensitivity becomes negligible at Ω =3840 rpm over approximately the same range of gas phase flow (Fig. 2.20 c).

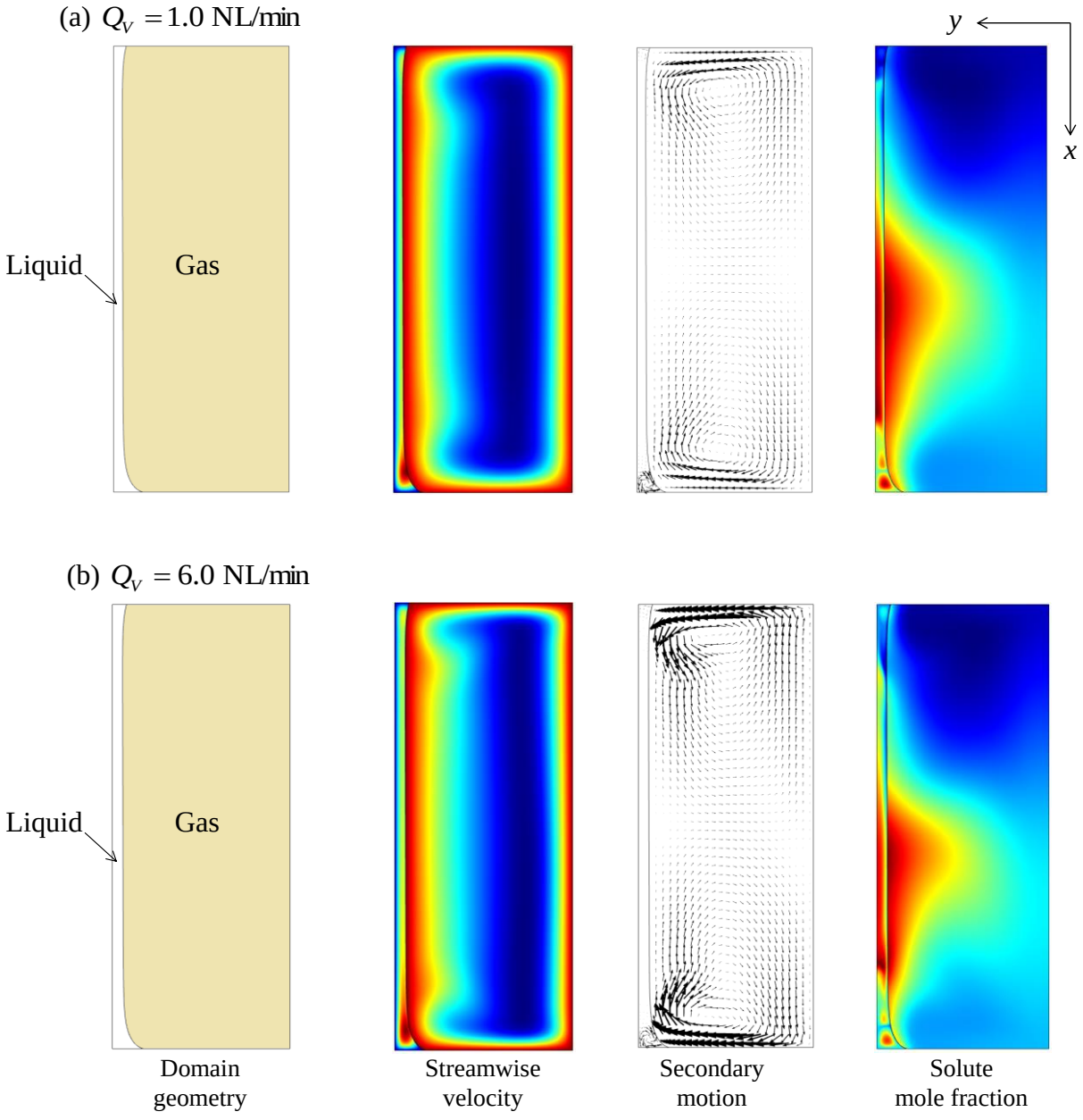

Figure 4.17. Numerical results at Ω = 3200 rpm and Q_L = 2.5 NL/min for two different gas phase flow rates.

Another effect of gas phase flow rate observed in Fig. 4.17 is on Coriolis secondary motion. The velocity vectors for the two cases are plotted using the same scale factor, showing clearly that the strength of secondary motion in the gas side increases as the

gas flow rate increases. This is mainly due to the effect of the term $2\rho_V \Omega w_V$ which determines the strength of this motion. The consequence of increasing the secondary motion on the main flow is also evident in Fig. 4.17, relatively thinner momentum layers at the two end walls at the higher gas phase flow rate

Bringing in mind the observations discussed above, the mass transfer mechanism can be understood. Fig. 4.18 shows the variation of the mass transfer coefficients over the computed range of gas phase flow rate. It is obvious that the individual gas phase mass transfer coefficient increases with the gas phase flow rate. This is consistent with the noticeable improvement in Coriolis secondary motion with the gas phase flow rate. This convective motion, in effect, can short-circuit the species diffusion and hence enhances mass transfer. On the other side, the individual liquid phase mass transfer coefficient decreases slightly with the gas phase flow rate. This is clearly attributed to the slight increase in the liquid layer thickness which decreases the species diffusion. Based on the behaviour of these individual parameters, the overall mass transfer coefficient increases slightly with the gas phase flow rate, showing a clear dependency on the mass transfer action in both phases.

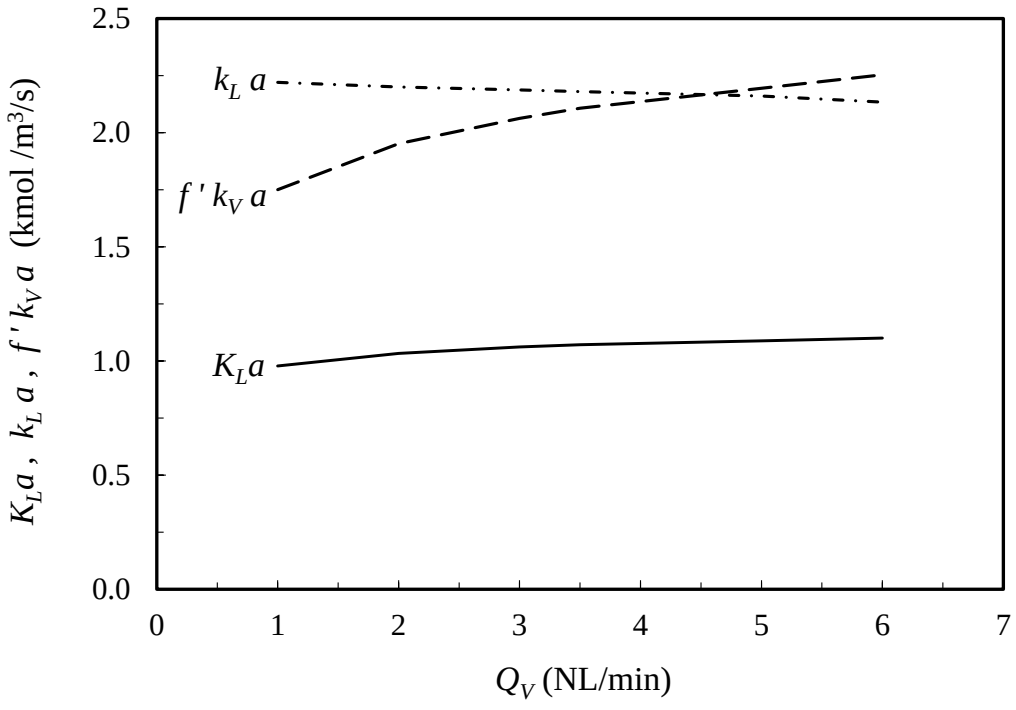

Figure 4.18. Values of the individual and overall mass transfer coeffiecnets over the computed range of gas phase flow rate where Ω = 3200 rpm and Q_L = 2.5 NL/min.

4.7 Wide Channel Solution

The case of an infinitely wide spiral channel ($W \to \infty$) with negligible effect of gravity reduces the governing equations to the ones that describe just one spatial dimension. The analytical solution to these equations is developed in MacInnes et al. (2012). The results are explicit analytical functions for w velocity and mole fraction distribution in the *y*-direction across each phase layer. These functions allow prediction of the parameters of interest (the liquid layer thickness, phase flow rates and the individual mass transfer coefficients) at a given state of contacting in a spiral channel.

The flow in a wide channel is equivalent to that between two parallel plates without end-walls (top and bottom walls of the channel which are perpendicular to the phase layers). The presence of the end-walls, in principle, gives rise to the curvature of the interface through the contact angle (i.e. θ_{W1} and θ_{W2} in Fig. 4.2). Accordingly, the solution developed in MacInnes et al. (2012) is based on contacting of two phases separated by a flat interface since there are no end-walls. Also, it is assumed that the flow is subject to a high rotation rate which is able to overcome the curvature of the interface due to the surface tension and the interface tilt due to the effect of gravity. Fig. 4.19 depicts this case of contacting using the same geometric parameters given in Fig. 4.1 but without end-walls.

The end-walls also are responsible for the spatial variation of streamwise velocity which produces with the effect of the rotation the secondary motion in each phase. In the case of the infinite channel, the streamwise velocity is independent of the *x*-direction and thus there is no secondary motion. Under these conditions, the 2-D governing equations presented in the previous sections can be reduced and solved analytically and the solution results are given in the next subsections.

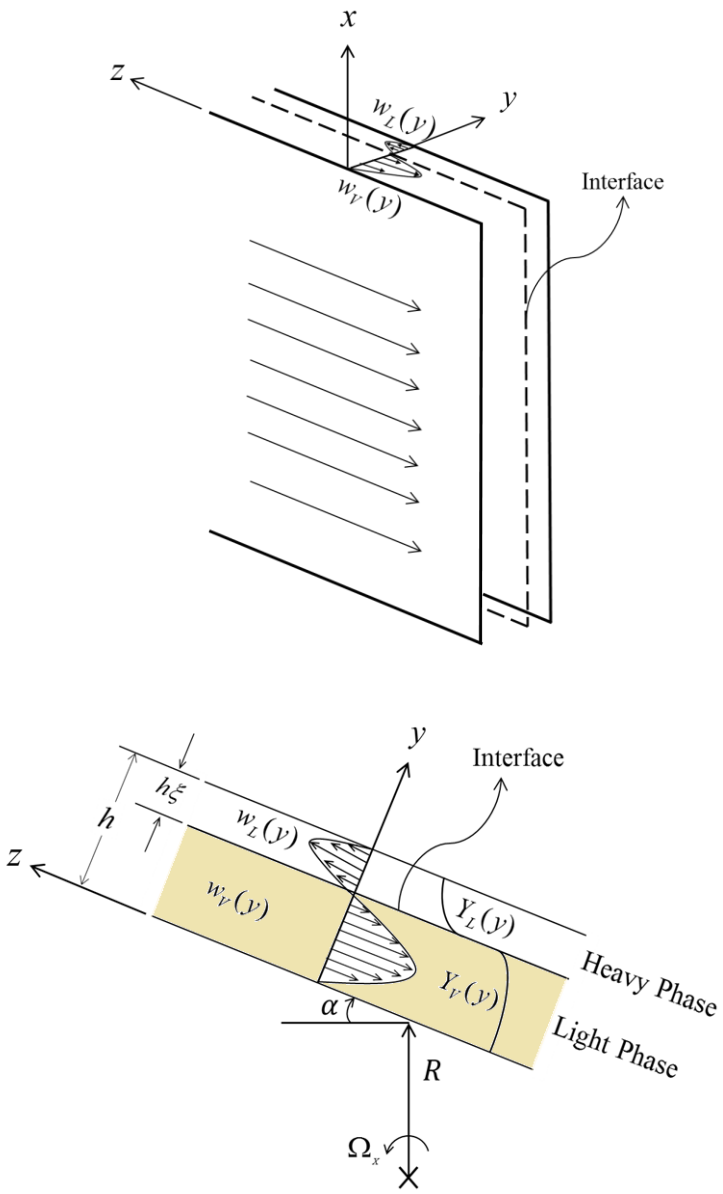

Figure 4.19. Two phase contacting in a wide spiral channel: (a) a segment of a spiral channel without end-walls and (b) top view showing the geometric parameters.

4.7.1 Hydrodynamic Parameters

The relevant parts of the solution of the flow equations are the phase volumetric flow rates (Q_V and Q_L). Here, these values are measured experimentally and hence a direct comparison with the experiments can be made by reproducing these measured values. The full analytical expressions for Q_V and Q_L are given in MacInnes et al. (2012) and can be re-expressed as:

$$Q_V = -\frac{Wh^3}{12\mu_V}\frac{dp_0}{dz}\frac{(1-\xi)^2\left[3(1-\gamma_r)\mu_r + (1-\rho_r\gamma_r)(1-\xi)(1-\xi+4\mu_r\xi)\right]}{1-(1-\mu_r)\xi} \tag{4.50}$$

$$Q_L = -\frac{Wh^3}{12\mu_V}\frac{dp_0}{dz}\frac{\mu_r\xi^2\left[3(1-\rho_r\gamma_r)(1-\xi)^2 + (1-\gamma_r)\xi(4(1-\xi)+\mu_r\xi)\right]}{1-(1-\mu_r)\xi} \tag{4.51}$$

where ρ_r and μ_r are ratios of viscosity and density for the two phases,

$$\rho_r = \frac{\rho_V}{\rho_L} \quad \text{and} \quad \mu_r = \frac{\mu_V}{\mu_L} \tag{4.52}$$

and γ_r is the ratio of centrifugal body force acting on the heavy phase to the pressure force:

$$\gamma_r = \frac{\rho_L R\sin\alpha}{dp_0/dz}\Omega^2 \tag{4.53}$$

Eq. 4.53 can be expressed in terms of flow rate ratio ($q = Q_V/Q_L$) and phase physical properties by dividing Eq. 4.50 by Eq. 4.51 and solving for γ_r:

$$\gamma_r = \frac{1-4(1-\mu_r)\xi+3(2-\mu_r(3+q))\xi^2-2(2-\mu_r(3+q))\xi^3+(1-\mu_r)(1+\mu_r q)\xi^4}{\mu_r\xi^2[3-2(3+2q)\xi+(3+(4-\mu_r)q)\xi^2]+\rho_r(1-\xi)^2[1-2(2(1-2\mu_r)\xi+(1-\mu_r(4+3q))\xi^2]} \tag{4.54}$$

The above equations allow the essential hydrodynamic parameters of two phase contacting in a rotating spiral channel to be predicted. For example, from Eqs. 4.50 to 4.54, the liquid layer thickness represented by ξ can be predicted at given phase flow rates by knowing only the phase physical properties (ρ_r and μ_r), the geometric parameters (W, h and the component $R\sin\alpha$) and the rotation rate. From ξ, q and the phase physical properties, γ_r can be calculated from Eq. 4.54. Then, the pressure gradient along the channel can be found straightforward from Eq. 4.53.

4.7.2 Mass Transfer Coefficients

In terms of the mass transfer parameters, it is sufficient to introduce the expressions for the individual mass transfer coefficient since these are the most relevant parameters and allow a comparison with the experiments through the overall mass transfer coefficient of one of the phases. These expressions are given in MacInnes et al. (2012) as:

$$k_V = \frac{n_V D_V}{h} \frac{35\left\{1-\xi\left[2-\mu_r(4-\xi)-\xi\right]-\gamma_r\left[3\mu_r\xi^2+\rho_r(1-\xi)(1-\xi+4\mu_r\xi\right]\right\}^2}{13+2\gamma_r(1-\xi)(A+B)+\gamma_r^2(1-\xi)(C+D)+\xi(E+F)} \tag{4.55}$$

$$k_L = \frac{n_V D_V}{h} \frac{35\left\{\xi\left[2+\xi(1-\mu_r)-\xi\right]-3+\gamma_r\left[3\rho_r(1-\xi)^2+\xi(4-94-\mu_r)\xi)\right]\right\}^2}{n_r D_r \xi\left\{G+2\gamma_r(H-I)+\gamma_r^2(J+K)\right\}} \tag{4.56}$$

The normalised physical properties used in Eqs. 4.55 and 4.56 are the same for those in γ_r but with two additional parameters: ratios of molar density (n_r) and solute diffusion coefficient (D_r) and these are:

$$n_r = \frac{n_V}{n_L} \quad \text{and} \quad D_r = \frac{D_V}{D_L} \tag{4.57}$$

Further, γ_r and ξ can be calculated independently, as mentioned, from the hydrodynamic equations while the variables A to K are functions only of the physical properties and ξ and can be found from the equations listed in Table 4.4 (MacInnes et al, 2012).

Some characteristics can be drawn from the infinite-width channel solution. First, the mass transfer coefficients are independent of the solute mole fraction gradient along the channel (dY_{LB}/dz and dY_{VB}/dz) and nor do they depend on the level of the solute mole fraction. Second, at a constant phase flow rates ratio (which is determined by the solute equilibrium distribution, f') and constant interface position (ξ), k_V and k_L are independent of the level of the flow rate in each phase.

Table 4.4. Functions used in Eqs. 4.55 and 4.56.

$$A = 7\mu_r\xi^2\{\xi[8-13\mu_r-4\xi(1-\mu_r)]-4\}$$

$$B = \rho_r(1-\xi)\{\xi[39-82\mu_r-\xi(39-4\mu_r(34-33\mu_r))+(1-\mu_r)(13-41\mu_r)\xi^2]-13\}$$

$$C = 63\mu_r^2\xi^4+14\mu_r\rho_r(1-\xi)\xi^2[4(1-\xi)+13\mu_r\xi]$$

$$D = \rho_r^2(1-\xi^2)\{13+\xi[13(\xi-2)+2\mu_r(41(1-\xi)+66\mu_r\xi]\}$$

$$E = 2\mu_r(1-\xi)^3(41-13\xi)$$

$$F = \xi(1-\xi)\mu_r^2[132+\xi(13\xi-82)]-13\{5-\xi[10-\xi(10-(5-\xi)\xi]\}$$

$$G = 63-\xi\{70+\xi[36-56\mu_r-30(1-\mu_r)\xi-13(1-\mu_r)^2\xi^2]\}$$

$$H = 7\rho_r(1-\xi)^2[\xi(5+4(1-\mu_r)\xi)-9]$$

$$I = \xi\{91-\xi[141-28\mu_r-(9+26\mu_r)\xi-(1-\mu_r)(41-13\mu_r)\xi^2]\}$$

$$J = 63\rho_r^2(1-\xi)^4+14\rho_r(1-\xi)^2\xi[13(1-\xi)+4\mu_r\xi]$$

$$K = \xi^2\{132+\xi[132(\xi-2)+\mu_r(82(1-\xi)+13\mu_r\xi)]\}$$

4.8 Comparison with Wide-channel Solution

The wide-channel case can be employed to assess the 2-D numerical solution by comparing the predictions of these two different approaches to solve the governing equations. To reduce the 2-D numerical model to the wide-channel case, the interface shape is treated as flat and symmetry boundary conditions are applied at the end-walls of the spiral channel. The symmetry condition imposes zero normal velocity and vanishing both viscous stresses and solute diffusion flux at the end walls. In this way, the effect of the end-walls is neglected and the problem is approximated to two-phase contacting in a channel with large aspect ratio ($W/h \to \infty$). The comparison has been done over different phase flow rate ratios ($0.2 < q_n < 12$) using the same phase physical properties (Table 4.2), rotation rate and channel geometry used in the previous computations.

As expected, the same analytical results of the wide channel solution have been re-produced numerically over the whole range of the conditions tested. Fig. 4.20 shows representative results of a computation made at Q_L = 8.198 mL/min, Q_V = 3 NL/min and Ω = 3200 rpm using symmetry boundary conditions at the end walls. On the left is the

domain geometry where a flat interface divides the gas and the liquid phase. The variation of the velocity field and the flow direction of the phases can be seen from streamwise velocity contour plot. Qualitatively, the dark blue core in the gas region is the highest velocity (negative value) while the highest liquid phase velocity is approximately at the interface (red) and is a positive value. So, clearly, the phase streamwise velocities change only in the lateral *y*-direction and counter-current mode of flow is achieved. On the right is the solute mole fraction distribution in each phase and also, clearly, it varies only in the *y*-direction. By choosing a negative solute mole fraction gradient in the liquid phase, desorption mode of contacting is depicted here where the solute is being transferred from the liquid phase into the gas phase. The values of the individual mass transfer coefficients computed by the two solution approaches at the conditions shown in Fig. 4.20 are listed in Table 4.5.

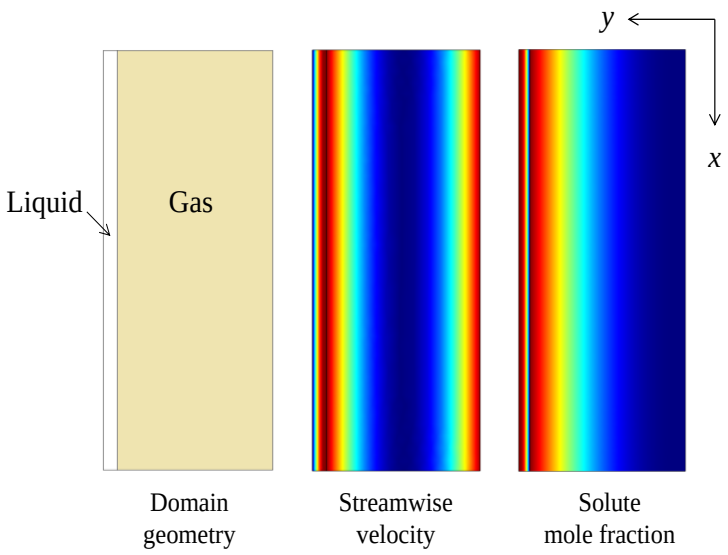

Figure 4.20. Numerical results for Q_L = 8.198 mL/min and Q_V = 3 NL/min at 3200 rpm, using a flat interface and applying symmetry boundary conditions at the end-walls.

Table 4.5. Values of the volumetric mass transfer coefficient calculated from the wide channel analytical solution (MacInnes et al. 2012) and the 2-D numerical solution.

Solution Approach	$k_V a$ (kmol /m^3/s)	$k_L a$ (kmol /m^3/s)
Analytical Solution (Eqs. 4.55 and 4.56)	1.0686	1.2230
Numerical Solution (Eqs. 4.46 and 4.47)	1.0673	1.2230

4.9 Summary

This chapter introduced a 2-D numerical model to simulate a mass transfer process of a dilute solute between two phases contacting in a section of rotating spiral channel. In the chapter, the main aspects of the numerical solution were described and illustrative computations were carried out. These computations served to highlight the general behaviour of counter-current gas-liquid contacting in a rotating spiral channel and the effects of gas and liquid phase flow rate individually. Hydrodynamics results of these computations were compared qualitatively with the previous experimental measurements and theoretical predictions for a single phase in a channel under rotation and the results were in agreement. At the end of this chapter, the analytical solution for a case where the spiral channel has infinite width was presented (MacInnes, et al, 2012) and a direct comparison with the 2-D numerical solution at symmetry boundary conditions was carried out.

The main conclusions from the computations made for the experimental channel, which has a relatively large aspect ratio, can be summarised as follows:

- As a general behaviour, strong Coriolis secondary motion in the gas phase occupied most of the channel while there are just two weak vortices in the liquid phase and they reside mainly in the meniscus regions.
- The streamwise velocities are distorted due to the effect of Coriolis acceleration.
- At fixed rotation rate (Ω=3200 rpm), increasing the gas phase flow rate produces stronger Coriolis motion. This motion improves the mass transfer in the gas side with a small effect on the liquid layer thickness.
- In the liquid phase, on the other hand, increasing the liquid phase flow increases the liquid layer thickness and changes the structure of Coriolis secondary motion. The motion becomes strongly active in the corners and generates small vortices, stretching gradually towards the central layer. This developed motion also can enhance mass transfer in the liquid side by convection.

Chapter Five

Mass Transfer Experiments

This chapter describes the experiments conducted in this thesis. The objective of these experiments is to investigate the performance of rotating spiral channel over a wide range of gas-liquid contacting conditions. This was made by studying separately counter-current desorption of four different organic solutes (ethanol, acetonitrile, acetone and MEK) from water into air at a dilute concentration. This collection of solutes was selected since they are completely soluble in water under ambient conditions, making them difficult to strip (Lamarre and Shearouse, 1994). Furthermore, they have different equilibrium characteristics (f'). This means that the relative flow rates of the contacting phases can vary considerably with solute type, giving a wide range of conditions to examine the spiral performance.

In this chapter, the experiments strategy and the operating conditions are discussed in the first section. This is followed by a description of the experimental apparatus, including the flow networks and the rotating spiral unit. After that, the operational considerations of the spiral unit are illustrated. At the end of the chapter, the experimental measurements are discussed, giving details about the determination of the phase flow rates, the method developed to collect valid samples and the techniques used to analyse them.

5.1 Experiments Strategy and Conditions

The four different solutes were tested here at three different contacting temperatures (24, 30 and 49 °C). This range of temperatures gives considerably different values of the equilibrium constant (f') for a given solute in the water-air system and affects somewhat the phase properties. So, in other words, different phase and solute systems in terms of f' have been tested and these systems are given in Table 5.1. The details of f' determination are described in Chapter 6. Table 5.1 also lists the maximum level of the solute mole fraction added to the liquid feed in the experiments, $Y_{LB}(0)$. For each system, the value of $Y_{LB}(0)$ was selected to ensure that: (1) both phases remained at a dilute level and (2) a reliable measurement of the remaining solute content in the liquid phase after

contacting could be obtained. So $Y_{LB}(0)$ ranged from 0.015 for MEK (which has the largest equilibrium curve slope) to 0.05 for ethanol (the lowest slope), giving a maximum mole fraction in the gas phase not exceeding about 0.08 for any of the solutes at equilibrium.

Table 5.1. Seven phase and solute systems used in the experiments characterised by the value of solute equilibrium distribution where $Y_{LB}(0)$ is the solute mole fraction in the liquid feed.

Solute	$Y_{LB}(0)$	T_S (°C)	f'
Ethanol	0.05	30	0.232
	0.05	49	0.651
Acetonitrile	0.03	30	0.812
	0.03	49	1.84
Acetone	0.02	24	1.15
	0.02	49	3.83
MEK	0.015	49	5.5

Examining systems having different f' requires different flow rate ratio of the contacting phases to be achieved. For each phase and solute system (f'), three values of gas flow rate (Q_V) were tested (1.3, 3 and 6.2 NL/min), where the largest flow rate was near the upper limit of the laminar regime ($\mathrm{Re}_V \approx 1800$). At each fixed value of gas flow rate, the liquid flow rate (Q_L) has ranged over about 60 times (approximately from 0.2 mL/min to 12 mL/min). This range of Q_L was determined based on pre-calculations with the wide-channel model and the purification relation (Eq. 3.51) to ensure different extent of separation (d_L) to be reached for each phase and solute system. Additionally, all of the tests were made at a rotation rate of 3200 rpm for which the liquid layer remains reasonably uniform in thickness with only small meniscus heights at the end walls as shown in Chapter 4. This level of rotation rate with a liquid phase outlet passage open to atmosphere fixes the operating pressure in the spiral to be 1.8 bara and that is used all the experiments.

Under these operating conditions, the solute mole fraction at the liquid outlet , $Y_{LB}(L)$, was measured as a function of the phase flow rates for each system. Measurement of $Y_{LB}(L)$, Q_V and Q_L along with the phase properties enabled calculation of the experimental mass transfer coefficient and hence the specific throughput using the basic relations developed in Chapter 3. In this way, the spiral performance was quantified and investigated over different phase flow rates, which affect directly the mass transfer as shown in the computations made in Chapter 4.

5.2 Experimental Apparatus

Fig. 5.1 shows a photograph of the experimental apparatus used throughout this work to test the seven phase and solute systems listed in Table 5.1. The experiments were carried out essentially on the same rotating unit used in the hydrodynamic study of MacInnes and Zambri (2015). At the top is a variable speed motor connected to an inverter to produce the required rotation rate. This motor drives a shaft inside a seal unit (Fig. 5.1 b). The shaft allows a spiral element to be mounted on its head (Fig. 5.1 c). Passages in the shaft lead from individual seals to corresponding holes in the spiral element that connect to the ends of the spiral channel. The bottom of the spiral channel is shown in Fig. 5.1 c. On the top right of Fig. 5.1 a, a monitor shows an image of the outer revolutions and the outer end (reservoir) of the spiral channel during operation. The image is taken using a camera (Fig. 5.1 c) and a strobe light (Fig. 5.1 a) synchronised with the rotation speed of the spiral. This visualisation system enables the liquid layer to be seen at any section along the channel and that helps to establish and control the contacting process in the spiral during the experiments. Additionally, Fig. 5.1 a shows the external flow network used to transfer the contacting phases individually to and from the rotating spiral unit. Usually, the liquid phase is supplied by either a pressurised pot or a syringe pump (shown on the right side of Fig. 5.1 a) while the air by a compressor.

To give a clear description of the journey of the fluid phases through the experimental apparatus and to understand how the contacting is achieved, the overall flow network is described in the next subsection. This is followed by a brief description of the main components of the rotating unit. This description helps to get insight into the function of these components, the circuit of fluids inside the unit and the unit operational considerations.

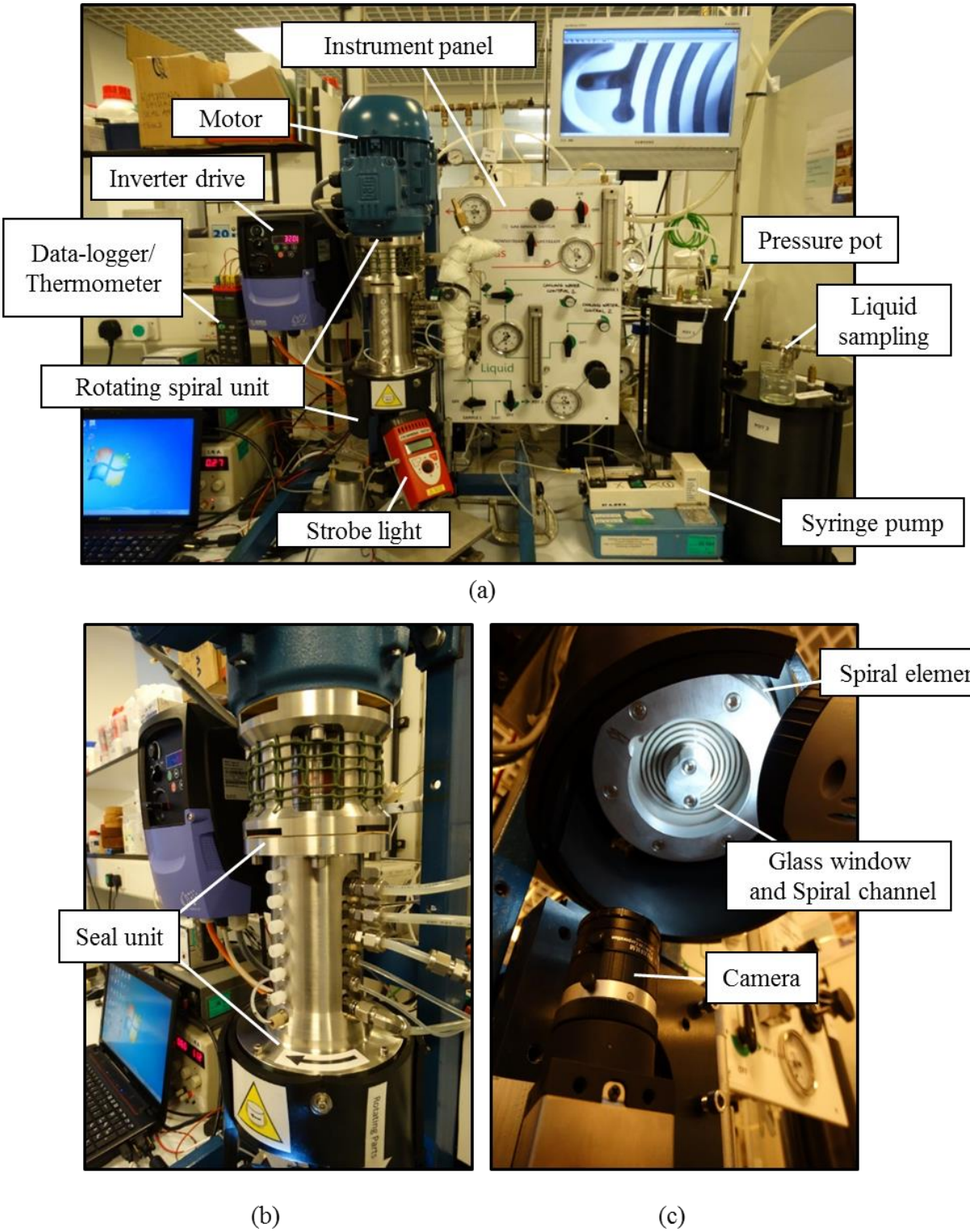

Figure 5.1. (a) The experimental apparatus, (b) rotating spiral unit showing the flow connections (six tubes connected to six ports along the right side of the seal unit) and (c) the bottom of the rotating unit showing the monitoring camera and the spiral channel covered by a toughened glass window.

5.2.1 Overall Flow Network

A schematic diagram of the overall flow network is shown in Fig. 5.2. The red and green lines are plastic tubes which are used, respectively, to transfer the air and the solution from the supply points (the beginning of lines A and B) to the rotating unit and from the rotating unit to the collection points (the end of lines C and D). The tubing diameters for the gas lines is 1/4 inch and for the liquid lines is 1/8 inch. These diameters ensure relatively minor pressure drops in these connecting tubes. Additionally, there is a cooling water flow (blue line) to remove the frictional heat generated by the seals and shaft bearings.

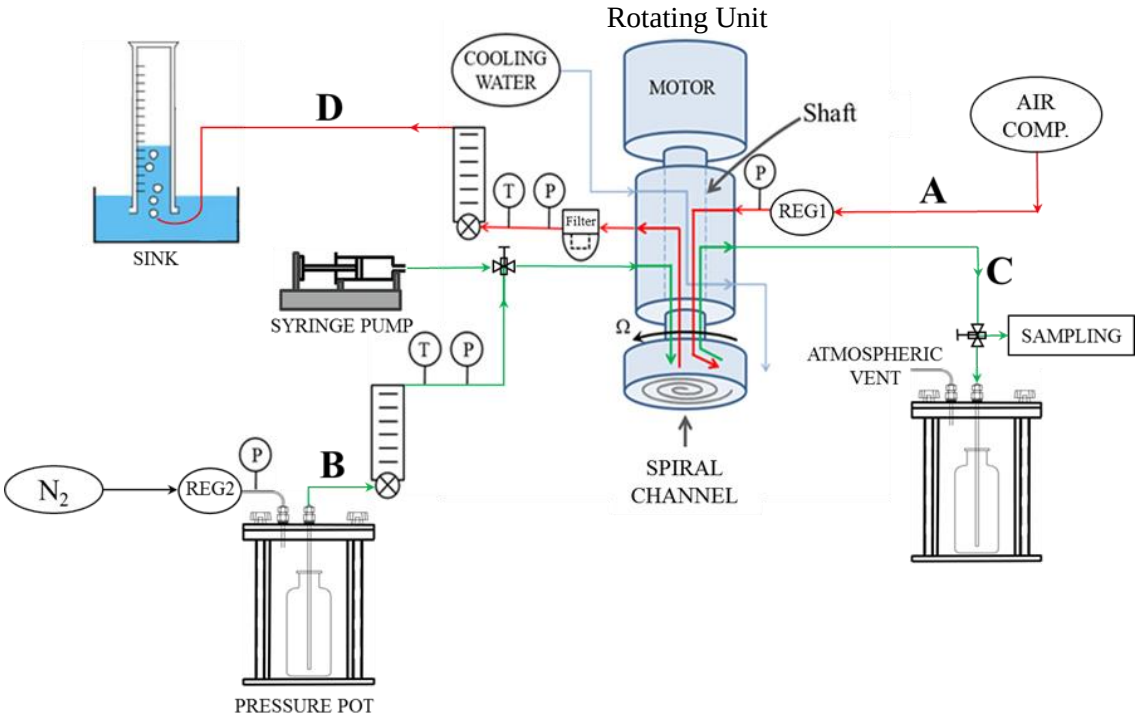

Figure 5.2. Overall flow network of the apparatus. The green and red lines are passages for the solute solution and air transport, respectively. The blue line is the cooling water passage.

In the experiments, the air (red lines) is introduced from a compressor to the rotating unit through a regulator (REG 1). This regulator allows adjusting the pressure of the inlet air so the liquid outlet is correctly balanced. Inside the rotating unit, the air flows through a rotating shaft to enter the spiral channel at its outer end. It flows through the spiral channel where counter-current contacting occurs with the solution. After that, the air

leaves the spiral from the inner end to return through the shaft, exiting from the rotating unit. Air coming out the rotating unit then flows through a filter to remove the excess liquid droplets existing in the air as a result of water vapour condensation. As a final stage, the filtered air flows through a needle valve and a variable area flow meter before ending its journey at a sink to be measured using an upturned graduated cylinder.

For the liquid phase (green line), a nitrogen-pressurised 'pot' is used followed by a rotameter with a needle valve (Vögtlin) to supply the solution to the rotating unit. Using the nitrogen is a precautionary step to reduce the risk of fire, since the four chosen solutes are flammable and present in the atmosphere of the pot at nearly the lower flammability limit (LFL) (Gibbon et al., 1994). During the operation, the pressure of the pot is fixed at 20 psig using a regulator (REG 2) and the liquid flow rate is adjusted using the rotameter needle valve. For the case of the ethanol solution, which has the lowest f' value, operating at a liquid flow rate below 1 mL/min was necessary to achieve a reasonable degree of purification ($-f'q_n > 1-d_L$). In this case, a syringe pump was employed (Razel Scientific Instruments) to feed the liquid using a 3-way valve to select between it and the pressure pot. This arrangement, i.e. the rotameter and the syringe pump, span the liquid flow rate from 0.2 mL/min to about 13 mL/min. Similar to the gas-phase, the liquid flows in the rotating unit through the shaft to reach the inner end of the spiral channel. In the spiral, the liquid flows from the inner end to the outer end counter-currently to the air, and then flows out through another 3-way valve to direct the outlet liquid stream either to a 500 mL bottle (placed in an atmospheric chamber) or to a small metal tube for sampling into a vial. It is useful to indicate here that the liquid column formed in the outlet passage between the outer end of the spiral and the atmospheric vent (line C) serves as a manometer to determine the pressure in the spiral. Details of the pressure calculation are given in Appendix B.

5.2.2 Rotating Spiral Unit

The rotating unit is the main part of the apparatus. The overall dimensions of this unit are about 20 cm in height and 10 cm in diameter. Fig. 5.3 shows a schematic section view through the unit. From the top, it consists essentially of the spiral element, an external case, rotating shaft and individual secondary parts (glass window, ball bearings, seals and lock nut).

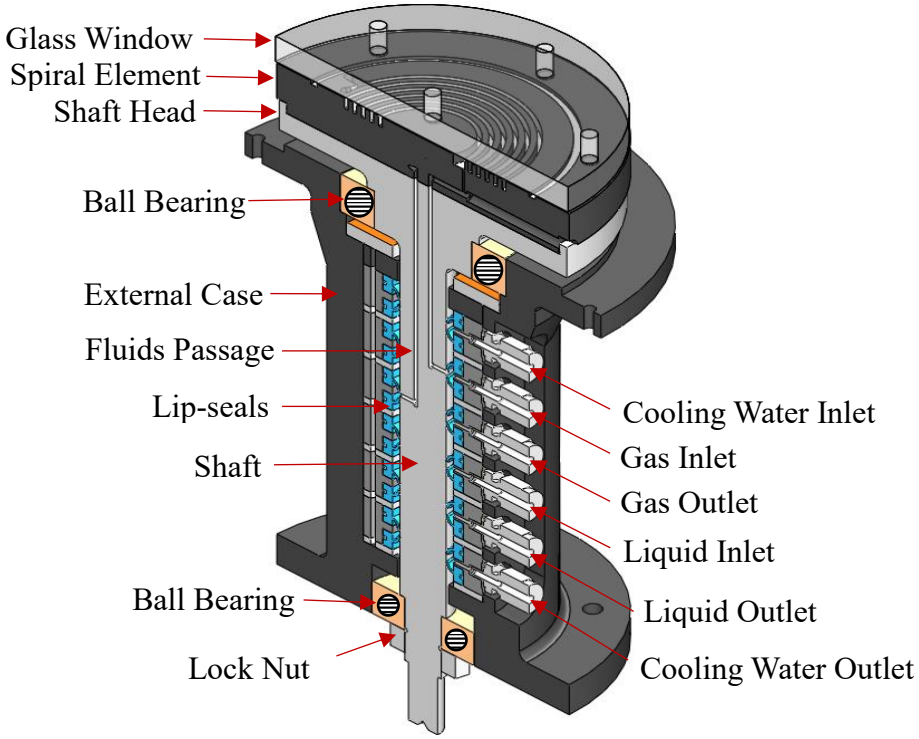

Figure 5.3. A section view showing the anatomy of the rotating unit. The unit is drawn inverted relative to its orientation in the experimental rig (Figs. 5.1 and 5.2).

The external case of the rotating spiral unit is made from 316L stainless steel. This case has six ports which are connected to external flow tubing (shown on the right hand side of Fig. 5.3), one inlet and one outlet for each of the contacting phases and for the cooling water. Because it is important to transfer the fluids reliably from the static passages to the rotating spiral channel, lip seals are used (blue-coloured parts in Fig. 5.3). These seals are made from carbon fibre-PTFE (Ceetak Sealing Solutions). Inside the case, the seals are stacked in pairs along the shaft to form six sealed chambers (annular gaps between the seals and passage holes located at the shaft circumference). The four pairs in the middle guide the contacting phases (inlet and outlet for the gas and the liquid) so that they can flow independently through passages along the shaft to the spiral element where the contacting occurs. The remaining two pairs of seals (on the top and bottom of the unit) allow continuous flow of cooling water through four cooling passages (not shown in Fig. 5.3) made along the shaft to carry away the frictional heat generated due to rotation. In this work, the spiral temperature was adjusted by varying the cooling water flow rate and determined indirectly using the method described in MacInnes and Zambri (2015). A brief detail of the method is presented in Appendix B.

Fig. 5.4 shows three pairs of seals and the described fluid transfer arrangement. As one can see, each pair is formed by installing two seals in a T-section metal holder. To clamp the seals in the holder, spacing washers are placed between the seal pairs. Each washer has a groove to provide a passage for liquid leaking from the seal to drain. In general, there is no evidence of water leakage during operation. For the gas phase, a pressure test is made regularly after each experiment to check the seal conditions by quantifying the rate of gas leakage. This is made by filling the gas passage by a pressurised air. For functional seals, the gas leakage rate is typically less than a few percent of the lowest gas flow rate used in this work.

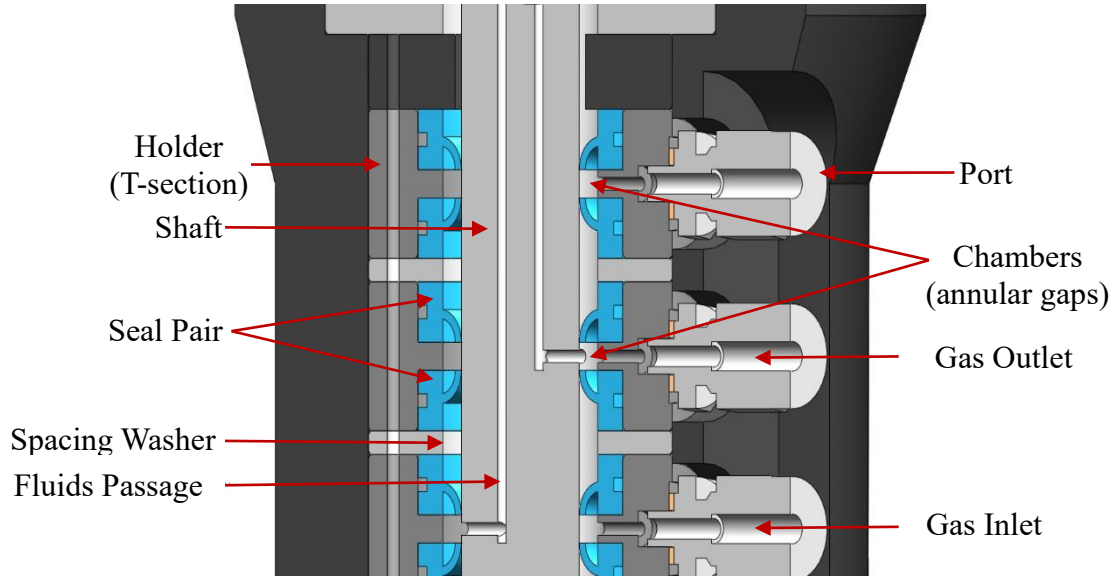

Figure 5.4. Close-up section from Fig. 5.3 showing the relationship between the shaft passage, the lip-seal pairs and the connection fittings.

It is clear from Figs. 5.3 and 5.4 that the shaft is a key link between the seal unit and the spiral element. The shaft is made from 316L stainless steel and fixed inside the case by two ball bearings (located top and bottom) supported by a lock nut to prevent vertical movement during operation, as shown in Fig. 5.3. One of the important design parameters of the shaft is the external surface since it affects directly the sealing performance. In this work, this part of the shaft has been improved in relation to that used in MacInnes and Zambri (2015). Rather than hardening the shaft by treating the native metal, here the external surface was coated by tungsten carbide layer to a thickness of about 100 μm (Engineering Performance Coatings).

5.2.2.1 Spiral-channel Element

The passages in the shaft transfer the contacting phases to and from the spiral element, as shown in Fig. 5.3. In the element, the two phases are brought together in a single spiral channel to establish the rotating spiral contacting. The element is fabricated from polyether ether ketone (PEEK) which has excellent chemical resistance and mechanical properties. Also, it is one of the most thermally stable polymers (Patel et al., 2010). This ensures the stability of the element structure during the operation over the temperature range of interest.

The underside of the element is shown in Fig. 5.5 where the spiral channel can be seen. This channel is formed by milling the PEEK surface using a computer-controlled milling machine, yielding a channel 1.5 mm height (h), 4 mm depth (W) and 910 mm long (L). The spiral path is an Archimedean spiral with a fixed distance between adjacent revolutions of 2 mm, giving $R\sin\alpha = 5.57 \times 10^{-4}$ m. In the experiments, the spiral channel was covered with a toughened glass window (10 mm thick) which allowed an optical access and served as a seal between the channel revolutions (Fig. 5.5). So the fluids in the spiral channel were in contact with PEEK (from three sides) and the glass window (underside).

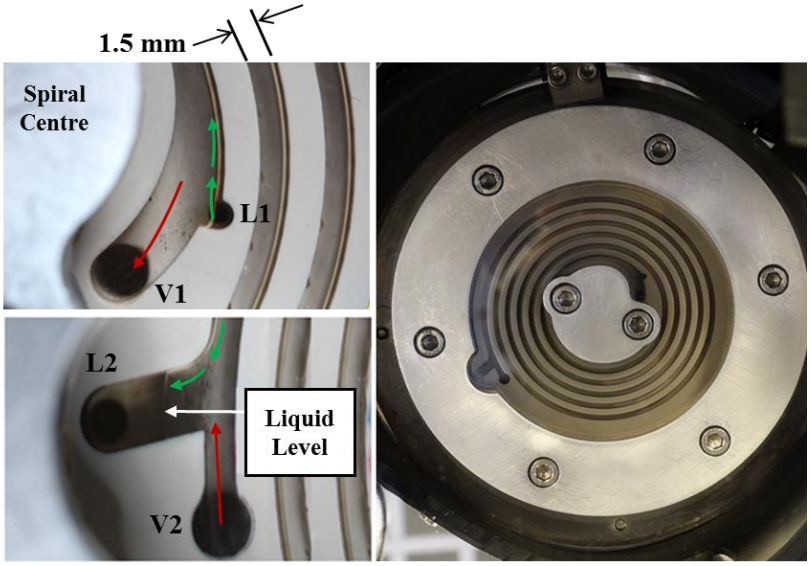

Figure 5.5. Underside of the spiral element showing the outer and the inner ends of the channel and the flow direction of the contacting phases. The green and red arrows represent the liquid solution and air, respectively. The reservoir at the outer end (L2) shows the typical liquid level formed during operation.

The contacting phases transfer to and from the spiral element and hence the spiral channel through 4 holes in the shaft head (two inlets and two outlets). Because the element is clamped firmly to the shaft head, the phases transfer directly from these holes to four radial passages incorporated inside the element. These radial passages, in turn, guide the phases to and from the inner and outer ends of the spiral channel (L1, L2, V1, and V2 in Fig. 5.5). The liquid phase is fed from the inner hole of the spiral (L1) which is near to the centre, leaving the spiral at L2, whereas the gas is introduced from the outer end of the channel (V2), coming out from V1. In this way, counter-current contacting in the rotating spiral channel was established.

5.3 Operational Considerations

Having described the main components of the rotating spiral unit, the operational considerations can be discussed now. These are the thermal steady-state of the rotating unit and the balance of the pressure at the outer end of the spiral channel between the inlet gas phase (V2 in Fig. 5.5) and the outlet liquid phase (L2).

5.3.1 Thermal Steady-State of the Rotating Unit

As described previously and shown in Fig. 5.3, ball bearings are used in the rotating unit to support the shaft rotating mechanism. The heat generated from these bearings under rotation is significant and can transfer through the systems, reaching the spiral channel where the two phases contact. Moreover, the seals are additional sources of heat generation and can augment the amount of heat transferred to the system. Such frictional heat generation due to rotation needs a period of time to propagate through the rotating unit (in which the spiral is placed) such that a uniform temperature distribution is reached. Any measurements should be avoided until reaching this case of thermal steady-state otherwise the contacting will be tested under transient conditions, which is not within the scope of this work. Establishing a steady thermal condition was achieved by monitoring the lower bearing temperature since it is the main source of heat and the nearest to the spiral channel region (Fig. 5.3). The measurement was made using a thermocouple inserted in the rotating unit with the sensing tip about 2 mm from the bearing. A reading was taken every minute using data logging (HH309A, Omega Engineering) from the start of the rotation until the end of each experiment. A typical variation of the bearing temperature (T_b) over time is shown in Fig. 5.6 for two different cooling-water flow rates.

As one can see in Fig. 5.6, the temperature started rising rapidly just beyond t = 0 and reached a roughly steady level after about 45 min. This steady state prevailed until the end of the experiment with about 2 °C rms (root mean square) deviation in temperature. Such deviation is expected since in each experiment a wide range of phase flow rates is tested and that could disturb the thermal equilibrium due to introducing the new flow rates. Thus, one should expect that the effective temperature on the spiral for each single test may differ by a couple of degrees or less. However, accepting the uncertainties introduced by these fluctuations reduces the experimental time considerably since it is not necessary to wait for 45 min after every single change made in the phase flow rates during the experiment. Further, the current apparatus does not allow for easy temperature control. Therefore, small temperature adjustments after changing the phase flow rates is not expected to be a practical approach. According to that, t > 45 min is taken as a safe rule to ensure that the rotating unit is thermally stable and ready to start the experiments and take the measurements.

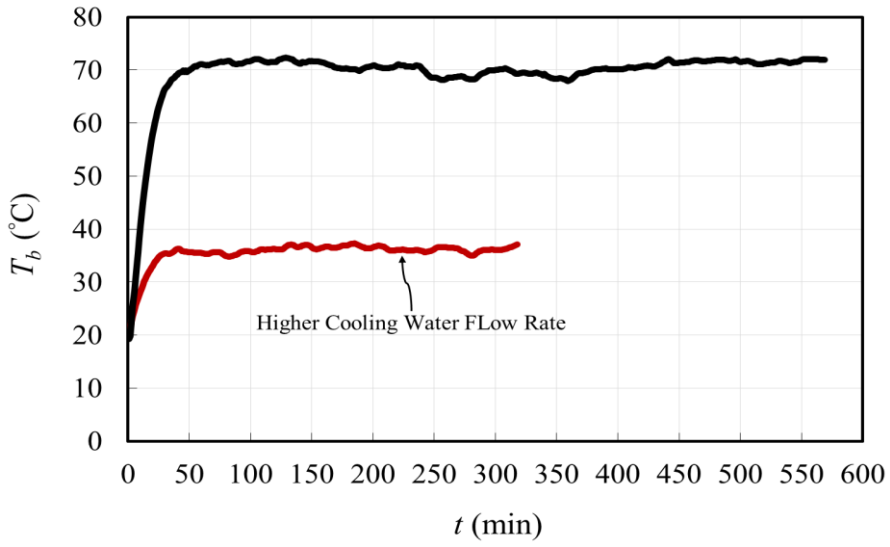

Figure 5.6. Bearing temperatures recorded at two different cooling-water flow rates.

5.3.2 Pressure Balance

To establish the situation where the two phases flow counter-currently side by side inside the spiral channel, balancing the pressure at the spiral reservoir between the inlet gas and the outlet liquid is essential. This is achieved by adjusting the inlet gas pressure so that it balances the level of the hydrostatic pressure gained by the liquid phase ($1/2\,\rho_L R^2\Omega^2$), which dictates the pressure at the spiral outer end. The level of the liquid

in the spiral reservoir is employed as an indicator to balance the pressure. When the pressure of the gas becomes greater than that of the liquid phase, the level of the liquid in the reservoir decreases, eventually allowing the gas phase to flow in the outlet pathway of the liquid phase, as shown in Fig. 5.7 a. On the other hand, when the hydrostatic pressure exceeds the pressure of the inlet gas phase, the liquid overflows from the reservoir, occupying a part of the inlet gas phase pathway (Fig. 5.7 b). In this case, pre-contacting occurs outside the spiral channel. As a consequence, the entering gas is not free of solute which reduces the purification as illustrated in Fig. 3.6 in Chapter 3. Thus, in practice, once the level of the rotation rate has been decided, that determines the amount of the hydrostatic pressure, balancing the pressure is then just a matter of adjusting the inlet gas pressure such that the level of the liquid phase is fixed at a specific position within the reservoir. Fig. 5.7 c shows the intended situation and the other cases where $P_{air} > P_{Liquid}$ and $P_{air} < P_{Liquid}$.

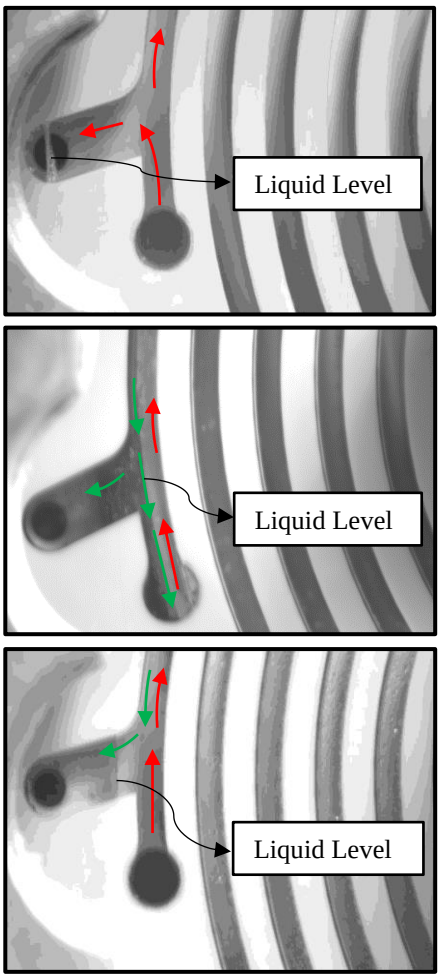

(a) This is the case when $P_{air} > P_{Liquid}$. The level of the liquid will drop and the gas phase flows through the liquid passage (red arrows).

(b) When $P_{air} < P_{Liquid}$, the liquid will overflow from the reservoir and pre-contacting will occur (green arrows).

(c) This is a typical case when $P_{air} = P_{Liquid}$. The level of the liquid is fixed in the outer reservoir and the phases flow counter-currently.

Figure 5.7. Three different cases demonstrate the pressure balance in the outer end of the spiral.

5.4 Experimental Measurements

The quantities needed from each experiment to calculate the mass transfer parameters ($K_L a$, Φ_L and Φ_{LN} outlined in Chapter 3) are the phase flow rates on the spiral (Q_V and Q_L) and the inlet and outlet solute mole fractions for the gas phase and the liquid phase. Also, there are other parameters are needed such as the spiral temperature and pressure to determine f' and the other physical properties. To find these essential quantities, three measurements were made experimentally in addition to the temperature and pressure of the contacting. These are the outlet volumetric gas flow rate, outlet liquid flow rate and the outlet solute mole fraction in the liquid phase, shown as red symbols in Fig. 5.8 below.

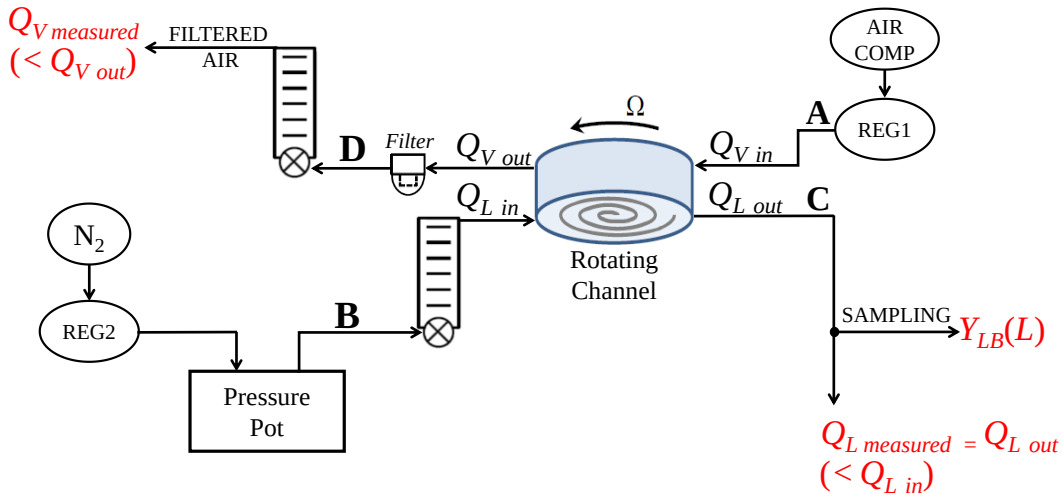

Figure 5.8. A simplified flow diagram of Fig. 5.2 showing the measured quantities.

To translate the measured phase flow rates into those on the spiral and to collect valid samples at the liquid outlet, i.e. $Y_{LB}(L)$, there are some issues that need to be taken into account. For example, throughout the contacting process water evaporation can occur. As a consequence, the measured phase flow rates for some cases can be appreciably underestimated than those on the spiral if they are not corrected for water content. Further, different phase flow rate ratios are tested in a single run. Any adjustment made requires to make sure that the samples have been collected at the end of line C (Fig. 5.8) only after reaching steady-state conditions. In practice, there are two steps in ensuring the establishment of a steady-state condition. First, monitoring the bearing temperatures of the rotating unit to make sure that the apparatus comes thermally to a steady condition. This has been discussed in the previous section and the results show that changing the

flow rate has negligible effect on the apparatus thermal status. Second, waiting enough time for the flow and the concentration field in the spiral and the passages leading to the sampling point (line C) to reach a steady condition for given phase flow rates.

In this work, a simplified evaporation model and an experimental procedure are developed to address the issues discussed above since they affect directly the phase flow rates on the spiral and the measured solute mole fractions at the liquid outlet. These measures are discussed in detail within the relevant subsections below where the experimental measurements are described. As pointed out previously, the determination the spiral pressure and temperature is given in Appendix B. This left the determination of phase flow rates and solute concentrations and these are discussed below.

5.4.1 Flow Rate Measurements

As shown in Fig. 5.8, the gas and liquid phase flow rates are measured during the experiments at the end of downstream passages (the end of line C and D for the liquid and the gas, respectively). Since air is weakly soluble in water (Sander, 2015) and is essentially filtered at the end of line D, a water displacement method was used to determine the gas flow rate. This was made by timed collection of the outlet gas volume in an upturned graduated cylinder immersed in a sink of water. The conditions where the gas was collected were within a few percent of 20 °C (laboratory ambient) and atmospheric pressure (the liquid level in the cylinder is just few centimetres above the sink level). In this way, the gas flow rates were documented at normal conditions. The measurements taken for all the experiments conducted are presented chronologically in Fig. 5.9 where rms is about 1% for the average flow rate values of 1.3, 3 and 6.2 NL/min.

For the liquid phase, four different aqueous solutions (ethanol, acetonitrile, acetone and MEK) were tested. These solutions have different viscosities even they are intended to be at dilute levels. For example, the 5% ethanol solution tested is about 20% more viscous than the other solutions (Khattab et al., 2012). For this reason, the liquid rotameter installed at the upstream passage (line B in Fig. 5.8) was employed as an indicator rather than a measuring tool and the flow rates were measured directly at the outlet. The measurements were carried out by collecting liquid mass for a measured time. The collected mass was then converted to a volumetric flow rate using water density estimated from a correlation at the ambient temperature (White, 2008). This approach was used for all the studied systems. However, some tests for ethanol systems, as

mentioned, have been carried out using a syringe pump to deliver flow rates below 1 mL/min. Such flow rates are dictated by the small value of f' for these particular systems (f' = 0.232 and 0.651) to achieve a practical degree of purification. In this case, the flow rate delivered by the pump was determined simply by adjusting the pump driver speed and knowing the syringe size to determine the flow area. At the same time, the flow rate delivered by the pump was also measured downstream by collecting mass in a measured time. This helps in evaluating the amount of water lost on the spiral due to evaporation as will be seen in the next section.

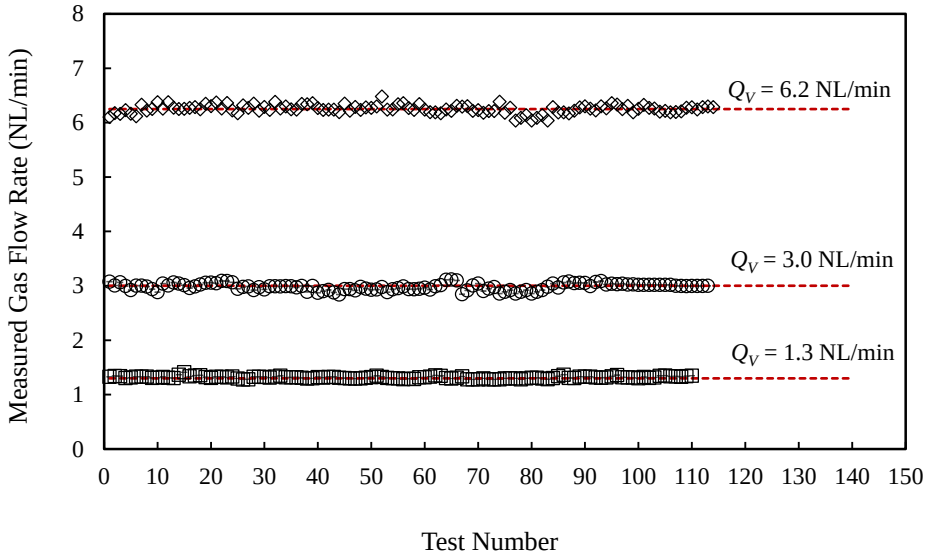

Figure 5.9. Gas flow rate measurements.

5.4.1.1 Simplified Evaporation Model

On the spiral, water evaporation can occur simultaneously with the solute transport since the air used in the experiments is dry (supplied by a compressor). The implication is that the phase flow rates measured can be underestimated than the actual flow rates on the spiral (Fig. 5.8). Evaluating the effect of evaporation is possible by approximating that the gas is fully saturated with water both at the exit from the spiral (at the spiral temperature) and at the collection point (at the ambient temperature). Based on this approximation, a simplified model was developed. The model has two purposes: first to evaluate the effect of water evaporation in general and second to estimate the phase flow rates on the spiral.

The approximate physical picture of water evaporation on the spiral is depicted schematically in Fig. 5.10. The liquid phase is introduced into the spiral channel at $Q_{L\,in}$ and leaves at a lower flow rate ($Q_{L\,out}$) due to the water evaporation ($\dot{n}_W$). On the other hand, dry air enters the spiral coming from a compressor at $Q_{V\,in}$. On the spiral, the air flows side by side with the liquid phase, leaving the spiral fully saturated with water vapour ($Q_{V\,out}$) at the spiral temperature and pressure. The outlet gas then flows through the shaft, coming out from the rotating unit to pass through the filter. Throughout this distance, the gas phase will be dominated by the ambient temperature, causing a water vapour condensation ($\dot{n}_{WM}$) due to changing the gas conditions. This condensation continues until the gas phase reaches to the sink where it is collected and measured at normal conditions (1 bar and 20 °C).

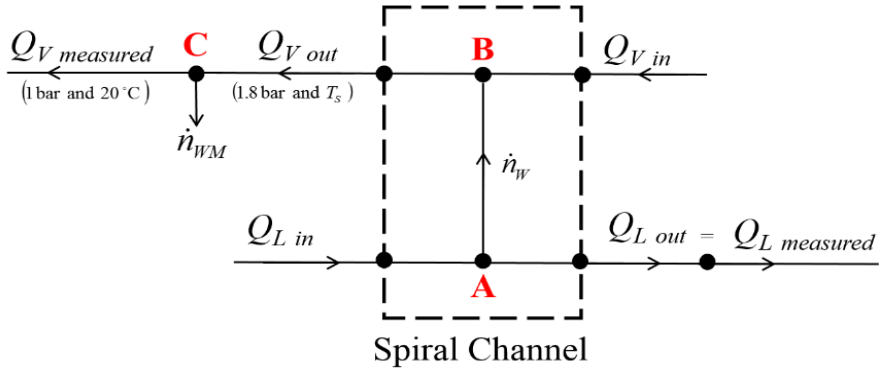

Figure 5.10. A schematic diagram of water evaporation where $\dot{n}_W$ is the amount of water evaporated on the spiral and $\dot{n}_{WM}$ is the total amount of water lost from the outlet gas phase due to condensation, from leaving the spiral channel until being collected and measured at the sink.

At spiral conditions, the water mole fraction in the gas phase (Y_{WV}), which is approximated to be in equilibrium with the solution (water and solute), can be determined reliably using Raoult's law (Smith et al., 2005):

$$Y_{WV} = \frac{P^{\text{sat}}}{P_S} Y_{WL} \tag{5.3}$$

where Y_{WL} is the water mole fraction in the liquid phase, P^{sat} is the vapour pressure and P_S is the spiral pressure.

For a dilute solute, $Y_{WL} \approx 1$ and Eq. 5.3 is reduced to:

$$Y_{WV} = \frac{P^{sat}}{P_S} \tag{5.4}$$

In Eq. 5.4, the water vapour pressure can be calculated at the spiral temperatures using Antoine equation (Smith et al., 2005) while the spiral pressure (P_S) is fixed at 1.8 bara. These conditions give a water vapour content (mole fraction) of 0.0167, 0.025 and 0.065 for a gas leaving the spiral at temperatures of 24, 30, 49 °C, respectively. The predicted mole fractions can be used to quantify the effect of evaporation by making a mole balance using the notation in Fig. 5.10. Thus, a balance on the water without solute (since it is dilute) in the spiral channel gives:

For the liquid phase: $$n_L Q_{L\,in} = n_L Q_{L\,out} + \dot{n}_W \tag{5.5}$$

For the gas phase: $$n_V Q_{V\,out} Y_{WV} = \dot{n}_W \tag{5.6}$$

where $\dot{n}_W$ is the total molar flow rate of water evaporated along the spiral and n_V and n_L are the molar densities of the gas and the liquid phase, respectively.

From Eqs. 5.5 and 5.6, the water volumetric flow rate can be determined in terms of the water mole fraction in the gas phase, phase flow rates and molar densities:

$$Q_{L\,in} - Q_{L\,out} = \frac{n_V Q_{V\,out} Y_{WV}}{n_L} \tag{5.7}$$

To give a sense of the amount of water evaporated with respect to the liquid flow rate fed to the spiral, Eq. 5.7 is normalised by the inlet liquid flow rate ($Q_{L\,in}$):

$$\frac{Q_{L\,in} - Q_{L\,out}}{Q_{L\,in}} = \frac{\Delta Q_L}{Q_{L\,in}} = \frac{n_V Q_{V\,out}\, Y_{WV}}{n_L Q_{L\,in}} \tag{5.8}$$

Now, it is clear from Eq. 5.8 that the amount of water evaporated in relation to the inlet liquid flow rate is a function of temperature (implied in Y_{WV}) and the phase flow rates for given spiral pressure and phase densities. This equation represents the change in the liquid phase flow rate along the spiral channel and can be used to give a rough estimate of how the evaporation affects the liquid flow rate. Fig. 5.11 shows the results of Eq. 5.8 for air-water system, using the three gas flow rates used in the experiments (1.3, 3 and 6.2 NL/min) and liquid flow rates from 0.1 to 100 mL/min, at the three different spiral temperatures (Table 5.1).

As shown in Fig. 5.11, the change in liquid flow rate due to water evaporation is significant at the small liquid flow rate. This suggests that the studied systems with low f' are the most affected by evaporation, since it is necessary for these systems to operate at a low liquid flow rate to achieve a practical degree of purification. But the effect of evaporation is minor for the systems with large f' since it allows a large liquid flow rate to be tested. Accordingly, the ethanol systems are the most affected by evaporation (f' = 0.232 and 0.651), whereas for the acetone and MEK systems (f' = 3.83 and 5.5, respectively) the effect is lower. Also, it is clear that at a given gas and liquid flow rate the fraction of water evaporated increases as the spiral temperature increases. Thus, for acetone system at 24 °C, the evaporation has a less effect on the liquid phase flow rate relative to the other systems and is expected to be minor since the range of liquid flow used to test this system is between 1 to 10 mL/min.

Additionally, the model results are compared to experimental measurements for the case of syringe pump feeding, which was used for f' = 0.232 and 0.651 systems. In this case, $Q_{L\,in}$ was determined from the pump speed and syringe size and $Q_{L\,out}$ was measured by collecting mass in a specific time period. Form these values, the amount of water evaporated was determined experimentally at the three gas flow rates and compared to the model results to check its reliability, as shown in Fig. 5.11. It is clear from the figure that there is a scatter in the experimental measurements (symbols) in general. This scatter could be attributed to the fact that the effective temperature on the spiral may have been lower or higher than the values used in the evaporation model. This is consistent with the variations in the bearing temperature measurements noticed in Fig. 5.6. Regardless of the scatter, however, there is an obvious agreement between the model predictions and the data. This gives a support for the validity of approximating that the gas leaves the spiral fully saturated and suggests that the model can be used to quantify the amount of water evaporated under these conditions.

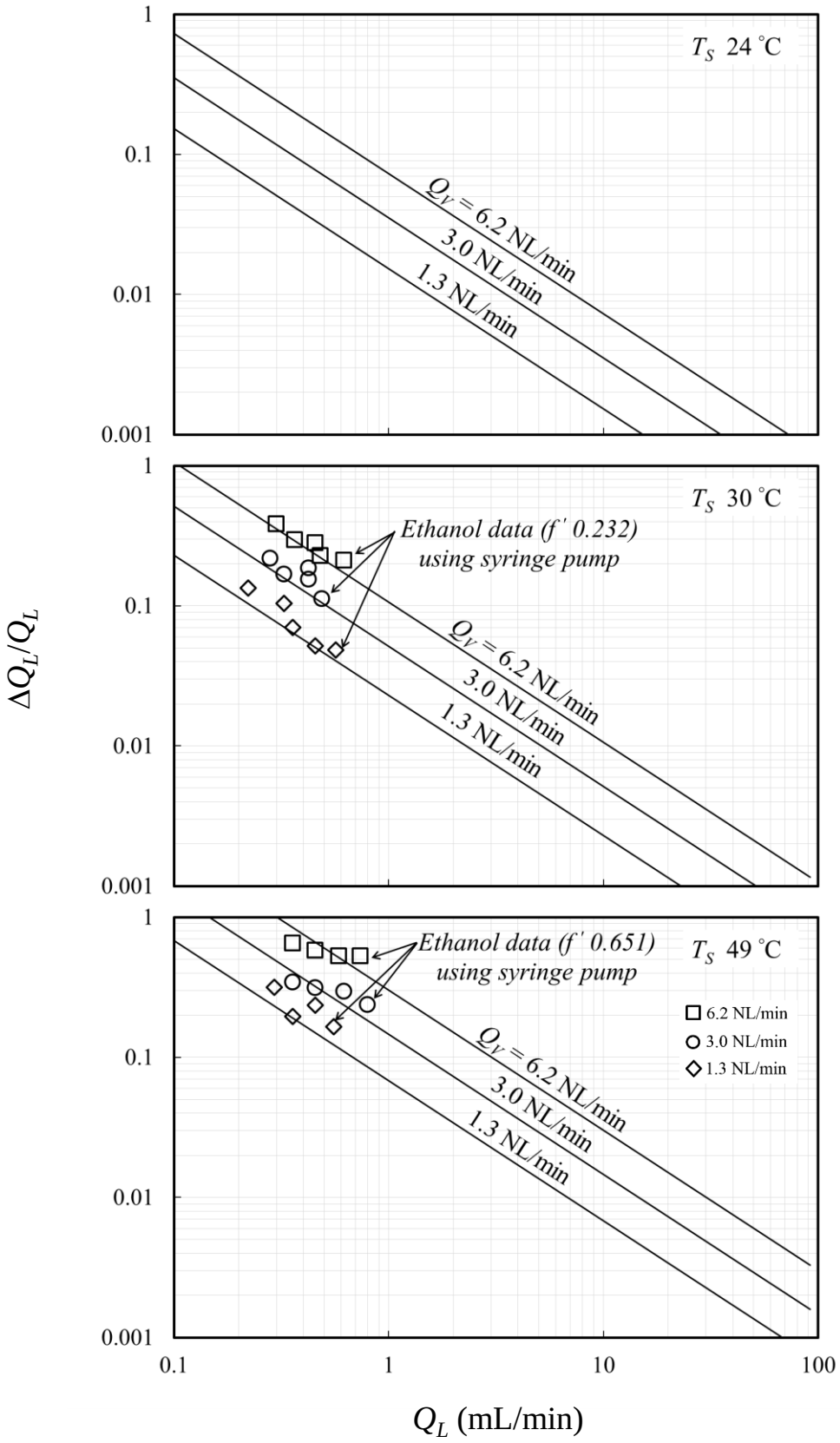

Figure 5.11. Measured (symbols) and predicted (lines) amount of water evaporated on the spiral over different spiral temperatures and phase flow rates.

5.4.1.2 Spiral Inlet and Outlet Flow Rates

To this point, the above model helps in evaluating the effect of water evaporation on the liquid flow rate and can be used also to quantify the inlet liquid flow rate ($Q_{L\,in}$ in Fig. 5.10) and the inlet and outlet gas flow rate ($Q_{V\,in}$ and $Q_{V\,out}$) from the measured quantities. According to Fig. 5.10, $Q_{V\,out}$ can be calculated by making an overall material balance around node C:

$$n_V Q_{V\,out} = n_{VN} Q_{V\,measured} + \dot{n}_{MW} \tag{5.9}$$

where n_V and n_{VN} are the molar densities at the spiral exit and at the collection point (sink), respectively. $\dot{n}_{WM}$ is the total amount of water condensed due to changing the saturation conditions from those on the spiral (1.8 bara and T_S) to normal conditions (1 bar and 20 °C) at the collection point. Saturation at the collection point is ensured by making line D (Fig. 5.8) sufficiently long to reach ambient temperature.

$\dot{n}_{WM}$ in Eq. 5.9 can be found by making a material balance on the water around node C,

$$\dot{n}_{WM} = Y_{WV} n_V Q_{V\,out} - Y_{WN} n_{VN} Q_{V\,measured} \tag{5.10}$$

where Y_{WV} and Y_{WN} are the water mole fractions in the gas phase at the spiral and normal conditions, respectively, and can be estimated using Raoult's law (Eq. 5.4).

Now, substituting Eq. 5.10 in Eq. 5.9 gives $Q_{V\,out}$ as:

$$Q_{V\,out} = \frac{n_{VN}}{n_V} \frac{(1-Y_{WN})}{(1-Y_{WV})} Q_{V\,measured} \tag{5.11}$$

The change in the gas phase flow rate along the spiral due to water evaporation can also be determined:

$$\frac{Q_{V\,out} - Q_{V\,in}}{Q_{V\,out}} = Y_{WV} \tag{5.12}$$

Form $Q_{V\,out}$ (Eq. 5.11), the inlet liquid flow rate ($Q_{L\,in}$) can be calculated using Eq. 5.7 where $Q_{L\,out}$ is the same as the liquid flow rate measured downstream. Accordingly, Eq. 5.7 can be re-expressed in terms of the measured liquid flow rate as:

$$Q_{L\,in} = Q_{L\,measured} + \frac{n_V Q_{V\,out} Y_{WV}}{n_L} \tag{5.13}$$

5.4.1.3 Effect of Solute Transfer

Despite the solute concentrations used in the experiments are intended to be at dilute levels, its transfer might change the phase flow rates. This change can be estimated approximately by a solute mole balance using the schematic diagram shown in Fig. 5.12. So a mole balance at node A gives:

$$\text{Overall:} \quad n_L Q_{L\,in} = \dot{n}_S + n_L Q_{L\,out} \tag{5.14}$$

$$\text{Solute:} \quad n_L Q_{L\,in} Y_{LB}(0) = \dot{n}_S + n_L Q_{L\,out} Y_{LB}(L) \tag{5.15}$$

where $Y_{LB}(0)$ is the inlet solute mole fractions as given in Table 5.1 and $Y_{LB}(L)$ is the outlet solute mole fraction measured for each experiment, as described in Section 5.4.2. $\dot{n}_S$ is the total amount of solute transferred along the spiral.

From Eqs. 5.14 and 5.15, one can find the change in the liquid flow rate due to solute transfer,

$$\frac{Q_{L\,in} - Q_{L\,out}}{Q_{L\,in}} = \frac{Y_{LB}(0) - Y_{LB}(L)}{1 - Y_{LB}(L)} \tag{5.16}$$

Similarly, the change in the gas phase flow rate can be found by making an overall balance at node B and using Eq. 5.14 to eliminate $\dot{n}_S$:

$$\frac{Q_{V\,out} - Q_{V\,in}}{Q_{V\,out}} = \frac{n_L Q_{L\,in}}{n_V Q_{V\,out}} \left(\frac{Y_{LB}(0) - Y_{LB}(L)}{1 - Y_{LB}(L)} \right) \tag{5.17}$$

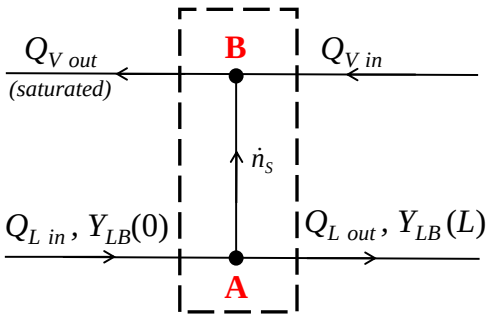

Figure 5.12. Diagram showing the change in the phase flow rate due to solute transfer where $\dot{n}_S$ is the total amount of solute transferred along the spiral.

5.4.1.4 Spiral Flow Rates

The flow of the phases changes with distance along the spiral channel due to both solute transfer and water evaporation. Calculations using Eqs. 5.16 and 5.17 show that the change in the flow rate associated with solute transfer for either phase remains less than 7%. The effect of water evaporation is also generally small. For the gas phase, the largest change is less than 7% (Eq. 5.12) at the highest operating temperature (49 °C). For the liquid flow rate, however, the relative change could be very large at low liquid flow rates (as shown in Fig. 5.11). In general, results with considerable change are excluded from the final data based on a sensitivity analysis. This analysis was made using the mass transfer relation (Eq. 3.32) to determine the change in the mass transfer coefficient due to uncertainties in the measurements of flow rates. Further, the same relation was used to quantify the effect of uncertainties in the solute concentration measurements (discussed in the next section) and the liquid phase molar density. The transfer of the solute along the channel changes the mean molecular mass of the liquid phase and hence the liquid phase molar density which appears explicitly in Eq. 3.32. Appendix C gives the details of this sensitivity analysis and shows the change in $K_L a$ with the measurements uncertainties.

As discussed in Chapter 3, the mass transfer coefficient relation (Eq. 3.32) was derived based on assuming constant flow rates and properties. To avoid bias in calculating $K_L a$, the flow rate values were taken as the average of the inlet and outlet values for each phase. Also, the liquid molar density was taken as constant and equal to the average of the inlet and outlet values.

5.4.2 Composition Measurement

The other bulk quantities required to quantify the experimental mass transfer coefficient (Eq. 3.32) are the inlet and outlet solute mole fractions in the gas and the liquid phase. For all the experiments, the inlet air stream was solute-free. The composition of the feed solution was prepared using high purity raw materials and deionised water (the specifications of these materials are given in Appendix D). This means that the inlet solute mole fraction of the gas phase and the liquid phase are known for each test. This left only the task of measuring the outlet solution composition, $Y_{LB}(L)$, to complete the required solute mole fraction information since the outlet gas phase composition can be

determined directly from the overall balance. Measuring the outlet solute mole fraction in the liquid phase was made carefully through two essential steps: (a) sampling and (b) composition analysis.

5.4.2.1 Sampling of the Outlet Liquid Phase

For each phase and solute system, different phase flow rate ratios were tested in a single run. Any changes in the contacting conditions result in changes in the flow and concentration field in the spiral and the liquid downstream passage (line C in Fig. 5.8) leading to the sampling point. Therefore, sampling should be avoided until the flow and concentration field in the spiral and downstream passage have reached a steady-state condition. The concept of steady state is relatively simple: wait the time required for the spiral fields to become steady and for the liquid in the downstream passage to come to the spiral outlet concentration. Fig. 5.13 shows an example of a chromatography result of ethanol solution samples collected over time after a change was made in the spiral condition.

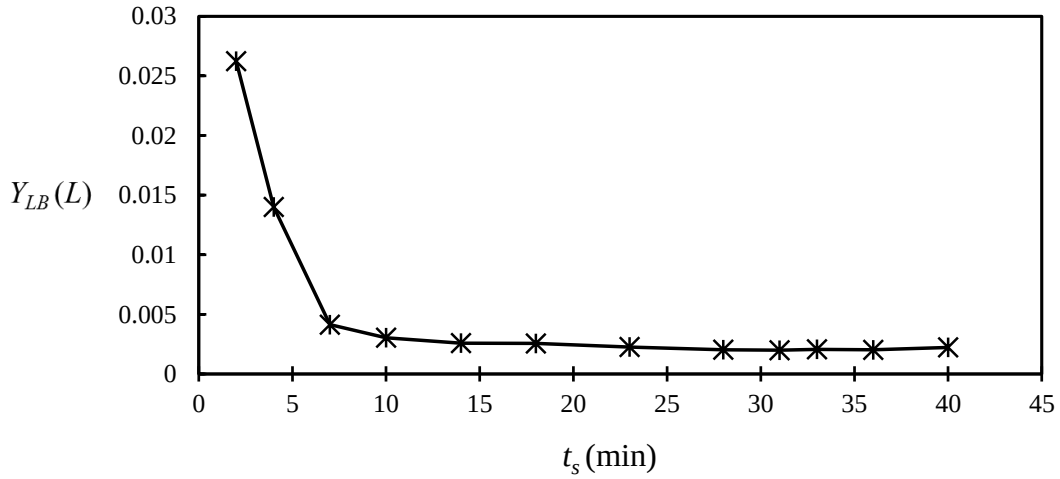

Figure 5.13. Transient of ethanol concentration (mole fraction) measured after changing the liquid flow rate from 2.3 to 0.37 mL/min at a constant gas flow rate (3 NL/min).

In principle, the clearing of the downstream passage after any change made in the spiral condition takes place first in the core of the passage where the fluid velocity is the highest and last at the channel wall where the velocity approaches zero (the clearance occurs by diffusion out into the moving fluid). The consequence is that much of the pre-existing fluid in the passage is cleared out rapidly, but the fluid near the walls takes a long

time to clear. Thus, the rapid decrease in the concentration observed in Fig. 5.13 (t_S < 10 min) probably corresponds to the fast fluid at core of the passage while the long tail (i.e. t_S >10 min) corresponds to the fluid near the walls. In practice then, the mean residence time is a key parameter to determine the total time required to collect a valid sample (Levenspiel, 1999). It has been noticed that the higher the liquid flow rate (which corresponds to a lower residence time) the shorter the transient period (sample time) is. Based on this concept, an experimental procedure was developed to determine the minimum sample time to collect a valid sample for a given flow rate. For each phase and solute system, stimulus-response experiments were carried out by making a sharp change in the spiral conditions (e.g. changing the liquid flow rate from 10 mL/min to 1 mL/min) and collecting samples over time from the start of the change and measuring them. In the experiments, the liquid phase residence time (t_{mL}) is found directly from the liquid flow rate (Q_L) which is measured during the test and the total volume of liquid passage (V_L) which is fixed, thus:

$$t_{mL} = \frac{V_L}{Q_L} \tag{5.18}$$

To represent the transient data collected for the studied systems in a single plot and find the minimum sample time at different conditions, the time is expressed in terms of the mean residence time (see Eq. 5.19). Also, the concentration scale is changed such that the steady state concentration corresponds to 1. This is done by normalising the measured concentration, $Y_{LB}(t)$, using the concentration before the change (Y_{LB} at t_0) and that after reaching steady state (Y_{LB} at t_f), thus:

$$t^*_{mL} = \frac{Q_L}{V_L} t_S \tag{5.19}$$

$$Y^*_{LB} = \frac{Y_{LB}(t) - Y_{LB}(t_0)}{Y_{LB}(t_f) - Y_{LB}(t_0)} \tag{5.20}$$

Using this normalisation, data collected can be plotted in a single plot, as shown Fig. 5.14. It is obvious from this figure that the concentration transients collapse reasonably well at t^*_{mL} > 12 where Y^*_{LB} = 1 corresponds to the steady state condition. This suggests that beyond t^*_{mL} = 12 should be a safe rule to collect valid samples. Accordingly, one can conclude from Eq. 5.19 that for all cases the minimum sample time for a given

flow rate must be:

$$t_S > 12V_L/Q_L \qquad (5.21)$$

where V_L is fixed and equals 1.6 mL and Q_L is a measured quantity during the tests.

Eq. 5.21 was used throughout all experiments as a rule to collect valid samples. At each new adjusted condition, Q_L was measured first and then t_S (from Eq. 5.21) was calculated to determine the minimum time to reach steady state conditions and hence a sample could be collected and measured.

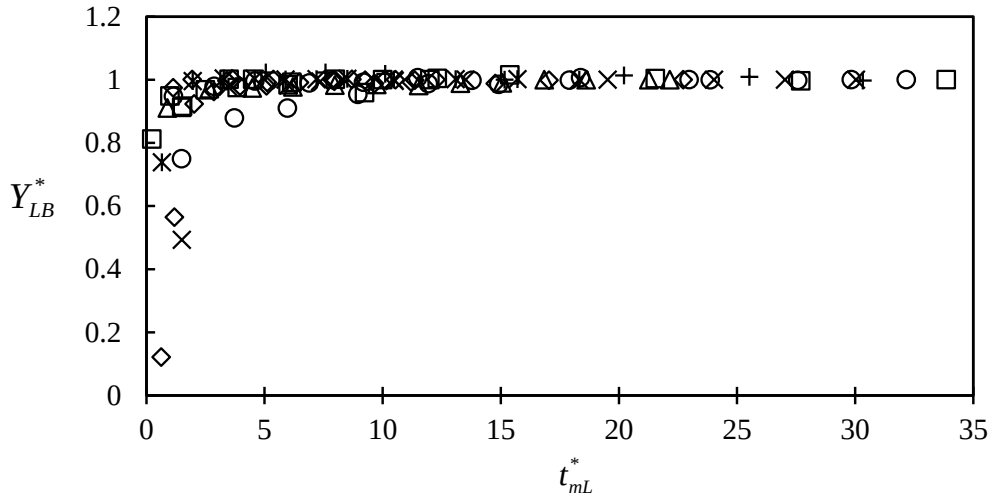

Figure 5.14. The transient experiments carried out separately for the selected phase and solute systems (ethanol, acetonitrile, acetone and MEK) by changing Q_L from approximately 10 mL/min to about 1 mL/min (except ethanol to less than 1 mL/min) and over the three gas flow rates (1.3, 3 and 6.2 NL/min).

For each flow rate ratio tested, at least two samples of the outlet liquid were collected using vials (Sigma-Aldrich) with sealed caps (caps with silicon/PTFE septa). The volume of the vials used ranged between 1-3 mL, depending on the analysis method requirement. To avoid losing solute to the atmosphere during the sampling process, the sampling outlet (a steel tube) was immersed in the already collected liquid and was not removed until the vial was completely filled. Further, as a precautionary step, all samples were analysed immediately after each experiment. In this way, the time between the sampling and the analysis was reduced and, therefore, any possible changes to the sample composition (small leak, evaporation, unknown slow reactions) were minimised, if not avoided.

5.4.2.2 Liquid-phase Composition Analysis

Two instrumental analysis techniques were used to quantify the composition of the four different solutions tested in this work. These are gas-chromatography (GC) and UV-visible spectrophotometry. Gas-chromatography is essentially a separation technique in which the sample mixture is vaporised and then swept by a carrier gas (creating a mobile phase) to pass over an immiscible stationary phase (either a solid or a liquid). The separation then, occurs because the components of the mixture tend to distribute themselves between the two phases. Some of these components are strongly held by the stationary phase and move slowly with the moving phase while others travel rapidly because they are weakly retained by the stationary phase. As a result of these differences in travelling rates, mixture components are separated into discrete groups, allowing them to be analysed using a suitable detector (Harries et al., 2007). UV-spectrophotometry technique, however, is different. It is based on exposing a sample (a solute in a solvent for example) to a beam of light at a specific wavelength between 190 nm - 900 nm. During this operation, some of the light will be absorbed by the solute and some will transmit. The amount of light absorbed is proportional directly to the concentration of the solute and the sample thickness in the light path (Harries et al., 2007). Based on this principle, mixtures can be analysed qualitatively and quantitatively. For this work, Table 5.2 lists the solution type and the corresponding technique used to analyse them. As one may note, two different types of gas-chromatography were used, GC with a thermal conductivity detector (TCD) and GC with an ionised flame detector (FID), to analyse the ethanol and acetonitrile solutions, respectively. The spectrophotometry, on the other hand, was used for both acetone and 2-butanone (MEK).

Table 5.2. Summary of solution types and corresponding analysis techniques.

Solution Type	Measurement Technique	Instrument Model	Calibration Curve Uncertainty
Ethanol	Gas-Chromatography-TCD	Varian 3900	0.90%
Acetonitrile	Gas-Chromatography- FID	Perkin Elmer AutoSystem XL	1.40%
Acetone	UV-visible Spectrophotometery	Ultrospec 2100 Pro	0.40%
2-butanone (MEK)	UV-visible Spectrophotometery	Ultrospec 2100 Pro	0.50%

Before engaging in the analysis of the samples, a strict calibration method was adopted to ensure the reproducibility of the instruments used in this work and hence establishing a reliable calibration curve. This includes, for each instrument, carrying out the calibration process three times independently (often has been made in three different days), using a new series of standards each time. This helps to identify the precision of the instrument and also shows clearly whether there are any errors in the preparation of the standard samples. The results showed that the reproducibility of the instruments used, in general, is within 1% and the data of each system could be represented by a fit with rms deviations of about 0.9%, 1.4%, 0.4% and 0.5% for ethanol, acetonitrile, acetone and MEK, respectively (Table 5.2). Appendix E presents the calibration details including the measurements and the fitting functions used in this work to determine the solute concentration.

Also, as a long term monitoring procedure, the functioning of the instruments was checked regularly throughout the work. This was done by running standard samples (at least three) before each run. When the instrument was not within the limit of uncertainties determined in Table 5.2, measures had been taken to diagnose and resolve the problem. For the sake of the completeness, the details of the methods used to analyse each individual solution are described in the next subsections.

5.4.2.2.1 Ethanol Concentration Measurement

Gas chromatograph (GC) technique is the one of the reliable analytical methods to quantify the ethanol concentration in aqueous solutions (Weatherly et al, 2014; Abdulrazzaq et al., 2016). The analysis can be accomplished rapidly to a high accuracy and precision. In this work, for example, the typical run times were just over 3 min with uncertainties less than 1%. All the ethanol solution samples were analysed using a gas chromatograph (Varian 3900) equipped with a thermal conductivity detector, following the method described by Abdulrazzaq et al. (2016). The injection volume used for both calibration and sample analysis was 0.4 μL and the injection was carried out manually using a 1 μL syringe (SGC, Australia). The column used for all measurements was a packed column type HAYESEP P (80-100 mesh) with an internal diameter of 3 mm and a length of 2.08 m (Varian, USA). The GC oven and injection port temperatures were set at 150 °C and 180 °C, respectively. The carrier gas used was nitrogen at 400 mL/min. Finally, ethanol and water retention times were about 2 min and 0.8 min, respectively.

Typical chromatograms obtained using this set-up are shown in Fig. 5.15. Fig. 5.15 a and 5.15 b show the analysis of the feed composition , $Y_{LB}(0)$, before and after 6 hrs experimental use where the large peak on the left represents the water and the small one on the right is the ethanol. These two measurements were performed to evaluate the stability of the feed composition during a run. As an experimental routine, this type of evaluation was made throughout all the experiments. The results show that the difference in feed composition before and after a run was always within the measurement uncertainty (below 0.9%). Thus, the solution inlet concentration (whether supplied by a nitrogen-pressurised 'pot' or a syringe pump) was fixed throughout all tests performed.

For the outlet composition, Fig. 5.15 c and Fig. 5.15 d show the analysis of two samples. The first was sampled after running only the solution in the spiral while the outlet gas phase (air) was off (Fig. 5.15 c) and the second was sampled after normal operation (i.e. contacting with the gas phase). As expected, the result show no change in the outlet composition with respect to the feed composition when the air was off whereas a reduction in the ethanol peak size was observed (Fig. 5.15 c) when operating at normal conditions. These two experiments demonstrate clearly that contacting of the two phases was achieved and desorption of ethanol solute from the water into the air occurred.

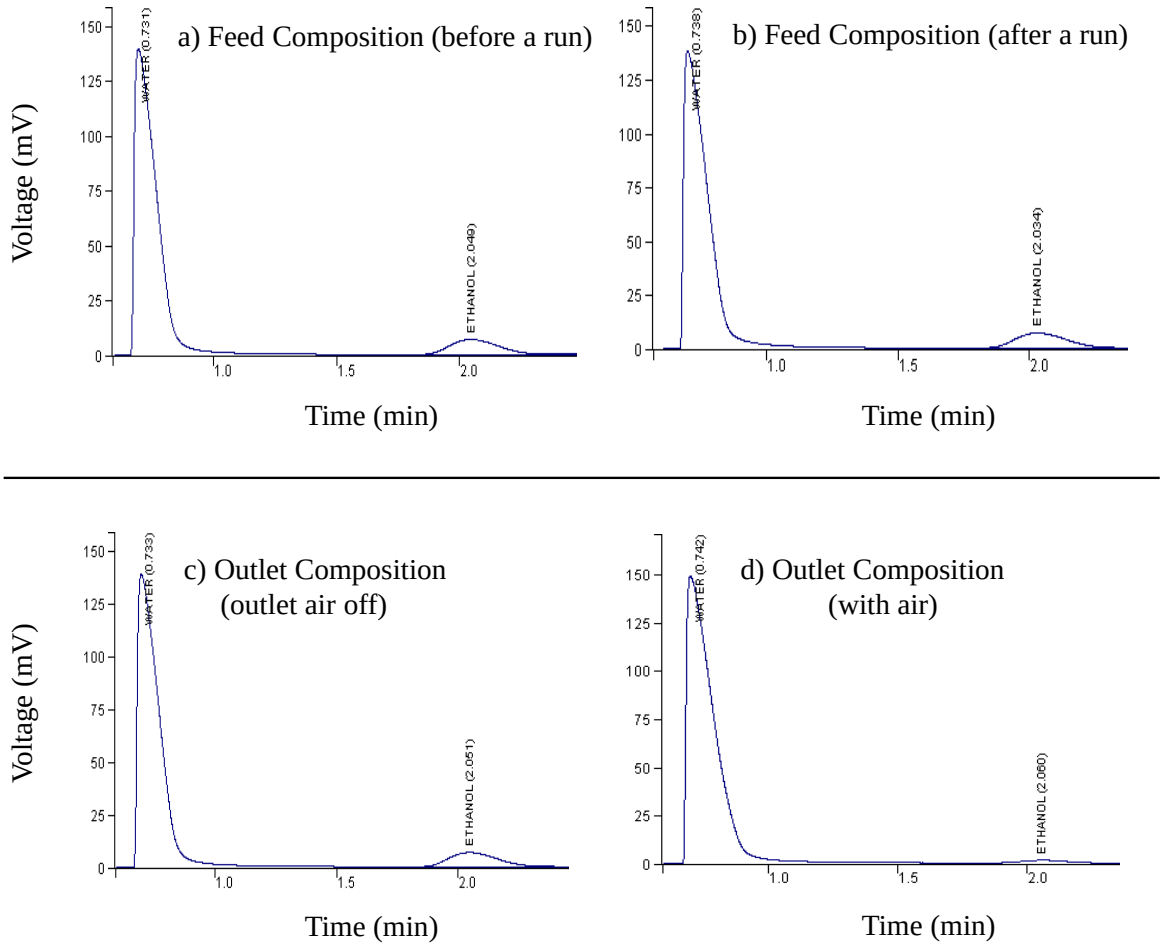

Figure 5.15. GC-TCD chromatograms for ethanol solutions: (a) feed composition before a run, (b) feed composition after 6 hrs experimental use, (c) outlet composition where the outlet gas phase is off and (d) outlet composition after counter-current contacting with the gas phase.

5.4.2.2.2 Acetonitrile Concentration Measurement

For the acetonitrile solutions, all analyses were carried out using a gas chromatograph (Perkin Elmer AutoSystem XL) supplied with ionised flame detector (FID). The analysis method was developed by the chemistry department of the University of Sheffield. For this ste-up, the suitable injection volume was 0.1 µL and the sample was injected using an autosampler. The column used was a capillary column, type Alltech AT1 (30 m length and 0.32 mm internal diameter) coated with 5 µm pure dimethylpolysiloxane. The GC oven and the injector temperatures were set at 200 °C and 250 °C, respectively. Hydrogen was used as a carrier gas (2.4 mL/min) and the split ratio was 20:1. The acetonitrile retention time was approximately 1 min and that was out of 10 min of an analysis time. Fig. 5.16 shows a typical chromatogram of an analysis with an acetonitrile peak emerging at a retention time of 1.07 min.

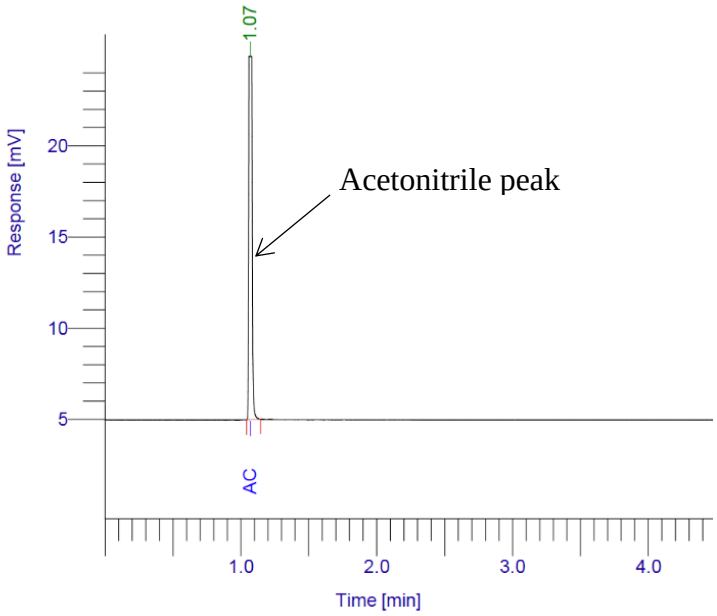

Figure 5.16. A chromatogram of GC-FID showing the acetonitrile peak.

5.4.2.2.3 Acetone and MEK Concentration Measurement

For acetone and MEK solutions, UV-visible spectrophotometry was used to analyse the samples. This technique has been successfully used for these types of solutes in various studies (Gierczak et al., 1998; Schutze and Herrmann, 2004; Nadasdi et al., 2010). In this work, all tests were carried out using Ultrospec 2100 pro (Amersham Biosciences) at room temperature and ambient pressure. Disposable plastic cuvettes (semi-micro, Fisherbrand) with a volume 1.5 mL and pathlength 1 cm were used to hold the samples during the tests.

As a part of the procedure, the device was zeroed using a blank of deionised water (the same source of water was used throughout the calibration and experiments) before each single test. This isolates the effect of both the solvent (water) and the cuvette and hence the light absorbance measured by the device is merely due to the presence of solute. It was found that an effective absorbance could be obtained at 280 nm wavelength for both acetone and MEK. This wavelength was fixed and used throughout the calibration (Appendix E) and analyses. Using the same wavelength for both solutes was found to be consistent with the literature. Schutze and Herrmann (2004) and Nadasdi et al. (2010) reported that the difference in absorption spectrum between the two solutes is just a few nanometres. In addition, this particular wavelength is within the acetone and MEK absorption bands which are approximately between 230-340 nm.

5.5 Summary

The chapter described step by step the mass transfer experiments conducted in this thesis. All desorption experiments were studied in a spiral channel with 1.5 mm height (h), 4 mm depth (W) and 910 mm long (L). The operating conditions were: pressure of 1.8 bara, rotation rate of 3200 rpm and three different temperatures (24, 30 and 49 °C). Three different gas phase flow rates were tested (1.3, 3.0 and 6.2 NL/min) over a range of liquid flow rates. The experimental apparatus used to collect the data was described, including the flow network and the rotating spiral unit. The time needed to reach a thermal steady-state was discussed along with the necessity to balance the pressure at the outer end of the spiral between the inlet gas and the outlet liquid.

The last part of this chapter focused on the measurements of the phase flow rates and the solute mole fraction at the liquid outlet. The effect of water evaporation and the transfer of the solute on the phase flow rates was quantified. While the solute has a minor effect on the phase flow rates, water evaporation can cause appreciable change in the liquid phase flow rate along the channel especially at small Q_L values. As a policy here, data showing considerable change were rejected based on a sensitivity analysis using the mass transfer relation (Appendix C). Furthermore, for the purpose of $K_L a$ determination, the phase flow rates and the liquid phase molar density were taken constant and equal to the average of the inlet and outlet. At the end of the chapter, an experimental method to collect valid samples was discussed and the techniques used to analyse the liquid phase composition were described.

Chapter Six

Phase and Solute Properties

Theoretical predictions using the models presented in Chapter 4 and calculations of the experimental mass transfer coefficient using the relations in Chapter 3 require a reliable knowledge of the phase and solute physical properties. In particular, the solute diffusion coefficients, the density and viscosity of each phase and the solute equilibrium distribution are required. These properties are determined in this work using either a fundamental theory, standard empirical relations or data from the literature. This chapter presents the method used to determine each property. The chapter is organized into two main sections. The first section deals with the determination of solute properties while the second section covers the details of phase properties determination.

6.1 Solute Properties

6.1.1 Solute Equilibrium Distribution (f')

Determination of vapour-liquid equilibrium data using the fundamental thermodynamic relations is possible. The modified Raoul's law provides a realistic description of the equilibrium behaviour of the selected solutes under the conditions of interest. As argued in Chapter 4, the spiral pressure varies little along the channel and the temperature is approximately uniform. So the gas phase can be treated as incompressible (perfect). Further, water exhibits considerably non-ideal behaviour with the selected organic solutes (Bergmann and Eckert, 1991; Sherman et al., 1996; Kojima et al., 1997), and that is exactly the case where the law is applicable. The modified Raoult's law is expressed as follows:

$$Y_V = \frac{P^{sat}\gamma}{P} Y_L \qquad (6.1)$$

where Y_V and Y_L are the solute mole fractions in the gas and liquid phase, respectively, P^{sat} is the pure solute vapour pressure and γ is the activity coefficient in the liquid phase which is a function of the temperature and Y_L.

To a good approximation, the solute vapour pressure (P^{sat}) in Eq. 6.1 can be estimated from Antoine's equation (Smith et al., 2005):

$$P^{sat} = \exp\left(A - \frac{B}{T(^{\circ}C) + C} \right) \tag{6.2}$$

where *A*, *B*, and *C* are constants for a given solute and their values are listed in Table 6.1 along with the temperature application range of Eq. 6.2 (Smith et al., 2005). These constants produce P^{sat} values in units of kPa. The activity coefficient is estimated using the UNIQUAC model combined with experimental data at a given temperature and over the relevant range of solute mole fractions. This model is recommended for the selected collection of solutes and needs only two experimental points to determine γ over the full range of mole fractions (Anderson and Prausnitz, 1978; Poling et al., 2001). Appendix F gives the model equations and the estimation method. The other parameter required to be determined in Eq. 6.1 is the pressure (P). This parameter is fixed and measured experimentally to be 1.8 bara as shown in Appendix B. Using this information, Eq. 6.1 can be used to determine the equilibrium curves. The calculations start from specifying the type of the solute and the spiral temperature. These allow the determination of the vapour pressure from Eq. 6.2 using the values of constants in Table 6.1. Next, values of solute mole fraction in the liquid phase (Y_L) are assumed within the experimental range of solute mole fractions (from zero up to the inlet mole fraction in the liquid phase). At each assumed value of Y_L, the activity coefficient is estimated using the UNIQUAC model and hence the corresponding Y_V is determined from Eq. 6.1.

Table 6.1. Antoine equation constants and the temperature application range.

Solute	*A*	*B*	*C*	*T* (°C)
Ethanol	16.895	3795.17	230.918	3 – 96
Acetonitrile	14.895	3413.10	250.523	-27 – 81
Acetone	14.314	2756.22	228.06	-2 – 77
MEK	14.133	2838.24	218.69	-8 – 103

Fig. 6.1 shows the equilibrium curve calculated from Eq. 6.1 for each solute over the relevant range of solute mole fractions and spiral temperatures. In each single plot, the maximum Y_L represents the inlet solute mole fraction in the liquid phase used in the experiments. It is clear from Fig. 6.1 that the equilibrium relation is not a strong curving function and a linear presentation is possible, i.e. $Y_V = f' Y_L$. To give a best estimate of f', the sum of the squared difference between the values of Y_L calculated from Eq. 6.1 and those from the proposed linear function ($Y_V = f' Y_L$) is minimised. This gives values of f' between 0.232 for ethanol system at 30 °C to 5.5 for MEK at 49 °C (as shown in Fig. 6.1) with a maximum rms deviation of about 3%. These values are used in this work to represent the solute equilibrium distribution for each system at a given temperature and over the range of mole fractions of interest.

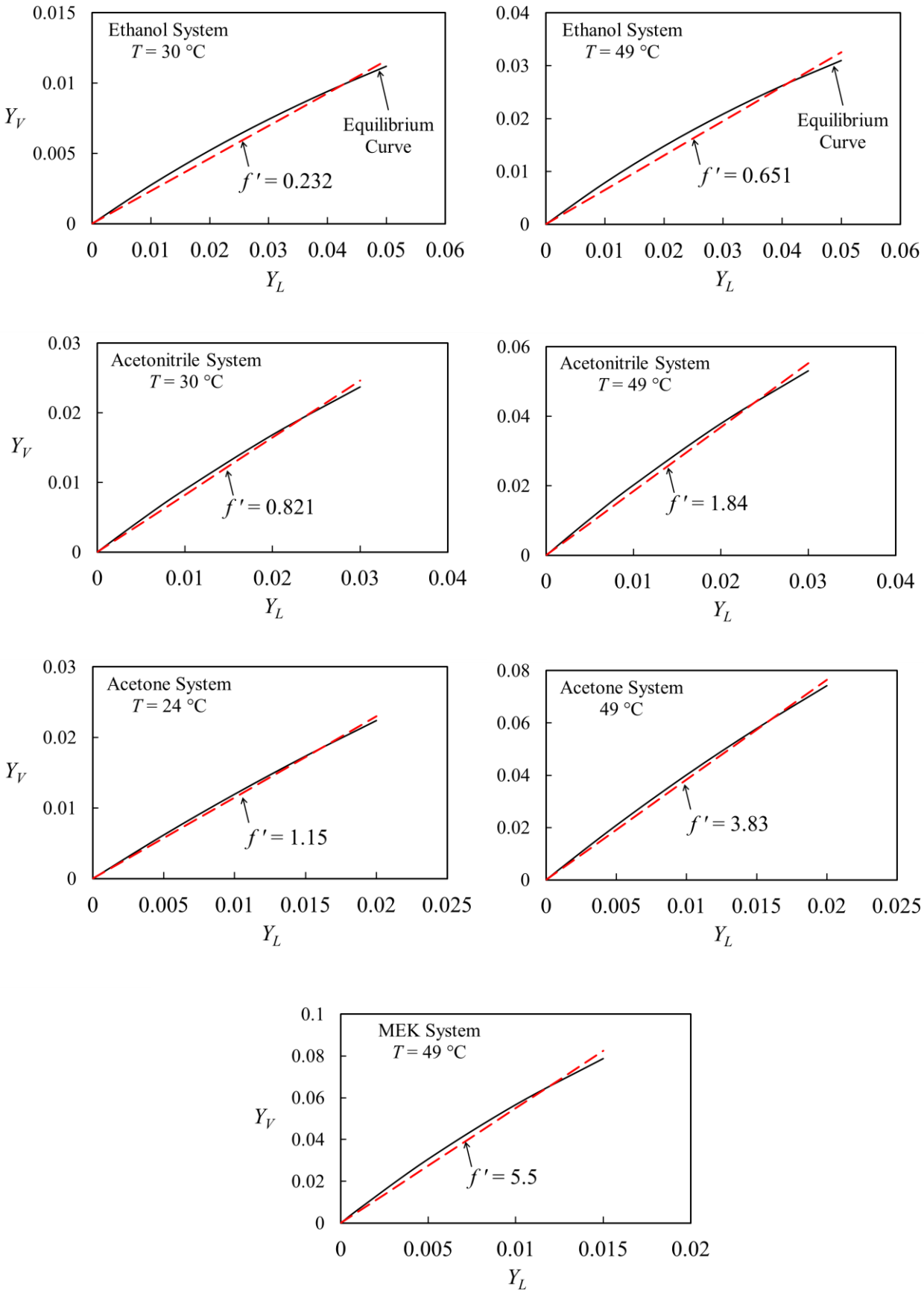

Figure 6.1. Solute equilibrium distribution at P_S = 1.8 bara and spiral temperatures.

6.1.2 Solute Diffusion Coefficients

6.1.2.1 Diffusion Coefficient in the gas Phase

For the purpose of the determination of the gas phase diffusion coefficient, the gas mixture is treated as a binary system of air and solute. This is reasonable since the solute diffuses into a gas mixture consisting mostly of air with a small percent of water vapour (at most 6 mol% which represents the saturation mole fraction at 49 °C). For binary gas systems, there are several theoretical and semi-empirical equations in the literature for estimating the solute diffusion coefficient (D_V). Many of these equations are reviewed and compared to experimental data by Poling et al. (2001). One of the most reliable and easy to use equations is that developed by Fuller et al. (1969) (Sherwood et al., 1975; Poling et al., 2001; Seader and Henley, 2006). This equation is used here to estimate D_V for the selected solutes in the gas phase. The equation is given below where the subscripts 'S' and 'A' refer to the solute and air, respectively:

$$D_V = \frac{0.00143\,T^{1.75}}{P M_{SA}^{1/2}\left[(v_S)^{1/3} + (v_A)^{1/3}\right]^2} \tag{6.3}$$

In Eq. 6.3, D_V is in cm^2/s, P is in bar, T is in K and M_{SA} can be found from the molar mass of the solute (M_S) and air (M_A):

$$M_{SA} = \frac{2}{(1/M_S) + (1/M_A)} \tag{6.4}$$

The quantities v_S and v_A are the dimensionless diffusion volumes of the solute and air, respectively. The diffusion volume of air is 19.7 and for the selected organic solutes, it is calculated by summing the atomic diffusion volumes given in Table 6.2 (Fuller et al., 1969). This gives solute diffusion volumes of 35.45, 33.86, 38.58 and 41.18 for ethanol, acetonitrile, acetone and MEK, respectively.

Table 6.2. Dimensionless atomic diffusion volumes (Fuller et al., 1969).

Atom	**C**	**H**	**O**	**N**
Diffusion Volume	15.9	2.31	6.11	4.53

For each solute, the results of Eq. 6.3 are listed in Table 6.3 at the spiral pressure (1.8 bara) and temperatures along with relevant experimental data reported in the literature. According to Eq. 6.3, D_V is proportional to $T^{1.75}/P$ for a given solute. This relation is used to convert the experimental diffusivities at the given conditions (pressure and temperature) to those of the spiral and hence a comparison under the same conditions with the correlation is made, i.e.:

$$\frac{D_{V2}}{D_{V1}} = \left(\frac{P_1}{P_2}\right)\left(\frac{T_2}{T_1}\right)^{1.75} \tag{6.5}$$

As one can see in the table below, the maximum deviation between the values estimated from Eq. 6.3 and the corresponding experimental data is less than 6%. The sensitivity of the numerical computation to the possible error in D_V was explored. The results showed that the largest change in the gas phase mass transfer coefficient did not exceed 0.5%. This, perhaps, is expected since the mass transfer mechanism in the gas phase is largely affected by the Coriolis secondary motion over the range of gas flow rates of interest. Thus, any changes in the amount of molecular diffusion due to changes in the diffusion coefficient are not expected to be significant.

Table 6.3. Gas-phase diffusion coefficients calculated using Eq. 6.3 at 1.8 bara and spiral temperatures and experimental values from the literature corrected to the same conditions using Eq. 6.5.

Solute	T_S (°C)	calc. $D_V \times 10^6$ (m^2/s)	expt. $D_V \times 10^6$ (m^2/s)	*dev.%* *	*Ref.*
Ethanol	30	7.11	7.50	5.5	Kwon et al.(2004)
	49	7.92	8.40	5.7	Arnold (1930)
Acetonitrile	30	7.79	7.54	3.3	Poling et al. (2001)
	49	8.66	8.39	3.2	Poling et al. (2001)
Acetone	24	5.93	6.04	1.8	Kwon et al.(2004)
	49	6.67	6.82	2.2	Lugg (1968)
MEK	49	5.92	5.74	3.1	Lugg (1968)

* $dev.\% = \left|\frac{calc.D_V - expt.D_V}{expt.D_V}\right| \times 100$

6.1.2.2 Diffusion Coefficient in the Liquid Phase

The diffusion coefficient of the solute in the liquid phase (D_L) is much smaller than that in the gas phase and concentration-dependent (Poling et al., 2001). Most of the literature reviewed agree that D_L is difficult to estimate because of the lack of a well-developed theory for the liquid state (Sherwood et al., 1975; Poling et al., 2001; Seader and Henley, 2006; Bird et al., 2007). For the case of infinite dilution, however, there are several proposed empirical equations that can estimate D_L successfully for binary systems, giving a representative diffusion coefficient over a range of solute mole fractions up to 0.05, or perhaps 0.1 (Poling et al., 2001). The Wilke-Chang equation is widely used and gives a reasonably good prediction of D_L for dilute solutes in aqueous solutions (Sherwood et al., 1975; Bird et al., 2007). This equation is employed here to estimate D_L for the selected solutes in water and is given as:

$$D_L = \frac{7.4\times10^{-8}(\varphi M_L)^{0.5}T}{\mu_L \mathrm{V_S}^{0.6}} \qquad (6.6)$$

where D_L is in cm^2/s, T is in K, and M_L and μ_L are the molar mass and viscosity (cP) of the liquid phase, respectively. For water, μ_L is estimated using a correlation given by White (2008). This correlation is a function of temperature only and applicable for a temperature range of 0 – 100 °C:

$$\ln\frac{\mu_L(\text{Pa s})}{1.788\times10^{-3}} = -1.704 - 5.306\left(\frac{273}{T(K)}\right) + 7.003\left(\frac{273}{T(K)}\right)^2 \qquad (6.7)$$

In Eq. 6.6, $\mathrm{V_S}$ is the molar volume of the solute (mL/mol) at its normal boiling point. This parameter is determined by summing the atomic contribution using the values listed in Table 6.4. This gives molar volumes of 59.2, 56.3, 74 and 96.2 mL/mol for ethanol, acetonitrile, acetone and MEK, respectively. The other parameters required in Eq. 6.6 is the associate factor φ. Wilke and Chang (1955) recommend φ to be 2.6 for water. However, this value has been revised for dilute solutes in aqueous solutions in an independent study made by Hayduk and Laudie (1974). They used data for 89 different substances in water and found a better accuracy can be obtained from Eq. 6.6 if φ = 2.26. This value is taken and fixed in all calculations made with Eq. 6.6.

Table 6.4. Atomic volumes (Wilke and Chang, 1955).

Atom	**C**	**H**	**O**	**N (Doubly Bonded)**
Volume (mL/mol)	14.8	3.7	7.4	15.6

The values of D_L predicted by Eq. 6.6 are listed in Table 6.5. In the same table, the results are also compared with interpolated experimental data for ethanol and acetone at infinite dilution. As can be seen, the deviation between the predicted values and those reported in the literature is about 10% and that is within the expected accuracy of Eq. 6.6 (Bird et al., 2007). However, there is a clear dependency of D_L on the liquid phase viscosity which appears explicitly in Eq. 6.6. In this work, the presence of the solute increases the viscosity of the liquid phase and hence decreases D_L. Thus, it should be expected that the deviation shown in Table 6.5 will increase by some percent if one considers D_L at the inlet solute concentration. For example, D_L for 5% ethanol solution at 30 °C is 1.32×10^{-5} cm^2/s (Pratt and Wakeham, 1974), widening the deviation to about 15% in relation to the value estimated by Eq. 6.6. This means also that D_L varies along the channel by approximately 5% (at most) in relation to the D_L value at infinite dilution (1.4×10^{-5} cm^2/s) reported in Pratt and Wakeham (1974). Nevertheless, computation with the 2-D model for the ethanol system shows that 15% deviation in D_L leads only to a few percent change in mass transfer coefficient. This suggests that using Wilke and Chang equation does not lead to a significant error in the mass transfer coefficient for these particular systems under the conditions of the experiments.

Table 6.5. Liquid-phase diffusion coefficients calculated using Eq. 6.6 at the spiral temperatures and experimental values from the literature.

Solute	T_S (°C)	calc. $D_L \times 10^9$ (m^2/s)	expt. $D_L \times 10^9$ (m^2/s)	*dev.%* *	*Ref.*
Ethanol	30	1.53	1.4	9.2	Pratt and Wakeham (1974)
	49	2.36	2.14	10.2	Pratt and Wakeham (1974)
Acetonitrile	30	1.58	-	-	-
	49	2.43	-	-	-
Acetone	24	1.15	1.27	9.2	Tyn and Calus (1975)
	49	2.07	1.89	9.4	Tyn and Calus (1975)
MEK	49	1.77	-	-	-

* $dev.\% = \left| \frac{calc.D_L - expt.D_L}{expt.D_L} \right| \times 100$

6.2 Phase Properties

The other physical properties required in the 2-D model and WCM computations are the density and viscosity of the contacting phases. To simplify the determination of these properties, the conditions of the experiments at the inlet for each phase are used (i.e. solute-free air and solution at the inlet solute mole fraction). This approximation is justifiable since the water vapour content in the gas phase has a relatively small effect on the density and the viscosity of air, about 4 and 6% reduction in the density and viscosity, respectively, at 49 °C (Tsilingiris, 2008). Furthermore, the solute mole fractions remain at a dilute level in both phases (Fig. 6.1). So the transferring of solute does not have a strong effect on the phase physical properties, with the exception of the ethanol solution viscosity and that will be discussed in Section 6.2.2. Details of the density and viscosity determination for each phase are described in the following subsections.

6.2.1 Gas-phase Properties

As pointed out previously, the change in the pressure along the channel is small and the temperature is approximately uniform. Thus, the gas phase can be treated as an ideal gas and the density can be calculated directly:

$$\rho_V = \frac{PM_V}{RT} \tag{6.8}$$

where M_V is the air molar mass (28.97 kg/kmol) and R is the gas constant.

For the viscosity, data reported in Kadoya et al. (1985) suggest that the air viscosity is a function of temperature and only weakly dependent on the pressure between 1 and 25 bar and a range of temperature between 200 and 650 K. In this work, the experimental conditions lie between these limits. It is reasonable, therefore, to estimate gas viscosity as a function of temperature since the pressure dependence of the viscosity is negligible at the spiral conditions. The Sutherland law is simple and gives sufficiently accurate results for air viscosity at a temperature range from -40 up to 500 °C (White, 2008):

$$\frac{\mu}{\mu_0} = \left(\frac{T}{273.15}\right)^{3/2}\left(\frac{273.15+S}{T+S}\right) \tag{6.9}$$

where S is the Sutherland constant and μ_0 is the gas viscosity at 273.15 K. For air, the values of these constants are S = 110.56 K and μ_0 = 1.7894×10^{-5} Pa s. Using Eqs. 6.8 and 6.9, the density and the viscosity of the air at the spiral pressure and temperatures can then be calculated. These values are given in the table below.

Table 6.6. Air propetries at the spiral pressure and temperatures.

T_S (°C)	ρ_V (kg/m^3)	$\mu_V \times 10^5$ (Pa s)
24	2.11	1.83
30	2.06	1.85
49	1.95	1.94

6.2.2 Liquid-phase Properties

For the liquid phase, the viscosity and density reported in the literature at the relevant temperatures and inlet solute mole fraction are used in this work. This is the case for all the studied systems except for 1.5% MEK solution because no data were found. Alternatively, the density and viscosity of this particular solution were estimated at 49 °C using the volume mixing rule since it is the most dilute system. The density and viscosity of pure MEK at 49°C used in the calculation are 773 kg/m^3 and 3.03×10^{-4} Pa s, respectively (Habibullah et al., 2011) and those for water at the same temperature are 988.5 kg/m^3 (White, 2008) and 5.56×10^{-4} Pa s (Khattab et al., 2012).

The calculated properties of the MEK solution, along with those for the other solutions collected from the literature, are listed in Tables 6.7 and 6.8. The former shows the density of the solutions at the relevant temperatures and inlet solute mole fraction and the latter shows the values of viscosity at the same conditions. Some of these values were taken directly and others were interpolated from the measured values. The density and viscosity of pure water are also listed in these same tables. These values correspond to full purification of the liquid phase and are used here to assess the maximum variation in the density and viscosity along the channel due to solute transfer.

It is clear from Table 6.7 that the variation of the liquid phase density along the channel is less than 2% in all cases. On the other hand, the values of the viscosity listed in Table 6.8 show a clear sensitivity to the solute concentration. The complete removal of the solute drops the viscosity to about 33 percent for the ethanol system at 30 °C. In general, such drop has two effects. First, it leads to increase the diffusion coefficient along the channel and that is estimated to be about 5% as pointed out in Section 6.1.2.2. Second, it produces a thinner liquid layer in the spiral at a given rotation rate. MacInnes and Zambri (2015) have shown that at the lowest liquid flow rate tested (0.2 ml/min), this reduction in viscosity decreases the liquid layer thickness (measured at the minimum) by approximately 18% at 3200 rpm. All these observations may affect the mass transfer and are taken into account when it comes to discussing the results presented in Chapter 7 and Chapter 8.

Table 6.7. Density of the studied solutions and pure water at the relevant spiral temperatures.

Solute	T_S (°C)	$Y_{LB}(0)$	ρ_W (kg/m^3) (pure water)	ρ_L (kg/m^3) (water+solute)	*dev.%**	*Ref.*
Ethanol	30	0.05	994.0	977.7	1.67	Khattab et al. (2012)
	49	0.05	983.1	965.5	1.82	Khattab et al. (2012)
Acetonitrile	30	0.03	995.7	984.9	1.10	Saleh et al.(2006)
	49	0.03	988.5	976.2	1.26	Saleh et al.(2006)
Acetone	24	0.02	997.1**	986.2	1.11	Thomas and McAllister (1957)
	49	0.02	988.5**	976.2	1.26	Thomas and McAllister (1957)
MEK	49	0.015	988.5**	973.0	1.59	Volume Mixing Rule

* $dev.\% = \left| \frac{\rho_W - \rho_L}{\rho_L} \right| \times 100$

** The water density at 24 and 49 °C is estimated using a correlation given in White (2008) because they are not given in Thomas and McAllister (1957):

$\rho(\text{kg/m}^3) = 1000 - 0.0178 \left| T\ ^\circ C - 4\ ^\circ C \right|^{1.7}$

Table 6.8. Viscosity of the studied solutions and pure water at the relevant spiral temperatures.

Solute	T_S (°C)	$Y_{LB}(0)$	$\mu_W \times 10^4$ (Pa s) (pure water)	$\mu_L \times 10^4$ (Pa s) (water+solute)	*dev.%**	*Ref.*
Ethanol	30	0.05	7.98	11.9	32.9	Khattab et al. (2012)
	49	0.05	5.56	6.68	16.8	Khattab et al. (2012)
Acetonitrile	30	0.03	8.00	8.43	4.63	Saleh et al.(2006)
	49	0.03	5.61	5.83	3.79	Saleh et al.(2006)
Acetone	24	0.02	8.99	10.33	12.72	Howard and McAllister (1958)
	49	0.02	5.56	6.32	10.70	Howard and McAllister (1958)
MEK	49	0.015	5.56	5.51	0.9	Volume Mixing Rule

* $dev.\% = \left| \frac{\mu_W - \mu_L}{\mu_L} \right| \times 100$

6.3 Summary

The chapter has described the methods used to determine the physical properties of the seven phase and solute systems studied experimentally. These properties are used throughout this work to make model predictions and to derive values of mass transfer coefficients from the experimental measurements. Table 6.9 below compiles all these properties and categorises them according to solute type and spiral temperature.

Table 6.9. Physical properties of the seven phase and solute systems studied experimentally.

Solute	M_S (kg/kmol)	T_S (°C)	f'	D_V (m^2/s)	D_L (m^2/s)	ρ_V (kg/m^3)	μ_V (Pa s)	$Y_{LB}(0)$	μ_L (Pa s)	ρ_L (kg/m^3)
Ethanol	46.1	30	0.232	7.11×10^{-6}	1.53×10^{-9}	2.06	1.85×10^{-5}	0.05	1.19×10^{-3}	977.7
		49	0.651	7.92×10^{-6}	2.36×10^{-9}	1.95	1.94×10^{-5}	0.05	6.68×10^{-4}	965.5
Acetonitrile	41.1	30	0.812	7.79×10^{-6}	1.58×10^{-9}	2.06	1.85×10^{-5}	0.03	8.43×10^{-4}	984.9
		49	1.84	8.66×10^{-6}	2.43×10^{-9}	1.95	1.94×10^{-5}	0.03	5.83×10^{-4}	976.2
Acetone	58.1	24	1.15	5.93×10^{-6}	1.15×10^{-9}	2.11	1.83×10^{-5}	0.02	1.03×10^{-3}	986.2
		49	3.83	6.67×10^{-6}	2.07×10^{-9}	1.95	1.94×10^{-5}	0.02	6.32×10^{-4}	977.5
MEK	72.1	49	5.5	5.92×10^{-6}	1.77×10^{-9}	1.95	1.94×10^{-5}	0.015	5.51×10^{-4}	973

Chapter Seven

Experimental Results

This chapter presents the mass transfer results collected using the experimental channel and the procedures discussed in Chapter 5. In the experiments, seven phase and solute systems in terms of f' have been tested. For each of these systems, the outlet solute mole fraction in the liquid phase, $Y_{LB}(L)$, was measured over a range of liquid flow rates (Q_L), at each of three different gas rate values (1.3, 3 and 6.2 NL/min). This allows the purification $d_L = Y_{LB}(L)/Y_{LB}(0)$ to be determined over a wide range of contacting conditions and these results are presented first in this chapter (Section 7.1). These raw measurements, i.e. Q_V, Q_L and $Y_{LB}(L)$, along with the phase properties (Table 6.9) determine the experimental mass transfer coefficients from Eq. 3.32 over the tested range of phase flow rates. These derived coefficients, which correspond directly to the contacting effectiveness of the experimental channel, are also presented, and they are discussed in Section 7.2.

In terms of the models presented in Chapter 4, the wide-channel model (WCM) is employed here to help interpretation of the experimental results while the comparison with the 2-D model results is delayed until the next chapter. Experimentally, the aspect ratio of the liquid layer, $W/h\xi$, is at least 30 and that for the gas layer, $W/h(1-\xi)$, is about 3. These are considered relatively large aspect ratios and thus the behaviour predicted by the WCM should be a good qualitative guide (if not quantitatively precise for some cases). At the end of this chapter, comparison of the spiral performance, based on the extensive data presented here, and performance for the packed bed column, rotating packed beds and membrane microchannel is made using experimental data for these approaches from the literature.

7.1 Purification (d_L)

7.1.1 Effect of f'

Results for d_L measured at the intermediate gas phase flow rate (3 NL/min) for the seven phase and solute systems are shown in Fig. 7.1. These results are presented to highlight general trends and the effect of f' on the level of purification over a range of liquid phase flow rate, approximately from 0.2 to 12 mL/min.

The first thing to note in Fig. 7.1 is that desorption has been achieved successfully for each system, reaching approximately solute-free water ($d_L \approx 0$) for low enough liquid flow rate. The exception is the data for f' = 0.232 where a liquid flow rate approaching 0.1 mL/min is required to achieve a complete removal of solute. Operating at such small level of liquid flow rate requires an extended data sampling time. Further, it would be associated with more uncertainties regarding layer formation ($h_{Lm} < 20$ µm) therefore, it was avoided. It is also clear from Fig. 7.1 that at a fixed f' the liquid phase purity decreases, i.e. larger d_L, as the liquid phase flow rate increases. The physical explanation for this behaviour is that increasing the liquid flow rate decreases the residence time of the liquid phase (t_{mL}). So practically this means that less contacting time will be available for the two phases and as a result, the purity of the liquid phase decreases as increasing Q_L. Another possible explanation is that increasing the liquid phase flow rate excessively at fixed both f' and the gas phase flow rate causes a situation where the amount of gas phase (solvent) becomes saturated with the solute. Hence, the more increasing the liquid phase flow rate the less purity is obtained since the gas phase is not able to remove more solute. Qualitatively, similar behaviour has been noticed for the variation of d_L with the liquid flow rate at the smaller and larger gas flow rates (1.3 and 6.2 NL/min). So the experimental results shown in Fig.7.1 represent a general behaviour.

The effect of f' on the degree of purification is also evident in Fig. 7.1. In all cases, increasing f' leads to improving the purity of the liquid phase, i.e. smaller d_L, at a given Q_L. Equivalently, as f' increases, the liquid flow rate that can be processed increases at a given level of purification (d_L). These two effects can be understood in terms of the limit placed by f' on the phase flow rate ratio. From Chapter 2 (Eq. 2.9),

$$-f'q_n = -f'\frac{n_V Q_V}{n_L Q_L} > 1 - d_L \qquad (7.1)$$

At the fixed solvent flow rate (Q_V = 3 NL/min), increasing f' increases the capacity of this same amount of solvent to hold solute. According to Eq. 7.1, therefore, a larger amount of Q_L can be treated at a given d_L as f' increases or purer liquid phase (has smaller d_L) can be produced at a given Q_L without violating the equation (inequality) in either case.

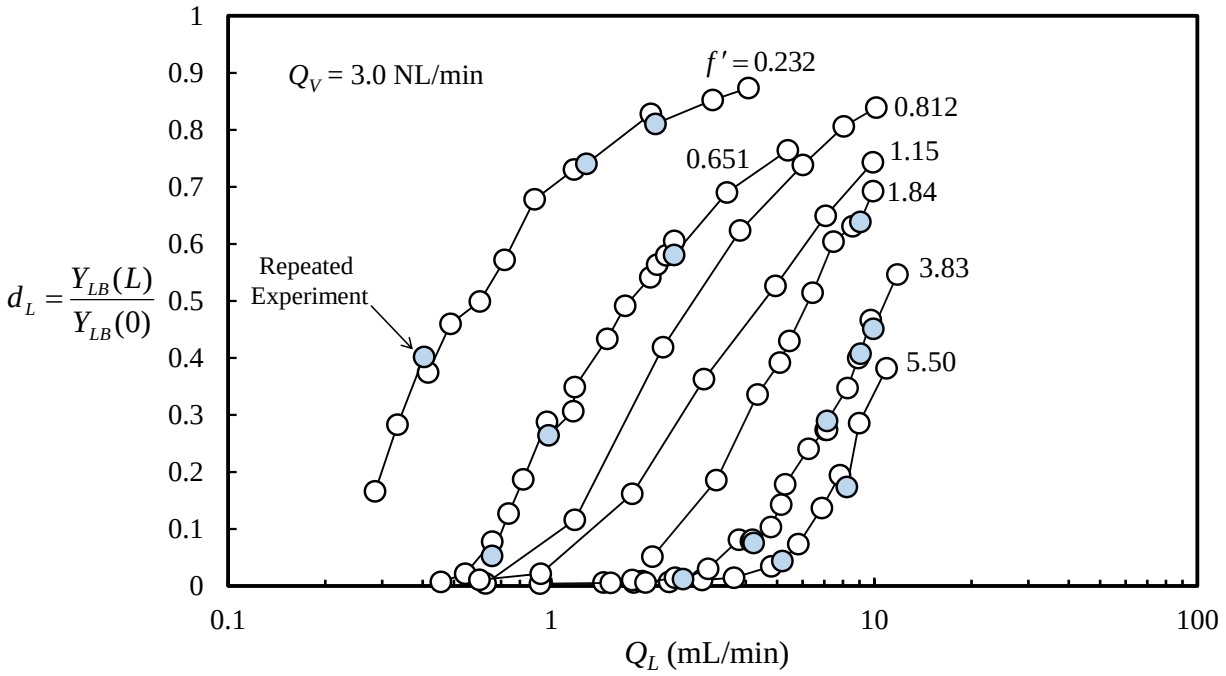

Figure 7.1. Purification measured at Q_V = 3 NL/min over a range of Q_L values for the seven phase and solute systems. The other contacting parameters are spiral pressure of 1.8 bara and rotation rate of 3200 rpm. The shaded circles are repeated experiments at the same conditions.

7.1.2 Effect of Gas-phase Flow Rate

The results for all gas flow rates are shown in Fig. 7.2 and plotted for each f' value separately. In each single plot, the d_L values are presented as a function of Q_L for each of the three gas phase flow rates (1.3, 3, and 6.2 NL/min). The solution of the wide-channel model at the corresponding conditions is also shown in the plots using the properties determined in Chapter 6 (Table 6.9). The symbols are the experimental points and the shaded dashed lines are the model calculations where the lighter shade corresponds to the larger value of Q_V.

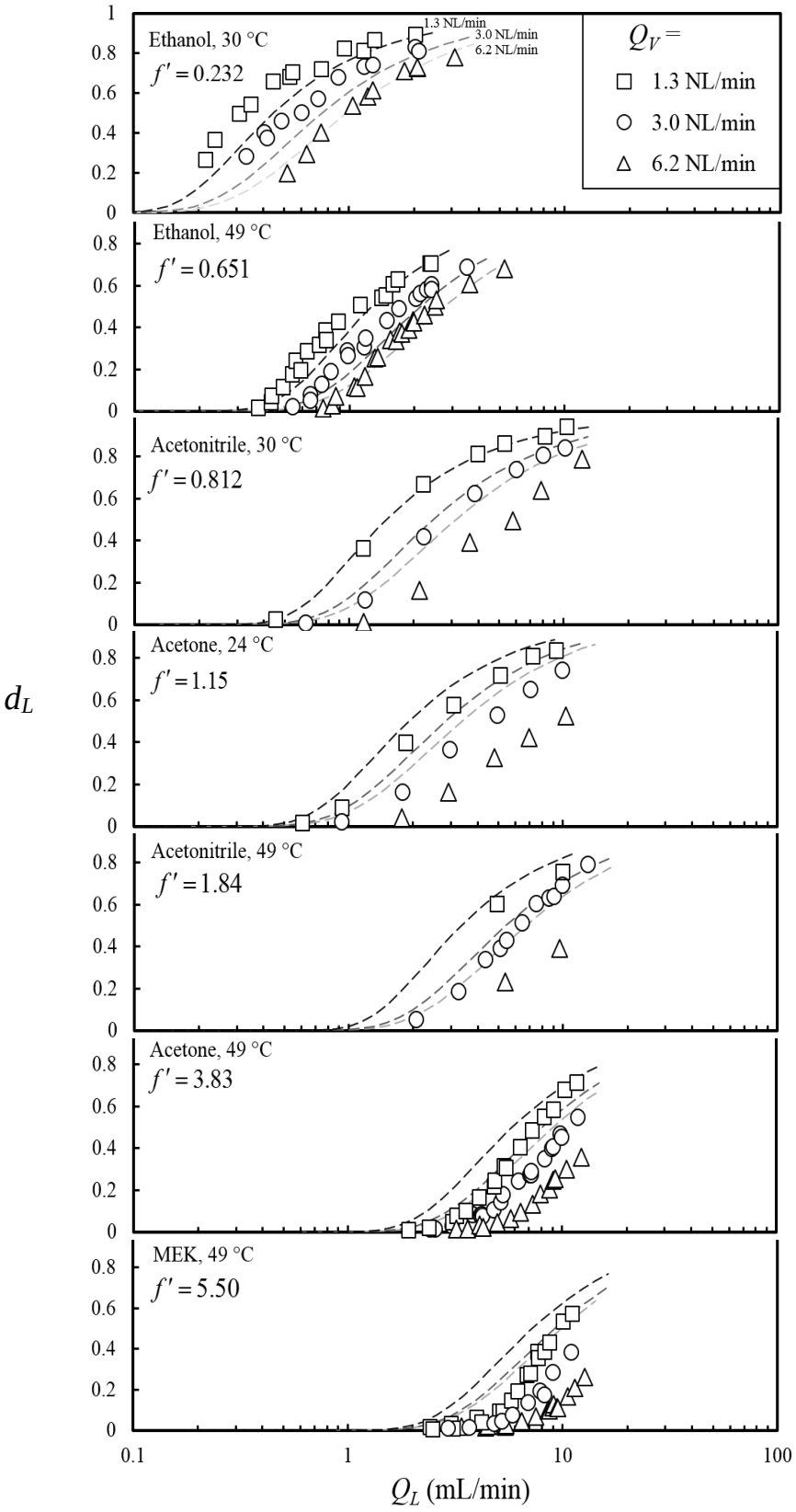

Figure 7.2. Measured purification (d_L) at the three fixed gas flow rates over a range of liquid flow (symbols). The shaded dashed curves are the predictions of the wide channel model (the lighter shade corresponds to the larger value of the gas phase flow rate).

The effect of the liquid phase flow rate has been discussed in the preceding section and, again, it is clear that for each system (f') increasing Q_L decreases the purity of the liquid phase (larger d_L) because t_{mL} decreases. In terms of the gas phase flow rate (solvent phase), the effect is different. In all cases, increasing Q_V at a fixed liquid flow rate ensures adequate solvent supply to desorb more solute and hence produces a high degree of purification. Similarly, the liquid phase flow rate for which a given purification is achieved increases with the solvent flow rate. These general trends are captured by the WCM. However, differences become most pronounced as both f' and gas phase flow rate increase. For f' = 5.5 (MEK) and Q_V = 6.2 NL/min, for example, the purification in the experiment is improved many fold relative to the wide channel model. This improvement must be a consequence of the effect of the end walls which are present in the experimental spiral channel, but not in the WCM. As discussed in Chapter 4, the presence of the end walls causes two main changes in relation to an infinitely wide channel. First, the interface is not flat as that used in WCM calculations but it is curved due to the menisci at the end walls and tilted due to the effect of gravity. The second change is the presence of Coriolis secondary motions. These changes could explain the differences between the experiments and the WCM model as f' and Q_V increase.

At a given d_L value, increasing f' for a fixed gas flow rate corresponds to increasing liquid phase flow rate. The computations performed in Chapter 4 (Fig. 4.14) demonstrate that both the liquid layer thickness and the strength of Coriolis motion increase as Q_L increases. When the liquid layer is thick, the deformation in interface shape becomes secondary (MacInnes and Zambri, 2015) and the layer can be considered as flat. This leaves only the effect of Coriolis motion in the experimental channel which can enhance the mass transfer due to convection. This main difference explains the improvement in mass transfer in the experiments relative to the model predictions as f' increases above 0.812. For a fixed f', the greater change in the mass transfer with gas flow rate for the experiments is also consistent with effects of Coriolis motion, but this time in the gas phase. The pattern of the gas phase Coriolis motion has been computed and shown in Chapter 4 (Fig. 4.17) at conditions close to those used in the experiments. As pointed out there, this motion occupies most of the channel and is stronger than that in the liquid side. As increasing the gas phase flow rate, the Coriolis motion becomes

more effective since the term responsible for producing this motion (i.e. $2\rho_V \Omega w_V$) becomes larger. Accordingly, as observed in Fig. 7.2, an increasingly improved purification is found in the experiments relative to the model predictions as Q_V increases.

7.1.3 Purification Factor ($-f'q_n$)

Plotting the measured purification as a function of $-f'q_n$ places the results in the context of the purification function developed in Chapter 3 (Eq. 3.51). So a direct check whether the experimental data follow the common trends shown in Fig. 3.5 or not is possible. Fig. 7.3 shows all of the experimental points plotted in this way along with the purification function for the $\Phi_L t_{mL}$ values of 0.4, 0.8, 1.6, 3.2, 6.4 and 12.8. The experimental points are plotted as circles for the three fixed gas flow rates and shaded dark to light with increasing gas flow rate.

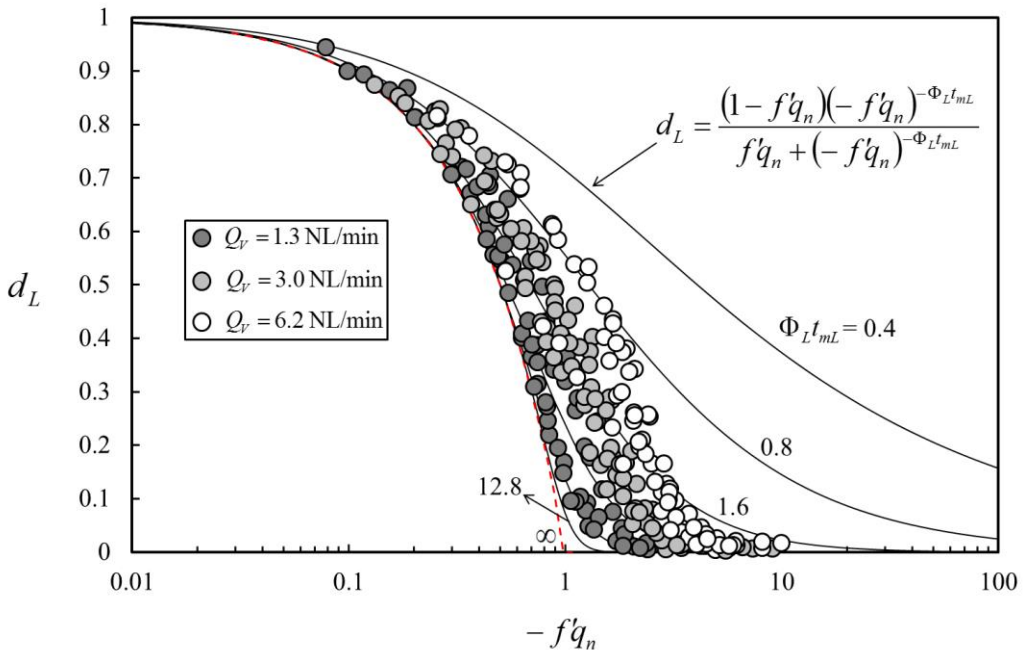

Figure 7.3. Variation of d_L in terms of the purification factor ($-f'q_n$). Symbols are the experimental points and solid curves are the purification function results (Eq. 3.51 with d_V = 0).

It is helpful to remind here that the dashed red curve, $\Phi_L t_{mL} \to \infty$ in Fig. 7.3, is the maximum separation that can be achieved at a given $-f'q_n$. This is equivalent to achieving perfect equilibrium between the inlet liquid flow and the outlet gas flow which requires a contactor of infinite length. As expected, all the data respect this limit imposed

by the thermodynamic equilibrium which is $d_L = 1 + f'q_n$ and no data fall under the red curve, i.e. purification that is impossible. Additionally, there is a clear pattern in Fig. 7.3 to the spread of data over the values of $\Phi_L t_{mL}$, data with larger gas flow rates (light shade circles) tend to produce smaller $\Phi_L t_{mL}$.

At this stage, there is a temptation to judge the effectiveness of the contacting for any given experimental point in terms of the value of $\Phi_L t_{mL}$. However, as discussed in Chapter 3, higher purification can be achieved simply by increasing the residence time, t_{mL}, and this cannot be considered effective contacting since no increase in specific throughput, Φ_L, may accompany this. The pattern observed in Fig. 7.3, i.e. the spread out of data according to gas phase flow rate, supports this argument. At a fixed q_n ($n_V Q_V / n_L Q_L$), the residence time of the liquid phase is related inversely to the liquid phase flow rate and hence the gas phase flow rate. Since the results clearly spread out according to gas flow rate and hence residence time, the change in $\Phi_L t_{mL}$ in the experiments may be mainly due to the effect of residence time and hence contacting effectiveness cannot be judged from the plot.

7.2 Contacting Effectiveness

7.2.1 Mass Transfer Coefficients

Specific throughput (Φ_L) is the appropriate way to judge the effectiveness of contacting at a given $-f'q_n$. As shown in Chapter 3 in relation to Eq. 3.43, Φ_L is the product of $K_L a / n_L$ and a function of $-f'q_n$. Therefore, at a particular value of $-f'q_n$, $K_L a$ behaviour corresponds directly to that of Φ_L. The $K_L a$ values derived from the data are plotted in Fig. 7.4 as a function of $-f'q_n$ for three representative values of f' (0.232, 0.812 and 3.83). The results for f' = 0.232 (ethanol at 30 °C), f' = 0.812 (acetonitrile at 30 °C) and f' = 3.83 (acetone at 49 °C) are plotted as triangles, diamonds and circles, respectively. As in Fig. 7.3, the data are shaded dark to light as the level of the gas phase flow rate increases. For comparison, the wide channel model results for the three f' values and gas flow rates are also plotted and indicated as shaded dashed curves (again the lighter shade corresponds to the larger Q_V).

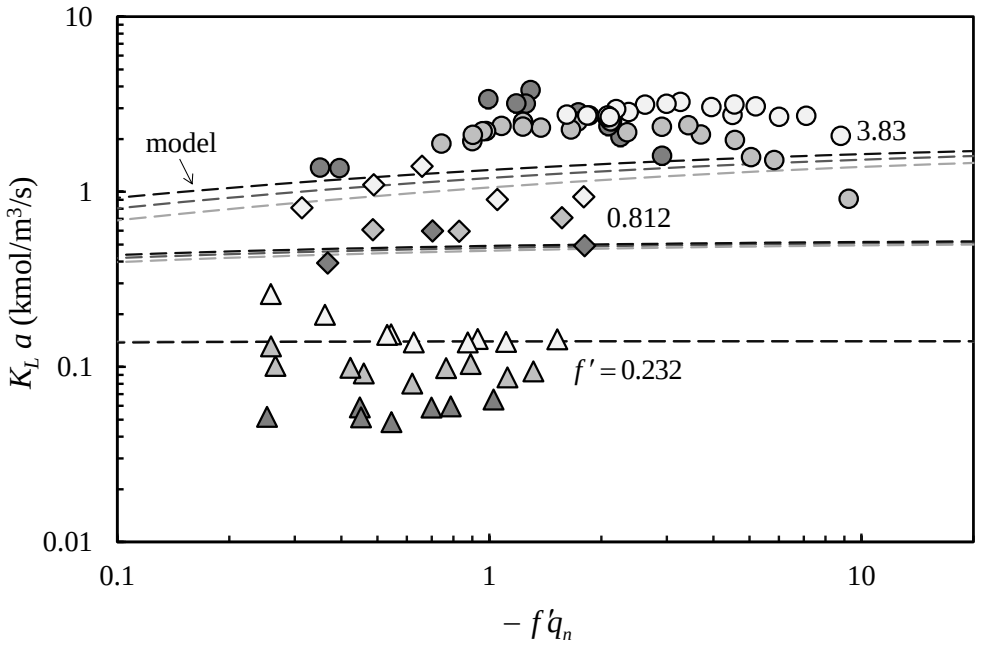

Figure 7.4. Overall volumetric mass transfer coefficients for three f' values (0.232, 0.812 and 3.83). Symbols are experiments at Q_V = 1.3, 3 and 6.2 NL/min (the lighter shade corresponds to the larger values of Q_V). The dashed lines are the wide channel model results at the corresponding conditions and shaded as the experimental points (dark to light as Q_V increases).

The causes of the differences between the model and the data have been discussed in the previous section and attributed to the presence of ends walls which are responsible for: (1) deformation of the interface shape and (2) the generation of Coriolis secondary motion. Apart from these differences, there are some interesting trends observed in $K_L a$ as f' and $-f'q_n$ vary and these trends are examined in the below subsections.

7.2.1.1 Effect of f'

As can be seen in Fig. 7.4, both the data and the model display a common trend in that $K_L a$ increases with f'. The ratio of the interfacial area per unit volume of the passage (a) is approximately equal h^{-1} and independent of f', so any change in the volumetric mass transfer coefficient is due only to change in K_L. The direct relation between K_L and the individual mass transfer coefficients and f' is given in Chapter 3 (Eq. 3.26) as $K_L = (1/f' k_V + 1/k_L)^{-1}$. In this equation, it is clear that increasing f', will increase the contribution of the mass transfer effect in the gas flow (k_V) to the overall mass transfer coefficient. However, this holds only if the gas phase mass transfer

coefficient makes a significant contribution. In other words, the gas-side resistance ($1/f'k_V$) is not negligible in relation to that in the liquid side ($1/k_L$) and this occurs only if $f'k_V$ is similar in magnitude or smaller than k_L. The individual mass transfer coefficients can be calculated using the wide channel model. This model gives approximate values that can help to evaluate the contribution of the phases to the overall mass transfer. The calculated coefficients are shown in Fig. 7.5 below as functions of f' for the intermediate gas flow rate and $-f'q_n = 1$. The physical properties used in the model calculations are the averages of the values listed in Table 6.9 (Chapter 6).

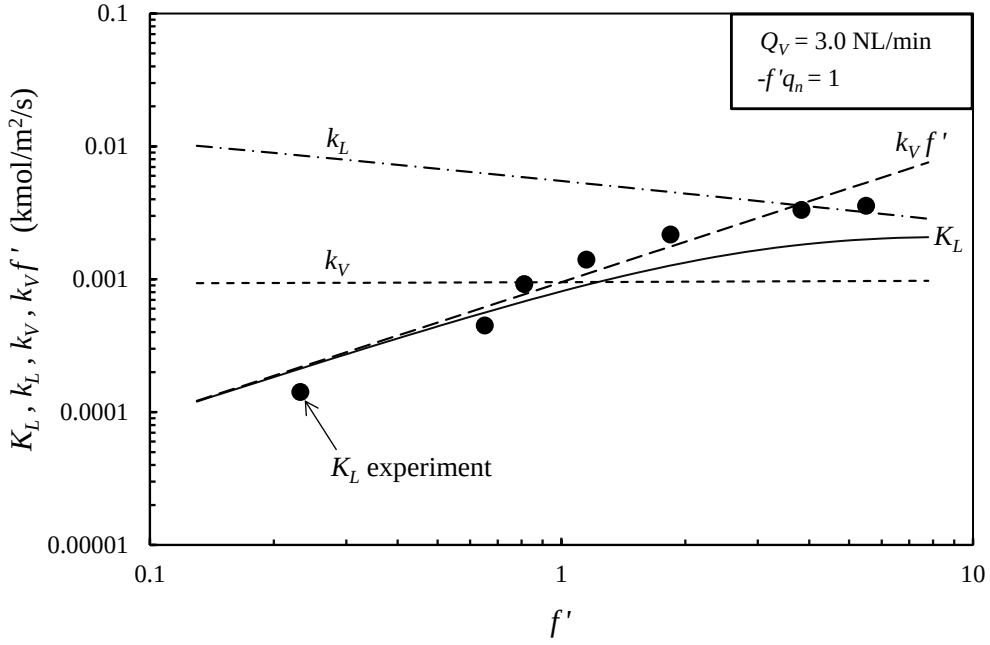

Figure 7.5. Wide channel model calculations showing the dependency of the mass transfer coefficients on f' for $-f'q_n = 1$ and Q_V = 3 NL/m. Symbols are corresponding values of K_L interpolated from the experimental results.

As can be seen in Fig. 7.5, k_V is roughly uniform while k_L decreases as f' increases. Both are expected since the gas phase flow rate and $-f'q_n$ are fixed. So the liquid phase flow rate must be increased as f' increases to maintain $-f'q_n = 1$. Any increase in the liquid phase flow rate leads to increasing the liquid layer thickness (diffusion distance). As a result, k_L decreases with f'. Comparing the contribution of the individual coefficients, k_L remains larger than the increasing value of $f'k_V$ up to about $f' = 4$. So, clearly, $f'k_V$ appears to have an appreciable effect on K_L over this range of the data.

Beyond f' = 4, the decrease in k_L value continues but remains modest below $f'k_V$ up to the maximum f' studied here, which is f' = 5.5. This also indicates that the overall coefficient continues to be affected to some extent by $f'k_V$ at this range of f' (4 < f' < 5.5).

The experimental values of K_L for all the studied systems at Q_V = 3 NL/min and $-f'q_n$ =1 are also shown in Fig. 7.5 (solid circle symbols). These values have been determined from the experimental K_La results interpolated to $-f'q_n$ = 1 using a specific interfacial area (a) calculated from the interface shape shown in Fig. 4.3, which is $a = 1.02/h^{-1}$. Comparing the experimental values to those from the wide channel model, the same pattern observed in Fig. 7.4 is revealed, as expected. Mass transfer in the experiments becomes increasingly more effective compared to the model results as f' increases, which corresponds to increasing Q_L at fixed Q_V and $-f'q_n$. This behaviour is again due to the convective effect of Coriolis motion in the liquid and the gas phase which can increase the contribution of both individual coefficients to K_L.

The results shown in Fig. 7.5 are for the intermediate Q_V and $-f'q_n$ = 1. At the higher and lower experimental gas phase flow rates the picture is the same, although the f' value for which $f'k_V = k_L$ is somewhat reduced for the higher value of Q_V and somewhat increased for the lower gas phase flow rate. Additionally, the general behaviour is not considerably change for other values of $-f'q_n$. Based on the analysis made in Fig. 7.5, therefore, it should be clear that the increasing K_La with f' observed in Fig. 7.4 is essentially because f' increases the effect of k_V. A plot of Φ_L would show exactly the same pattern of improvements with f' as that observed for K_La at a given $-f'q_n$. This is clear since Φ_L differs from K_La only by the value of the $-f'q_n$ function, $(1+f'q_n)/f'q_n \ln(-f'q_n)$, and the liquid phase molar density (n_L), according to Eq. 3.43. The function is fixed for a given value of $-f'q_n$ and n_L is roughly constant (Table 6.9). Accordingly, Φ_L also increases with f' at given $-f'q_n$ and Q_V values.

7.2.1.2 Effect of $-f'q_n$

The other main point emerging from the experimental results shown in Fig. 7.4 concerns the behaviour of $K_L a$ as $-f'q_n$ varies. It is helpful to consider first the results for f' = 3.83. At this particular f', $K_L a$ shows, interestingly, a common pattern for each of the three Q_V values: it first increases, reaches a peak and then decreases as $-f'q_n$ increases. Considering the effects of the end walls outlined previously (interface shape and Coriolis motion), one can understand the causes of this pattern observed at f' = 3.83. At a fixed Q_V, increasing $-f'q_n$ corresponds to decreasing the liquid phase flow rate. As a consequence, the liquid layer thickness is also decreasing since the component $\rho_L R \sin\alpha\, \Omega^2$ is constant. At Ω = 3200 rpm used in the experiments, the profile of the liquid layer is approximately uniform at the central region with the menisci at the ends. Since the interface shape is independent of the flow, these menisci have constant heights (h_m) relative to the central layer and are not influenced by changing Q_L or the associated change in the liquid layer thickness. In the experiments, for example, the meniscus height on the glass side remains at about 180 μm while the thickness of central region drops from about 120 to 20 μm (MacInnes and Zambri, 2015) over the range of Q_L spanned by the data. To give a clear sense of how this can change the flow section of the liquid phase, Fig. 7.6 shows these two extremes of liquid layer thickness with interface and channel drawn to scale.

Considering the dependence of liquid flow passage on the liquid layer thickness shown in Fig. 7.6, it seems clear that the solute mass flux, which is inversely proportional to h_{Lm}, will be larger in the middle of the layer than the corners. So, as $-f'q_n$ increases, for f' = 3.83 in Fig. 7.4, the liquid phase flow rate decreases and hence the mass transfer coefficient in the liquid side (k_L) rises as a result of the decreasing h_{Lm}. Consequently, $K_L a$ increases reaching a peak value at a certain $-f'q_n$. By further increasing $-f'q_n$, however, two main effects occur in terms of the flow and hence the mass transfer. First, the central layer becomes very thin (as in Fig. 7.6 b) and barely allows to a small amount of liquid to flow because of high shear stresses developed in this region. In this case, a great fraction of the overall flow will be in the corner regions where the diffusion distance is large and the mass transfer in the central thin layer becomes not important. Second,

the strength of Coriolis motion decreases as a result of decreasing the liquid phase flow rate. Thus, an effective Coriolis convection in the corner regions is not to be expected. As direct consequence of these two effects, the liquid phase mass transfer coefficient drops at large $-f'q_n$ values as most of the liquid phase flows in the corner regions where the mass transfer is poor (large diffusion distance associated with weak Coriolis convection). Further, it is clear in Fig. 7.4, again for f' = 3.83, that the position of the peak shifts to larger $-f'q_n$ as Q_V increases. At larger Q_V, a particular value of Q_L leads to a larger $-f'q_n$ value. This suggests that there is a certain liquid phase flow rate, and hence liquid layer thickness, that determines the peak. It is known from the hydrodynamic study of MacInnes and Zambri (2015) and the computational results shown in Chapter 4 (Fig. 4.17) that the gas flow rate does not greatly affect the liquid layer thickness. So it should be expected that the liquid flow rate must be the same at the peak regardless of the gas flow rate.

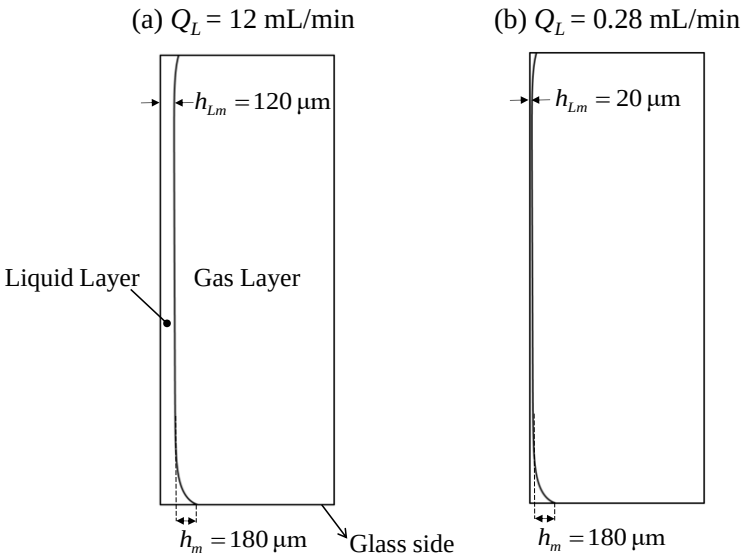

Figure 7.6. Liquid layer thickness at the minimum point (h_{Lm}) and the meniscus height at the glass side (h_m) measured by MacInnes and Zambri (2015) at liquid phase flow rates correspond to the maximum and the minimum liquid flow rate used in the current work.

Another behaviour observed in Fig. 7.4 is that for the other values of f', the same pattern (i.e. rise and fall in mass transfer coefficient with increasing $-f'q_n$) is not evident. Perhaps, this is because that the other systems are less affected by the variation in the liquid layer thickness and hence Q_L. This was the case for f' = 0.232 and 0.812

at $-f'q_n = 1$ according to the wide-channel results shown in Fig. 7.5. A similar analysis can be made over the range of $-f'q_n$ which covers the range of the experiments. This is shown in Fig. 7.7 for the three representative values of f' shown in Fig. 7.4. For each phase and solute system, the physical properties listed in Table 6.9 (Chapter 6) are used in the WCM calculations. As can be seen clearly in the figure, the individual liquid phase mass transfer coefficient (k_L) affects, in general, the overall coefficient at large f', but it diminishes as decreasing f'. This supports the idea that the small values of f' have an overall coefficient that is less affected by k_L over the experimental range of $-f'q_n$. Thus, a pronounced peak might not be expected at $f' = 0.232$ and 0.812. Similar behaviour to that just described for $f' = 0.232$, 0.812 and 3.83 is found for $f' = 0.651$, 1.15 and 5.5, which are shown in Fig. 7.8. Again, a clear peak is observed only for the largest value of f', although $f' = 1.15$ data may capture the tailing off from peak.

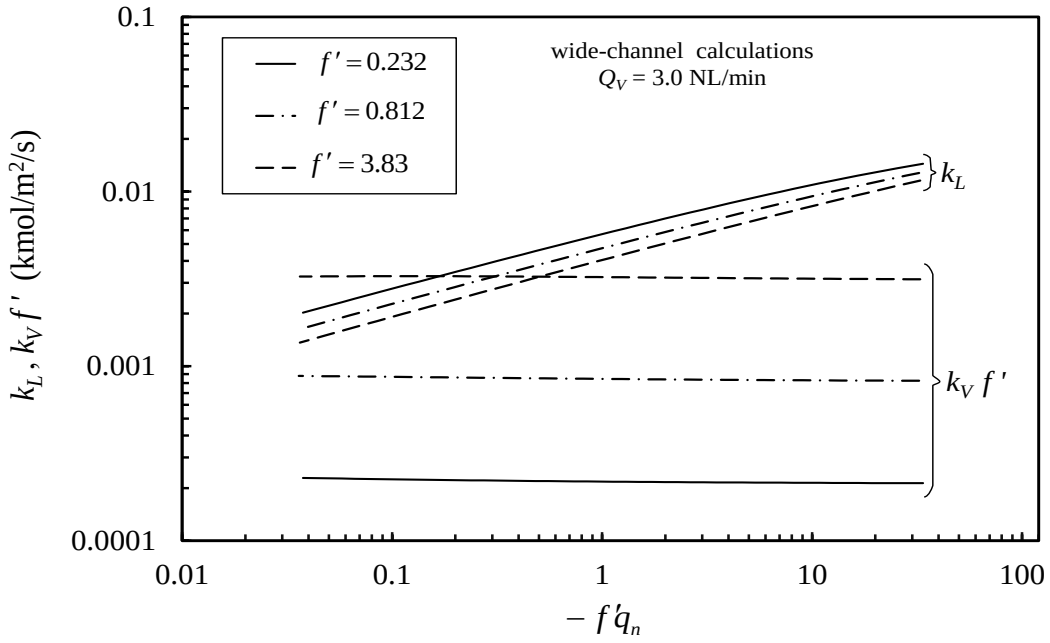

Figure 7.7. Variation of individual mass transfer coefficients with the purification factor for infinitely wide channel. Solid lines are values for the three f' in Fig. 7.4 at $Q_V = 3$ NL/min.

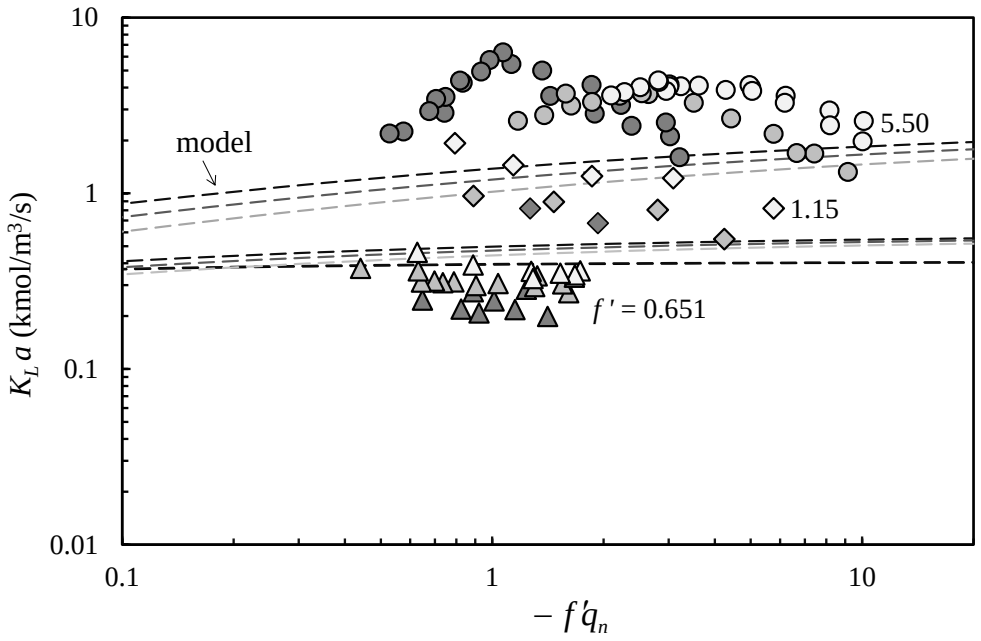

Figure 7.8. Overall volumetric mass transfer coefficients for three different values of f' (0.651, 1.15 and 5.5). Again, the dashed lines are the wide channel model results at the corresponding conditions and shaded as the experimental points (dark to light as Q_V increases).

7.2.2 Liquid Layer Thickness

The above results suggest that there is a particular value of liquid layer thickness at which the peak in mass transfer coefficient occurs. Direct support for this idea is possible by plotting $K_L a$ as a function of the liquid layer thickness. As mentioned in Chapter 2, liquid layer thickness measurements at the minimum point of the layer are reported in MacInnes and Zambri (2015) over a wide range of liquid viscosity. These measurements were taken at the same rotation rate and range of liquid phase flow rate used in the present experiments, but at a fixed gas phase flow rate equal to 1.15 NL/min. Although this gas phase flow rate is lower than those used here, the liquid layer thickness at 3200 rpm is relatively not sensitive to the level of the gas phase flow rate as shown in the computations made in Chapter 4 (Fig. 4.17). Accordingly, these measurements are applicable to the conditions of the present experiments. Fig. 7.9 below shows all the liquid layer thickness data (symbols) and they are plotted as a function of $\mu_L Q_L$.

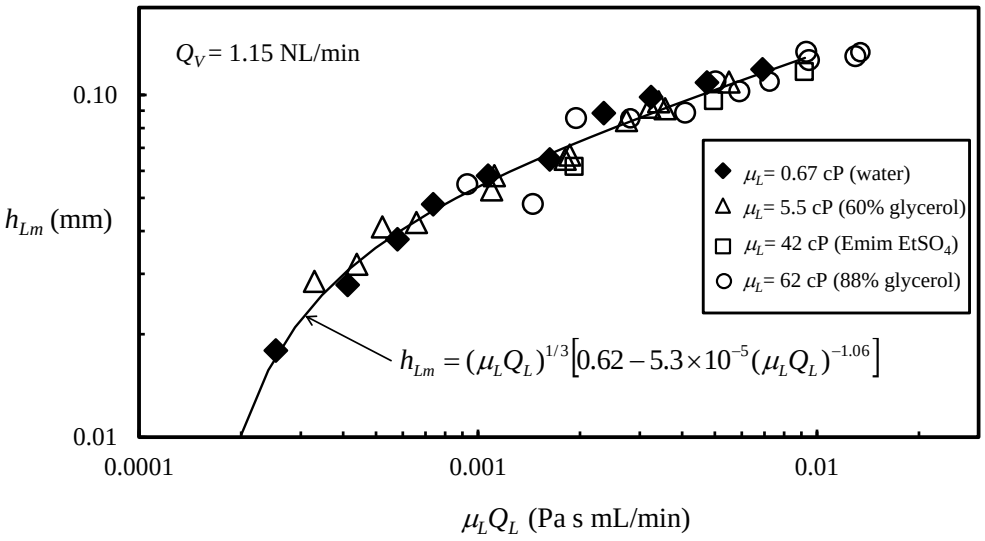

Figure 7.9. Correlation for liquid layer thickness as a function of $\mu_L Q_L$ for the experimental channel and 3200 rpm rotation rate. Data are reported in MacInnes and Zambri (2015).

As can be seen, the data collapse well even though there is a difference of about two orders of magnitude between the lowest and highest viscosity tested in that work. Essentially, plotting the data against the parameter $\mu_L Q_L$ eliminates the difference in viscosity between the tested fluids since any decrease in viscosity will need an increase in the liquid flow rate to produce the required shear stresses to maintain a given liquid layer thickness (MacInnes and Zambri, 2015). In this way, representing the data by a single correlation is possible and this is indicated as a solid line in Fig. 7.9 (in terms of h_{Lm} and $\mu_L Q_L$ in the units given in the axis labels). This function enables the liquid layer thickness for each experimental point in the present work to be determined using the measured liquid phase flow rate for that point and the corresponding viscosity value from Table 6.9. Additionally, it has been demonstrated in the previous section (Figs. 7.4 and 7.8) that $K_L a$ has a significant dependency on f'. This can be removed approximately by normalising the overall mass transfer coefficient by f' so $K_L a / f'$ instead of $K_L a$ is plotted against h_{Lm} determined from the correlation in Fig. 7.9. Fig. 7.10 shows these results where explicitly the relation between the overall mass transfer coefficient and liquid layer thickness for all the seven systems at the three different gas phase flow rates can be seen.

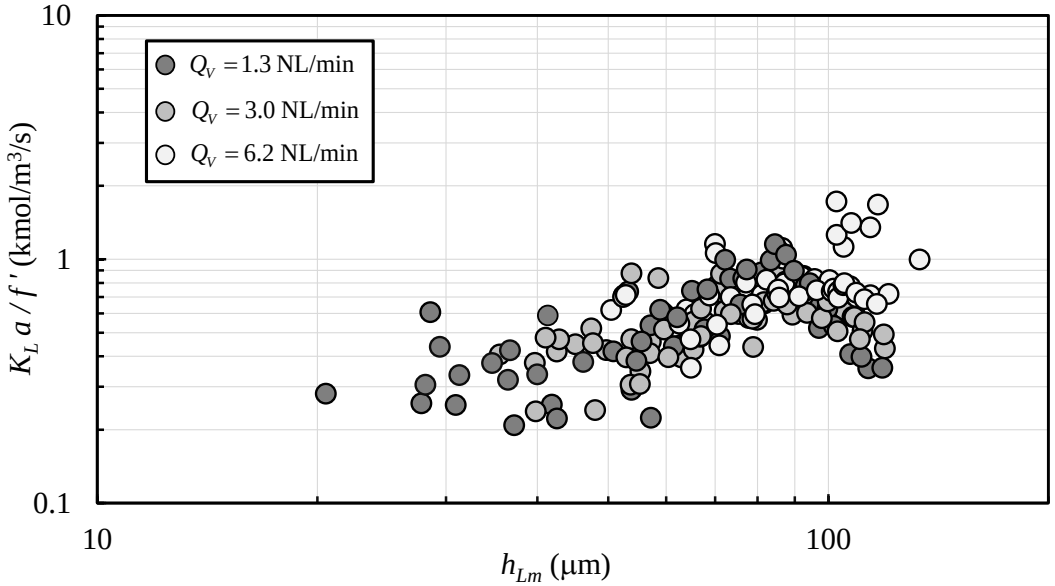

Figure 7.10. All data for normalised overall volumetric mass transfer coefficient plotted as a function of liquid layer thickness.

Interestingly, the above figure shows that the data for the most part cluster together revealing a common peak, an approximately at a liquid layer thickness of around 80 to 90 μm for these phase and solute properties and this particular channel under rotation rate of 3200 rpm. The data that deviate (in particular, those at large h_{Lm} which lie right above the clustered points) correspond to systems with f' = 0.232, 0.812 and 1.15. As one may note in Table 6.9, these f' values are achieved with relatively low temperatures and hence have relatively large values of viscosity. Viscosity for acetone at 24 °C (f' = 1.15) and for ethanol at 30 °C (f' = 0.232), for example, are about double the typical viscosity level and that for acetonitrile at 30 °C (f' = 0.812) is about 50% larger than typical. At a constant centrifugal body force and fixed layer thickness, such high viscosities correspond to low liquid flow rates (Fig. 7.9). Accordingly, the Coriolis motion in the liquid layer are further damped for these systems due to decreasing the liquid phase flow rates. Thus, these systems might have $K_L a$ values which are affected by the mass transfer processes in the liquid side at different h_{Lm} and hence a shift in peak position. The effect of viscosity could be augmented by the level of the gas phase flow rate since these points collected at Q_V = 6.2 NL/min. The strength of Coriolis secondary motion in the gas phase increase with Q_V and consequently this changes the relative contribution of the indivudal mass transfer coefficents ($f' k_V$ and k_L) to $K_L a$. In this case, it must be expected that the experimental points at the largest Q_V will have $f' k_V$ shifted upwards

from what is shown in Fig. 7.7, increasing at these points the impact of k_L on the overall coefficients which is essential to determine the peak.

Despite the deviation in some data, the peak observed in Fig. 7.10 demonstrates clearly the flexibly of rotating spiral contactor to operate at the optimum $K_L a$ by varying only the liquid phase flow rate, independent of the gas phase flow rate. This likely indicates that the optimum $K_L a$ can always be adjusted to occur at the optimum $-f\dot{q}_n$ by varying only the gas phase flow rate, thus simultaneously optimum contactor size and optimum usage of solvent can be achieved.

7.3 Performance Comparison

Up to this point, the mass transfer characteristics of the experimental spiral have been demonstrated over different solute properties and a range of phase flow rates. These mass transfer data can be used now to assess the performance of rotating spiral contacting relative to alternative gas-liquid counter-current contacting approaches. The parameter used to judge the contacting performance is the total specific throughput. This parameter has been presented in Chapter 3 (Eq. 3.47) and defined as the volume flow rate of the phase being treated (the gas phase for absorption or the liquid phase for desorption) divided by the passage volume of the contactor used. So higher specific throughput means a smaller contactor size is required to produce the same throughput at the same degree of purification or, equally, means for the same contactor size a higher throughput can be achieved at a given purification.

The two different categories of contactors discussed in Chapter 2 are considered in this comparison: the parallel-flow and the dispersed-phase contactors. For the former, the data reported by Adiche (2018) for desorption of acetone-water-N_2 system using a membrane microchannel contactor are considered. For the latter, data for the conventional packed column, which is commonly used in industry, and the rotating packed bed, which has emerged recently as a proposed way of improving mass transfer by using enhanced body force, are used. Houston and Walker (1950) reported mass transfer data for the packed bed column over a wide range of both gas and liquid flow rates. Similar to the experiments done here, they studied the mass transfer of different solutes having different f' between air and water contacting counter-currently. For the rotating packed bed, mass transfer of different solutes using different packing types have been studied by many authors and again for the same phase system (water-air) and over a range of gas and liquid flow rates. This includes studies carried out by Liu et al. (1996), Chen and Liu (2002), Lin et al. (2004), Lin and Chien (2008), Chiang et al. (2009) and Hsu and Lin (2012). All these studies are summarised in Table 7.1 where the values of void fraction (ε) and solute equilibrium distribution (f') are given. The values of ε listed are needed to convert the volumetric mass transfer values from a column or bed basis to a flow passage basis. The values of f' are taken from equilibrium information in the papers and are needed to calculate the total specific throughput values from the reported mass transfer coefficients.

Table 7.1. Parameters and conditions for the packed column, rotating packed bed and membrane microchannel assembled from literature.

Reference	Solute (f')	T (°C)	Packing	void fraction ε	Mode
Packed Column Data					
Houston & Walker (1950)	ethanol (0.322) methanol (0.282) ammonia (1.08) acetone (2.52)	27	Raschig rings	0.72	absorption
Rotating Packed Bed Data					
Liu et al. (1996)	ethanol (0.220)	20	rectangular solids	0.53	desorption
Chen & Liu (2002)	isopropyl alcohol (0.612) acetone (2.37) ethyl acetate (7.47)	25	beads	0.40	absorption
Lin et al. (2004)	isopropyl alcohol (0.612) ethyl acetate (7.47)	25	wire mesh	0.96	absorption
Lin & Chien (2008)	ethanol (0.290) acetone (2.37) ethyl acetate (7.47)	25	wire mesh blades	0.99	absorption
Chiang et al. (2009)	ethanol (0.389)	30	wire mesh	0.94	absorption
Hsu & Lin (2012)	methanol (0.275) 1-butanol (0.663)	25	wire mesh blades	0.99	absorption
Membrane Microchannel Data					
Adiche (2018)	Acetone (1.77)	23	-	0.39	desorption

7.3.1 Absorption Relations

Most of the studies listed in Table 7.1 are for absorption and the relations in Chapter 3 used for the spiral desorption data do not apply directly. However, as for desorption, mass transfer relations for a solute being transferred from the gas phase to the liquid phase can be derived using the same quantities (q_n, f' and ξ) and the coordinate system given in Chapter 3 (Fig. 3.1). Thus, using the definitions of these quantities in terms of heavy phase 'L' and light phase 'V', the corresponding absorption relations may be expressed as:

Corresponding to Eq. 3.32: $$\frac{-K_V a\, L}{n_V w_{VB}(1-\xi)} = \frac{Y_{VB}(L)-Y_{VB}(0)}{\overline{\Delta Y_{VB}}} \tag{7.2}$$

Corresponding to Eq. 3.42: $$\ell_e = \frac{n_V w_{VB}(1-\xi)}{K_V a}\frac{\ln(-f'q_n)}{(1+f'q_n)} \tag{7.3}$$

Corresponding to Eq. 3.43: $$\Phi_V = \frac{-w_{VB}(1-\xi)}{\ell_e} = \frac{-K_V a}{n_V}\frac{(1+f'q_n)}{\ln(-f'q_n)} \tag{7.4}$$

Corresponding to Eq. 3.45: $$\frac{-K_V a\, L(1+f'q_n)}{n_V w_{VB}(1-\xi)} = \ln\left\{\frac{1-f'a_L+f'q_n(1-a_V)}{a_V-f'a_L}\right\} \tag{7.5}$$

Corresponding to Eq. 3.46: $$N_e = -\frac{1}{\ln(-f'q_n)}\ln\left\{\frac{1-f'a_L+f'q_n(1-a_V)}{a_V-f'a_L}\right\} \tag{7.6}$$

Corresponding to Eq. 3.47: $$\Phi_{VN} = \frac{\Phi_V}{N_e} = \frac{K_V a}{n_V}(1+f'q_n)\left[\ln\left\{\frac{1-f'a_L+f'q_n(1-a_V)}{a_V-f'a_L}\right\}\right]^{-1} \tag{7.7}$$

For the rotating packed bed, the average product of the mass transfer coefficient and specific interfacial area can be used in the calculations. This gives:

Corresponding to Eq. 3.54: $$-\frac{\overline{K_V a}\,\pi H\varepsilon(r_O^2-r_I^2)}{N_V} = \frac{Y_{VB}(r_O)-Y_{VB}(r_I)}{\overline{\Delta Y_{VB}}} \tag{7.8}$$

Corresponding to Eq. 3.56: $$\Phi_V = -\frac{\overline{K_V a}}{n_V}\frac{(1+f'q_n)}{\ln(-f'q_n)} \tag{7.9}$$

The relation of number of stages for rotating packed bed is exactly as that for packed bed column (Eq. 7.6). Consequently, the same equation of the total specific throughput is obtained (Eq. 7.7) and used for rotating packed bed since $\Phi_{VN} = \Phi_V / N_e$.

7.3.2 Normalised Specific Throughput

For absorption, Eq. 7.7 can now be used to calculate the total specific throughput and hence a comparison of results for absorption and desorption is possible, although this requires two adjustments. First, the volumetric flow rate used in the specific throughput for absorption is inherently greater than that for desorption. This is due to the large difference between the densities of the gas and the liquid phases. Such difference in specific throughput can be adjusted easily by using molar flow rate rather than volumetric flow rate per passage size. This means multiplying the specific throughput by the phase molar density, i.e. $n_V \Phi_{VN}$ and $n_L \Phi_{LN}$. Secondly, the increasing $K_L a$ and hence specific throughput with f' for desorption can be adjusted approximately by dividing $n_L \Phi_{LN}$ by f' (as for $K_L a$ in Fig. 7.10). For absorption, such adjustment is not needed since $K_V a$ is less sensitive to f', provided that the gas phase mass transfer coefficient dominates the overall coefficient. This can be seen in the relation between f' and K_V: $K_V = (1/k_V + f'/k_L)^{-1}$ (Eq. 3.26). So the final normalised total specific throughputs allowing comparisons across different approaches, mass transfer modes and conditions are $n_V \Phi_{VN}$ (absorption) and $n_L \Phi_{LN} / f'$ (desorption).

To make the comparison, the values of the total specific throughput are calculated from Eqs. 3.47 and 7.7 using the reported flow rates and the mass transfer coefficients in the case of the packed columns, rotating packed beds and membrane. Additionally, the removal of the solute is taken to be 90 % ($d_L = a_V$ = 0.1) which fixes the number of equilibrium stages in the total specific throughput relations (Eqs. 3.46 and 7.6). Experimental points violating the limit placed by f' on the phase flow rate ratio (e.g. Eq. 7.1 for desorption) simply means achieving this particular degree of separation is not possible. Thus, data with $-f'q_n$ less than $1 - d_L$ = 0.9 (for desorption) or $-f'q_n$ greater than $1/(1 - a_V)$ = 1/0.9 (for absorption) cannot be plotted, as occurs with all of desorption data of Liu et al. (1996) and some data for spiral and other approaches.

7.3.3 Comparison Results

Fig. 7.11 shows the normalised total specific throughput plotted against $-f'q_n$ for desorption and $-1/f'q_n$ for absorption. In this way, the abscissa measures solvent usage relative to the minimum possible for both absorption and desorption, placing the two operations on the same basis.

The rotating spiral data are indicated as red circles in Fig. 7.11 and cluster relatively in a coherent manner as a function of the purification factor. The grey diamonds are the Houston and Walker (1950) data for a static packed column. Unlike a rotating spiral, the packed column data tend to spread broadly in both the vertical and horizontal direction. Horizontally, the data extending far beyond $-1/f'q_n = 10$ simply indicates that an excessive amount of solvent (liquid phase) is used relative to the throughput of the processed gas phase. The spread of data in the vertical direction, on the other hand, is essentially a consequence of the gas flow rate used which affects directly the specific throughput. (The larger the gas phase flow rate the higher the specific throughput.) However, the highest points for the packed column are near the limit of the theoretical gas flow rate producing flooding (Houston and Walker,1950). As discussed in Chapter 2, the maximum allowable throughput of the gas phase in a packed column is normally determined by the flooding behaviour which is one of the inherent limitations in this approach. So the highest data of the packed bed shown in Fig. 7.11 are probably the maximum performance that can be achieved. Comparing to the rotating spiral channel, it is clear that the total specific throughput of the spiral is about three to four times larger than that for packed bed in the expected region of optimum operation which is around $-f'q_n$ between 2 and 4.

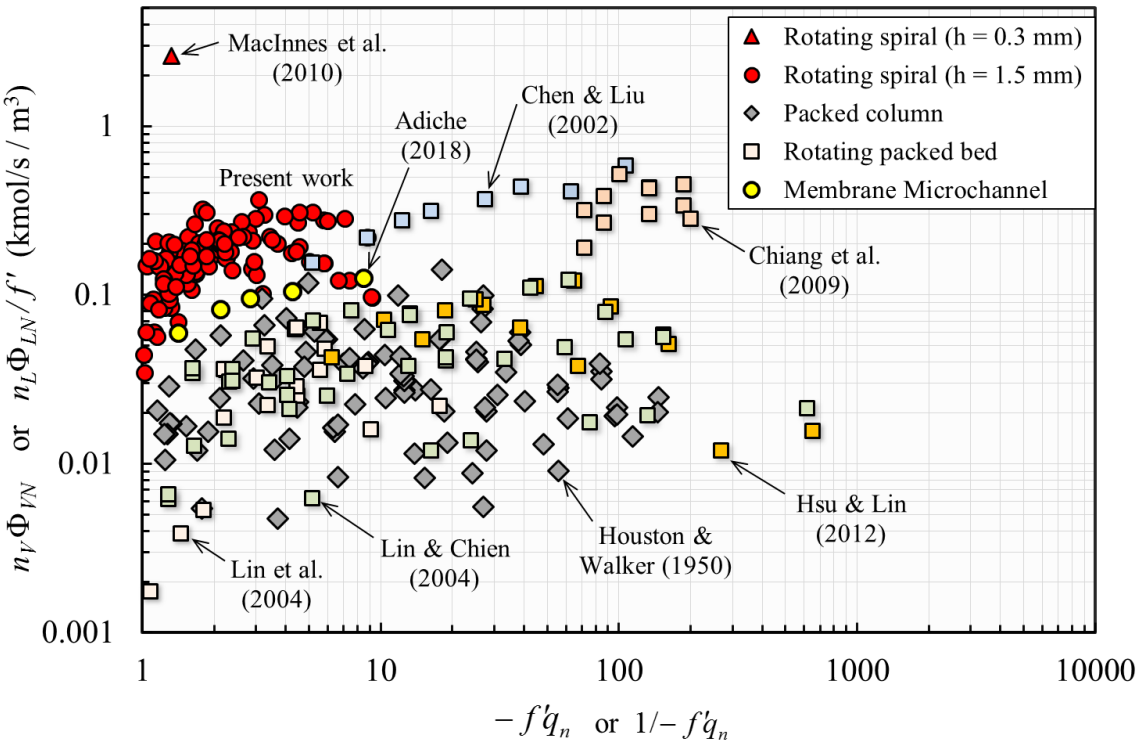

Figure 7.11. Total specific throughput based on a mole flow rate determined from experimental data for the rotating spiral, packed column, rotating packed beds and membrane microchannel over different phase flow rate, contacting conditions and mass transfer modes. Data for the packed bed, rotating packed bed and membrane are from the references listed in Table 7.1.

For rotating packed beds, the data are shown as squares with different shading. Similar to the packed column, these data extend to large $-1/f'q_n$, with some experimental points at phase flow rates ratio well above 100. This corresponds to over a one-hundred fold increase in the amount of solvent flow rate at a particular specific throughput and hence an excessive use of solvent flow rate. Over the large range of $-1/f'q_n$, a pronounced increase in the rotating packed bed performance can be observed for some data (Chiang et al., 2009 and Chen and Liu, 2002) relative to that for the packed bed. This improvement may be attributed to the enhanced body force which allows operation at higher gas phase velocity in relation to the static packed bed. This effect can be seen clearly in the plot of Sherwood correlation shown in Chapter 2 (Fig. 2.4) which shows the possible enhancement in gas phase velocity as increasing the acceleration term (i.e. replacing g by $R\Omega^2$). However, interestingly, such performance drops and becomes comparable to the performance of the conventional packed column as flow rate ratio

decreases below 10. This is except for two data points of Chen and Liu (2002) which achieve a specific throughput just 35% lower than for the rotating spiral in a range of $-1/f'q_n$ less than 10. Since all of the packed bed data in Fig. 7.11 (whether rotating or not) are for absorption, decreasing $-1/f'q_n$ corresponds to decreasing liquid phase flow rate. As mentioned in Chapter 2, Burns and Ramshaw (1996) observed that at low liquid flow rate the liquid phase travels through the rotating packed bed as segregated rivulets and flying droplets rather than continuous film, leaving most of packing area not effectively-wetted. Thus, at low liquid flow rate, one would expect that this maldistribution becomes more pronounced and hence the contacting efficiency decreases dramatically and becomes as that for the packed bed or even less (Lin et al. 2004). This is consistent with the experimental study carried out by Sandilya et al. (2001) which finds that the transfer coefficient of a conventional packed bed can be larger than that for a rotating packed bed as a result of this liquid phase maldistribution.

For the parallel-flow contactor, the data are shown as yellow circles. These data are for desorption of acetone from water into N_2 using membrane with two meandering channels: 3 mm for the gas phase and 100 μm for the liquid phase. While the phase and solute system and the contacting conditions are approximately similar to those achieved in the spiral, it is clear that the spiral data produce a larger specific throughput by a factor of 2 at $-f'q_n$ value between 2 and 4. This difference could be attributed to the presence of the Coriolis secondary motion in rotating spiral contacting and the additional mass transfer resistance added by membrane. These two factors must result in a better contacting in the spiral in relation to membrane microcontactor. However, it is clear that the performance of this contactor shows an improvement in relation to packed bed column by about 50% at $-f'q_n$ between 1 and 2.

Finally, increasing the spiral channel specific throughput can be achieved by decreasing the channel height (h). As pointed out in Chapter 2, stripping distillation of a binary system has been carried out by MacInnes et al. (2012) in a rotating spiral channel with h = 300 μm at Ω = 5000 rpm. The individual mass transfer coefficients have been computed over the full range of bulk mole fraction (Ortiz-Osorio et al., 2009) and these can be converted to specific throughput using Eqs. 3.26 and 3.47. This has been done by calculating $K_L a$ and f' at dilute concentration for the more-volatile species being

transferred from the liquid phase into the gas phase as for desorption process. The experimental point of MacInnes et al (2010) is shown as a red triangle in Fig. 7.11. As can be seen, this rough estimation gives specific throughput about 12 times greater than that for the 1.5 mm spiral channel used in the current experiments. Thus, reducing channel size appears to be a direct approach to improve the rotating spiral performance, without imposing any limitations.

7.4 Summary

Measurements of desorption of four different organic solutes from water into air were presented in this chapter over a range of water flow rates, air flow rates and solute equilibrium distribution. The results showed that that the spiral can handle this wide range of phase and solute systems achieving approximately solute-free water when the appropriate flow rate ratio is chosen. These mass transfer measurements were used to quantify the contacting effectiveness of the spiral, representing by the overall volumetric mass transfer coefficient based on the liquid side ($K_L a$). The results showed that the contacting effectiveness increases with f' due to increasing the gas phase contribution ($f' k_V$) to K_L. Also, interestingly, it was found that the mass transfer coefficient varies with $-f'q_n$, forming a clear peak at the three different gas phase flow rates for the large f' values. This behaviour depends on the liquid phase making a significant contribution to K_L. Exploration with the wide channel model, which can compute the individual mass transfer coefficients, suggests that K_L is more affected by the individual liquid phase mass transfer coefficient for the systems with f' = 3.83 and 5.5 than the other systems with lower f'.

Using the liquid layer thickness measurements reported in MacInnes and Zambri (2015) for the same channel, it was found that the peak in $K_L a$ occurs approximately at the same liquid layer thickness (80-90 μm), independent of the gas phase flow rate. This feature of rotating spiral contacting enables selection of gas phase flow rate to achieve the optimum phase flow rate ratio ($-f'q_n$) for a given solute and, at the same time, $K_L a$ is optimum.

At the end of the chapter, a comparison of spiral performance with the conventional packed column, rotating packed bed and membrane mircochannel contactors was made. The normalised specific throughput (molar flow rate of the treated stream divided by the passage volume) was used as the comparison criterion, where maximum specific throughput corresponds to minimum device volume to achieve a given separation. Interestingly, it was found that the rotating spiral is able to operate in the appropriate range of phase flow rate ratio and gives the highest normalised specific throughput, demonstrating clearly the capability of this approach to produce a controlled contacting.

While the wide-channel model captures some trends of the data, considerable differences were found due to the effect of end walls in the experimental channel. This makes it necessary to include this effect to understand the mechanism of mass transfer in the experimental channel. For this purpose, the 2-D computational model presented in Chapter 4 will be used and the results are given in the next chapter.

Chapter Eight

Computational Results

This chapter is about the results obtained following the 2-D computational model presented in Chapter 4. The chapter is divided into three main parts. The first presents computations to compare with the experiments of MacInnes and Zambri (2015). As pointed out, the 2-D model considers the case of a dilute solute where the mass transfer has no appreciable effect on the phase physical properties (density and viscosity). Therefore, the solution of the flow equations is completely independent of the species equation and can be handled separately. This opens up the possibility of using the hydrodynamic data reported in MacInnes and Zambri (2015) to assess the hydrodynamic part of the model separately before taking into account any mass transfer contribution. It is expected that such assessment would be helpful since it includes a direct comparison based on the liquid layer thickness which is, arguably, the most important parameter in terms of the mass transfer. The second part presents a comparison with the current mass transfer results, in particular the purification measurements and mass transfer coefficients presented in Chapter 7 (Figs. 7.2, 7.4 and 7.8). Finally, the chapter closes with a parametric study. The computations made in Chapter 4 demonstrate the effect of the gas and liquid flow rates at a fixed rotation rate. In this chapter, the focus will be on three further important parameters: rotation rate, channel aspect ratio and the variation of both the gas phase and liquid phase for a given phase and solute system.

8.1 Prediction of Liquid Layer Thickness

As mentioned previously, MacInnes and Zambri (2015) reported measurements of liquid layer thickness at the minimum point of the interface profile (h_{Lm}) for the air-water system. The experiments were conducted in the same channel described in Chapter 5. All the measurements were taken locally at the outer revolution of the channel, at a radial position of R_0 = 34 mm, over a range of conditions. Here, three sets of experiments are considered in which the value of h_{Lm} is measured over a range of liquid flow rate (Q_L), fixed gas flow rate (Q_V = 3.54 NL/min) and three different rotation rates (Ω =1480, 2400 and 3840 rpm). The operating conditions (pressure and temperature) for each rotation

rate are given in that same work and they are 2.1 bara (constant) and 307, 310 and 313 K, respectively, for 1480, 2400, and 3840 rpm (MacInnes and Zambri, 2015). So the density and viscosity of each phase are fully defined. Using the phase properties and values of the contact angles used in the previous computations (Table 4.2), the interface shape is computed individually at R_0 = 34 mm for each rotation rate as described in Chapter 4 (Section 4.3). Fig. 8.1 shows the computational geometry and the computed interface profile at the corresponding value of rotation rate. It is helpful to remember that while the interface has a fixed shape at each rotation rate, its position and hence h_{Lm} may change in response to flow rates.

Now, all the parameters required to predict the minimum liquid layer thickness (h_{Lm}) from the numerical solution are defined and these are:

- The geometry of the computational domains including the true shape of the interface (Fig. 8.1).
- The flow and continuity equations for each phase (listed in Section 4.2.4).
- The suitable boundary conditions (discussed in Section 4.4).
- The phase physical properties estimated at the experimental conditions and the other constant parameters such as $R\sin\alpha$ and Ω.

The numerical solution of the equations, however, is not intended explicitly to track the minimum liquid layer thickness. This is obvious since h_{Lm} is not one of the dependent variables. But instead the solution can determine the velocity profile in each phase and hence Q_L and Q_V at a given interface position (defined by h_{Lm}) and pressure gradient level (dp_0/dz). As pointed out, Q_V is fixed while Q_L is varying in the set of the experiments considered here. Thus, following the same solution approach described in Chapter 4 (Section 4.5.5), h_{Lm} can be predicted by only adjusting the level of dp_0/dz at a given h_{Lm} value such that Q_V calculated matches that measured experimentally while Q_L is determined from the solution. For each rotation rate, this same approach is employed over a range of Q_L covering that of the experiments. This is done with a maximum error less than 0.5 % between the predicted and the measured gas phase flow rate. The details of the results are discussed in the next section.

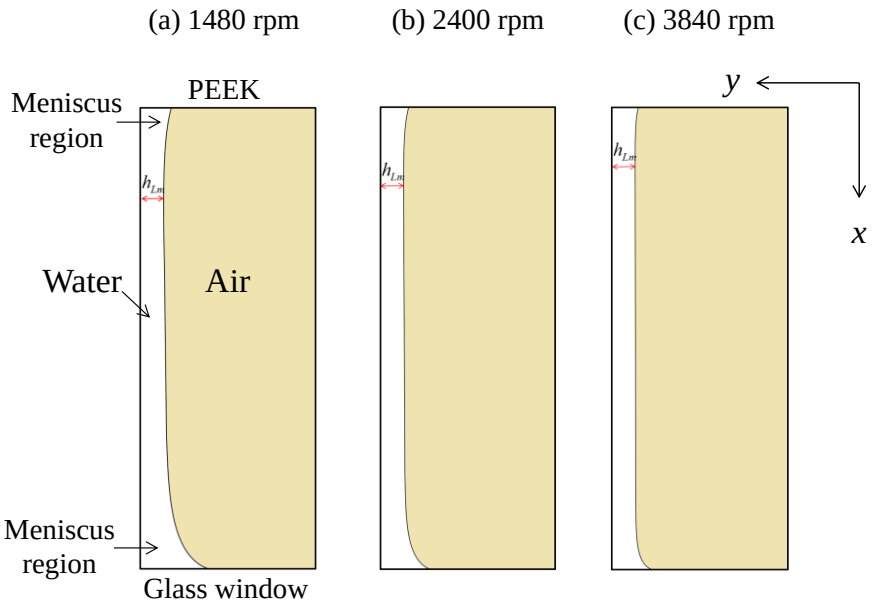

Figure 8.1. Computational geometry divided by an interface located at a particular h_{Lm} value. The interface is computed at radial position R_0 = 34 mm for conditions typical of the experiments: (a) T = 307 K, ρ_V = 2.41 kg/m^3 and ρ_L = 994 kg/m^3, (b) T = 310 K, ρ_V = 2.39 kg/m^3 and ρ_L = 992.2 kg/m^3 and (c) T = 313 K, ρ_V = 2.02 kg/m^3 and ρ_L = 992.13 kg/m^3. The pressure for all the cases is 2.1 bara.

8.1.1 Results and Discussion

Fig. 8.2 shows the h_{Lm} measurements (symbols) and the prediction of the 2-D model (red curves) as a function of Q_L for the three different rotation rates. The wide channel model (WCM) results, which are shown as grey dashed curves, are also included. These results are used here to provide the reference case of two phases separated by a flat interface.

As can be seen in Fig. 8.2, the general behaviour is captured well by the 2-D model and the results are in a good agreement with the experimental measurements, particularly at Ω=1480 and 3200 rpm. At Ω=2400 rpm, however, the 2-D model relatively under-predicts the minimum liquid layer thickness approximately at Q_L > 3 mL/min. The inset in Fig. 8.2 shows clearly the behaviour. This could be attributed to the experimental scatter which is obvious in the data at this rotation rate in relation to other values and that may lead to such difference.

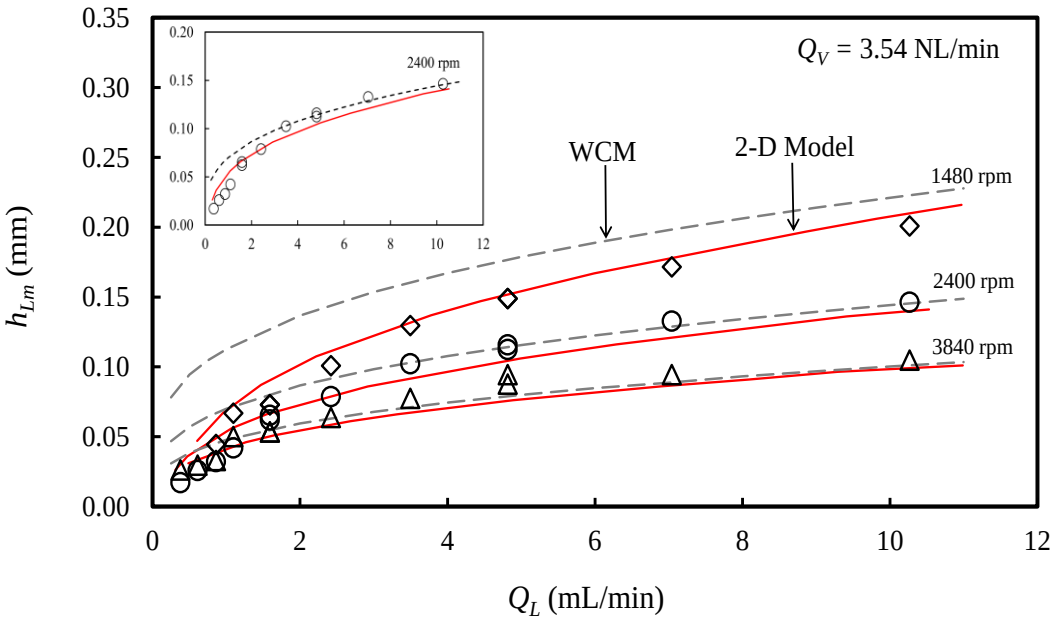

Figure 8.2. A comparison between the values of the minimum liquid layer thickness measured experimentally (symbols) and predicted by the wide channel model (grey dashed curve), and corresponding values predicted by the 2-D model (red curves) at Ω = 1480, 2400 and 3840 rpm.

In terms of the two models, it may be noted that the 2-D model and the WCD (dashed curve) are in agreement particularly at the high liquid flow rate and rotation rate. However, at low liquid flow rates and Ω =1480 rpm, there is a clear difference between the values of h_{Lm} predicted by the WCM and those of the 2-D model. This behaviour can be explained mainly in terms of the shape of the interface. At Ω =1480 rpm, the actual interface is tilted with large meniscus heights at the end-walls, as shown in Fig. 8.1 a. At low liquid flow rates, the liquid layer thickness is small and the areas of these menisci become a large fraction of the total flow area. In this case, the effect of the meniscus heights becomes significant in determining the flow since they lead to uneven distribution (higher local flow rate through the menisci regions than the middle of the layer). This effect is taken into account by 2-D model through the full representation of the interface shape and can be seen clearly in Fig. 8.3. The figure shows contour plots of the computed streamwise velocity component in the liquid phase at five different values of Q_L for Ω =1480 rpm. The area of the meniscus region is determined as that shown in Fig.8.3 (corner flow area). Based on this area, the ratio of the local flow rate in the meniscus region (Q_{LC}) to the total liquid phase flow rate is computed for each single case and is

given in the same figure (Q_{LC}/Q_L). Clearly from Fig. 8.3, a significant portion of the liquid phase flows in the corner (dark red core) due to the interface deformation. For Q_L = 0.6 mL/min, for example, 77% of the total liquid flow rate flows in the meniscus region, leaving the rest of the liquid passage carrying less than a quarter of the overall flow rate. However, this ratio decreases as Q_L increases since the middle of the layer becomes thicker and hence a larger area will be available for the liquid phase there, as expected. The wide channel model, on the other hand, considers a flat interface. This means that the flow is distributed evenly and hence at the same Q_L, a larger amount of fluid flows in the middle of the layer comparing to the amount in the actual situation (Fig. 8.3). This causes a thicker liquid layer thickness compared to that predicted by the 2-D model and that measured experimentally. Accordingly, a poor agreement with both the experiments and the 2-D model is seen in the results at Ω =1480 rpm.

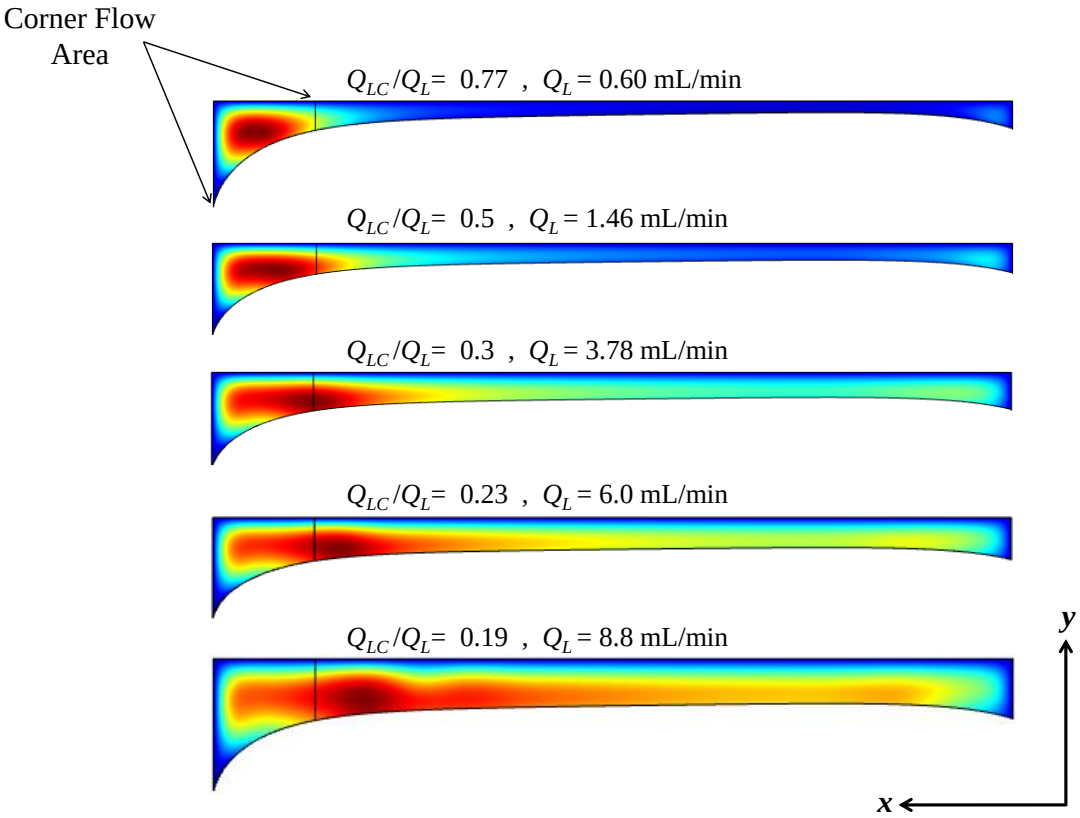

Figure 8.3. Contour plots of the streamwise velocity in the liquid layer at different liquid phase flow rates and Ω = 1480 rpm where Q_{LC} is the local liquid phase flow rate through the large meniscus region computed based on a corner area determined as shown in the figure.

However, as pointed out, the difference between the wide channel model and the 2-D model becomes smaller as the liquid flow rate and the rotation rate increase (e.g. $Q_L >$ 6 mL/min and Ω =3840 rpm in Fig. 8.2). Bearing in mind the effect of the interface shape on the liquid phase distribution, the reasons for this behaviour must be understood. As the rotation rate increases, the interface becomes less tilted with small menisci (nearly flat) as shown in Fig. 8.1. Add to that, the contribution of middle part of the layer becomes larger in relation to these small menisci as the liquid flow rate increases. Hence, one can infer that the combined effect of increasing the flow rate and the rotating rate makes the menisci to be much less important or even negligible and thus a good agreement with the WCM is obtained at both high rotation rate and high liquid flow rate.

8.2 Prediction of Mass Transfer Parameters

In this section, the results of the full 2-D model are compared to the experimental measurements of the current work. For the liquid layer thickness (Fig. 8.4), the comparison is made with h_{Lm} values measured at a fixed radial position in the channel with no mass transfer included. This simplifies the comparison since all needed is local information about the interface shape at this particular radial position and physical properties of pure air-water system, containing no solute. Here, the situation is different and there are some aspects needed to be considered in order to make a reliable comparison. The increasing radial position (R_0) with distance along a spiral channel means that the interface shape is not constant, but varies along the channel. Fig. 8.4 shows the interface shape computed at the inner, outer and an intermediate radial position along the experimental channel for 3200 rpm. As can be seen in the figure, most of the liquid layer is insensitive to the variation in R_0 value with relatively small changes confined at the lower end of the channel (glass side). So the effect is relatively modest and the interface shape used here is calculated using the intermediate radial position (25 mm) (Ayash and MacInnes, 2017).

Further, the value of the surface tension is taken to be that of pure water at 25 °C (0.07 N/m). In general, two parameters affect the surface tension: the temperature and the presence of the solute. The variation of surface tension with temperature is negligible within the experimental range. However, the presence of solute reduces somewhat the

water surface tension, depending on the amount and the chemical nature of the solute (Howard and McAllister, 1958; Roemer and Leppert, 1968; Vazquez et al., 1995; Yang et al., 1998; Rafati et al., 2010). Here, for example, the effect of adding 5% (by mole) ethanol to water reduces the water surface tension by about 35% while the effect of adding 2% (by mole) acetone is about one half that of ethanol. The effect of the maximum variation in surface tension on the interface shape is tested at R_0 = 25 mm and it is minor relative to the effect of R_0 shown in Fig. 8.4. So taking the value of water surface tension is suitable since the effect is small and confined at channel end. The other physical properties used in the interface calculations are the phase densities and these values are listed in Table 6.9. Finally, the contact angles are needed and they are taken as those shown in Table 4.2 which are for the air and water contacting in the same experimental channel (MacInnes and Zambri, 2015). These values are consistent with those reported in the relevant literature (Comyn et al., 1996; Kowalczuk and Drzymala, 2016).

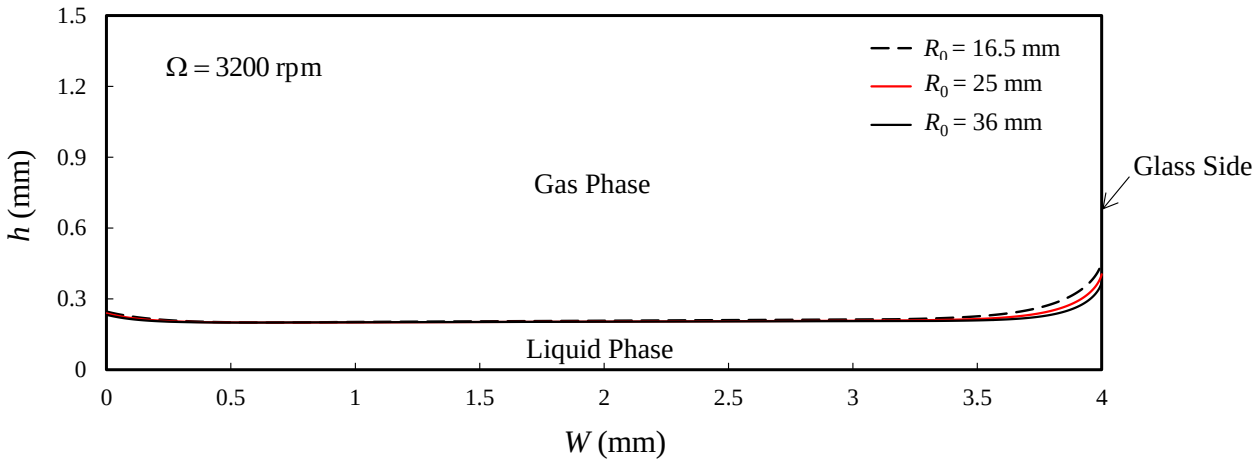

Figure 8.4. Interface shape computed at three different radial position corresponding to the inner, outer and an intermediate radial position along the experimental channel where $\sigma = 0.07$ (N/m), the phase densities are the average of the values given in Table 6.9 and the contact angles are those given in Table 4.2.

The approximations discussed above ensure the constancy of the interface shape along the channel. Using a fixed interface shape (red curve in Fig. 8.4), the numerical computation allows a prediction of the local mass transfer coefficients at certain values of bulk mole fraction level (Y_B) and bulk mole fraction gradient (dY_B/dz). Changing Y_B and dY_B/dz corresponds to performing computations at different locations along the

channel and hence an effective transfer coefficient can be determined. However, explorations of the effect of Y_B level and dY_B/dz for the experimental channel suggest a negligible effect of the choice of bulk value and gradient (Ayash and MacInnes, 2017). So which particular values are used is only constrained by a selection that avoids the value of mole fraction falling outside the physically-possible range of zero to unity at all positions in the section. Since the mass transfer coefficients do not depend significantly on the local value and gradient of bulk mole fraction, it follows that the mass transfer coefficients are exactly constant along the channel for the above approximations and it is unnecessary to compute mass transfer coefficients as a function of position along the channel.

8.2.1 Purification (d_L)

The d_L experimental values as a function of phase flow rates and the corresponding WCM results were discussed in Chapter 7 in relation to Fig. 7.2. Of these results, the values for f' = 1.15 and 3.83 are compared to those predicted by the 2-D numerical model. The data for those systems are selected since they show interestingly a pronounced difference in relation to WCM results. This difference is expected to be mainly due to the effect of the Coriolis secondary motion. So a comparison with these systems can clearly demonstrate the effect of this motion since it is taken into account by the 2-D model.

Fig. 8.5 shows the d_L values calculated for a series of computations spanning the experimental range of gas and liquid flow rates along with the experimental results. The experimental points are shown as open symbols (square, circle and triangle) while the corresponding red symbols represent the prediction of the 2-D model. For reference, the result for the wide-channel model (computed from the analytical solution given in Chapter 4) is also included in the figure and is shown as a shaded dashed curve, the lighter shade corresponds to the larger gas phase flow rate.

As can be seen in Fig. 8.5, the computation closely predicts the experimental findings and it is likely that the minor deviations observed are mainly the result of interface shape approximations and experimental uncertainties. Generally, the results show three essential characteristics. First, the degree of purification decreases, i.e. d_L

increases, with increasing the liquid phase flow rate due to decreasing liquid phase residence time. Second, the d_L decreases as the gas phase flow rate increases since that same phase can hold more solute. Finally, there is an improvement in the degree of purification as the value of f' increases, which is also due to increasing the capacity of the gas phase. All of these trends are captured by the two models but with different quantitative success. The differences, in general, become more pronounced as both Q_L and Q_V increase. Since in the wide-channel model there is no effect of secondary motion, it is natural to suspect that this motion is what causes the considerable improvement in the experiments and 2-D results comparing to WCM results.

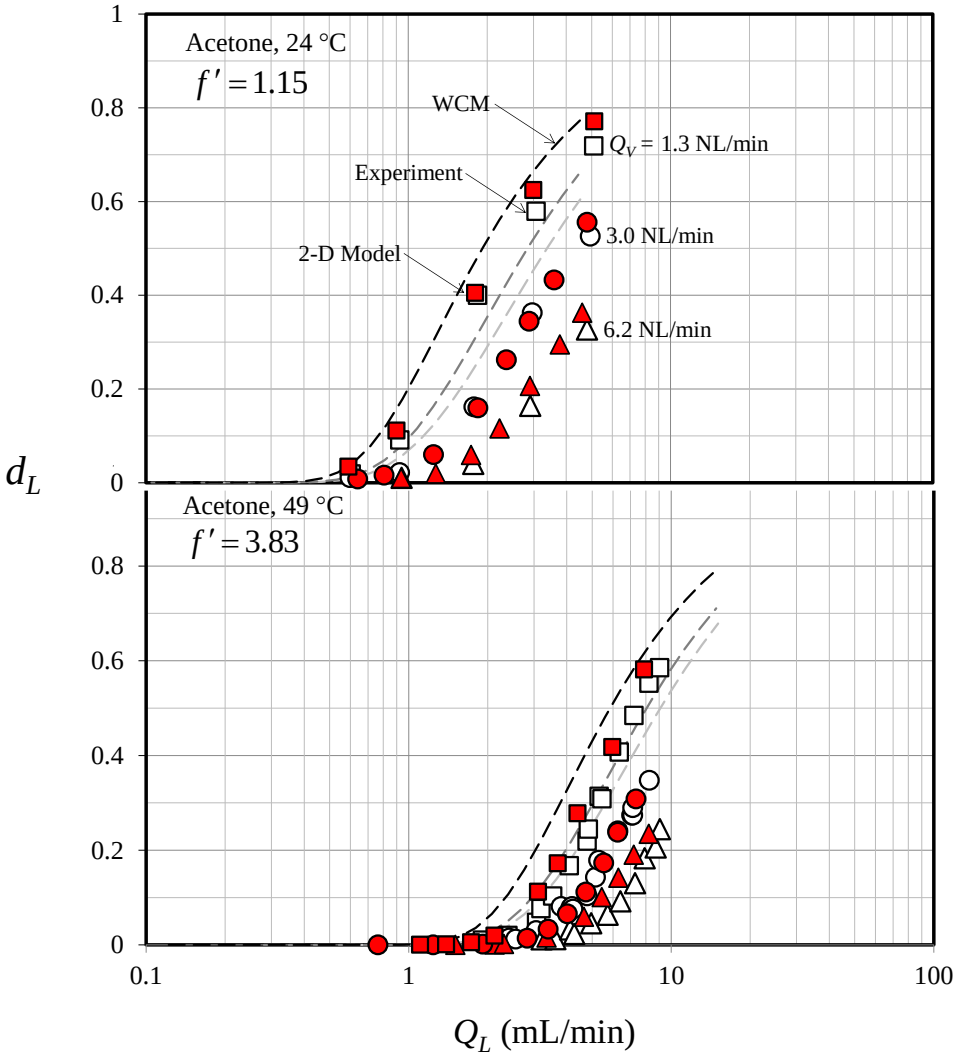

Figure 8.5. Measured purification (open symbols) and the prediction of the 2-D model (red symbols) at the three fixed gas flow rates over a range of liquid flow. The shaded dashed curves are the prediction of the wide channel model (the lighter shade corresponds to the larger Q_V value).

It is helpful at this stage to examine briefly the role of the secondary motion, that produces the improvement in mass transfer in relation to the WCM, using the 2-D model. This is done by making a series of computations with and without the Coriolis terms in the 2-D equations and solving for d_L. The data at Q_V = 6.2 NL/min for f' = 1.15 shown in Fig. 8.5 are selected for demonstration and the results are plotted in Fig. 8.6. First, the computation can be checked by reproducing the wide channel case. This is done by imposing a flat interface and introducing symmetry boundary conditions at each end wall. The results are shown in Fig. 8.6 as open circles and is clearly in agreement with the analytical solution (dashed curve). Reintroducing the end wall boundary conditions and the correct interface shape for the actual channel, but leaving out the Coriolis terms and hence the secondary motion, leads to the results at the same gas phase flow rate shown as cross symbols. It is clear from the results that the curving of the interface reduces the mass transfer significantly in relation to the flat interface results, particularly at low liquid phase flow rate. The hydrodynamic results discussed in the previous section indicate that at a low liquid phase flow rate the middle of the layer becomes thinner and the enlarged menisci regions divert most of the liquid flow (Fig. 8.3). Consequently, the reduction in the degree of separation values seen in the results (crosses) at low Q_L is because that the enlarged space for liquid flow in the regions of the menisci tend to reduce mass transfer by increasing both the characteristic streamwise velocity and diffusion length, overcoming the opposite tendency from the thinning of the central section of the liquid layer. Next, it proves interesting to add the Coriolis terms back into the equations, taking the computation back to the original result over the range of liquid flow rate (red triangles). As can be seen, the Coriolis terms in the gas phase and liquid phase bring the mass transfer coefficient up to the original level, proving clearly the strong effect of Coriolis secondary motion.

The series of computations shown in Fig. 8.6 decouples the effect of Coriolis secondary motion and the interface shape and, accordingly, two main points can be inferred, First, the Coriolis secondary motion is responsible for the difference between the WCM and the experiments, as expected. Second, the interface curvature (cross symbols) can decrease the mass transfer and this effect is much more pronounced as the liquid phase flow rate decreases.

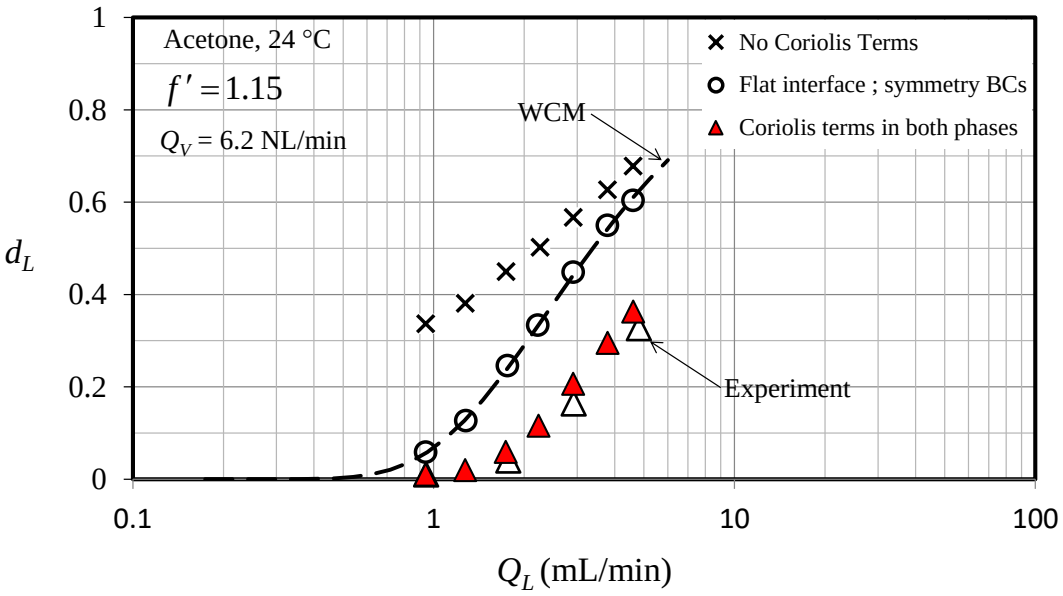

Figure 8.6. As in Fig. 8.5 for f' = 1.15 and Q_V = 6.2 NL/min over the same range of liquid flow rate. Red triangles are the 2-D computations, open triangles the experimental measurements and the dashed curve the wide-channel model result. The cross and the circle symbols explore the contribution of Coriolis motion and the interface shape to the mass transfer process in the experimental channel.

8.2.2 Mass Transfer Coefficient

The experimental mass transfer coefficients presented in Chapter 7 (Figs. 7.4 and 7.8) are now compared with the 2-D model predictions for the intermediate gas phase flow rate (3 NL/min). Figs. 8.7 and 8.8 below, which correspond to Figs. 7.4 and 7.8 respectively, show the experimental data (grey symbols) along with the 2-D predictions (red symbols). Again, the WCM result is included and it is shown as a dashed curve.

In general, for the different phase and solute systems, the results in Figs. 8.7 and 8.8 show that the 2-D computation convincingly captures the mass transfer performance over a large range of the experimental data. However, there are some differences which can be seen clearly at some values of f'. It is helpful to discuss first those seen at f' = 3.83 (Fig. 8.7) and f' = 5.5 (Fig. 8.8) where the 2-D model over-predicts the mass transfer coefficients at large values of $-f'q_n$.

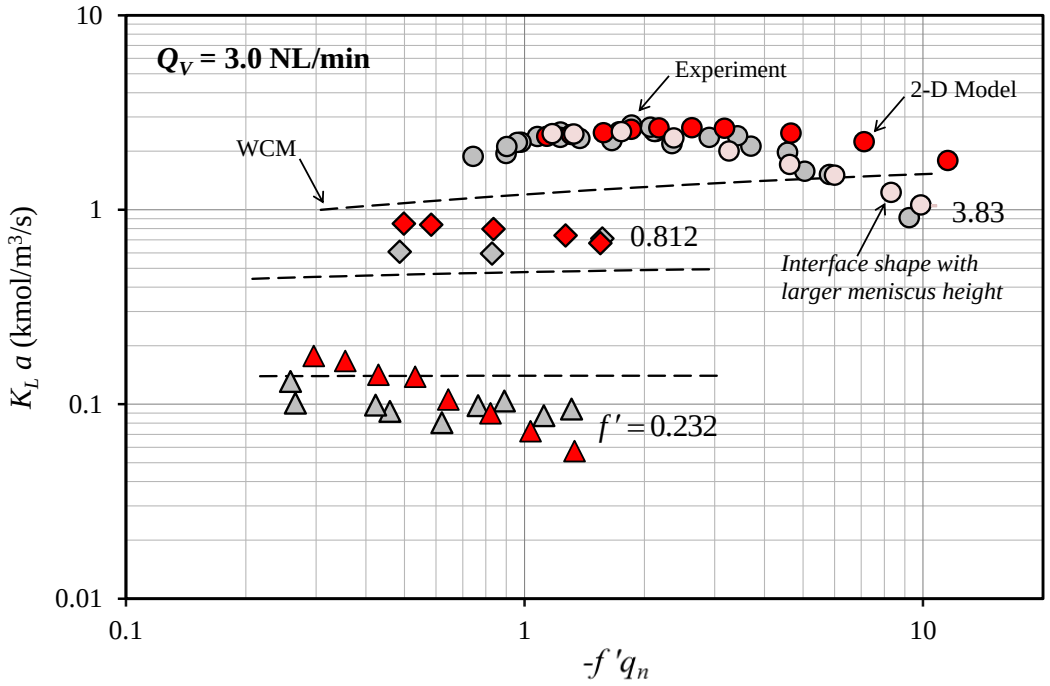

Figure 8.7. Overall volumetric mass transfer coefficients for three f' values (0.232, 0.812 and 3.83) at Q_V = 3.0 NL/min. The grey symbols are the experiments and the red ones are the 2-D model predictions at the corresponding conditions. The dashed lines are the wide channel model results.

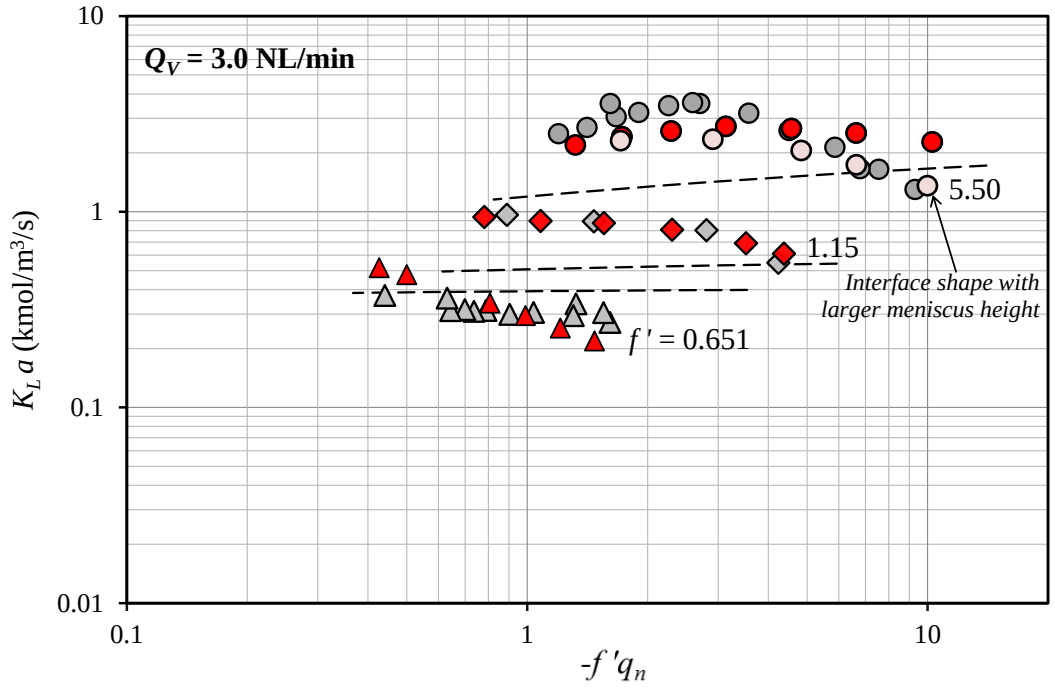

Figure 8.8. As in Fig. 8.7 but for f' = 0.651, 1.15 and 5.5. Again, the dashed lines are the wide channel model results at the corresponding conditions and the shaded symbols are the experimental points (grey points) and the 2-D results (red points).

Perhaps, it is not coincidence that the differences between the 2-D model and the data become noticeable at large $-f'q_n$ only for the two systems with high f' values. At a fixed gas phase flow rate, large $-f'q_n$ corresponds to small liquid phase flow rate. Further, for those two systems, the overall coefficient is strongly affected by the mass transfer resistance in the liquid phase over the whole range of $-f'q_n$. The WCM results discussed in Chapter 7 suggests this behaviour and is confirmed here by looking at the individual mass transfer coefficients predicted by the 2-D model. This is likely because such high f' values increase the contribution of the gas phase side in relation to that of liquid side according to the overall mass transfer coefficient relation, $K_L = (1/f' k_V + 1/k_L)^{-1}$. Thus, the discrepancy between the 2-D model and the data may simply be a consequence of the interface shape approximations (radial position, surface tension and contact angles) and hence the effect of liquid layer on k_L which determines K_L. At a relatively small liquid phase low rate, the flow and hence the mass transfer becomes especially sensitive to the size of the menisci regions. This view is consistent with the attenuation of mass transfer occurring at low liquid flow rate in Fig. 8.6 (the cross symbols). So any uncertainties in the interface shape and hence the menisci region sizes will translate directly into the mass transfer performance since these regions determine the character of the flow and the diffusion length at small Q_L values. This assessment is confirmed by repeating the computations for f' = 3.83 and 5.5 with an interface shape determined at R_0 = 16.5 mm. Because this radial position is less than that used in the computations (R_0 = 25 mm), the effective meniscus height will be relatively larger (Fig. 8.4) and hence a better agreement is expected. It is important to recognise here that this change in the meniscus height is artificial since R_0 is not constant along the channel. However, the same change may occur during the contacting process, simply, due to a variation in the contact angles by some degrees. The results with larger meniscus height are shown in Figs. 8.7 and 8.8 as circles with fainter shade. As can be seen, the small change in the meniscus height brings the model closer to the experiment at large $-f'q_n$. However, as $-f'q_n$ decreases, the liquid layer will thicken. Accordingly, the sensitivity to the meniscus heights, and hence the interface shape approximations, will be secondary and the 2-D model predictions are in agreement with the experiments irrespective of meniscus size.

One might argue that the same behaviour must be seen in the other systems, i.e. the difference between the 2-D model and the experiments increases with $-f'q_n$. This difference, as discussed, is mainly due to the effect of the meniscus heights on k_L and hence the overall coefficient (K_L) which is not necessarily the case as f' decreases. For f' = 0.812 (Fig. 8.7) and f' = 1.15 (Fig. 8.8), for example, the overall mass transfer coefficients are less affected by the mass transfer in the liquid side over the $-f'q_n$ range. So any small changes in meniscus height due to using an average radial position or larger values of surface tension and contact angles would have a small influence on the mass transfer performance. This probably explains the agreement of the 2-D model with the experiments for these intermediate values of f'. For f' = 0.232 (Fig. 8.7) and f' = 0.651 (Fig. 8.8), on the other hand, the situation is more complicated. The 2-D model shows a gradual increase as $-f'q_n$ decreases while the data are relatively less sensitive to $-f'q_n$ values over the experimental range if one considers the scatter in the data. It is useful to remember here that these systems are for ethanol and are tested in a lower range of liquid phase flow rate than for the other systems. For ethanol solution, the viscosity changes by about 30% along the channel (Table 6.8) so the liquid layer thickness is no longer constant along the channel. Further, since the experiments are carried out at small values of liquid phase flow rates, the effect of water evaporation is expected to be strong. This means that the liquid phase flow rate is not constant but changes significantly along the channel. The variation in both the viscosity and flow rate of the liquid phase is not taken into account by the 2-D model and that may lead to such anomalous behaviour which is observed only in the data of these systems (f' = 0.232 and f' = 0.651).

8.3 Model Parametric Analysis

The comparisons made in the previous sections show clearly the capability of the 2-D computational model to predict over a wide range of experimental conditions. So it can be employed now to demonstrate the effect of some key parameters which have not been tested experimentally. Three main parameters are considered in this study: rotation rate, channel aspect ratio and different phase flow rates. To simplify the task, desorption of acetone from water into air is taken as a reference case (f' = 1.15). The properties of this system used in the computations are given in Table 6.9. Further, the purification

factor is fixed at 1.2 (except where indicated otherwise) which is not expected to be unreasonable value for desorption process (i.e. $-f'_n > 1-d_L$).

8.3.1 Different Rotation Rates

One of the most key parameters that this technology is based on and is fully under external control is the rotation rate. The effect of rotation rate on the mass transfer process is examined here by computing for a range from 1000 to 20,000 rpm with the phase flow rates held constant at $Q_V = 3$ NL/min and $Q_L = 2.2$ mL/min ($-f'_n = 1.2$). This has been done by adjusting both the liquid layer thickness and dp_0/dz until the computed flow rates are correct. Fig. 8.9 shows the computed streamwise velocity, secondary flow and solute mole fraction distribution over the range of the rotation rate. In each contour plot, the colours are shaded from blue through green to red corresponding to the range of values from minimum to maximum. Also, it is important to note that the vector plots, which reveal the secondary flow, are plotted with an arrow length is proportional to the transverse velocity magnitude and using the same scale factor in all the cases for each phase.

In general, the three main features of gas-liquid contacting can be seen clearly in the results shown in Fig. 8.9: (1) small liquid layer with small vortices at the corners, (2) curved interface and (3) gas phase velocity skewness with strong Coriolis motion there. Interestingly, the rotation rate has a strong influence on these features. First of all, the effect of increasing the rotation rate on both the interface shape and thickness of the phase layers is evident in Fig. 8.9. As increasing Ω both the transverse centrifugal component ($R\Omega^2 \cos\alpha$) which determines the interface shape and the longitudinal component ($R\Omega^2 \sin\alpha$) that drives the liquid phase increase. So in the figure, the meniscus height, the interface tilt and the liquid layer thickness decrease simultaneously with the rotation rate, as expected. Fig. 8.10 shows the variation of the liquid layer thickness, which is represented by the liquid phase volume fraction (ξ), over the tested range of the rotation rate. As can be seen, ξ decreases by approximately a factor of 10 as the rotation rate increases from 1000 to 20,000 rpm.

Further, the effect of the rotation rate on the pattern of streamwise velocity, the strength of the secondary motion and hence the solute mole fraction distribution is also

evident in Fig. 8.9. Considering the gas phase first, increasing Ω increases the level of the Coriolis terms in v and w equations. Accordingly, the strength of Coriolis secondary motion and the distortion of the gas streamwise velocity profile become more pronounced with increasing the rotation rate. In the liquid layer, on the contrary, the streamwise velocity increases while the secondary motion diminishes as rotation rate increases. This, perhaps, is not surprising since increasing the rotation rate is associated with a sharp decrease in the liquid layer thickness, as shown in Fig. 8.10. As the layer thickness decreases, the viscous effect becomes important relative to the Coriolis effect and hence a weaker Coriolis motion generates. The order of magnitude of the viscous force relative to the Coriolis force, known as Ekman number, is readily estimated in each phase (e.g. Kheshgi and Scriven, 1985):

$$\mathrm{Ek}_L = \frac{\nu_L}{\Omega h^2 \xi^2} \qquad \text{and} \qquad \mathrm{Ek}_V = \frac{\nu_V}{\Omega h^2 (1-\xi)^2} \tag{8.1}$$

For the conditions of the computations in Fig. 8.9, the kinematic viscosity (ν) of the gas and liquid are 8.7×10^{-6} and 10^{-6} m^2/s, respectively, Ω ranges from 105 up to 2095 rad/s and the value of ξ varies from 0.15 at low rotation rate to about 0.015 at the highest (Fig.8.10). At low rotation rate, these values give Ek_L = 0.18 and Ek_V = 0.05. So, clearly, the magnitude of viscous force to Coriolis force is higher in the liquid side than that in the gas side. At high rotation rate, the forces become comparable in the liquid (Ek_L = 0.92) while their ratio decreases by about 25 times (Ek_V = 0.0018) in the gas. According to the values of Ekman number, the secondary flow is attenuated in the liquid side and it becomes more active in the gas as the rotation rate increases. This simple order of magnitude analysis suggests that the magnitude of the secondary flow in relation to streamwise velocity in the liquid side decreases with the rotation rate while it increases in the gas phase. Numerical values that support this suggestion are shown in Fig. 8.11 where the secondary flow is represented by $\overline{V}_L$ and $\overline{V}_V$ (the root mean square of the velocity in the liquid and gas phase section, respectively) and they are expressed as:

$$\overline{V}_L = \sqrt{\frac{1}{A_L}\left(\int_A u_L^2 \, dA_L + \int_A v_L^2 \, dA_L\right)} \qquad \text{and} \qquad \overline{V}_V = \sqrt{\frac{1}{A_V}\left(\int_A u_V^2 \, dA_V + \int_A v_V^2 \, dA_V\right)} \tag{8.2}$$

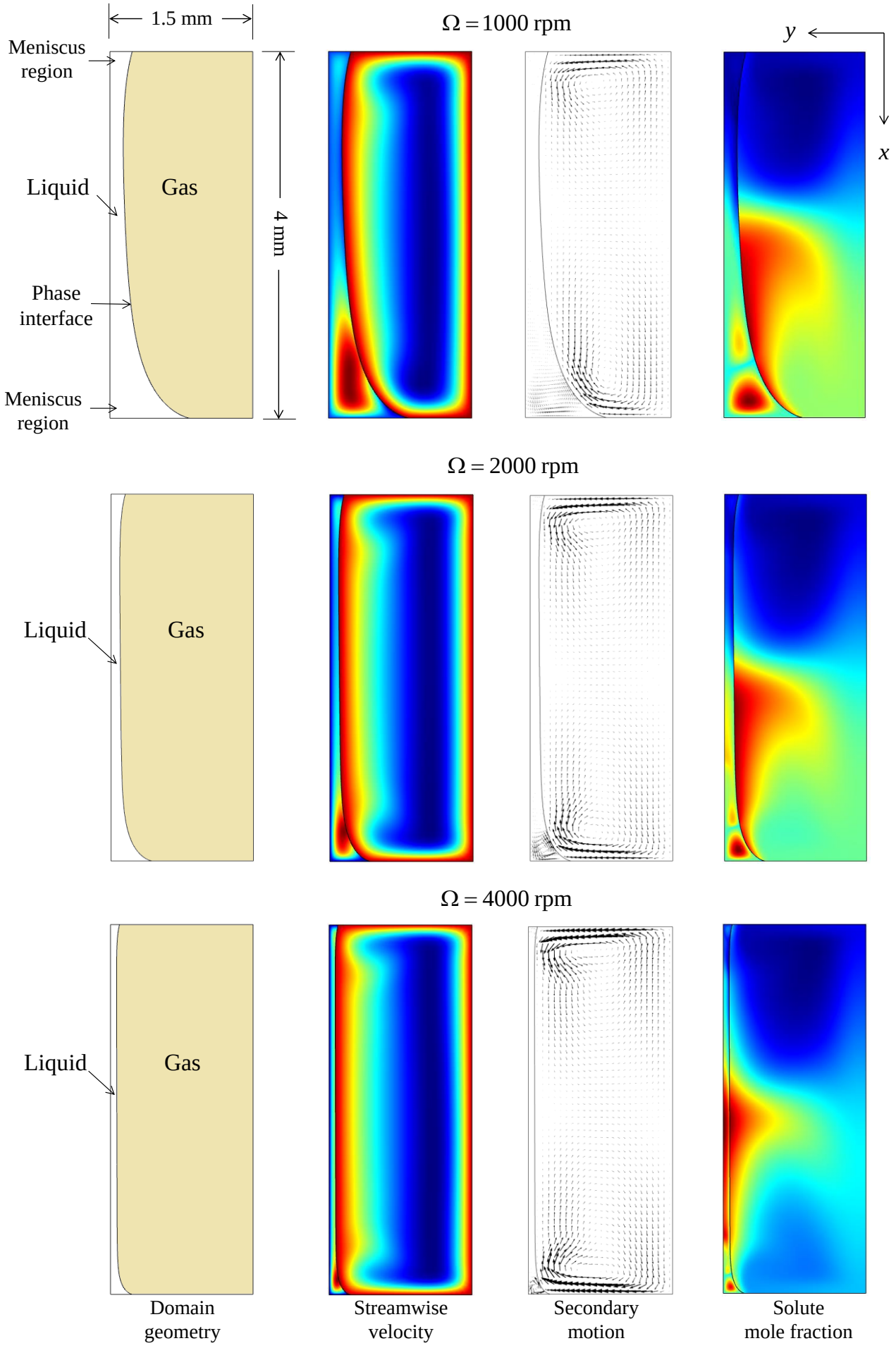
1.5 mm
Ω = 1000 rpm
y
x
Meniscus region
Liquid
Gas
Phase interface
Meniscus region
4 mm
Ω = 2000 rpm
Liquid
Gas
Ω = 4000 rpm
Liquid
Gas
Domain geometry
Streamwise velocity
Secondary motion
Solute mole fraction

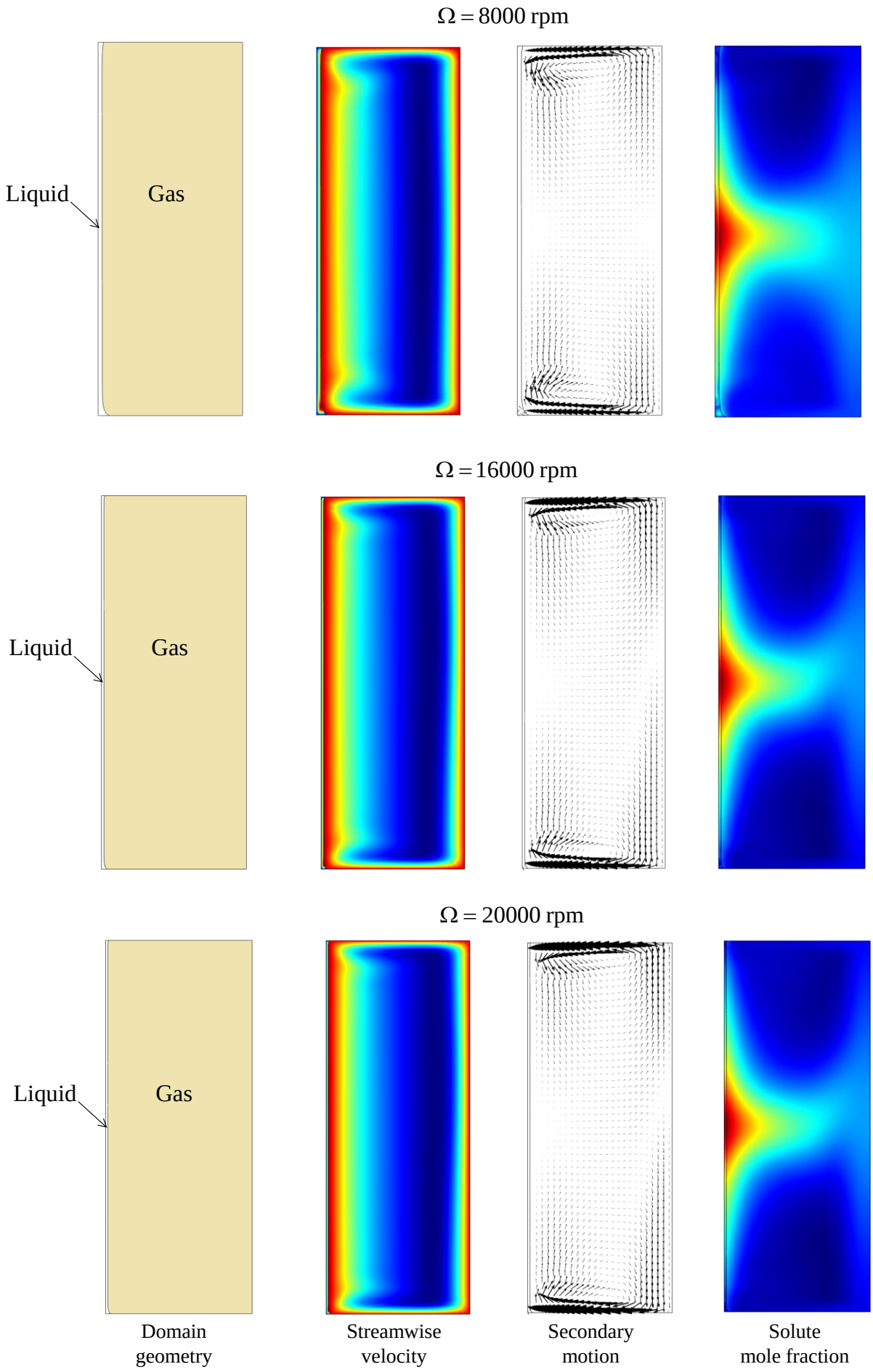

Figure 8.9. Numerical results (streamwise velocity, secondary flow and the solute mole fraction distribution) for different rotation rates at Q_V = 3 NL/min and Q_L = 2.2 mL/min ($-f'q_n$ = 1.2).

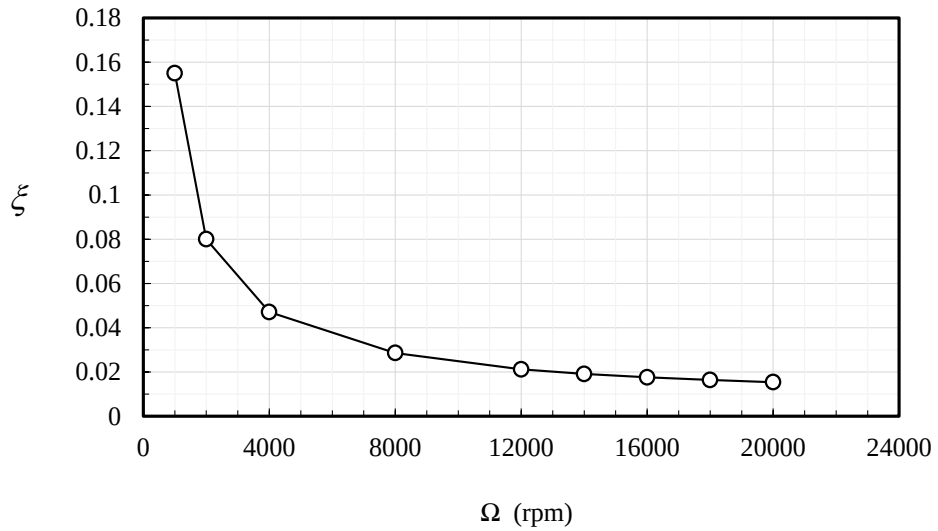

Figure 8.10. Computed volume fraction of the channel occupied by the liquid phase at different rotation rates. The flow conditions as in Fig. 8.9.

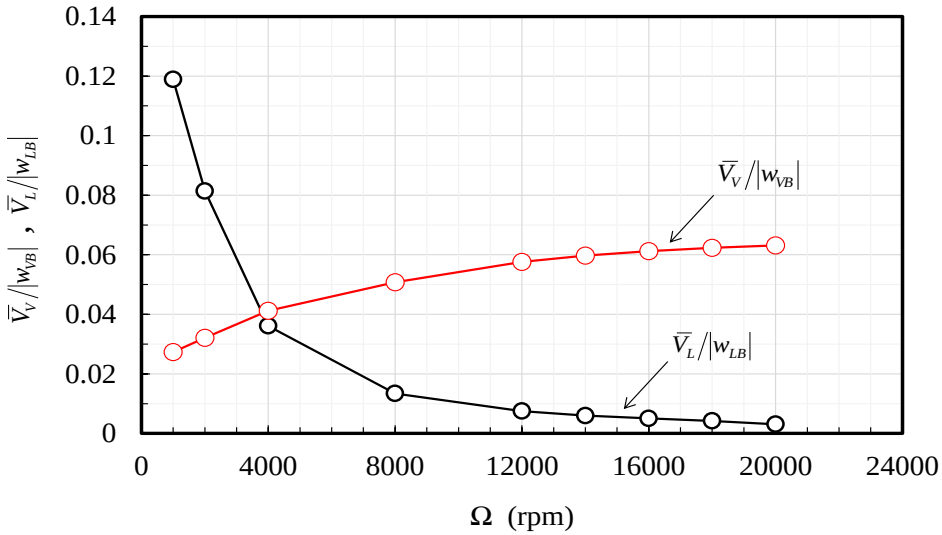

Figure 8.11. Root-mean-square velocity normalised by the streamwise velocity in each phase at different rotation rates. The flow conditions as in Fig. 8.9.

In terms of the mass transfer, the change in the solute mole fraction distribution with the rotation rate in Fig. 8.9 is linked directly with the changing in the interface shape. At $\Omega = 1000$ rpm, for example, the top and the bottom difference in the liquid layer thickness causes a strong difference in the streamwise liquid velocity which clearly has a strong influence on the solute distribution. In the bottom meniscus region, where the streamwise liquid velocity is highest, variation in the solute mole fraction is more pronounced than the top, where liquid velocity is low. The overall solute variation along the liquid layer has an evident effect on the solute distribution in the gas phase, a higher solute mole fraction at the bottom and the middle than that at the top. As the rotation rate increases, the relation between the size of the red core in the meniscus region (solute maxima) and

the strength of the streamwise velocity there becomes less pronounced. This is expected since as the rotation rate increases the liquid layer becomes approximately flat, resulting in a smaller variation in streamwise liquid velocity distribution. As a result, approximately a symmetric solute distribution is obtained, as can be seen in the results at $\Omega \geq 8000$ rpm.

Looking now at the mass transfer coefficient, the variation in mass transfer performance with the rotation rate can be quantified. Fig. 8.12 below gives the values of the overall volumetric mass transfer coefficients over the tested range of rotation rate.

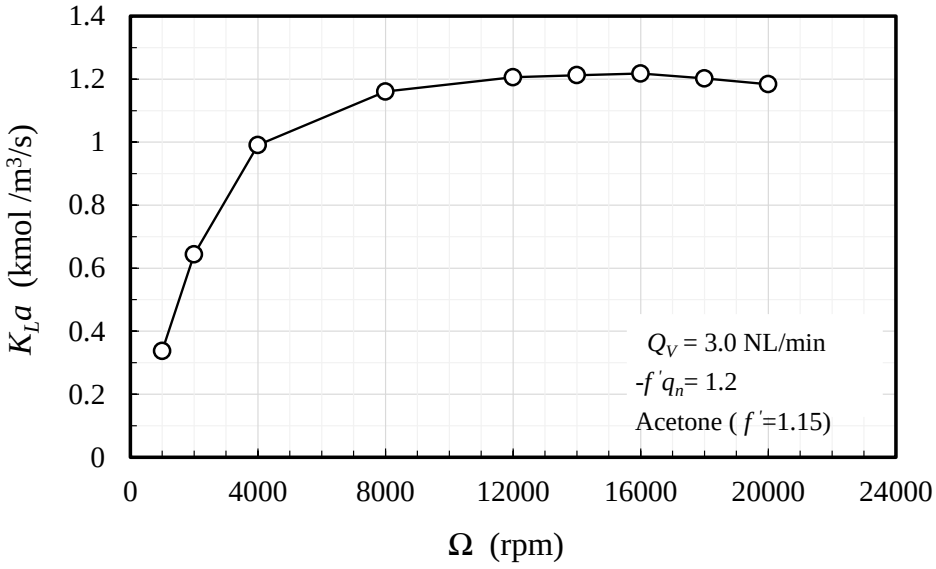

Figure 8.12. Computed overall mass transfer coefficients against the rotation rate. The flow conditions as in Fig. 8.9.

It is important to note that the maximum change in the interfacial area per unit volume (a) associated with the change in the interface shape is about 5%. So the behaviour shown in the above figure is essentially due to the change in K_L values. The data show clearly that the mass transfer performance increases rapidly with the rotation rate up to about Ω = 8000 rpm. This is attributed to the sharp decrease in the liquid layer thickness (seen in Fig. 8.10) and the noticeable increase in the strength of the gas phase secondary flow (Fig. 8.11) with the rotation rate which together lead to enhancing the mass transfer in the channel. Beyond Ω = 8000 rpm, however, the mass transfer responds weakly to the change in the rotation rate: increasing slightly and then decreasing and thus forming a broad peak with a maximum at around Ω = 16,000 rpm. This is consistent with the slow variation in both the liquid layer thickness and the secondary flow seen in Figs.

8.10 and 8.11, respectively, over the same range of rotation rate. As pointed out, these parameters determined mainly the mass transfer effect. Hence, a small change in the K_L has been seen in the results at $\Omega \geq 8000$ rpm with an optimum at $\Omega = 16{,}000$ rpm, representing the best interaction of ξ , $\bar{V}_L/|w_{LB}|$ and $\bar{V}_V/|w_{VB}|$.

The effect of the rotation rate on desorption of acetone over a range of $-f'q_n$ is also tested and the results are shown in Fig. 8.13. This is simply made by decreasing only the liquid phase flow rate. Again, at a given $-f'q_n$, there is an improvement in mass transfer coefficient with the rotation rate. Also, it is clear that $K_L a$ increases rapidly first between 2000 and 8000 rpm and then slowly as the rotation rate increases. These trends are similar to those observed in Fig. 8.12 and they are attributed to the same reasons discussed above: the decrease in the liquid layer thickness and the increase in the gas Coriolis motion. Finally, there is a clear pattern over the range of $-f'q_n$ and that is the slope of $K_L a$ curve changes gradually with the rotation rate. This is because of the variation in the interface shape with Ω shown in Fig. 8.9 (domain geometry). At $\Omega = 2000$ rpm, the interface shape is strongly curved with large menisci, causing decreasing the mass transfer as $-f'q_n$ increases since $-f'q_n \propto 1/Q_L \propto 1/\xi$. As the rotation increases, the interface deformation becomes less pronounced. As a result, the solute mass transfer increases with $-f'q_n$ at Ω > 4000 rpm since increasing $-f'q_n$ reduces the liquid layer thickness (ξ) and the effect of the meniscus heights is negligible.

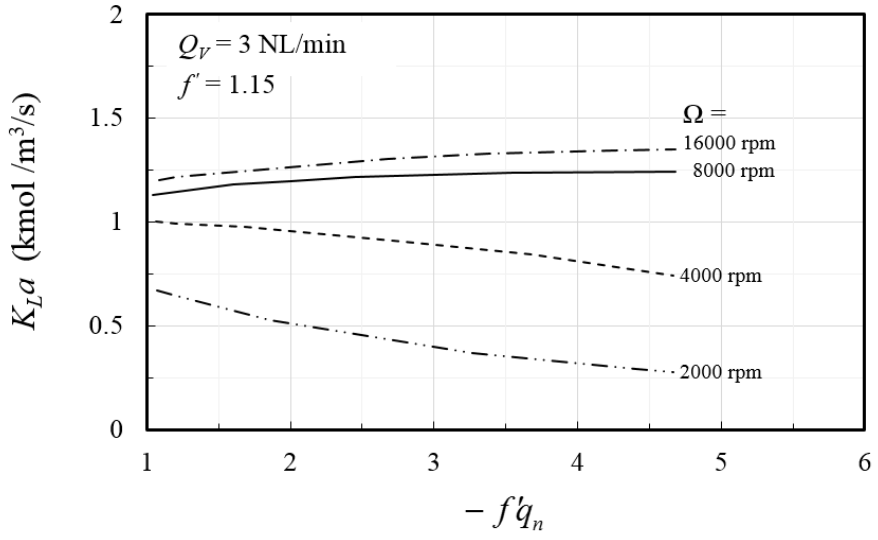

Figure 8.13. Computed overall mass transfer coefficients for different purification factor over different rotation rate.

8.3.2 Different Channel Aspect Ratio

All the experiments are made using a channel with a relatively large aspect ratio ($W/h \approx 2.5$). However, this design parameter may affect the mass transfer performance and is examined here by varying W (the channel dimension parallel to the phase layers). Varying only W and keeping h constant ensures approximately a constant interfacial area per unit volume ($a \approx h^{-1}$) for the tested cases. Therefore, any changes in mass transfer would be a direct result of changes in K_L values. A channel with three different widths are simulated: W = 1, 2 and 3 mm in addition to that used in the original design (4 mm). The standard set of plots for each case is shown in Fig. 8.14 where Ω = 3200 rpm and, again, the phase flow rates are held constant at Q_V = 3 NL/min and Q_L = 2.2 mL/min ($-f'q_n$ = 1.2).

It is clear in Fig. 8.14 that the variation in channel width has a strong influence on the main features of the contacting process. First of all, reducing the channel width increases the interfacial surface force to the centrifugal force (δ_C/W, Eq. 4.34). This results in a more curved interface between the phases. Further, the variation in channel width affects directly the character of the main flow and the Coriolis secondary motion and hence the solute distribution in both phases. For the liquid phase, decreasing the channel width results in a thicker liquid layer to conserve the mass and hence allows to the same amount of liquid to flow in a smaller channel. So, for example, the fraction of liquid phase (ξ) increases about 2.5 times (from 0.055 to 0.137) as W decreases from 4 to 1 mm. As a direct consequence of that, the difference between the centre of the layer and its ends becomes minor as W decreases. Thus, at W = 1 mm, the liquid phase flows approximately evenly everywhere, causing a strong variation in streamwise liquid velocity. The effect of streamwise liquid velocity distribution on the Coriolis motion is evident in Fig. 8.14. Since the variation in streamwise velocity under rotation causes the generation of the secondary flow, it is natural to see that the rotation of the smaller channel gives rise to stronger vortices occupying most the liquid passage relative to those with sufficiently large channel width.

It is also clear in Fig. 8.14 that the gas phase Coriolis motion becomes more active in the smaller channel. This is mainly due to the large increase in the gas phase velocity associated with the large reduction in the size of the passage available for the same phase.

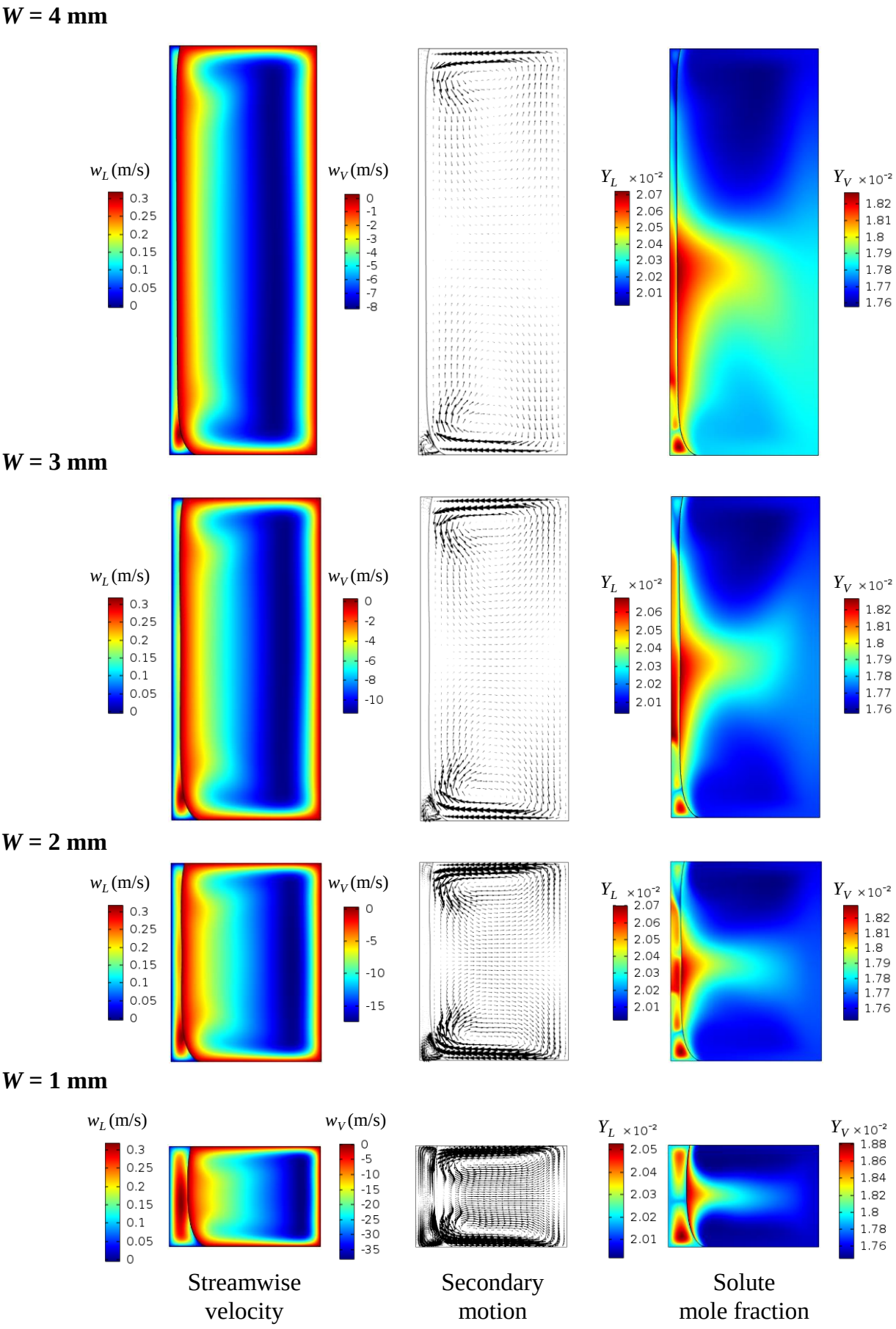

Figure 8.14. Effect of different channel aspect ratio. The conditions are Q_V = 3 NL/min, Q_L = 2.2 mL/m ($-f'q_n$ = 1.2) and Ω = 3200 rpm.

Quantitative information about the solute mass transfer is shown in Fig. 8.15. The figure shows the molar flux of the solute along the interface for the four different channels. The results in the figure indicate clearly that the solute flux increases as the channel width decreases. The ratio of the flux at corner relative to that at the middle of the layer increases markedly as W decreases. This is certainly because of the pronounced evolution in the secondary motion noticed in both phases in Fig. 8.14, which appears to have a strong influence on mass transfer in the small channel. This effect is confirmed by looking at the mass transfer coefficient values. Fig. 8.16 shows these values against the channel width. As expected, the transfer coefficient is proportional inversely with the channel size, reaching the maximum at W = 1 mm.

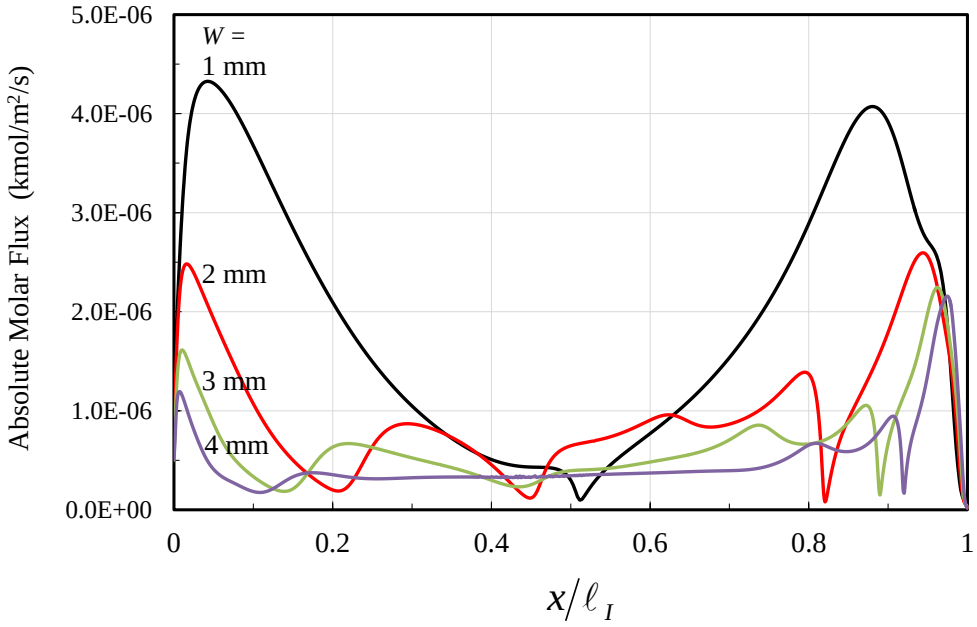

Figure 8.15. Solute molar flux along the phase interface for channel with different widths. The conditions as in Fig. 8.14.

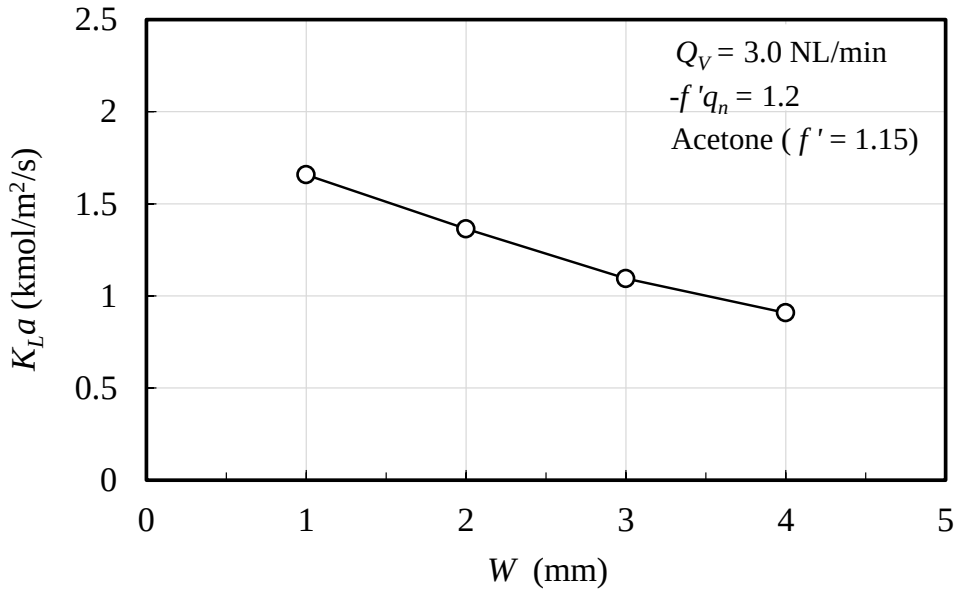

Figure 8.16. Values of the overall mass transfer coefficient against the channel width. The conditions as in Fig. 8.14.

The results so far demonstrate clearly that the small channel is more efficient in desorbing acetone from water at the flow conditions of Fig. 8.14 where $-f'q_n$ = 1.2. The effect of channel aspect ratio over a range of $-f'q_n$ is also tested here by changing Q_L at Q_V = 3 NL/min and Ω = 3200 rpm. The values of the overall mass transfer coefficients are shown in Fig. 8.17. Again, it is clear in the figure that using a small channel can enhance mass transfer over the tested range of $-f'q_n$. At $-f'q_n$ = 4, for example, the mass transfer performance increases approximately by a factor of 2 as W decreases from 4 to 1 mm.

Another behaviour can be observed in Fig. 8.17 that there is a peak in $K_L a$ values for W = 1 mm while for the other channel widths $K_L a$ decreases with $-f'q_n$. Looking at the individual mass transfer coefficients, this behaviour can be understood. In Fig. 8.18, the term $f' k_V a$ (dashed lines) and $k_L a$ (solid lines) are plotted against $-f'q_n$ for W = 1 and 2 mm. It is clear in the figure that $k_L a$ is less affected by the change in the channel width relative to $f' k_V a$. Consequently, at W = 1 mm, $k_L a$ becomes more dominant than $f' k_V a$, dictating the behaviour of $K_L a$. This explains directly the different behaviour of $K_L a$ observed at this particular channel width in Fig. 8.17. The peak in the individual liquid phase mass transfer coefficient (red solid curve) and its effect on the overall mass

transfer coefficient is similar to that observed in the experimental data at the large values of f'. As pointed out, this peak is the best interplay of the liquid layer thickness, Coriolis secondary motion and bulk flow. More details about the role of these factors in determining the peak will be discussed in the next section.

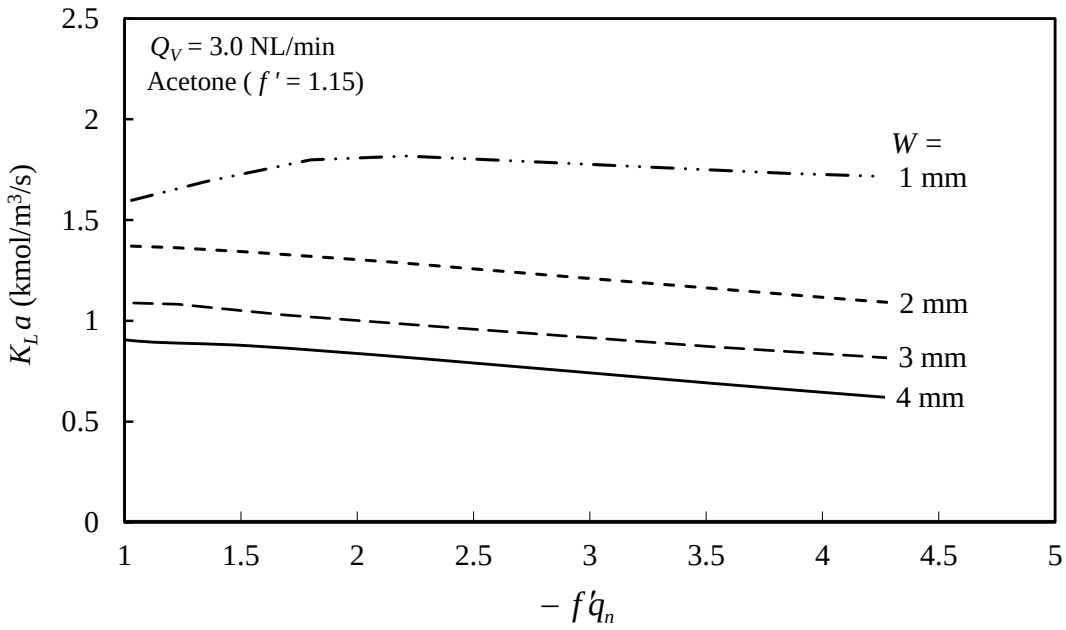

Figure 8.17. Values of the overall mass transfer coefficient over different values of purification factor. The conditions are Q_V = 3 NL/min and Ω = 3200 rpm.

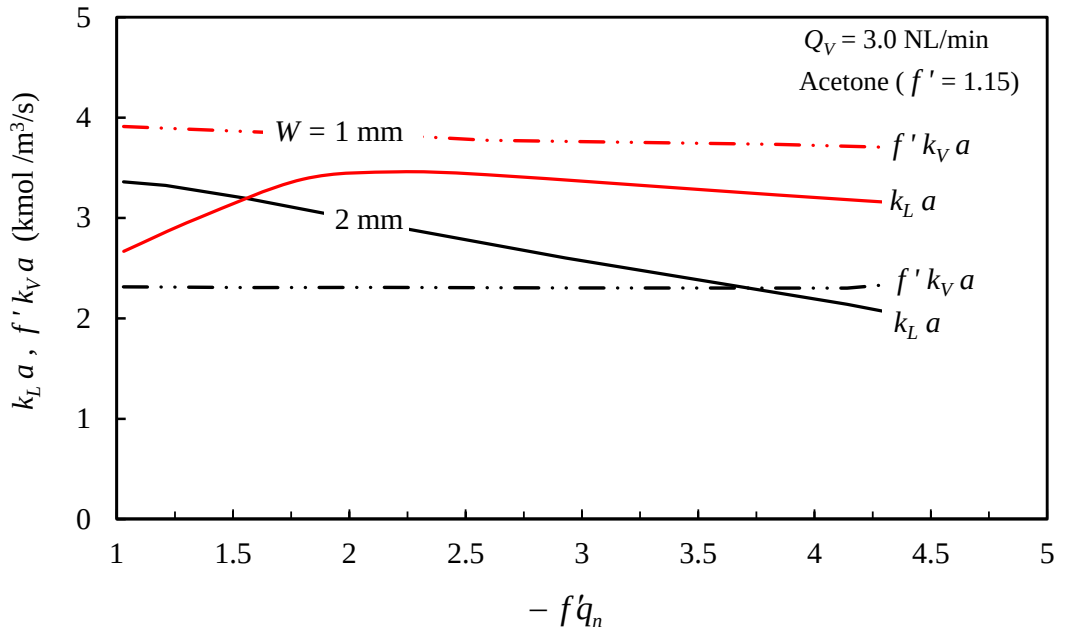

Figure 8.18. Values of the individual mass transfer coefficients over different values of purification factor. The conditions are Q_V = 3 NL/min and Ω = 3200 rpm.

8.3.3 Different Gas and Liquid Flow Rates

The experiments and the computations carried out in this work are based on fixing the flow rate of one of the phases, usually the gas phase, and change the other. However, it is important to examine how varying these parameters together affects the process of contacting. Fig. 8.19 below shows the sensitivity of the transfer coefficients to different values of gas and liquid flow rates. Again, the purification factor ($-f'q_n$) and f' are fixed at 1.2 and 1.15, respectively, for all the cases. Also, before discussing the results, it is worth mentioning that the range of gas and liquid flow rates shown in Fig. 8.19 corresponds to a range of Reynolds number of $\mathrm{Re}_L \approx 3-24$ and $\mathrm{Re}_V \approx 270-2150$.

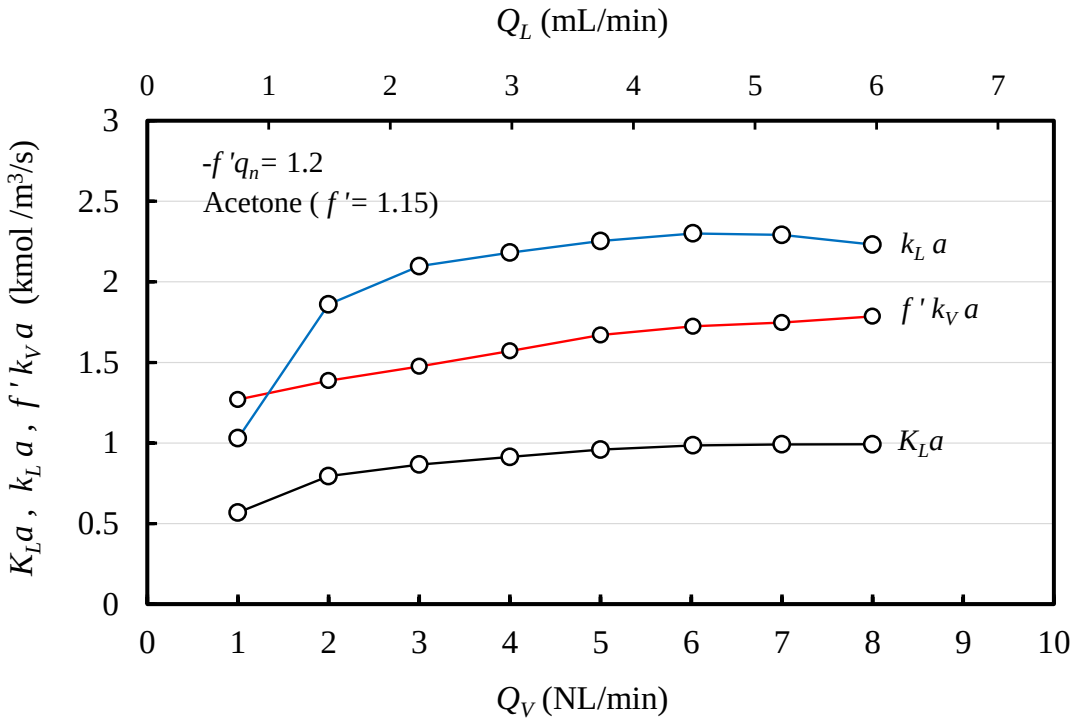

Figure 8.19. Mass transfer coefficients over different values of gas and liquid flow rates. The other conditions are f' = 1.15 , $-f'q_n$ = 1.2 and Ω = 3200 rpm.

Considering the results of the gas phase first (red curve), the behaviour is immediately evident: $f' k_V a$ increases gradually as the gas phase flow rate increases. There is no doubt that this effect is mainly due to increasing Reynolds number (ratio of convective effect to the viscous effect) which, in turn, results in a stronger Coriolis motion, enhancing mass transfer by convection. On the other hand, the solute mass transfer in the liquid side (blue curve) reveals an interesting behaviour. It can be seen

clearly that $k_L a$ increases as the liquid flow rate increases (labels on the upper abscissa) and then starts decreasing at around Q_L > 4.5 mL/min, forming a wide peak. This behaviour can be interpreted in terms of both the liquid layer thickness and the combined effect of the main flow and secondary flow. It must be clear now that at a low liquid flow rate, the interface shape imposes a situation where the diffusion length scale is large at the ends compared to that at the middle of the layer (due to the menisci formation) and a large fraction of the fluid is diverted there. Also, it must be known that small liquid flow rate means a weak secondary flow generated in the menisci regions. So the rapid increase in $k_L a$ with the liquid flow rate (from 0.7 to about 3 mL/min) is mainly because the menisci effect is minimised along with the expected increase in secondary motion with the liquid flow rate. The variation in menisci effect with the liquid phase flow rate can be seen clearly in Fig. 8.20 through the progression in solute mole fraction distribution. As the liquid flow rate increases, the liquid layer increases and hence a large portion of liquid flow rate is diverted in the middle of the layer, affecting directly the solute concentration distribution.

The effect of streamwise convection in the liquid side is also clear in Fig. 8.20 (i.e. $w_L \, dY_{LB}/dz$ perpendicular to the direction of diffusion, $D_L \nabla Y_{LB}$). Because w_L increases with distance from the wall, a strong variation in solute distribution occurs across the flowing liquid (i.e. colour changes from dark red to light red) and it increases with the liquid flow. Diffusive transfer, in general, is proportional directly with the difference in solute concentration. But increasing the liquid flow rate has an opposite effect as well. It leads to increasing both the layer thickness and hence the diffusion length scale and the axial mass transfer by the bulk flow. Thus, any dropping in mass transfer due to increasing the diffusion distance and the bulk flow appears to be over-compensated by the increased effect of secondary motions and the solute difference across the flowing fluid. This likely explains the continuous increase in $k_L a$ observed in Fig. 8.19, reaching an optimum at Q_L around 4.5 mL/min. Further increasing the liquid phase flow rate, however, the mass transfer will be more affected by the decreasing effect of liquid layer thickness and the axial mass transfer along the channel and hence $k_L a$ decreases.

The overall mass transfer coefficient is a direct result of the variation in the individual coefficients seen in Fig. 8.19, particularly $f' k_V a$. Accordingly, $K_L a$ increases first as

both $k_L a$ and $f' k_V a$ increases up to Q_V = 5 NL/min. Then, it remains approximately constant, following the same behaviour of $k_L a$ and $f' k_V a$.

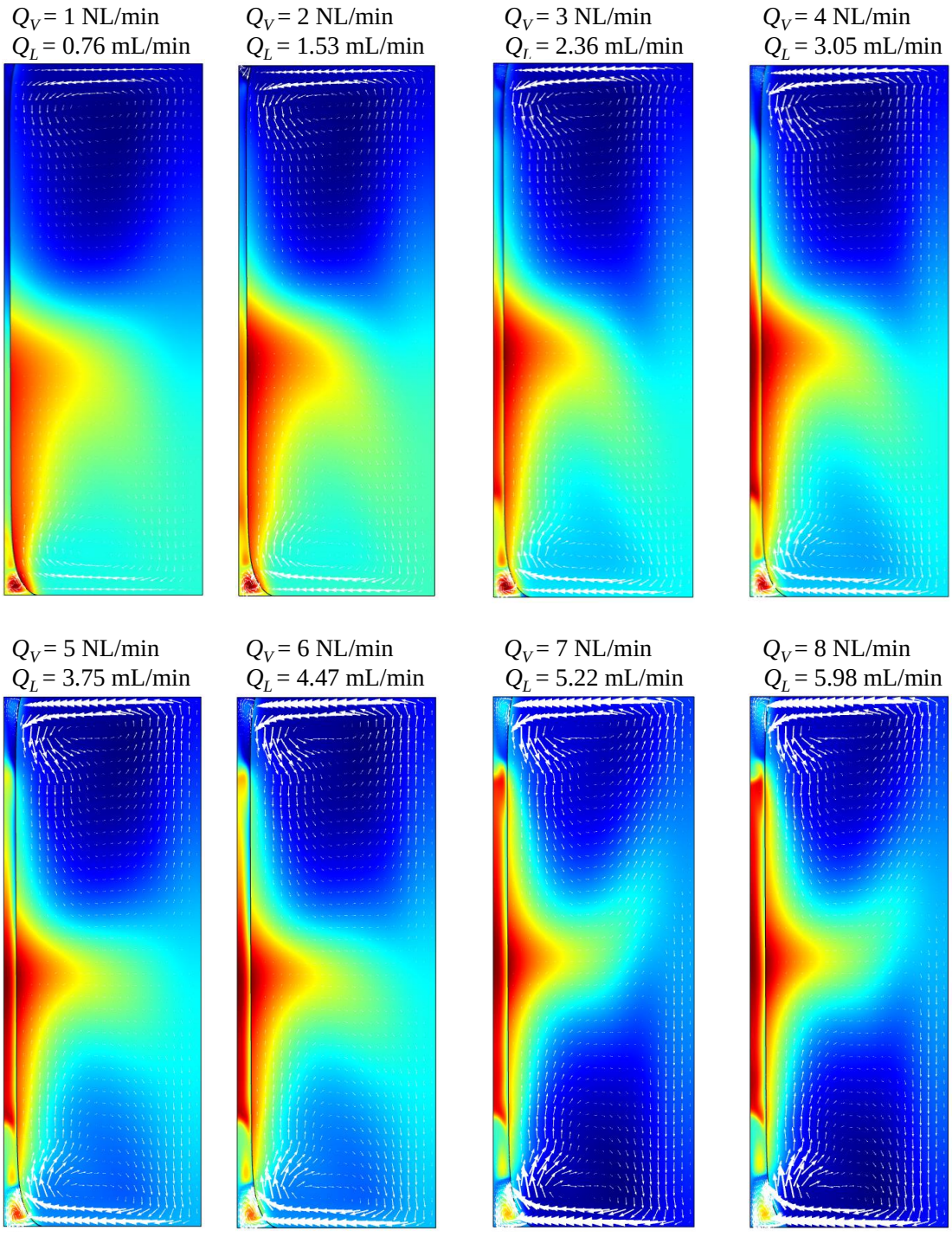

Figure 8.20. Solute mole fraction distribution and Coriolis secondary motion at different liquid and gas phase flow rates.

8.4 Summary

Computational results for gas-liquid contacting in a rotating spiral channel have been presented in this chapter. The first part of the chapter was dedicated to assessing the 2-D computational approach adopted in this research. It was tested by predicting a range of experimental data. The approach gives an excellent prediction of the liquid layer thickness (MacInnes and Zambri, 2015) and a good prediction of mass transfer parameters (d_L and $K_L a$) over a wide range of experimental conditions. However, it was less good at conditions where the liquid flow rate is small (or large $-f'q_n$) for the large f' values. The model sensitivity analysis using an interface shape with a larger meniscus size suggests that the difference is likely due to the approximations used in the interface shape calculations.

In the second part of the chapter, a parametric analysis was conducted to demonstrate the flexibility of rotating spiral contacting. In the analysis, the effect of three key parameters (rotation rate, channel aspect ratio and phase flow rates) on desorption of acetone was studied. Interestingly, the results showed that some of these parameters can be adjusted and others can be engineered to enhance the contacting process. First, by adjusting the rotation rate, the contacting process can be optimised. For a range between 1000-20,000 rpm, it was found that Ω=16,000 rpm gives a maximum mass transfer coefficient. Second, by changing the channel aspect ratio, the contacting process can be enhanced considerably. It was found that reducing the width from 4 mm to 1 mm increases the mass transfer coefficient approximately by a factor of two. Finally, at a given rotation rate and channel aspect ratio, the mass transfer can be enhanced by adjusting the flow rate of the contacting phases. It was found that increasing the flow rate of both phases increases the mass transfer coefficient also by about a factor of two.

Chapter Nine

General Conclusions and Future Trends

The rotating spiral technique is an emerging separation approach with the potential to handle any two immiscible fluid phases. In this work, experimental and 2-D numerical investigations of physical mass transfer in a rotating spiral channel were conducted over a wide range of phase and solute systems. The main aim was to understand and demonstrate the performance of this technique for gas-liquid contacting. The work began by establishing a theoretical framework based on a bulk analysis of counter-current contacting (Chapter 3). This enabled experimental analysis and a comparison between approaches under different contacting conditions. The term '*total specific throughput* ', which is the ratio of treated phase throughput to the contactor volume, was presented as the comparison criterion in this research. A 2-D computational model was detailed in Chapter 4 and a series of computations were conducted. The purpose of these computations was: (1) to understand the general character of the flow and the process of solute transfer at different gas and liquid phase flow rates and (2) to benchmark the numerical solution by predicting results for the wide-channel model, which has an analytical solution. Experimentally, desorption of four different dilute solutes from water into air were studied separately over a range of contacting conditions. The procedures to conduct the experiments and to take measurements were presented in Chapter 5. The list of physical properties used throughout this work were given in Chapter 6. The experimental findings and a comparison of the rotating spiral approach to other alternative approaches were discussed in Chapter 7. In Chapter 8, the predictions of the 2-D computational model were assessed and a parametric study was carried out to highlight the role of rotation rate, the channel aspect ratio and the effect of phase flow rates.

The main findings and conclusions of this research are presented in this chapter. This is followed by recommendations, suggesting research directions for further future work. It is helpful to note here that a detailed conclusion for each portion of this work were covered at the end of each chapter.

9.1 Conclusions

9.1.1 General Characteristics

The computations carried out in Chapter 4 revealed important characteristics of gas-liquid contacting in a spiral channel with a relatively large aspect ratio. The results indicated that there was strong Coriolis secondary motion in the gas phase, while in the liquid phase there were just two weak vortices active only in the meniscus regions. This secondary motion, in the gas-phase, has a strong distortional effect on the gas streamwise velocity. The distortion observed in the gas-phase and the structure of the Coriolis motion were consistent with the experimental findings and computations reported in the literature for a single fluid flow in a rotating channel. So there was a strong reason to believe that the essential features of the flow were captured by the 2-D computations. The main flow and the secondary flow determined the solute concentration distribution in the spiral, and hence, the mass transfer performance. The numerical results at Ω = 3200 rpm given in Chapter 4 clearly demonstrated that increasing the gas phase flow rate produced stronger Coriolis motion, thereby improving the mass transfer of the gas side, with little impact on the liquid layer thickness. In the liquid phase, on the other hand, it was found that increasing the liquid phase flow rate increased the liquid layer thickness and changed the structure of Coriolis secondary motion. The motion became vigorously active in the corners and produced small roll-cells, stretching towards the central part of the liquid layer. This evolved motion also enhanced the mass transfer in the liquid side through convection. Interestingly, the comparison between the model results (with and without Coriolis terms) and the mass transfer measurements made in Chapter 8 showed that the mass transfer could be doubled due to the effect of secondary motions in both the gas and liquid phases.

9.1.2 Rotating Spiral Performance

A wide range of experiments were performed to establish the performance of a rotating spiral channel by studying individually desorption of ethanol, acetonitrile, acetone and MEK from water using air as a stripping agent. The spiral temperature, gas phase flow rate and liquid phase flow rate were varied while the rotation rate and pressure were maintained at 3200 rpm and 1.8 bara, respectively. The experimental results were given in Chapter 7 and showed the capability of the spiral to handle this variety of systems, achieving approximately solute-free water when the appropriate flow rate ratio

was selected. Such simplification greatly reduces manufacturing and device design costs, in addition to providing an inherently flexible piece of equipment.

Also, one of the more significant findings emerged from the experiments was that there was a universal peak in the mass transfer coefficient at a liquid layer thickness between 80-90 μm. This occurred independently of the gas phase flow rate and prominently appeared in the data for the systems with large f' (3.38 and 5.5) where mass transfer was greatly affected by the liquid phase. At a small liquid phase flow rate, most of the liquid was shifted into the corners (menisci regions) where mass transfer was poor, a large diffusion path accompanied weak Coriolis motion. By increasing the liquid flow rate, the effect of menisci decreased with a stronger Coriolis motion, leading to an increased mass transfer coefficient, up until the peak value. Any further increasing of the liquid phase flow rate, however, resulted in the liquid layer thickness and the axial mass transfer along the channel increasing, and hence $K_L a$ decreased. The effect of menisci on the flow, and hence mass transfer, and the mechanism of peak determination is confirmed by the 2-D computational results given in Chapter 8.

Significantly, this finding strengthens the idea that the spiral can identify successfully the optimum contacting and this optimum prevails along the contacting channel. At a given rotation rate, the spinning of spiral produces a constant longitudinal body force which drives mainly the liquid phase along the channel and a transverse body force which keeps the phases separated. So the phases do not mix and hence the gas phase does not affect strongly the liquid layer thickness. Therefore, as in the experiments, by changing only the liquid phase flow rate, which in turn changes the liquid layer thickness, the peak in $K_L a$ can be identified. Since this peak is weakly dependent on the gas phase flow rate, it can be tailored to the desired $-f'q_n$ by changing only the gas phase flow rate. In principle, therefore, it seems that optimum contacting, represented by $K_L a$, and optimum usage of solvent, determined by $-f'q_n$, can be achieved simultaneously by using the rotating spiral technique.

9.1.3 Relative Performance

Before this study, evidence regarding spiral channel performance relative to other approaches was purely anecdotal. The rotating spiral can be thought of as a new contacting approach and it is important to be placed into the context of other alternative contacting methods. For this purpose, a total specific throughput based on molar flow rate was used to enable a fair comparison between results of absorption and desorption taken from different contactors and those collected by the current spiral. This comparison measure is linked inversely to the contactor size and contacting time scale. So a higher specific throughput means a smaller contactor size can be used to achieve a given throughput at a given purification. The comparison results were shown in Chapter 7 and indicated that the spiral channel allowed total specific throughput to be many times larger than that for the other methods. Comparison with dispersed-phase contactors data (packed column and rotating packed bed) showed that total specific throughput of the spiral was about three times larger in the expected region of operation which is around $1 < -f'q_n < 4$. For parallel-flow contactors, recent data of desorption of acetone using a membrane microchannel (Adiche, 2018) were considered in the comparison. Interestingly, the phase and solute system as well as the contacting conditions in this study were, approximately, the same as those tested in the spiral. However, the results also indicated that the spiral could produce a larger specific throughput by factor of two in relation to this contactor in the appropriate range of $-f'q_n$. This difference is, perhaps, due to the convective effect of the Coriolis motion in the spiral and the additional mass transfer resistance added by the membrane which together may lead to such difference.

9.1.4 Prediction of the 2-D Computational Model

The study adopted a computational model based on solving the governing equations in a 2-D section using an interface shape predicted independently. In this work, this computational model was assessed using a range of experimental data and the results were presented in Chapter 8. A comparison with the experimental data of MacInnes and Zambri (2015) showed that this model could reliably capture the liquid layer thickness over a range of liquid phase flow rates for three different rotation rates (1480, 2400 and 3840 rpm). In terms of the mass transfer, the 2-D model predicted the experimental mass transfer coefficient over most of the range of data but it also failed in some instances. In particular, the 2-D model over-predicted $K_L a$ values at a low liquid phase flow rate (or

large $-f'q_n$) for the systems with large f' (3.38 and 5.5). The model sensitivity analysis using an interface shape with a larger meniscus size suggested that the difference is likely due to the approximations used in the interface shape calculations. One of these approximations is using contact angles measured at static conditions. In practice, these angles might be more sensitive to other processes, such as evaporation, during the contacting process. Any changes in the contact angles affect the meniscus size, which is a crucial parameter in determining the mass transfer at low liquid phase flow rates. However, without adjusting the contact angles and using a local radial position (R_0 = 25 mm) and water surface tension (0.07 N/m), the 2-D model predicts convincingly the data especially over $-f'q_n$ values between 1 and 4 which are a typical for desorption process.

9.1.5 Model Parametric Study

The final piece of this research was a parametric study using the 2-D model to investigate the effect of three key parameters: rotation rate, channel aspect ratio and both the gas and liquid phase flow rate. The effect of these parameters has not been studied experimentally and it is important to understand their role in gas-liquid contacting process. For this objective, desorption of acetone (f' = 1.15) at $-f'q_n$ = 1.2 and Ω = 3200 rpm was taken a reference case to carry out the study.

Interestingly, the 2-D numerical results showed that the channel geometry can be engineered and the rotation rate and phase flow rates can be adjusted to enhance the rotating spiral contacting. It was found that reducing the channel width from 4 mm to 1 mm increased the mass transfer coefficient approximately by a factor of two. This reduction in channel width changed the strength of Coriolis motion in both phases. It became stronger and occupied most the gas and liquid phase passage, resulting in improving the mass transfer. Further, the rotation rate, which is a key operating parameter, was examined over a range between 1000-20,000 rpm. The results showed that by adjusting the rotation rate, the contacting process could be optimised. By increasing the rotation rate, three main changes occurred: (1) the shape of the interface flattened, (2) the liquid layer thickness decreased and (3) the Coriolis motion in the gas phase increased. These three changes improved the mass transfer of acetone in both phases achieving a maximum mass transfer coefficient at around Ω =16,000 rpm. The other parameter examined was the flow rate of the contacting phases. The flow rate of the

gas phase and the liquid phase can be controlled simultaneously at a desired $-f'q_n$ during operation. In practice, this can be done by simply adjusting a needle valve or pump setting. The 2-D model results showed that increasing the flow rate of both phases from Q_V =1 NL/min and Q_L = 0.76 mL/min to Q_V = 8 NL/min and Q_L = 5.98 mL/min increases the mass transfer coefficient by about a factor of two. This was mainly attributed to the convective effect of Coriolis motion in the gas and liquid phase. This study provides evidence that the 2-D modelling approach established here can be a useful tool for the improvement of the rotating spiral technique.

9.2 Future Trends

In this section, some recommendations for further development and investigation are suggested to build upon the current research systematically.

9.2.1 Experimental Work

9.2.1.1 Turbulent Flow Regime

The experiments in this work were restricted to laminar flow in order to ensure a stable flow in each phase. However, it may be possible to investigate the performance of the spiral at higher Reynolds number or possibly even reaching the turbulent flow regime in one of the phases. One of the most challenges of such study is to determine the Reynolds number limits that can be achieved practically in the two phases such that a stable flow can be obtained. Using the wide-channel model (Chapter 4) and conservative values of the Froude number (Fr = 0.5) and Weber number (We = 5) defined in Chapter 2, one can quantify roughly the maximum allowable limits of Reynolds number. The results over the broadest possible range of phase and solute systems (f') and the required range of rotation rates are shown in Fig. 9.1 and Fig. 9.2, respectively. The spiral geometrical parameters used in the calculations are R_0 = 25 mm (minimum radius of the spiral), t = 3 mm (spacing between the channels) and different heights (h). Fig. 9.1 clearly indicates that it is possible to achieve high Reynolds number (reaching turbulent flow) in the gas phase for systems with f' > 1 (Fig. 9.1). Equally, the results in Fig. 9.2 shows that the smaller channel, which provides a higher surface area per unit volume, requires larger rotation rate. Moving from a 7 mm channel height down to a 1 mm height at f' = 1, for example, increases the rotation rate by a factor of 75. Considering the

rotation rate as a practical constraint, one may judge that using experimental channel with $h \geq 3$ mm is a suitable practical size. These results can be used as a starting point to experimentally investigate the performance of the spiral at high Reynolds number which is, as far as we know, one of the interesting questions that has not yet been answered.

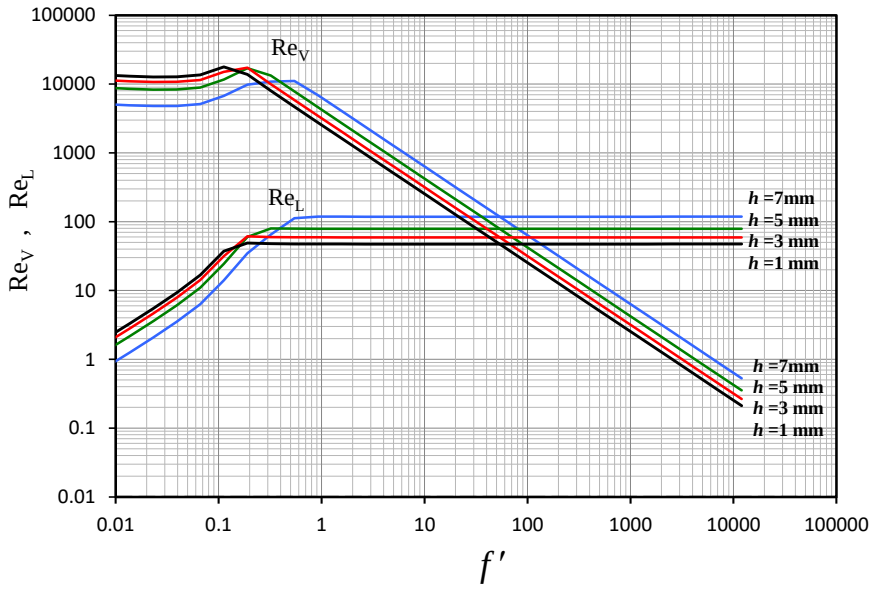

Figure 9.1. Reynolds numbers limits for various channel heights as a function of solute equilibrium distribution. The system is air-water at 25 °C and 1.8 bara. The other parameters are $\mathrm{Fr} = 0.5$, $\mathrm{We} = 5$, $R_0 = 25$ mm and $t = 3$ mm.

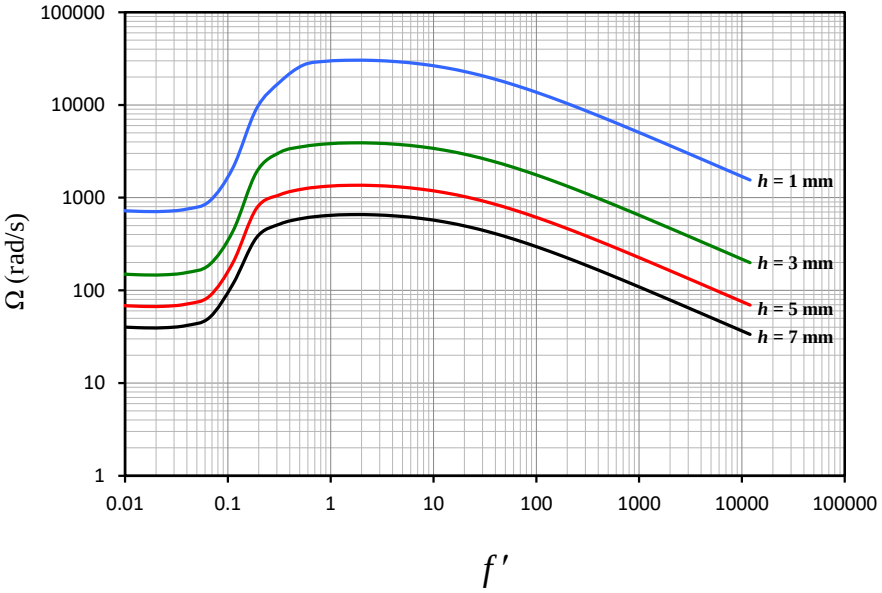

Figure 9.2. The range of rotation rates required for various channel heights versus solute equilibrium distribution. The system and the other parameters as in Fig. 9.1.

9.2.1.2 Other Applications

The process of gas-liquid contacting in a rotating spiral channel was demonstrated here. However, there are other applications within the capability of this approach that have not been investigated. Liquid-liquid extraction, perhaps, is the most attractive research area. The spiral can handle liquids with different viscosities and densities and that is key to effective liquid-liquid contacting. Using the same experimental and theoretical approach of the current study, many questions can be answered concerning liquid-liquid contacting such as the role of Coriolis force, phase Reynolds number and rotation rate. Furthermore, the present research showed the flexibility of spiral channel to produce a wide range of mass transfer measurements and these measurements can be predicted precisely over a range of conditions. This distinctive feature of the spiral can be employed in many analytical applications such as physical properties determination. In general, there is a lack of information about solute diffusion coefficients, particularly in the liquid phase, and solute equilibrium distribution. With the spiral technique, this necessary information can be determined rapidly and accurately for a given phase and solute system using the 2-D model in parallel with a few number of experiments. However, this inversion estimation method needs to be developed and tested over the largest conceivable range of solute properties and this is another research trend that can be further investigated.

9.2.2 Further Modelling Work

The 2-D model presented in the work was about a mass transfer process between two immiscible phases contacting in a section of rotating spiral channel. A case of dilute solute was considered and no other physical processes were included. However, this level of modelling can be extended by taking into account other effects such as heat transfer and chemical reaction. Processes such as distillation or chemical separation certainly require a more comprehensive model to be investigated thoroughly using the same 2-D analysis made in this work. Further, the 2-D approximations proposed in this research were based on replacing the solute concentration change at any location in the section ($\partial Y/\partial z$) by the local bulk gradient (dY_B/dz). For fast chemical reactions or the presence of a high concentration solute, the change in solute concentration along the channel may not occur in a gradual manner and hence this approximation may no longer be justified. So in this case, ideally, one would like to quantify the effect of this approximation. This requires

developing a numerical solution for the governing equations in a 3-D spiral segment, which is expected to be computationally expensive.

Further, studying the process of contacting in a turbulent regime (as suggested in Section 9.2.1) requires developing a turbulence model to deepen understanding of this complex process. This is another research direction that can be taken on board. It is expected that such a theoretical investigation along with the experiments suggested in the previous section will be a tremendous step to advance this novel technology.

9.2.3 Technology Developments

Further work to develop the spiral technology can be made. It is important to recognise that the flow rate of the gas phase and the liquid phase were small in the experimental channel. The maximum gas phase flow rate tested here, for example, was 6.2 NL/min which is equivalent to about 20 kg/day/channel. The idea of stacking multiple spiral channels is raised in MacInnes and Zambri (2015) since this increases the actual throughput. Scaling-out the contacting unit by stacking 25 channels identical to the one used in the experiments would result in a throughput of 500 kg/day/unit. The conceptual design of the unit and its dimensions are shown in Fig. 9.3. It is believed that such a flow rate would meet the production requirements of many small chemical industries. Achieving larger throughput could be conceived by using an array of units connected together. Of course, such development would not be straightforward and a research effort would need to be devoted to that direction in the future.

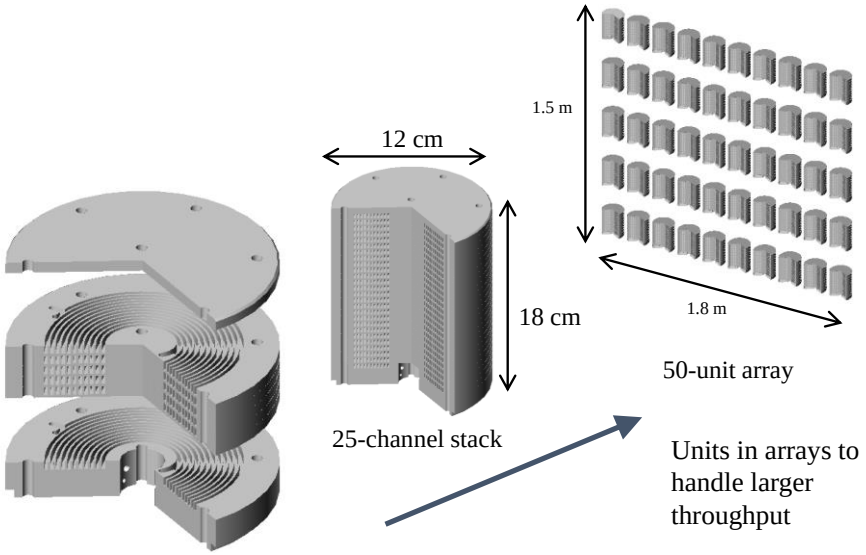

Figure 9.3. Conceptual design of a separation unit consisting of a multiple spiral channels.

References

Abdulrazzaq, N., Al-Sabbagh, B., Rees, J.M. and Zimmerman, W.B., 2016. Separation of azeotropic mixtures using air microbubbles generated by fluidic oscillation. *AIChE Journal*, *62*(4), pp.1192-1199.

Abrams, D.S. and Prausnitz, J.M., 1975. Statistical thermodynamics of liquid mixtures: a new expression for the excess Gibbs energy of partly or completely miscible systems. *AIChE Journal*, *21*(1), pp.116-128.

Adiche, C., 2018. Stripping of acetone from water in a microchannel device. *Separation and Purification Technology*, *199*, pp. 105–113.

Al-Rawashdeh, M., Cantu-Perez, A., Ziegenbalg, D., Löb, P., Gavriilidis, A., Hessel, V. and Schönfeld, F., 2012. Microstructure-based intensification of a falling film microreactor through optimal film setting with realistic profiles and in-channel induced mixing. *Chemical Engineering Journal*, *179*, pp. 318–329.

Al-Rawashdeh, M., Hessel, V., Lob, P., Mevissen, K., Schonfeld, F., 2008. Pseudo 3-D simulation of a falling film microreactor based on realistic channel and film profiles. *Chemical Engineering Science*, *63*(21), pp.5149–5159.

Al-yaqoobi, A., Hogg, D. and Zimmerman, W. B., 2016. Microbubble Distillation for Ethanol-Water Separation. *International Journal of Chemical Engineering*, *2016*, pp. 1–10.

Anderson, T. F. and Prausnitz, J. M., 1978. Application of the UNIQUAC Equation to Calculation of Multicomponent Phase Equilibria. 1. Vapor-Liquid Equilibria. *Ind. Eng. Chem. Process Des. Dev.*, *17*(4), pp. 552–561.

Anvaripour, B., Yoswathana, N., Ashtoif, N. and Arrowsmith, A., 1995. Stripping ethanol and acetone from water with modern packings. *Transactions on Ecology and the Environment*, *7*, pp. 493–500.

Aota, A., Mawatari, K. and Kitamori, T., 2009. Parallel multiphase microflows: fundamental physics, stabilization methods and applications. *Lab on a chip*, *9*(17), pp. 2470–2476.

Arnold, J. H., 1930. Studies in diffusion. I.–Estimation of diffusivities in gaseous systems. *Industrial and Engineering Chemistry*, *22*(10), pp. 1091–1095.

Atik, Z., Gruber, D., Krummen, M. and Gmehling, J., 2004. Measurement of Activity Coefficients at Infinite Dilution of Benzene, Toluene, Ethanol, Esters, Ketones, and Ethers at Various Temperatures in Water Using the Dilutor Technique. *J. Chem. Eng. Data*, *49*(5), pp. 1429–1432.

Ayash, A. A. and MacInnes, J. M., 2017. Mass Transfer Prediction of Gas-Liquid Contacting in a Rotating Spiral Channel. in *the 4th International Conference of Fluid Flow, Heat and Mass Transfer (FFHMT'17)*. Toronto, Canada, pp. 1–8.

Barua, S. N., 1954. Secondary flow in a rotating straight pipe. *Proc. R. Soc. Lond. A 227*, pp. 133–139.

Bašić, A. and Duduković, M.P., 1995. Liquid holdup in rotating packed beds: examination of the film flow assumption. *AIChE Journal*, *41*(2), pp.301–316.

Batchelor, G.K., 2000. *An introduction to fluid dynamics*. Cambridge University Press.

Beak, J. H. and Ko, C. H., 2000. Numerical Flow Analysis in a Rotating Square Duct and a Rotating Curved-Duct. *International Journal of Rotating Machinery*, *6*(1), pp. 1–9.

Benton, G. S., 1956. The Effect of the Earth's Rotation on Laminar Flow in Pipes. *J. Appl. Mech*, *23*, pp. 123–127.

Bergmann, D. L. and Eckert, C. A., 1991. Measurement of limiting activity coefficients for aqueous systems by differential ebulliometry. *Fluid Phase Equilibria*, *63*(1-2), pp. 141–150.

Bird, R.B., Stewart, W.E., and Lightfoot, E. N., 2007. *Transport Phenomena*. 2nd edn. John Wiley & Sons,Inc.

Boomkamp, P. A. M. and Miesen, R. H. M., 1996. Classification of instabilities in parallel two-phase flow. *International Journal of Multiphase Flow*, *22*(1967), pp. 67–88.

Brandani, S., Brandani, V., Del Re, G. and Di Giacomo, G., 1991. Activity coefficients from a virial expansion about their infinite-dilution values. *The Chemical Engineering Journal*, *46*(1), pp.35–42.

Bredwell, M.D. and Worden, R.M., 1998. Mass-transfer properties of microbubbles. 1. Experimental studies. *Biotechnology Progress*, *14*(1), pp.31–38.

Burns, J.R. and Ramshaw, C., 1996. Process intensification: visual study of liquid maldistribution in rotating packed beds. *Chemical Engineering Science*, *8*(51), pp.1347–1352.

Charpentier, J. C., Chimiques, I. and France, N., 1976. Review Paper Recent Progress in Two Phase Gas-Liquid Mass Transfer in Packed Beds. *Chemical Engineering Journal*, *11*(3), pp. 161–181.

Chasanis, P., Kehrmann, K. M., Kern, J., Zecirovic, R., Grünewald, M. and Kenig, E. Y., 2011. Investigation of a microstructured high efficiency contactor. *Chemical Engineering and Processing: Process Intensification*, *50*(11–12), pp. 1244–1251.

Chen, Y.S., Lin, C.C. and Liu, H.S., 2005. Mass transfer in a rotating packed bed with various radii of the bed. *Industrial & engineering chemistry research*, *44*(20), pp.7868–7875.

Chen, Y.S. and Liu, H.S., 2002. Absorption of VOCs in a rotating packed bed. *Industrial & engineering chemistry research*, *41*(6), pp.1583–1588

Chiang, C. Y., Chen, Y. S., Liang, M. S., Lin, F. Y., Tai, C. Y. Der and Liu, H. S., 2009. Absorption of ethanol into water and glycerol/water solution in a rotating packed bed. *Journal of the Taiwan Institute of Chemical Engineers*, *40*(4), pp. 418–423.

COMSOL, A., 2008. COMSOL multiphysics version 3.5, User's guide and reference guide. from: http://math. nju. edu.cn/help/mathhpc/doc/comsol/command. pdf. [Accessed 30/01/2015].

Comyn, J., Mascia, L., Xiao, G. and Parker, B.M., 1996. Plasma-treatment of polyetheretherketone (PEEK) for adhesive bonding. *International Journal of Adhesion and Adhesives*, *16*(2), pp.97–104.

Constantinou, A., Barrass, S., Pronk, F., Bril, T., Wenn, D. A., Shaw, J. E. A. and Gavriilidis, A., 2012. CO2 absorption in a high efficiency silicon nitride mesh contactor. *Chemical Engineering Journal* , 207–208, pp. 766–771.

Constantinou, A. and Gavriilidis, A., 2010. CO2 absorption in a microstructured mesh reactor. *Ind. Eng. Chem. Res.*, *49*(3), pp. 1041–1049.

Constantinou, A., Ghiotto, F., Lam, K.F. and Gavriilidis, A., 2014. Stripping of acetone from water with microfabricated and membrane gas–liquid contactors. *Analyst*, *139*(1), pp.266-272.

Coulson, J. M., Rcharson, J. F., Backhurst, J. R. and Harker, J. H., 2002. *Particle Technology and Separation Processes*. 5th edn. Bath, UK: The Bath Press.

Cussler, E. L., 1997. *Diffusion: Mass Transfer in Fluid Systems*. 3rd edn. UK: Cambridge University Press.

Cypes, S. H. and Engstrom, J. R., 2004. Analysis of a toluene stripping process: A comparison between a microfabricated stripping column and a conventional packed tower. *Chemical Engineering Journal*, *101*(1–3), pp. 49–56.

Eckert, J. S., 1970. Trays and packings: selecting Proper Distillation Column Packing. *Chemical Engineering Progress*, *66*(3), p. 39–44.

Edmister, W. C., 1957. Absorption and stripping-factor functions for distillation calculation by manual-and digital-computer methods. *AIChE Journal*, *3*(2), pp. 165–171.

French, H. T., 1987. Vapour pressures and activity coefficients of (acetonitrile + water) at 308.15 K. *The Journal of Chemical Thermodynamics*, *19*(11), pp. 1155–1161.

Fuller, E.N., Ensley, K. and Giddings, J.C., 1969. Diffusion of halogenated hydrocarbons in helium. The effect of structure on collision cross sections. *The Journal of Physical Chemistry*, *73*(11), pp.3679–3685.

Gabelman, A. and Hwang, S.T., 1999. Hollow fiber membrane contactors. *Journal of Membrane Science*, *159*(1-2), pp.61–106.

Geankoplis, C. J., 2003. *Transport Processes and Unit Operations*. 3rd edn. London: Prentice-Hall international (UK) Limited.

Gibbon, H.J., Wainwright, J. and Rogers, R.L., 1994. Experimental determination of flammability limits of solvents at elevated temperatures and pressures. In *Institution of Chemical Engineers Symposium Series* (Vol. 134, pp. 1-1). HEMSPHERE PUBLISHING CORPORATION.

Gierczak, T., Burkholder, J. B., Bauerle, S. and Ravishankara, A. R., 1998. Photochemistry of acetone under tropospheric conditions. *Chemical Physics*, 231, pp. 229–244.

Górak, A. and Stankiewicz, A., 2011. Intensified reaction and separation systems. *Annual review of chemical and biomolecular engineering*, *2*, pp.431–451.

Gregersen, M. M., Okkels, F., Bazant, M. Z. and Bruus, H., 2009. Topology and shape optimization of induced-charge electro-osmotic micropumps. *New Journal of Physics*, *11*(7), pp. 1–21.

Habibullah, M., Rahman, I. M. M., Uddin, M. A., Iwakabe, K., Azam, A. and Hasegawa, H., 2011. Densities and Viscosities of the Binary Mixtures of Phenylmethanol with 2-Butanone', *Journal of Chemical and Engineering Data*, *56*(8), pp. 3323–3327.

Haidl, J., Rejl, F. J., Valenz, L., Kordač, M., Moucha, T., Labík, L. and Schultes, M., 2016. Absorption in wetted-wall column with phase properties close to distillation conditions. *Chemical Engineering Science*, *144*, pp. 126–134.

Harries, D., Holler, J. F. and Crouch, S. R., 2007. *Principles of Instrumental Analysis*. 6th edn. Canada: Thomson Brooks/Cole.

Hart, J. E., 1971. Instability and Secondary Motion in a Rotating Channel Flow. *J Fluid Mech*, *45*(2), pp. 341–351.

Hartwick, R. P. and Howat, C. S., 1995. Infinite Dilution Activity Coefficients of Acetone in Water. A New Experimental Method and Verification. *J. Chem. Eng. Data*, *40*(4), pp. 738–745.

Hayduk, W. and Laudie, H., 1974. Prediction of diffusion coefficients for nonelectrolytes in dilute aqueous solutions. *AIChE Journal*, *20*(3), pp.611–615.

Hessel, V., Angeli, P., Gavriilidis, A. and Löwe, H., 2005. Gas-liquid and gas-liquid-solid microstructured reactors: Contacting principles and applications. *Industrial and Engineering Chemistry Research*, *44*(25), pp. 9750–9769.

Ho-Le, K., 1988. Finite element mesh generation methods: a review and classification. *Computer-Aided Design*, *20*(1), pp. 27–38.

Houston, R. and Walker, C., 1950. Absorption in Packed Towers. Effect of Molecular Diffusing on Gas Film Coefficient. *Industrial & Engineering Chemistry*, *42*(6), pp. 1105–1112.

Hovorkaa, Š., Dohnala, V., Rouxb, A. H. and Roux-Desgranges, G., 2002. Determination of temperature dependence of limiting activity coefficients for a group of moderately hydrophobic organic solutes in water. *Fluid Phase Equilibria ·*, *201*(1), pp. 135–164.

Howard, K.S. and McAllister, R.A., 1957. Surface tension of acetone-water solutions up to their normal boiling points. *AIChE Journal*, *3*(3), pp.325-329.

Howard, K. S. and McAllister, R. A., 1958. The viscosity of acetone-water solutions up to their normal boiling points. *AIChE Journal*, *4*(3), pp. 362–366.

Hsu, L. J. and Lin, C. C., 2012. Binary VOCs absorption in a rotating packed bed with blade packings. *Journal of Environmental Management*, *98*(1), pp. 175–182.

Huffman, J. R. and Urey, H. C., 1937. Separation of Oxygen Isotopes by a Fractionating Column. *Indutrial and Engineering Chemistry*, 29(5), pp. 531–535.

Hwang, Y. L., Keller, G. E. and Olson, J. D., 1992. Steam Stripping for Removal of Organic Pollutants from Water. 1. Stripping Effectiveness and Stripper Design. *Industrial and Engineering Chemistry Research*, 31(7), pp. 1753–1759.

Ikehata, J., Shinomiya, K., Kobayashi, K., Ohshima, H., Kitanaka, S. and Ito, Y., 2004. Effect of Coriolis force on counter-current chromatographic separation by centrifugal partition chromatography. *Journal of Chromatography A*, *1025*(2), pp. 169–175.

Iwakabe, K. and Kosuge, H., 2002. Determination and prediction of the isobaric vapor-liquid-liquid equilibrium data. in *the Proceedings of the International Conference on Distillation and Absorption*. Baden-Baden, Germany.

Javed, K. H., Mahmud, T. and Purba, E., 2006. Enhancement of mass transfer in a spray tower using swiriling gas flow. *Chemical Engineering Research and Design*, *84*(6), pp. 465–477.

Javed, K. H., Mahmud, T. and Purba, E., 2010. The CO2 capture performance of a high-intensity vortex spray scrubber. *Chemical Engineering Journal*, *162*(2), pp. 448–456.

Joel, A. S., Wang, M., Ramshaw, C. and Oko, E., 2017. Modelling, simulation and analysis of intensified regenerator for solvent based carbon capture using rotating packed bed technology. *Applied Energy*, 203, pp. 11–25.

Kadoya, .K, Matsunaga, N. and Nagashima, A., 1985. Viscosity and Thermal Conductivity of Dry Air in the Gaseous Phase. *J. Phys. Chem. Ref. Data*, *14*(4), pp. 947–970.

Khattab, I. S., Bandarkar, F., Fakhree, M. A. A. and Jouyban, A., 2012. Density, viscosity, and surface tension of water+ethanol mixtures from 293 to 323K. *Korean Journal of Chemical Engineering*, *29*(6), pp. 812–817.

Kheshgi, H. S. and Scriven, L. E., 1985. Viscous flow through a rotating square channel. *Physics of Fluids*, *28*(10), pp. 2968–2979.

Kister, H.Z., Haas, J.R., Hart, D.R. and Gill, D.R., 1992. *Distillation design* (Vol. 1). New York: McGraw-Hill.

Kohl, A. and Nielsen, R., 1997. *Gas Purification*. 5th edn. USA: Gulf Publishing Company.

Kojima, K., Zhang, S. and Hiaki, T., 1997. Measuring methods of infinite dilution activity coefficients and a database for systems including water. *Fluid Phase Equilibria*, *131*, pp. 145–179.

Kowalczuk, P. B. and Drzymala, J., 2016. Some remarks on attachment of a gas bubble to another phase both immersed in water. *Physicochemical Problems of Mineral Processing*, *52*(1), pp. 147–154.

Kumar, M. P. and Rao, D. P., 1990. Studies on a High-Gravity Gas-Liquid Contactor. *Industrial & engineering chemistry research*, *29*(5), pp. 917–920.

Kunz, R. G. and Baade, W. F., 2001. Vapor-liquid activity coefficients for methanol and ethanol from heat of solution data: application to steam-methane reforming. *Journal of hazardous materials*, *88*(1), pp. 53–62.

Kuvshinov, D., Bown, M. R., MacInnes, J. M., Allen, R. W. K., Ge, R., Aldous, L., Hardacre, C., Doy, N., Newton, M. I. and Mchale, G., 2011. Thermal conductivity measurement of liquids in a microfluidic device. *Microfluidics and Nanofluidics*, *10*(1), pp. 123–132.

Kwon, K.C., Ibrahim, T.H., Park, Y. and Simmons, C.M., 2004. Pseudo-binary molecular diffusion of vapors into air. *Advances in Environmental Research*, *8*(3-4), pp.667–678.

Lam, K. F., Sorensen, E. and Gavriilidis, A., 2013. Review on gas–liquid separations in microchannel devices. *Chemical Engineering Research and Design*. Institution of Chemical Engineers, *91*(10), pp. 1941–1953.

Lamarre, B. and Shearouse, D., 1994. Air Stripping Industrial Wastewater. *Pollution Engineering* :*(United States)*, *26*(9).

Langrish, T., Makarytchev, S., Fletcher, D. and Prince, R., 2003. Progress in Understanding the Physical Processes Inside Spinning Cone Columns. *Chemical Engineering Research and Design*, *81*(1), pp. 122–130.

Lee, G. H. and Baek, J. H. , 2002. A numerical study of the similarity of fully developed turbulent flows in orthogonally rotating square ducts and stationary curved square ducts. *International Journal of Numerical Methods for Heat & Fluid Flow*, *12*(3), pp. 241–257.

Lee, G. H. and Baek, J. H., 2006. Effect of aspect ratio on the similarity between developing laminar flows in orthogonally rotating ducts and stationary curved ducts. *International Journal of Numerical Methods for Heat & Fluid Flow*, *16*(4), pp. 494–508.

Lee G.H., Beak, J. H. , 2001. A numerical study on the similarity of laminar flows in orthogonally rotating rectangular ducts and stationary curved rectangular ducts of arbitrary aspect ratio. in *7th International Conference on Fluid Dynamics and Propulsion*. Egypt, pp. 1–6.

Leva, M., 1954. Flow Through Irrigated Dumped Packings-Pressure drop, Loading, Flodding. *In Chem. Eng. Progr. Symp. Ser.*, *50*(10), pp. 51–59.

Levenspiel, O., 1999. *Chemical Recation Engineering*. 3rd edn. New York: John Wiley & Sons, Inc.

Li, Q., Ito, K., Wu, Z., Lowry, C. S. and Loheide, S. P., 2009. COMSOL multiphysics: A novel approach to ground water modeling. *Ground Water*, *47*(4), pp. 480–487.

Li, Y., Lu, Y., Liu, X. J., Wang, G., Nie, Y. and Ji, J., 2017. Mass-transfer characteristics in a rotating zigzag bed as a Higee device', *Separation and Purification Technology*. *186*, pp. 156–165.

Lin, C.C. and Chien, K.S., 2008. Mass-transfer performance of rotating packed beds equipped with blade packings in VOCs absorption into water. *Separation and Purification Technology*, *63*(1), pp. 138–144.

Lin, C. C., Wei, T. Y., Liu, W. T. and Shen, K. P., 2004. Removal of VOCs from gaseous streams in a high-voidage rotating packed bed. *Journal of Chemical Engineering of Japan*, *37*(12), pp. 1471–1477.

Liu, H., Lin, C., Wu, S. and Hsu, H., 1996. Characteristics of a rotating packed bed. *Ind. Eng. Chem. Res.*, *35*(10), pp. 3590–3596.

Lobo, W. E., Friend, L., Hashmall, F. and Zenz, F., 1945. Limiting capacity of dumped tower packings. *Transactions of the American Institute of Chemical Engineers*, *41*(6), pp. 693–710.

Lockett, M. J., 1986. *Distillation Tray Fundamentals*. New York: Cambridge University Press.

Lugg, G. A., 1968. Diffusion coefficients of some organic and other vapors in air. *Analytical Chemistry*, *40*(7), pp. 1072–1077.

MacInnes, J. M., 2013. Prototype Channel Design Operation range for Rotating Spiral Phase Contacting. (Personal communication, 26th April 2015).

MacInnes, J. M., Ayash, A. A. and Dowson, G. R. M., 2017. CO2 absorption using diethanolamine-water solutions in a rotating spiral contactor. *Chemical Engineering Journal*, *307*, pp. 1084–1091.

MacInnes, J. M., Ortiz-Osorio, J., Jordan, P. J., Priestman, G. H. and Allen, R. W. K., 2010. Experimental demonstration of rotating spiral microchannel distillation. *Chemical Engineering Journal*, *159*(1–3), pp. 159–169.

MacInnes, J. M., Pitt, M. J., Priestman, G. H. and Allen, R. W. K., 2012. Analysis of two-phase contacting in a rotating spiral channel. *Chemical Engineering Science*, *69*(1), pp. 304–315.

MacInnes, J. M., Priestman, G. H. and Allen, R. W. K., 2005. A Spinning Micro-Channel Multiphase Contactor. in *:7th World Congress of Chemical Engineering*. Glasgow.

MacInnes, J. M. and Zambri, M. K. S., 2015. Hydrodynamic characteristics of a rotating spiral fluid-phase contactor. *Chemical Engineering Science*, *126*, pp. 427–439.

Mahmud, H., Kumar, A., Narbaitz, R. M. and Matsuura, T., 1998. Membrane air stripping : a process for removal of organics from aqueous solutions. *Separation Science and Technology*, *33*(14), pp. 2241–2255.

Makarytchev, S. V., Langrish, T. A. G. and Fletcher, D. F., 2005. CFD Analysis of Scale Effects in Spinning Cone Columns. *Chemical Engineering Research and Design*, *83*(8), pp. 951–958.

Makarytchev, S. V., Langrish, T. A. G. and Fletcher, D. F., 2002. CFD analysis of spinning cone columns: Prediction of unsteady gas flow and pressure drop in a dry column. *Chemical Engineering Journal*, *87*(3), pp. 301–311.

Makarytchev, S. V, Langrish, T. A. G. and Fletcher, D. F., 2004. Mass transfer analysis of spinning cone columns using CFD. *Chemical Engineering Research and Design*, *82*(6), pp. 752–761.

McCabe, W. L., Smith, J. C. and Harriott, P., 1993. *Unit Operations of Chemical Engineering*. 5th edn. New York: McGraw-Hill.

Mhiri, N., Monnier, H. and Falk, L., 2011. Intensification of the G/L absorption in microstructured falling film application to the treatment of chlorinated VOC's. Part III: Influence of gas thickness channel on mass transfer. *Chemical Engineering Science*, *66*(23), pp. 5989–6001.

Mochalova, N.S., Kholpanov, L.P. and Shkadov, V.Y., 1973. Hydrodynamics and mass transfer in a liquid layer at a rotating surface. *Journal of Engineering Physics and Thermophysics*, *25*(4), pp.1251–1256.

Monnier, H. and Falk, L. , 2011. Intensification of G/L absorption in microstructured falling film. Application to the treatment of chlorinated VOC's - part II: Modeling and geometric optimization. *Chemical Engineering Science*, *66*(12), pp. 2475–2490.

Monnier, H., Falk, L., Lapicque, F., Hadjoudj, R. and Roizard, C., 2010. Intensification of G/L absorption in microstructured falling film. Application to the treatment of chlorinated VOC's - part I: Comparison between structured and microstructured packings in absorption devices. *Chemical Engineering Science*, *65*(24), pp. 6425–6434.

Munjal, S., Dudukovć, M. P. and Ramachandran, P., 1989. Mass-transfer in rotating packed beds—I. Development of gas—liquid and liquid—solid mass-transfer correlations. *Chemical Engineering Science*, *44*(10), pp. 2245–2256.

Nadasdi, R., Zügner, G. L., Farkas, M., Dóbe, S., Maeda, S. and Motokuma, K., 2010. Photochemistry of Methyl Ethyl Ketone: Quantum Yields and S1/S0 -Diradical Mechanism of Photodissociation. *ChemPhysChem 2010, 11*(18), pp. 3883–3895.

De Nevers, N., 2012. *Physical and chemical equilibrium for chemical engineers*. 2nd edn. Hoboken, New Jersy: John Wiley and Sons. Inc.

Nielsen, C. H. E., Kiil, S., Thomsen, H. W. and Dam-Johansen, K., 1998. Mass transfer in wetted-wall columns: Correlations at high Reynolds numbers. *Chemical Engineering Science*, *53*(3), pp. 495–503.

Olesen, L. H., Okkels, F. and Bruus, H., 2006. A high-level programming-language implementation of topology optimization applied to steady-state Navier-Stokes flow. *International Journal for Numerical Methods in Engineering*, *65*(7), pp. 975–1001.

Ortiz-Osorio, J., MacInnes, J. M., Jordan, P. J., Priestman, G. H. and Allen, R. W. K., 2009. Computation of Mass transfer in Rotating Spiral Microchannel Distillation. in *:The Eighth World Congress of Chemical Engineering, Montreal, July 2009.*

Pan, S. Y., Wang, P., Chen, Q., Jiang, W., Chu, Y. H. and Chiang, P. C., 2017. Development of high-gravity technology for removing particulate and gaseous pollutant emissions: Principles and applications. *Journal of Cleaner Production*, 149, pp. 540–556.

Patel, P., Hull, T., Lyon, R., Stoliarov, S., Walters, R., Crowley, S. and Safronava, N., 2010. Investigation of the thermal decomposition and flammability of PEEK and its carbon and glass-fibre composites. *Polymer Degradation and Stability*, *96* (1), pp. 12–22.

Pepper, D. W. and Heinrich, J. C., 2006. *The finite element method: basic concepts and applications*. 2nd edn. USA: CRC Press.

Pilo, C. W. and Dahlbeck, S. W., 1960. Apparatus for Intimate Contacting of Two Fluid Media Having Different Specific Weight. U.S. Patent No. 2,941,872 .

Pinilla, E. A., Diaz, J. M. and Coca, J., 1984. Mass Transfer and Axial Dispersion in a Spray Tower for Gas-Liquid Contacting. *The Canadian Journal of Chemical Engineering*, *62*(5), pp. 617–622.

Pividal, K. A., Birtigh, A. and Sandler, S. I., 1992. Infinite Dilution Activity Coefficients for Oxygenate Systems Determined Using a Differential Static Cell', *J. Chem. Eng. Data*, *37*(4), pp. 484–487.

Placek, A., 1942. Process and apparatus for treating liquids with a gaseous medium. U.S. Patent 2,281,616.

Podbielniak, W.J., Kaiser, H.R. and Ziegenhorn, G.J., 1970. The history of penicillin production. In *Chem Eng. Symp Ser*, *66*, pp. 43–50.

Podbielniak, W. J., 1935. Centrifugal Fractionation Method and Apparatus. U.S. Patent 2,003,308.

Podbielniak, W. J., 1936. Method of Securing Counter-current Contact of Fluids by Centrifugal Action. U.S. Patent 2,044,996.

Podbielniak, W. J., 1937. Method and Apparatus of Refining Hydrocarbon Oil. U.S. Patent 2,093,645.

Podbielniak, W. J., 1938. Apparatus for Effecting Counter-current Contact Between Fluids. U.S. Patent 2,109,375.

Podbielniak, W. J., 1942. Method of Securing Counter-current Contact between Fluids. U.S. Patent 2,286,157.

Poling, B. E., Prausnitz, J. M. and O'connell, J. P., 2001. *The properties of gases and liquids*. 5th edn. New York: Mcgraw-hill.

Pratt, K. C. and Wakeham, W. A., 1974. The Mutual diffusion coefficient of ethanol-water mixtures: determination by a rapid, new method. *Proc. R. Soc. Lond. A*, *336*(1606), pp. 393–406.

Prince, M. J. and Blanch, H. W., 1990. Bubble coalescence and break-up in air-sparged bubble columns. *AIChE Journal*, *36*(10), pp. 1485–1499.

Pyle, L., 1994. Processed Foods with Natural Flavour: The Use of Novel Recovery Technology. *Nutrition & Food Science*, *94*(1), pp. 12–14.

Rafati, A.A., Bagheri, A. and Najafi, M., 2010. Experimental data and correlation of surface tensions of the binary and ternary systems of water+ acetonitrile+ 2-propanol at 298.15 K and atmospheric pressure. *Journal of Chemical & Engineering Data*, *55*(9), pp.4039–4043.

Ramshaw, C. and Mallinson, R.H., Imperial Chemical Industries Ltd, 1981. Mass transfer process. U.S. Patent 4,283,255.

Ramshaw, C., 1993. Opportunities for Exploiting Centrifugal Fields. *Heat Recovery Systems & CHP*, *13*(6), pp. 493–513.

Rasoul, A. A., 2014. *Modelling of vapour-liquid-liquid equilibria for multicomponent heterogeneous systems*. Ph.D thesis. Teesside University.

Reddy, J. N., 1984. *An intorduction to the Finite Element Method*. New York: McGraw-Hill, Inc.

Rejl, F. J., Haidl, J., Valenz, L., Moucha, T. and Schultes, M., 2016. Analogy of absorption and distillation processes. Wetted-wall column study. *Chemical Engineering Science*, *153*, pp. 146–154.

De Rivas, A. and Villermaux, E., 2016. Dense spray evaporation as a mixing process. *Physical Review Fluids*, *1*(1), pp. 1–15.

Roemer, R.B. and Leppert, G., 1968. Surface tensions of water-methyl ethyl ketone mixtures. *Journal of Chemical & Engineering Data*, *13*(1), pp.28-30.

Saffarionpour, S. and Ottens, M., 2018. Recent Advances in Techniques for Flavor Recovery in Liquid Food Processing. *Food Engineering Reviews*, *10*(2), pp. 1–14.

Saleh, M. A., Akhtar, S., Ahmed, M. S., Saleh, M. A., Akhtar, S. and Ahmed, M. S., 2006. Density , viscosity and thermodynamic activation of viscous flow of water + acetonitrile. *Physics and Chemistry of Liquids*, *44*(5), pp. 551–562.

Sander, R., 2015. Compilation of Henry's law constants (version 4.0) for water as solvent. *Atmos.Chem.Phys.*, *15*(8), pp. 4399–4981.

Sandilya, P., Rao, D. P., Sharma, a. and Biswas, G., 2001. Gas-Phase Mass Transfer in a Centrifugal Contactor. *Industrial & Engineering Chemistry Research*, *40*(1), pp. 384–392.

De Santos, J. M., Melli, T. R. and Scriven, L. E., 1991. Mechanics of gas-liquid flow in packed-bed contactors. *Annu. Rev. Fluid Mech*, *23*(1) , pp. 233–260.

Schmidt, T.W., Phillips Petroleum Company, 1980. Determination of infinite dilution activity coefficients (γ∞) using molecular beams. U.S. Patent 4,214,158.

Schütze, M. and Herrmann, H., 2004. Uptake of acetone, 2-butanone, 2, 3-butanedione and 2-oxopropanal on a water surface. *Physical Chemistry Chemical Physics*, *6*(5), pp.965–971.

Seader., J. D. and Henley, E. J., 2006. *Separation Process Principles*. 2nd edn. John Wiley & Sons, Inc.

Selmi, M., Nandakumar, K. and Finlay, W. H., 1994. A bifurcation study of viscous flow through a rotating curved duct. *J.Fluid Mech.*, *262*, pp.353–375.

Sengupta, A., Peterson, P. A., Miller, B. D., Schneider, J. and Fulk, C. W., 1998. Large-scale application of membrane contactors for gas transfer from or to ultrapure water. *Separation and Purification Technology*, *14*(1–3), pp. 189–200.

Shaffer, D. L. and Daubert, T. E., 1969. Gas-liquid chromatographic determination of solution properties of oxygenated compounds in water. *Analytical Chemistry*, *41*(12), pp. 1585–1589.

Sheng, H. and Zhu, S., 2014. Weak Form & LiveLink for MATLAB Based Modified Uzawa Method for Solving Steady Navier-Stokes Equation. *In Comsol conference in Shanghai*.

Sherman, S. R., Trampe, D. B., Bush, D. M., Schiller, M., Eckert, C. a., Dallas, A. J., Li, J. and Carr, P. W., 1996. Compilation and Correlation of Limiting Activity Coefficients of Nonelectrolytes in Water. *Industrial & Engineering Chemistry Research*, *35*(4), pp. 1044–1058.

Sherwood, T. K., Pigford, R. L. and Wilke, C. R., 1975. *Mass Transfer*. McGraw-Hill.

Sherwood, T.K., Shipley, G.H. and Holloway, F.A.L., 1938. Flooding velocities in packed columns. *Industrial & Engineering Chemistry*, *30*(7), pp.765–769.

Simons, K., Nijmeijer, K. and Wessling, M., 2009. Gas-liquid membrane contactors for CO2 removal. *Journal of Membrane Science*, *340*(1–2), pp. 214–220.

Smith, B., 1963. *Design of equilibrium stage processes*. New York: McGraw-Hill Companies.

Smith, J. M., Van Ness, H. C. and Abbott, M. M., 2005. *Introduction to Chemical Engineering Thermodynamics*. 7th edn. New York: McGraw-HILL Eductation.

Speziale, C. G., 1982. Numerical study of viscous flow in rotating rectangular ducts. *Journal of Fluid Mechanics*, *122*, pp. 251–271.

Speziale, C. G. and Thangam, S., 1983. Numerical study of secondary flows and roll-cell instabilities in rotating channel flow. *Journal of Fluid Mechanics*, *130*, pp. 377-395.

Still, W. C., Khan, M. and Mitra, A., 1978. Rapid chromatographic technique for preparative separations with moderate resolution. *The Journal of Organic Chemistry*, *43*(14), pp. 2923–2925.

Sun, X., Constantinou, A. and Gavriilidis, A., 2011. Stripping of acetone from isopropanol solution with membrane and mesh gas–liquid contactors. *Chemical Engineering and Processing: Process Intensification*, *50*(10), pp.991–997.

Thomas, K. S. and McAllister, R. A., 1957. Densities of liquid-acetone-water solutions up to their normal boiling points. *A.1.Ch.E. Journal*, *3*(2), pp. 161–164.

Thomas, W.J. and Portalski, S., 1958. Hydrodynamics of countercurrent flow in wetted-wall columns. *Industrial & Engineering Chemistry*, *50*(7), pp.1081–1088.

Tochigi, K. and Kojima, K., 1976. The Determination of Group Wilson Parameters To Activity Coefficients By Ebulliometer. *Journal of Chemical Engineering of Japan*, *9*(4), pp. 267–273.

Todd, D. B. and Podbienlniak, W. J., 1965. Advances in centrifugal extraction. *Chemical Engineering Progress*, *61*(5), p.69.

Trent, D. L., 2003. Chemical Processing in High Gravity Fields. In: Stankiewicz A. & Mouljin, J. A. Re-Engineering the Chemical Processing Plant: Process Intensification, CRC Press. pp. 29–61.

Treybal, R. E., 1981. *Mass-Transfer Operations*. McGraw-Hill.

Tritton, D.J., 1988. Physical fluid mechanics. *Clarendon, Oxford*.

Tsilingiris, P. T., 2008. Thermophysical and transport properties of humid air at temperature range between 0 and 100 °C. *Energy Conversion and Management*, *49*(5), pp. 1098–1110.

Tyn, M.T. and Calus, W.F., 1975. Temperature and concentration dependence of mutual diffusion coefficients of some binary liquid systems. *Journal of Chemical and Engineering Data*, *20*(3), pp.310–316.

Van der Schaaf, J. and Schouten, J.C., 2011. High-gravity and high-shear gas–liquid contactors for the chemical process industry. *Current Opinion in Chemical Engineering*, *1*(1), pp.84–88.

Vazquez, G., Alvarez, E. and Navaza, J. M., 1995. Surface Tension of Alcohol + Water from 20 to 50 °C. *Journal of Chemical and Engineering Data*, *40*(3), pp. 611–614.

Vinci, B.J., Watten, B.J. and Timmons, M.B., 1996. Gas-phase axial dispersion in a spray tower. *Aquacultural engineering*, *15*(1), pp.1–11.

Vivian, J. E., Brian, P. L. T. and Krukonis, V. J., 1965. The influence of gravitational force on gas absorption in a packed column. *11*(6), pp. 1088–1091.

Wang, L., 1997. Effect of spanwise rotation on centrifugal instability in rotating curved non-isothermal flows. *Computational mechanics*, *19*(5), pp.420-433.

Weatherly, C. A., Woods, R. M. and Armstrong, D. W., 2014. Rapid analysis of ethanol and water in commercial products using ionic liquid capillary gas chromatography with thermal conductivity detection and/or barrier discharge ionization detection. *Journal of Agricultural and Food Chemistry*, *62*(8), pp. 1832–1838.

Weidlich, U. and Gmehling, J., 1987. A modified UNIFAC model. 1. Prediction of VLE, hE, and. gamma.. infin. *Industrial & engineering chemistry research*, *26*(7), pp.1372-1381.

Wenn, D. a, Shaw, J. E. a and Mackenzie, B., 2003. A mesh microcontactor for 2-phase reactions. *Lab on a chip*, *3*(3), pp. 180–6.

White, F. M., 2008. *Fluid Mechanics*. 6th edn. McGraw-Hill.

Wilke, C.R. and Chang, P., 1955. Correlation of diffusion coefficients in dilute solutions. *AIChE Journal*, *1*(2), pp.264–270.

Wörner, M., 2012. Numerical modeling of multiphase flows in microfluidics and micro process engineering: A review of methods and applications. *Microfluidics and Nanofluidics*, *12*(6), pp. 841–886.

Wright, A. J. and Pyle, D. L., 1996. An investigation into the use of the spinning cone column for in situ ethanol removal from a yeast broth. *Process Biochemistry*, *31*(7), pp. 651–658.

Yang, W. J., Fann, S. and Kim, J., 1994. Heat and fluid flow inside rotating channels. *Appl. Mech. Rev* ., *47*(8), pp. 367–396.

Yang, Y., Belghazi, M., Lagadec, A., Miller, D.J. and Hawthorne, S.B., 1998. Elution of organic solutes from different polarity sorbents using subcritical water. *Journal of Chromatography A*, *810*(1-2), pp.149-159.

Yang, Z., Zhang, G., Lin, L., Ren, D., Meng, Q. and Zhang, H., 2009. Effects of baffles on separation of aqueous ethanol solution with hollow fibers. *Frontiers of Chemical Engineering in China*, *3*(1), pp.68–72.

Zambri, M. K. S. (2014). Rotating Spiral Prototype Contactor: Design and Demonstration. Ph.D thesis. The University of Sheffield.

Zanfir, M., Gavriilidis, A., Wille, C. and Hessel, V., 2005. Carbon Dioxide Absorption in a Falling Film Microstructured Reactor: Experiments and Modeling. *Industrial & Engineering Chemistry Research*, *44*(6), pp. 1742–1751.

Zanfir, M., Sun, X. and Gavriilidis, A., 2008. Microstructured mesh contactor for asymmetric transfer hydrogenation with simultaneous stripping: Modeling and experiments. *Industrial and Engineering Chemistry Research*, *47*(23), pp. 8995–9005.

Zarei, T., Rahimi, R., Zarei, A. and Zivdar, M., 2013. Hydrodynamic characteristic of Conical Cap tray: Experimental studies on dry and total pressure drop, weeping and entrainment. *Chemical Engineering and Processing: Process Intensification*, *64*, pp.17-23.

Zarei, T., Farsiani, M. and Khorshidi, J., 2017. Hydrodynamic characteristics of valve tray: Computational fluid dynamic simulation and experimental studies. *Korean Journal of Chemical Engineering*, *34*(1), pp. 150–159.

Zhao, H., Shao, L. and Chen, J.F., 2010. High-gravity process intensification technology and application. *Chemical Engineering Journal*, *156*(3), pp.588–593.

Zhavoronkov, N.M., Malyusov, V.A., Mochalova, N.S. and Kholpanov, L.P., 1977. Mass transfer in a liquid layer of variable thickness on a rotating archimedes spiral taking account of the entrance region. *Journal of Applied Mechanics and Technical Physics*, *18*(6), pp.806–811.

Ziegenbalg, D., Löb, P., Kralisch, D., Hessel, V. and Schönfeld, F., 2010. Use of 'smart interfaces' to improve the liquid-sided mass transport in a falling film microreactor. *Chemical Engineering Science*, *65*(11), pp.3557–3566.

Zimmerman, W. B., 2004. *Process modelling and simulation with finite element methods*. World Scientific Series A on Stability, Vibration and Control of Systems, Singapore.

Zimmerman, W. B., Hewakandamby, B. N., Tesar, V., Bandulasena, H. C. H. and Omotowa, O. A., 2009. On the design and simulation of an airlift loop bioreactor with microbubble generation by fluidic oscillation. *Food and Bioproducts Processing*, *87*(3), pp. 215–227.

Zimmerman, W. B., Tesař, V. and Bandulasena, H. C. H., 2011. Towards energy efficient nanobubble generation with fluidic oscillation. *Current Opinion in Colloid and Interface Science*, *16*(4), pp. 350–356.

Appendix A

Equations and Boundary Conditions Implementation in Comsol Multiphysics

A.1 Equations Implementation

The built-in PDE interface in Comsol (Ver. 5.2) provides a general form, allowing implementation of partial differential equations (PDEs). Multiple dependent variables can be implemented in one-, two- or three-dimensional form for steady-state and time dependent problems. For the case considered here, this general form can be expressed as follows (COMSOL Multiphysics User's Guide, 2008):

$$\nabla \cdot \boldsymbol{\Gamma} = \boldsymbol{F} \tag{A.1}$$

where Γ and F are called '*the conservative flux vector*' and '*the source term*', respectively.

For the purpose of this work, two general PDEs (Eq. A.1) have been specified for each separate phase. One includes the three velocity components and the mole fraction (u, v, w and Y) while the other equation is just to define the pressure ($\hat{p}$). Separating the variables using two general PDEs allows independently selecting second-order Lagrange elements for all the variable except the pressure, for which first-order elements satisfy as discussed in Chapter 4 (Section 4.5.2). The only limitation to this treatment of equations is that by default extra boundary conditions will be specified for the pressure in Comsol and must be deactivated.

Having defined the variables for each phase (domain), the continuity, momentum and species equations (Chapter 4, Section 4.2.4) can be implemented using Eq. A.1. Comsol specifies Γ vector and $\boldsymbol{F}$ for each single variable defined to enter the governing equations. Typically, the divergence of Γ includes all the fluxes in a governing equation while F includes all the other terms that cannot be expressed as a divergence. As an illustrative example, the implementation of the governing equations of the gas phase (listed in Section 4.2.4) is shown in Table A.1 (e.g. Gregersen et al., 2009).

Table A.1. Gas-phase equations implementation in Comsol using Eq. A.1.

Variable	Equation	$\nabla \cdot \Gamma$	F
$\hat{p}_V$	Eq. 4.14	0	$-\frac{\partial u_V}{\partial x}-\frac{\partial v_V}{\partial y}$
u_V	Eq. 4.15	$\frac{\partial}{\partial x}\left(-\mu_V\frac{\partial u_V}{\partial x}+\hat{p}_V\right)+\frac{\partial}{\partial y}\left(-\mu_V\frac{\partial u_V}{\partial y}\right)$	$-\rho_V\mu_V\frac{\partial u_V}{\partial x}-\rho_V v_V\frac{\partial u_V}{\partial y}$
v_V	Eq. 4.16	$\frac{\partial}{\partial x}\left(-\mu_V\frac{\partial v_V}{\partial x}+\hat{p}_V\right)+\frac{\partial}{\partial y}\left(-\mu_V\frac{\partial v_V}{\partial y}\right)$	$-\rho_V\mu_V\frac{\partial v_V}{\partial x}-\rho_V v_V\frac{\partial v_V}{\partial y}-2\rho_V\Omega w_V$
w_V	Eq. 4.17	$\frac{\partial}{\partial x}\left(-\mu_V\frac{\partial w_V}{\partial x}\right)+\frac{\partial}{\partial y}\left(-\mu_V\frac{\partial w_V}{\partial y}\right)$	$-\rho_V\mu_V\frac{\partial w_V}{\partial x}-\rho_V v_V\frac{\partial w_V}{\partial y}$ $+\rho_V\Omega w_V\sin\alpha-2\rho_V\Omega w_V$
Y_V	Eq. 4.18	$\frac{\partial}{\partial x}\left(-D_V\frac{\partial Y_V}{\partial x}\right)+\frac{\partial}{\partial y}\left(-D_V\frac{\partial Y_V}{\partial y}\right)$	$-w\frac{dY_{VB}}{dz}-u_V\frac{\partial Y_{VB}}{\partial x}-v_V\frac{\partial Y_{VB}}{\partial x}$

It is important to recognize here that the continuity equation (Eq. 4.14) is not presented as an equation for variable u_V or v_V. This is because that Comsol does not permit defining two equations for a single variable. To circumvent this situation, the continuity equation is entered in the source term of $\hat{p}_V$. Such presentation is acceptable since the pressure gradient in *x* and *y* is already considered within Eqs. 4.15 and 4.16, respectively.

A.2 Boundary Conditions Implementation

In Comsol, the boundary conditions are classified into two main types: constraint (or Dirichlet) and Neumann boundary conditions. The first specifies explicit values or expressions of the variables on the boundary of the domain while the second defines values or expressions of the fluxes (derivatives) of the variables. These types of boundary conditions can be implemented using the following equations (COMSOL Multiphysics User's Guide, 2008):

$$0 = R_i \qquad \text{Constraint B.Cs} \tag{A.2}$$

$$-\vec{n}_i \cdot \Gamma_i = G_i - q_i u_i \qquad \text{Neumann B.Cs} \tag{A.3}$$

The term R_i in Eq. A.2 describes the constraint-type boundary conditions. Typically, Comsol dictates the explicit values or expressions of dependent variables to be implemented as constraints according to Eq. A.2. Taking the gas phase as an example, the no-slip boundary condition can be implemented as $R_1 = -u_v$, $R_2 = -v_V$ and $R_2 = -w_V$. As another example, the continuity of velocities at the phase interface can be obtained by defining $R_1 = -u_v + u_L, R_2 = -v_v + v_L$ and $R_3 = -w_v + w_L$. For the Neumann boundary conditions, the flux G_i is added on the boundary as can be seen in Eq. A.3. This term may represent an expression or a value of the gradient of the defined variables. The q_i is a coefficient which allows introducing a mixed boundary conditions (function and derivative) through the form $q_i u_i$ where u_i is a dependent variable. Here, in the case of symmetry boundary conditions, for example, G_i and q_i are set to be zero since a zero flux of all variables is required on the end-walls. Fig. A.1 summarises the conditions applied at the boundaries of each separate phase using Eqs. A.2 and A.3.

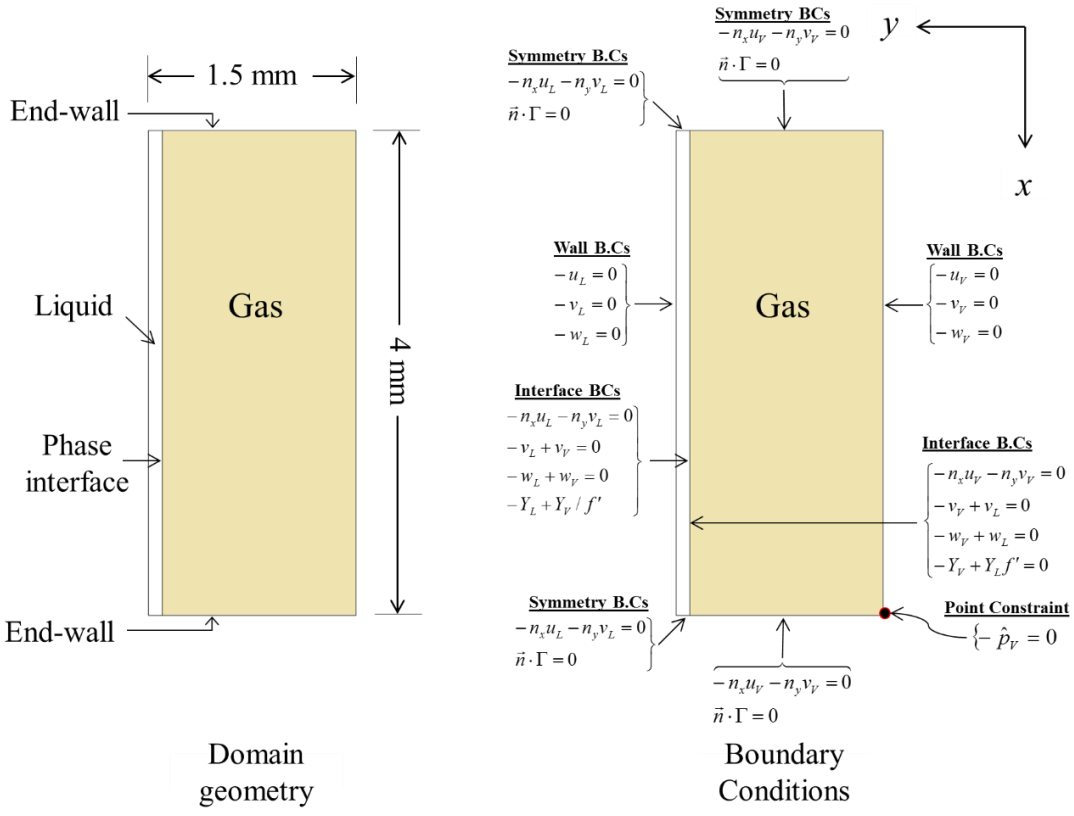

Figure A.1. A diagram showing the domain geometry (left-hand side) and the implemented boundary conditions (right-hand side).

In addition to the above boundary conditions, the specification of the piezometeric pressure ($\hat{p}$) and the solute mole fraction (Y) are also needed to solve the governing equations. In terms of the piezometeric pressure, a single value at any point in the solution domain is sufficient to establish the pressure field since the flow equations do not depend explicitly on the pressure level but on its gradient. This value is taken to be zero at a reference point in the gas phase (Fig. A.1). For the solute, on the other hand, it was found that specifying the mole fraction level at a reference point tends to be the highest value from which the entire mole fraction field establishes. Such uneven mole frication distribution is not physically-possible and might lead to error in estimating the bulk values (Y_{VB} and Y_{LB}) and hence mass transfer coefficient. To avoid that, the average solute mole fraction along the interface in one of the phases is constrained to a fixed value using a global constraint function in Comsol. This allows establishing the solute mole fraction field to satisfy this constraint without selecting preferentially a specific point in the solution domain and hence unbiased distribution can be obtained.

Appendix B

Spiral Pressure and Temperature Estimation

B.1 Spiral Pressure

The gas phase and the liquid phase are driven in the spiral channel essentially by the difference between the amount of the longitudinal body force and the pressure gradient along the channel ($\rho R\Omega^2 \sin\alpha - dp_0/dz$), against the viscous forces (as described in Chapter 4). For fully developed flow, dp_0/dz is the same for the two phases but they are different in $\rho R\Omega^2 \sin\alpha$ which is smaller for the gas phase (small density). Thus, the change in pressure along the channel is mainly due to the frictional losses in the gas flow and it is expected to be small since the viscosity of the gases, in general, is small. The 2-D computations made in this work show that the maximum gas flow rate used (which is 6.2 NL/min) needs approximately 3 kPa pressure difference to be driven over the spiral length. This confirms that the change in pressure over the spiral channel is small in relation to the absolute pressure, about 3% of atmospheric pressure. Therefore, for gas-liquid contacting, representing the spiral pressure by a single value would be an excellent approximation for purposes of gas and solute properties determination.

As shown in Chapter 5 (Fig. 5.7), the level of the pressure in the spiral is dictated by the amount of the centrifugal hydrostatic pressure $(1/2\,\rho_L R^2\Omega^2)$ in the liquid phase. This pressure can be determined using the manometer formed between the outer end of the spiral and the atmospheric vent (line C in Fig. 5.2 or 5.8 in Chapter 5 and is shown below in Fig. B.1 as a red line), (Todd and Podbielniak, 1965; MacInnes and Zambri, 2015). Thus, according to Fig. B.1, the spiral pressure (P_S) can be obtained by a force balance between the pressure difference across the manometer ends ($P_S - P_{atm}$), the frictional losses along the passage and the hydrostatic pressure changes (whether due to a change in the elevation (ΔZ) or the radial position for the rotating passages). This gives:

$$P_S - P_{atm} = \rho_L g \Delta Z + \underbrace{1/2\,\rho_L (r_R{}^2 - r_S^2)\Omega^2}_{\substack{\textit{Centrifugal hydrostatic} \\ \textit{change}}} + \underbrace{\rho_L g h_f}_{\substack{\textit{Pressure} \\ \textit{frictional losses}}} \qquad \text{(B.1)}$$

where r_R and r_S are the radial distances from the rotation centre to the spiral outer end and to the radial passage end of the shaft (which represents the end of the rotating part in the liquid passage as shown in Fig. B.1), respectively.

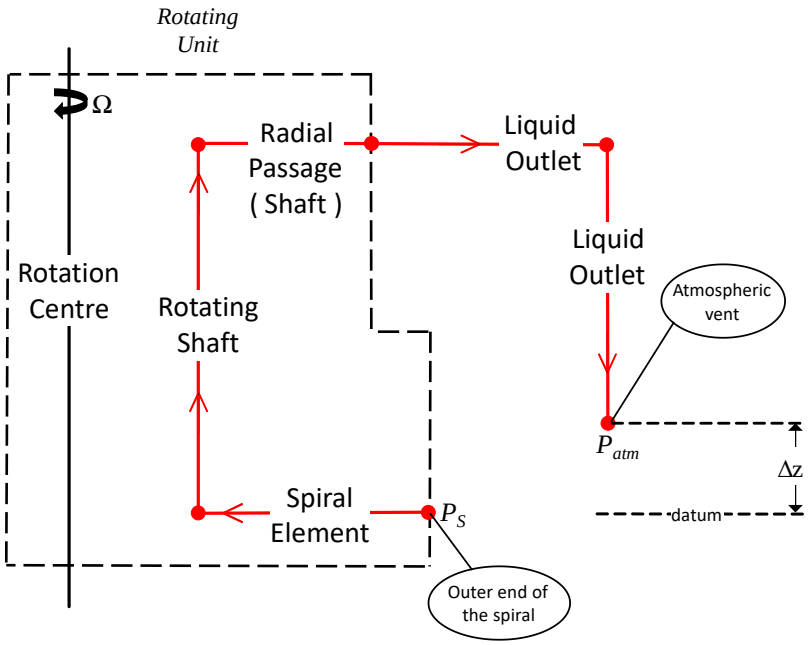

Figure B.1. A schematic diagram of the outlet liquid passage (line C in Fig. 5.2 or 5.8, Chapter 5). The passage consists of rotating and static sections and is shown as a red line.

In the experiments, ΔZ and the liquid outlet passage are sized to just a few centimetres. So, the change in the hydrostatic pressure and the passage frictional losses are negligible in relation to the change in the centrifugal hydrostatic pressure. This simplifies Eq. B.1 to:

$$P_S = P_{atm} + 1/2\,\rho_L (r_R{}^2 - r_S^2)\Omega^2 \qquad \text{(B.2)}$$

According to the above equation, the spiral pressure then, is determined by downstream liquid pressure which is atmospheric (P_{atm}), the liquid density (ρ_L), the level of the rotation rate (3200 rpm) and the radial distances. Therefore, the only parameters needed to determine the spiral pressure are the rotation rate which is fixed and the liquid density which depends on the liquid composition and temperature. For all tests, the solution is fed at a dilute level and leaves the spiral channel at a lower concentration. So, it should be expected that the liquid density in the outlet passage (after contacting) is approximately a density of water. Further, it is known that the change in temperature has a minor effect

on the densities of liquids (to about 1% when water temperature is increased from 20 to 50 °C). For the sake of the simplicity of calculations, therefore, the spiral pressure is determined based on a density of pure water at 25 °C since the liquid density is approximately constant under the experimental conditions. This gives 1.8 bara as a spiral pressure and this value is fixed and used for the purposes of physical properties and gas flow rate calculations.

B.2 Spiral Temperature

Since the gas phase and the liquid phase flow through passages of the same shaft and contact counter-currently in a single spiral channel, the temperature along the channel is assumed to be uniform and the same in both phases. This temperature is estimated using a method described in MacInnes and Zambri (2015), following an original work by Kuvshinov et al. (2011). The method is based on measuring the transient temperatures at the glass window (which is one of the channel ends wall) immediately after steady-state operation at a rotation rate of 3200 rpm. The glass temperature measurements start with stopping both the rotation and the flow of the fluids inside the spiral. Once the spiral element has come to stop, a thermocouple with a foam insulation is placed directly on the glass window and temperatures are recorded every 3 seconds using data logging (HH309A, Omega Engineering). In this way, the glass window is sandwiched between two insulation layers (the foam from one side and the PEEK spiral element from the other side) and one dimensional heat transfer is assumed between the glass ends. Under these conditions, MacInnes and Zambri (2015) argue that the final temperature (T_f) measured during the transient period is the same as the temperature at the middle of the glass during steady-state operation. Thus, with a simple energy balance across the glass at the steady condition, taking T_0 as an initial temperature, one can estimate the spiral temperature (T_S) during operation as:

$$T_S = 2(T_f - T_0) + T_0 \qquad \text{(B.3)}$$

It should be clear now that the identification of one-dimensional range in the measured transient temperatures data determines temperatures, T_0 and T_f, during steady-state operation. From these temperatures, the spiral temperature can be estimated using Eq. B.3.

The thermal characteristic time of the glass (δ^2/α) is 125 s where δ is the glass thickness (1 cm) and α is the glass thermal diffusivity (8×10^{-7} m^2/s). This small characteristic time suggests that a fast one dimension heat transfer occurs during a short period of time. This implies that the measured transient temperatures data can be separated into two different parts: (1) a short time scale, purely one-dimensional and from which the spiral temperature can be determined, and (2) a longer time scale including the heat transfer in the transverse direction of the glass and that of overall device. Kuvshinov et al. (2011) suggest a function to distinct these two parts for a similar application and is used here:

$$T(t)-T_0=\underbrace{(T_f-T_0)\left(1-\exp\left\{-\frac{t-t_0}{\tau}\right\}\right)}_{\text{One-dimensional term}}+\underbrace{\beta(t-t_0)}_{\text{Longer time scale}} \qquad \text{(B.4)}$$

To give the best estimate of T_0 and T_f and the parameters τ and β, the sum of the squared difference between the values of $T(t)$ measured and those determined from Eq. B.4 is minimised. As an example, Fig. B.2 shows a typical behaviour of the recorded temperatures with time (symbols) and the best fit (solid line) obtained using Eq. B.4. In this case, the initial and the final temperature are 20.9 and 25.44 °C, respectively, giving a spiral temperature about of 30 °C. This temperature is measured after operation at a higher cooling-water flow rate and is consistent with the level of the bearing temperature recorded (Chapter 5, Fig. 5.6).

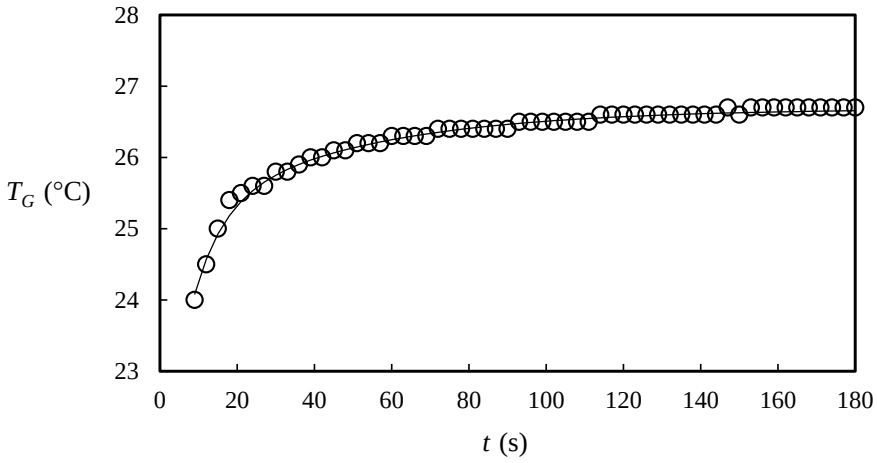

Figure B.2. Transient temperatures measured at the glass window after operation at the higher cooling water flow rate and the fitted function given in Eq. B.4.

Appendix C

Measurement Uncertainties

The experimental values of the mass transfer coefficients were determined using Eq. 3.32 in Chapter 3. It is useful here to re-write this equation to support discussion below:

$$K_L a = \frac{n_L w_{LB} \xi}{L} \frac{Y_{LB}(0) - Y_{LB}(L)}{\overline{\Delta Y_{LB}}} \tag{C.1}$$

$$\text{where} \quad \overline{\Delta Y_{LB}} = \frac{\Delta Y_{LB}(L) - \Delta Y_{LB}(0)}{\ln\left[\Delta Y_{LB}(L) / \Delta Y_{LB}(0)\right]} \quad \text{with} \qquad \Delta Y_{LB} = Y_{LB}^{*} - Y_{LB}$$

As mentioned in Chapter 5, three measured quantities are used to calculate $K_L a$ from the above equation: the liquid flow rate, the gas flow rate and the bulk solute mole fraction at the exit of the liquid phase. As one might note, the gas flow rate does not appear explicitly in Eq. C.1 but it is needed to calculate $Y_{VB}(0)$ from overall solute mole balance. In addition, the molar density of the liquid phase (n_L) must be known to calculate $K_L a$ from Eq. C.1. In deriving Eq. C.1 (Chapter 3), constant flow rates and properties were assumed while the water evaporation together with the solute transfer changes the phase flow rates and n_L along the channel. The uncertainty due to flow rate variation can be evaluated by recalculating $K_L a$ using the inlet phase flow rates rather than average values for each data point and noting the change. The results of such sensitivity analysis are shown in Fig. C.1 where the data are shaded such that the dark colour stands for the small gas flow rate used in the experiments. Similarly, uncertainty associated with n_L was assessed by using the value for pure water instead of the average molar densities of inlet and outlet stream and the results are shown in Fig. C.2. Eventually, there is an uncertainty associated with measuring the solute mole fraction in the outlet liquid stream. This was determined by calculating the change in mass transfer coefficient when the measured mole fraction was increased by one rms deviation which is within the range of uncertainties of the calibration curves given in Chapter 5 (Table 5.2).

As one can see in Figs. C.1, C.1 and C.3, the changes associated with the experimental measurements affect the data, in general, at both high and small values $-f'q_n$, reaching for some points more than 20%. Even though 20% will not change significantly the conclusions drawn in Chapter 7, the maximum accepted error in this work was taken to be not more than 12%. So all data for which the change associated with any one of the above tests exceeded 12% were excluded from the final data. This measure is considered to be a conservative estimate of the maximum uncertainty in the data presented for mass transfer coefficient and specific throughput.

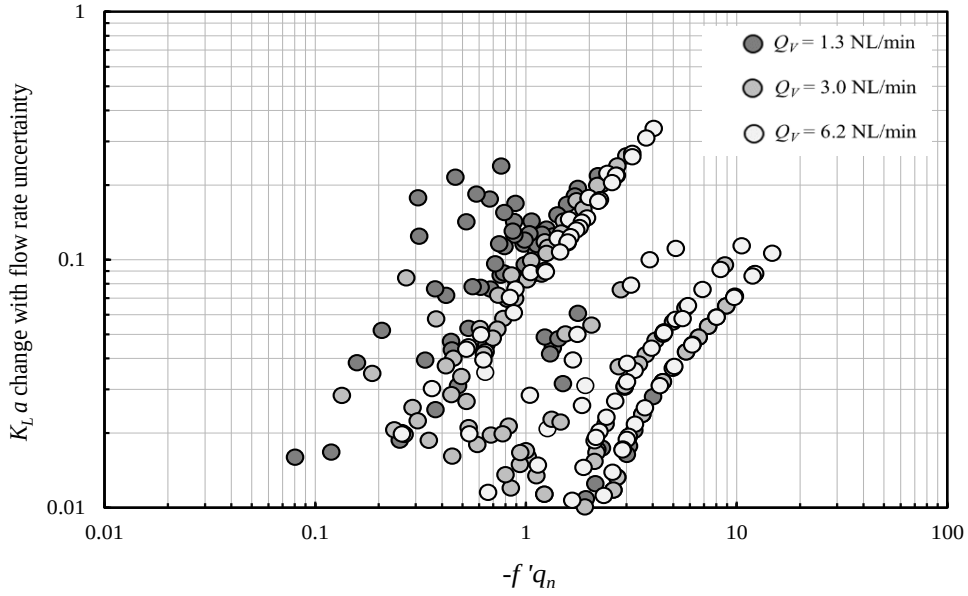

Figure C.1. Mass transfer coefficient variation with phase flow rates uncertainty.

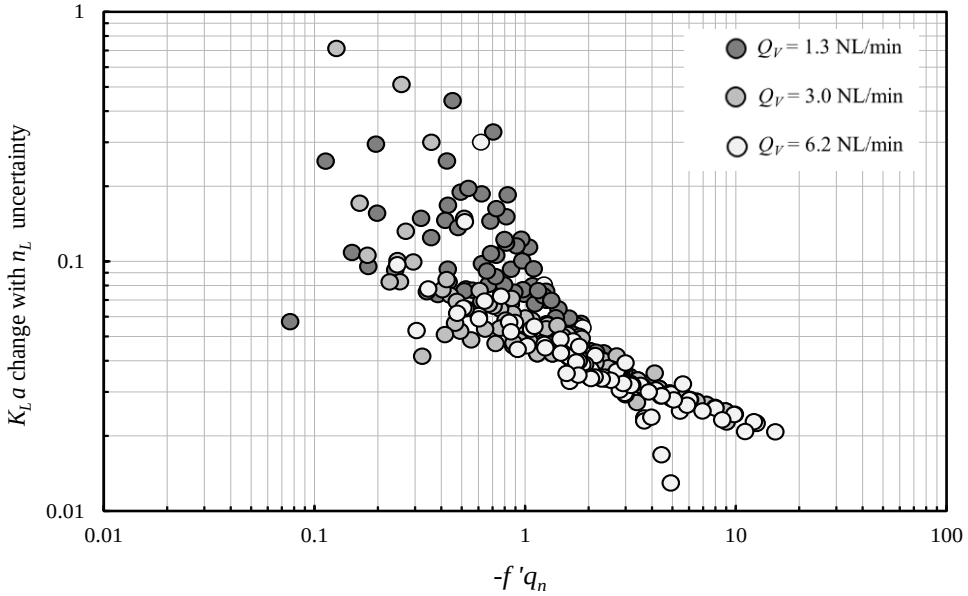

Figure C.2. Mass transfer coefficient variation with uncertainty of the liquid phase molar density.

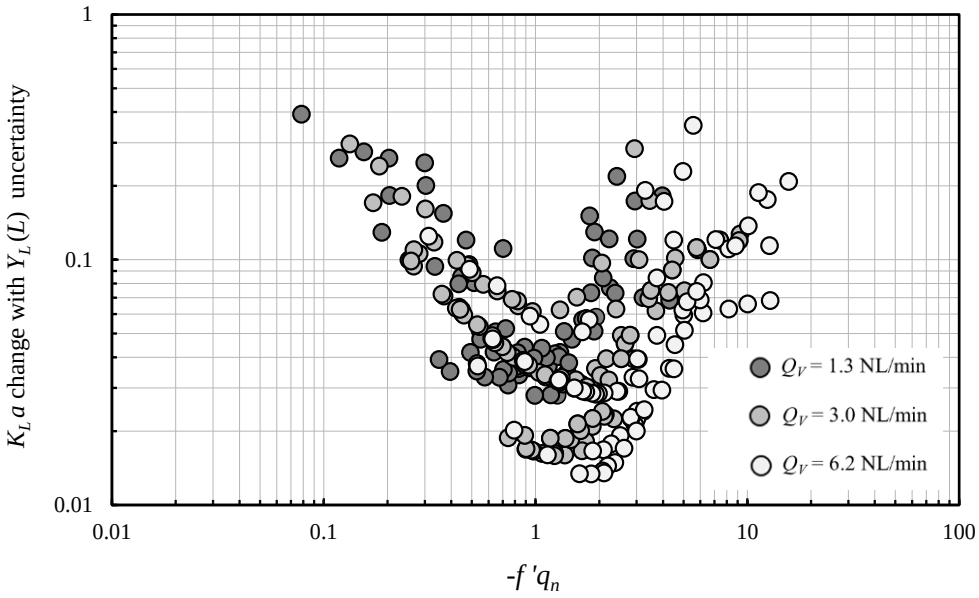

Figure C.3. Mass transfer coefficient variation with uncertainty of measuring the solute mole fraction in the exiting liquid.

Appendix D

List of Chemical Materials Used

In all experiments, the tested solutions were prepared experimentally using deionised water, which is supplied from a Milli-Q system, and one of the organic solutes listed in Table D.1:

Table D.1. Purities of the four organic solutes used in the experiments.

Name	**Formula**	**Purity**	**Manufacturer**
Ethanol	C_2H_6O	99.8%	Sigma-Aldrich
Acetonitrile	C_2H_3N	99.9%	Sigma-Aldrich
Acetone	C_3H_6O	99.9%	Sigma-Aldrich
2-Butanon (MEK)	C_4H_8O	99.7%	Acros organics

Appendix E

Gas Chromatography (GC) and Spectrophotometer Calibration

For each analytical instrument used in this work, the calibration process was repeated three times using new standard solutions in each time. As mentioned, gas chromatography was used to analyse the ethanol and acetonitrile solutions and spectrophotometry for acetone and MEK solutions. The measurements of the three calibration processes are gathered in a single plot for each instrument and are shown in the below figures along with the fitting functions. The uncertainty in the proposed functions was quantified using relative Root Mean Square (rms) error:

$$\text{rms} = \frac{\sqrt{\sum_{i=1}^{N}(\hat{X}_i - X_i)^2}}{X_{\max} - X_{\min}} \qquad \text{(E.1)}$$

where $\hat{X}_i$ is the predicted value by the function, X_i observed value and N the number of the samples.

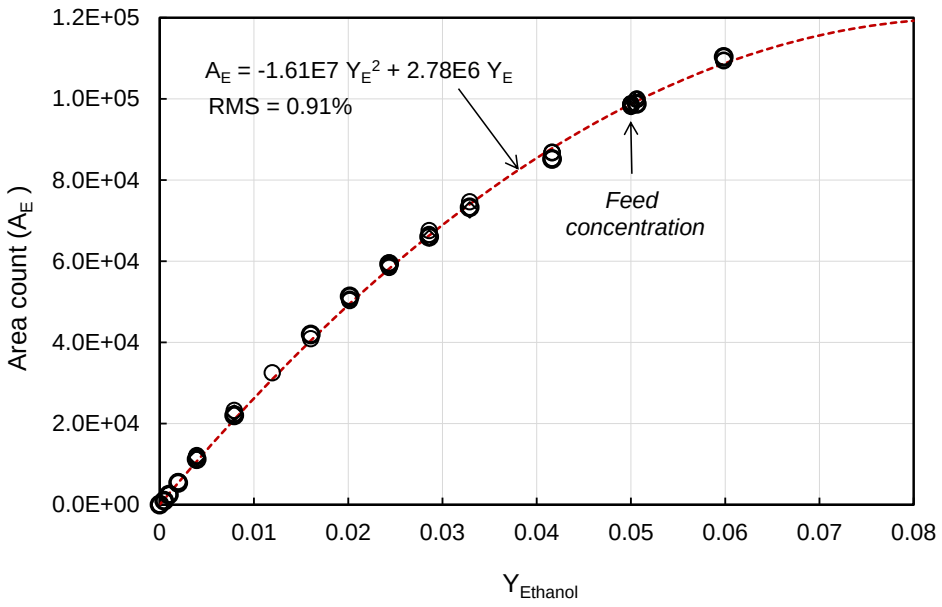

Figure E.1. Area count of ethanol peaks detected by GC-TCD (Varian 3900) as a function of ethanol mole fraction in the liquid phase.

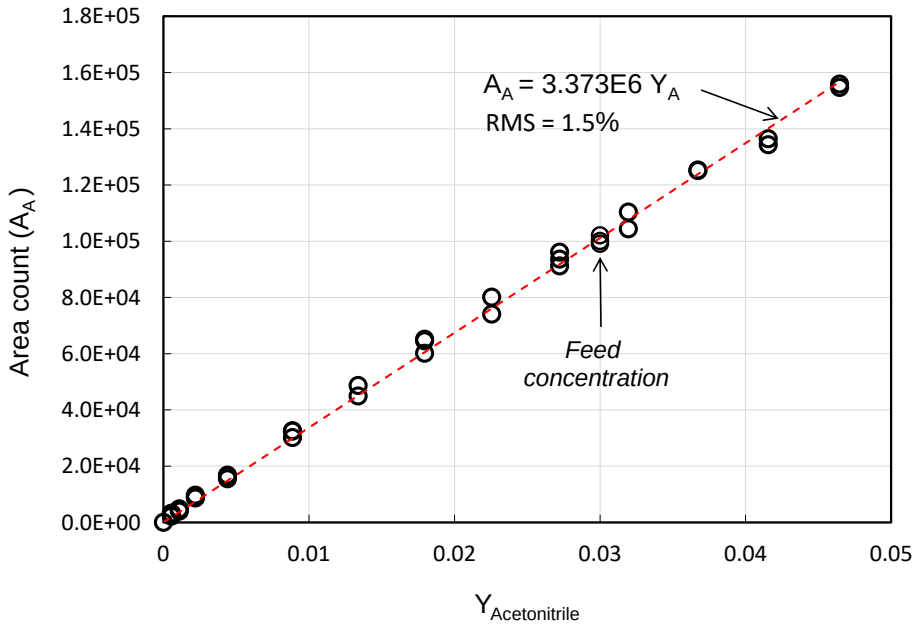

Figure E.2. Area count of acetonitrile peaks detected by GC-FID (Perkin Elmer AutoSystem XL) as a function of acetonitrile mole fraction in the liquid phase.

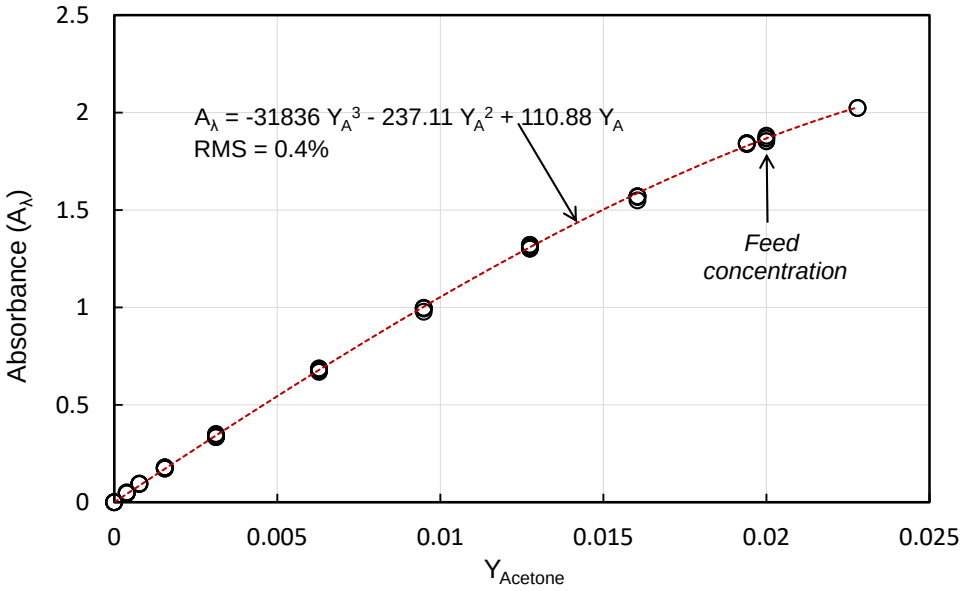

Figure E.3. UV absorbance of acetone solutions measured at a wavelength of 280 nm as a function of acetone mole fraction. The measurements were taken using spectrophotometer (Ultrospec 2100 Pro)

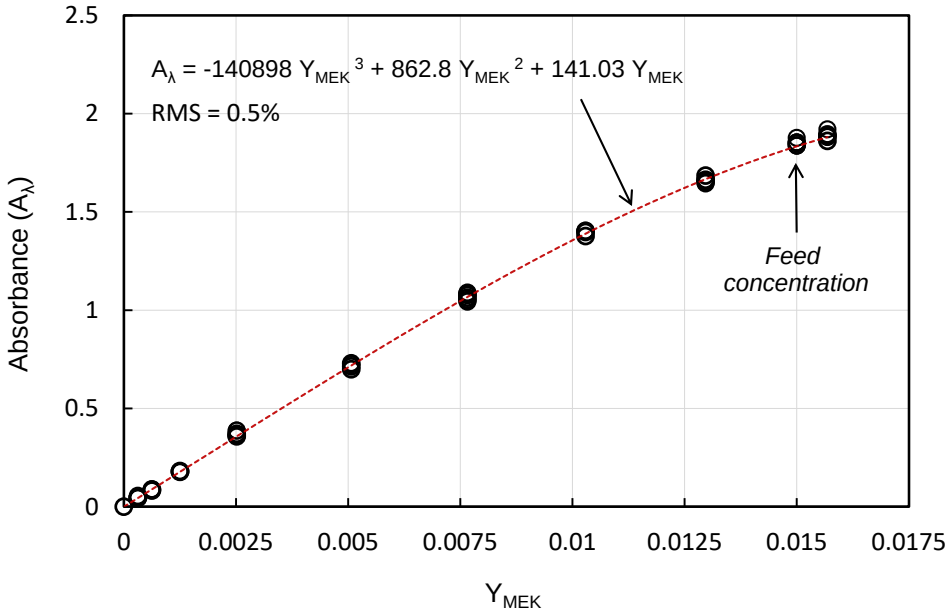

Figure E.4. UV absorbance of MEK solutions measured at a wavelength of 280 nm as a function of MEK mole fraction. The measurements were taken using spectrophotometer (Ultrospec 2100 Pro)

Appendix F

Activity Coefficient Determination

Modified Raoult's law was employed to predict the equilibrium data for each phase and solute system since all the selected solutes form non-ideal solutions with water. In the law, the departure from the non-ideality is represented by the solute activity coefficient in the liquid phase (γ). This parameter must be determined to obtain a reliable vapour-liquid equilibrium data and hence determine the solute equilibrium distribution. In this work, the UNIQUAC model (short for **UNI**versal **QUA**si**C**hemial) is used to estimate γ because of its flexibility to fit all the selected systems (Poling and Prausnitz, 2001). Also, it has only two adjustable parameters per binary system. These parameters can be estimated uniquely for each tested solute-water mixture from only two experimental data, allowing the determination of γ over the whole range of mole fractions. Here, the model equations are presented and the approach that leads to estimating γ for each phase and solute system is given.

F.1 UNIQUAC Model

The UNIQUAC model is a semi-empirical equation proposed for estimating the activity coefficients for a wide range of solutions, including ethanol, acetonitrile, acetone and MEK (Abrams and Prausnitz, 1975; Anderson and Prausnitz, 1978). For each solution, the model gives the activity coefficient for the solute (designated by 1) and water (designated by 2) as follows:

$$1\mathrm{n}\,\gamma_{12} = 1\mathrm{n}\frac{\Phi_1}{Y_{L1}} + \left(\frac{z}{2}\right) q_1 \ln\frac{\theta_1}{\Phi_1} + \Phi_2\left(l_1 - \frac{r_1}{r_2} l_2\right) - q_1' \ln\left(\theta_1' + \theta_2'\tau_{21}\right) + \theta_2' q_1'\left(\frac{\tau_{21}}{\theta_1' + \theta_2'\tau_{21}} - \frac{\tau_{12}}{\theta_2' + \theta_1'\tau_{12}}\right) \tag{F.1}$$

$$1\mathrm{n}\,\gamma_{21} = 1\mathrm{n}\frac{\Phi_2}{Y_{L2}} + \left(\frac{z}{2}\right) q_2 \ln\frac{\theta_2}{\Phi_2} + \Phi_1\left(l_2 - \frac{r_2}{r_1} l_2\right) - q_2' \ln\left(\theta_2' + \theta_1'\tau_{12}\right) + \theta_1' q_2'\left(\frac{\tau_{12}}{\theta_2' + \theta_1'\tau_{21}} - \frac{\tau_{21}}{\theta_1' + \theta_2'\tau_{21}}\right) \tag{F.2}$$

where Y_L is the component mole fraction and z is a constant and taken to be 10 as suggested in Anderson and Prausnitz (1978). The other parameters appearing in Eqs. F.1 and F.2 are Φ and θ which are the fraction of molecule size (segment fraction) and molecule outer surface area (area fraction), respectively, and they are given with θ', l_1 and l_2 as:

$$\Phi_1 = \frac{Y_{L1} r_1}{Y_{L1} r_1 + Y_{L2} r_2} \quad ; \quad \Phi_2 = \frac{Y_{L2} r_2}{Y_{L1} r_1 + Y_{L2} r_2} \tag{F.3}$$

$$\theta_1 = \frac{Y_{L1} q_1}{Y_{L1} q_1 + Y_{L2} q_2} \quad ; \quad \theta_2 = \frac{Y_{L2} q_2}{Y_{L1} q_1 + Y_{L2} q_2} \tag{F.4}$$

$$\theta'_1 = \frac{Y_{L1} q'_1}{Y_{L1} x_1 q'_1 + Y_{L2} q'_2} \quad ; \quad \theta'_2 = \frac{Y_{L2} q'_2}{Y_{L1} q'_1 + Y_{L2} q'_2} \tag{F.5}$$

$$l_1 = \left(\frac{z}{2}\right)(r_1 - q_1) - (r_1 - 1) \quad ; \quad l_2 = \left(\frac{z}{2}\right)(r_2 - q_2) - (r_2 - 1) \tag{F.6}$$

The parameters r, q and q' in the above equations are constants. These constants depend on the molecular-structure of the pure component where r represents the molecule size and q and q' are the molecule external surface area and the surface interaction, respectively. For the most components, q' has the same value as q except those that have $-OH$ group in their molecular-structure (e.g. ethanol and water). For these components, q' value is different than the molecular surface area (q) and this difference should be considered to obtain better results as recommended by Anderson and Prausnitz (1978). For the studied solutes and water, these parameters are given in Table F.1 and can be used directly in Eqs. F.3 to F.6 to calcaulate the structural parameters for these components.

Table F.1. Molecule Parameters for the solutes and water (Anderson and Prausnitz,1978).

Component	**Ethanol**	**Acetonitrile**	**Acetone**	**MEK**	**Water**
r	2.11	1.87	2.57	3.25	0.92
q	1.97	1.72	2.34	2.88	1.40
q'	0.92	1.72	2.34	2.88	1

The further variables appearing in Eqs. F.1 and F.2 are τ_{12} and τ_{21}. These two variables are expressed as:

$$\tau_{12} = \exp\left(-\frac{a_{12}}{T}\right) \quad ; \quad \tau_{21} = \exp\left(-\frac{a_{21}}{T}\right) \tag{F.7}$$

As one might see, τ_{12} and τ_{21} include the effect of temperature on the activity coefficient and also they have two variables (a_{12} and a_{21}). These are the UNIQUAC parameters and are independent of the component mole fraction but relatively dependent on the temperature.

Now, it is clear from Eqs. F.1 and F.2 that the activity coefficient is a function of component mole fraction, temperature, a_{12} and a_{21} which imply through τ_{12} and τ_{21}, and the structural parameters. For the studied systems, once the type of solute has been specified, the structural parameters for the solute and water are determined (i.e. Φ, θ, θ' and l) from Eqs. F.3 to F.6 using the values of r, q and q' given in Table F.1. At a given temperature, this leaves only a_{12} and a_{21} in Eq. F.7 as unknown variables. These parameters can be found from solving Eqs. F.1 and F.2 simultaneously using two activity coefficients data: γ_{12} for the solute and γ_{21} for the water. The values of a_{12} and a_{21}, once determined at a given temperature, are fixed and uniquely can be used to estimate the solute activity coefficient from Eq. F.1 at a given mole fraction and hence determine the equilibrium data using Modified Raoul's law over the range of interest of the mole fractions as described in Chapter 6.

F.2 Binary Parameters Determination

At a given temperature, the UNIQUAC parameters (a_{12} and a_{21}), as mentioned, must be determined from experimental data for each single solution. One of the possible sources of data is the activity coefficient at infinite dilution. These data are available and provide two experimental points for a binary system: the activity coefficient of solute (1) in water (2) at infinite dilation (γ_{12}^{∞}) and the value at the other end which is the activity coefficient of water (2) in solute (1) at infinite dilution (γ_{21}^{∞}). For each solute-water mixture, the values of γ_{12}^{∞} and γ_{21}^{∞} extracted from literature are given in Table F.2 with the corresponding temperatures and references. Some of these values are taken directly

and others are interpolated linearly since the change in activity coefficient is relatively linear and small with temperature for the selected solutes over the relevant range of temperatures (Tochigi and Kojima, 1976; French, 1987; Atik et al., 2004).

Table F.2. The experimental values of γ_{12}^{∞} and γ_{21}^{∞}.

System	T(°C)	γ_{12}^{∞}	γ_{21}^{∞}	*Ref.*
Ethanol (1) - Water (2)	30	5.03	2.58	[1],[2],[3],[4],[5]
	49	5.38	2.36	[1],[2],[3],[4],[5]
Acetonitrile (1) - Water (2)	30	11.3	7.78	[6]
	49	12.63	6.81	[6],[7],[8]
Acetone (1) - Water (2)	30	7.96	6.37	[9],[10]
	49	10	5.08	[8],[10]
MEK (1) - Water (2)	49	35.5	7.31	[1],[11]

[1] Atik et al. (2004)
[2] Pividal et al. (1992)
[3] Brandani et al. (1991)
[4] Schmidt (1980)
[5] de Nevers (2012)
[6] Kojima, et al. (1997)
[7] French (1987)
[8] Hovorkaa et al. (2002)
[9] Shaffer and Daubert (1969)
[10] Bergmann and Eckert (1991)
[11] Tochigi and Kojima (1976)

The values listed in Table F.2 are used to estimate a_{12} and a_{21} using Eqs. F.1 and F.2. In these equations, the mole fraction of solute and water at infinite dilution (i.e. Y_{L1} and Y_{L2}) are set equal to 10^{-4} in all the calculations. For each solute-water mixture at a given temperature, the values of a_{12} and a_{21} are found by adjusting their values to minimise the sum of the squared difference between γ_{12}^{∞} and γ_{21}^{∞} calculated from Eqs. F.1 and F.2 and the experimental values given in Table F.2. This is made using values of a_{12} and a_{21} reported in literature at different temperatures as initial guess since these parameters are not strongly dependent on temperature in general (Anderson and Prausnitz, 1978; Iwakabe and Kosuge, 2002; Rasoul, 2014). Table F.3 gives the best estimate of a_{12} and a_{21} for each system at the spiral temperatures. These values can be used in Eq. F.1 to estimate the activity coefficient for each system over the whole range

of mole fractions. However, it is useful to test the approach of finding a_{12} and a_{21} by comparing, the prediction of the UNIQUAC model with some experimental data and that will be discussed in the next section.

Table F.3. Binary Parameters for the studied systems estimated from the data listed in Table F.2 and UNIQUAC equations.

System	T(°C)	a_{12}(K)	a_{21}(K)
Ethanol (1) - Water (2)	30	-70.16	307.91
	49	-89	367.44
Acetonitrile (1) - Water (2)	30	597.71	-130.94
	49	493.73	-82.9
Acetone (1) - Water (2)	30	428.95	26.06
	49	672.54	10.23
MEK (1) - Water (2)	49	545.48	-5.39

F.3 Comparison with Experimental Data

To test the approach used to estimate a_{12} and a_{21}, which is based on using values of activity coefficients at infinite dilution, a comparison is made with experimental data available for the acetonitrile-water system at 35 °C. These data are reported in French et al. (1987). At 35 °C, the values of a_{12} and a_{21} are estimated using γ_{12}^{∞} = 11.58 and γ_{21}^{∞} = 7.61 (reported in that same work) and they are found to be 410.8 K and 47.4 K, respectively. From Eq. F.1, the activity coefficients of acetonitrile in water (γ_{12}) are estimated over the whole range of mole fraction using the values of a_{12} and a_{21} along with the structural parameters of acetonitrile. Fig. F.1 shows the estimated activity coefficients using the UNIQUAC model (dash line) and the experimental data (red circles). As one can see, the experimental data are captured very well by the UNIQUAC model over the whole range of mole fractions. This suggests that a reliable prediction of the activity coefficients can be obtained using parameters derived from γ_{12}^{∞} and γ_{21}^{∞}.

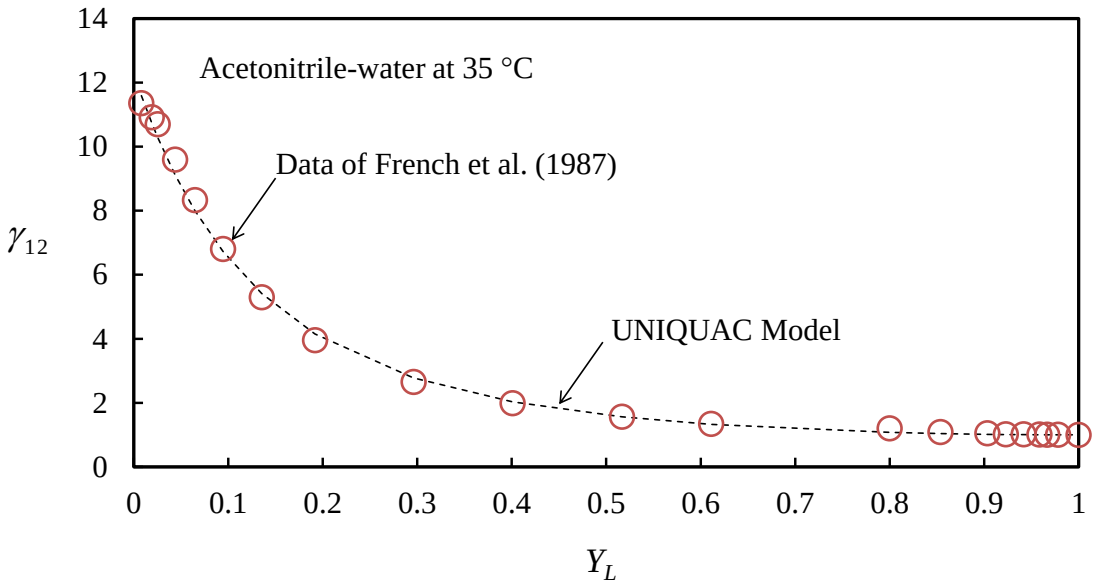

Figure F.1. Experimental activity coefficients of acetonitrile-water system at 35 °C and the predicted values using UNIQUAC model.

F.4 Results and Comparison with UNIFAC Model

For each system, the activity coefficients at the experimental range of temperatures are estimated using a_{12} and a_{21} listed in Table F.1. These results are shown in Fig. F.2 where the data are represented by red squares. Also, the results are compared to corresponding values predicted by UNIFAC model. This model treats the molecules as functional groups and has interaction parameters which are independent of temperature (Weidlich and Gmehling, 1987). Thus, it is a pure theoretical model and provides independent prediction of the activity coefficient and hence a reliable assessment of the UNIQUAC model prediction can be made. UNIFAC model has many variants. However, Dortmund-Modified UNIFAC (DMD-UNIFAC) is incorporated in ASPEN PLUS software (version 8.4) and is chosen to achieve the comparison since it produces good results for a large number of systems (Weidlich and Gmehling, 1987). The activity coefficients predicted by DMD-UNIFAC model for each system at the temperature of interest are shown in Fig. F.2 (solid line). The results show that there is a quantitate agreement between the values predicted by the UNIQUAC model supported by experimental data and the DMD-UNIFAC. Both models predict the activity coefficient over the full range of mole fractions at the same degree of precision except the evident differences over the small values of Y_L for acetonitrile, acetone and MEK systems at

49 °C. In either case, the DMD-UNIFAC model underpredicts the activity coefficient resulting in about 5% reduction in the value of f' for MEK system as a maximum. This difference could be attributed to two reasons. First, the uncertainties in the values of γ_{12}^{∞} and γ_{21}^{∞} used in UNIQUAC calculations. Second, the fact that the parameters of UNIFAC models do not take into account the effect of temperature, thus, the prediction of UNIFAC model might be less accurate at 49 °C which is considered relatively high temperature. Thus, for the worst-case scenario, 5% increasing in the value of f' for MEK system is the maximum error can be expected. Such error leads to about a few percent increasing in the mass transfer coefficient according to a computation made using the 2-D model for MEK system while for the others systems the error in estimating the activity coefficients and hence f' is negligible.

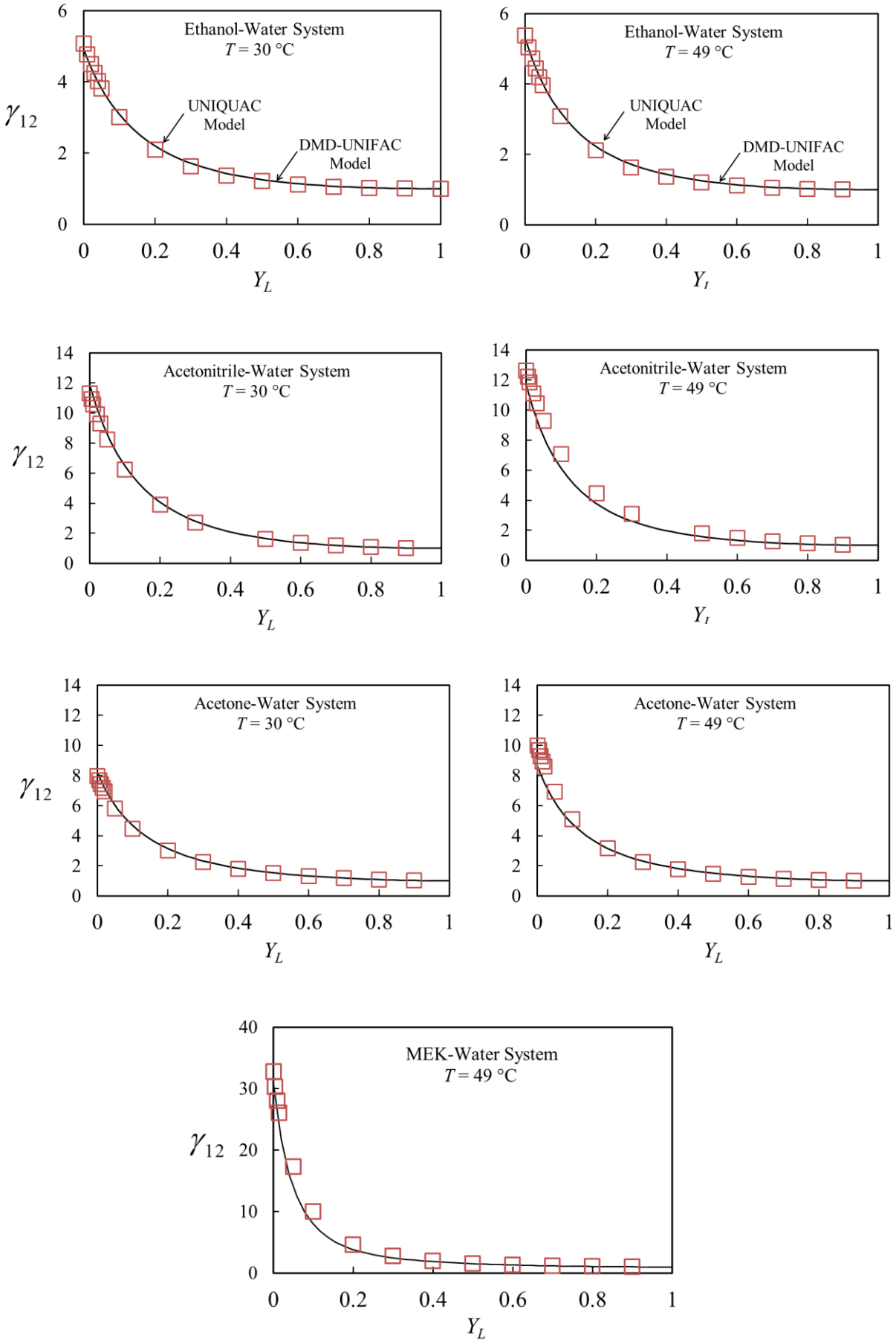

Figure F.2. The values of the solutes activity coefficients in water predicted by the UNIQUAC model and these by ASPEN PLUS using DMD-UNIFAC model.